Theris
2134

DIGITAL PROCESSING OF SATELLITE IMAGES FOR LITHOLOGICAL DISCRIMINATION AND CLASSIFICATION IN ARID REGIONS

Thesis
Submitted in fulfilment of the
requirement of the degree of
Doctor of Philosophy
at the

Department of Environmental Science
University of Stirling

by

Mohammad Abdulaziz Omar Al-Dail

January 1993

UNIVERSITY OF STIRLING LIBRARY
I
7/93

ACKNOWLEDGEMENT

I would like to express my sincere thanks to many individuals and organisations who helped me in various ways in writing this research .

First, I am greatfull to my supervisor Dr Alistair I. Watson, Department of Environmental Science, University of Stirling for his persistent supervision, encouragement and thoughtfull comments throughout my period of study, and to Professor Michael F. Thomas, Department of Environmental Science, University of Stirling For his supervision, support and constructive criticism.

I am also greatfull to the staff of the Environmental Science Department, in particular, Professor Donald Davidson for his friendly advice and comments in various subjects of my study; John McArthur chief technician, for his help in the use of remote sensing facilities at the early stage of this study; W. Jamieson, cartographer and C. Anderson technician for their help in producing some of the figures in this thesis.

I am also greatfull to the Deputy Ministry for Mineral resources (DGMMR) in Jeddah, in particular Mr. M. Rowaihi for providing a number of Geological maps and Reports and to Mr.A.al-dail,jeddah,for sending some of the reports needed. I would like to thank the Geology department of King Saud university, Riyadh for producing thin sections to several rock samples needed during my field visit.

The financial support by King Abdul-aziz City for Science and Technology (KACST) Riyadh is greatfully acknowledged.

Finally, I am indebted to all members of my family in particular my brother Saud for his help in different ways. My wife deserves a special thanks for her understanding, patience and unquestioning support, particularly in difficult moments.

DEDICATION

To my Father and Mother

and to my wife and my three childrens

DECLARATION

This Thesis is a record of the work carried by me in the department of environmental science, Stirling Univrsity. The work described herein is my own, except where indicated otherwise .

M. Al-Dail

TABLE OF CONTENTS

Acknowledgements II

Dedication III

Declaration IV

Table of Contents V

List of Figures X

List of Tables XV

Abstract XIX

CHAPTER 1: INTRODUCTION

1.1 Development of remote sensing 1

1.2 Development in geological remote sensing 4

1.3 Study objectives 6

1.4 Test area selection 7

1.5 Structure of the thesis 9

CHAPTER 2: TEST AREAS LOCATION AND GENERAL GEOLOGY

2.1 Introduction 11

2.2 Geological setting 13

2.3 Test areas 19

2.3.1 Silsilah ring complex (test area 1) 20

2.3.2 Jabal ar Raha (test area 2) 25

2.3.3 Aban Ahmar (test area 3) 29

2.3.4 Aban Asmar (test area 4) 34

CHAPTER 3: PHYSICAL PRINCIPLES OF REMOTE SENSING

3.1 Introduction 41

3.2 Electromagnetic radiation and spectrum 41

3.2.1 The visible region 45

3.2.2 The infrared (IR) region 45

3.3 Interaction of electromagnetic radiation with matter 46

3.3.1 Electron Transition 50

3.4 Interaction of electromagnetic radiation with earth's atmosphere 54

3.4.1 Scattering 56

3.4.2 Absorbtion 56

3.5 Interaction of EM radiation with rocks and minerals 57

3.5.1 Visible and NIR spectra 58

3.5.2 Mid IR spectra 59

3.6 Summary 63

CHAPTER 4: LANDSAT SATELLITE AND IMAGE PROCESSING SYSTEMS

4.1 Introduction 65

4.2 Landsat satellite programmes 65

4.2.1 Landsat MSS 70

4.2.2 Landsat TM 72

4.3 Computer compatable tape and data format 75

4.4 Digital processing systems 76

4.4.1 Microvax II 78

4.4.2 R-CHIPS software 79

4.4.3 IDRISI software 79

4.5 Preparation of the data 80

4.6 Summary 81

CHAPTER 5: DIGITAL IMAGE PROCESSING TECHNIQUES

5.1 Introduction 82

5.2 Pre-processing 84

5.2.1 Atmospheric correction 84

5.3 Contrast enhancement 88

5.3.1 Linear contrast stretch 90

5.3.2 Histogram equalise stretch 91

5.3.3 Balance contrast enhancement technique (BCET) 93

5.4 Spatial filtering 94

5.5 Colour composite and display 96

5.6 Band ratio 101

5.7 Principal component analysis (PCA) 103

5.8 Decorrelation stretch 105

5.9 Canonical transformation 107

5.10 Hue-Saturation-Intensity (HSI) transform 110

5.11 Summary 112

CHAPTER 6: LITHOLOGY DISCRIMINATION, METHODOLOGY AND RESULT

6.1 Introduction 114

6.2 Methodology 115

6.2.1 Principal component (PCA) and band ratio analysis 115

6.2.2 Canonical regression 116

6.2.3 Colour composite 118

6.2.4 Decorrelation stretch 120

6.2.5 Hue-Saturation-Intensity (HSI) transformation 120

6.3 Results 123

6.3.1 Silsilah ring complex (study area 1) 123

6.3.1.1 Principal component (PCA) and band ratio analysis 123

6.3.1.2 Canonical regression 133

6.3.1.3 Band colour composite and HSI transformation enhancement 139

6.3.2 Jabal ar Raha (study area 2) 146

6.3.2.1 Principal component (PCA) and band ratio analysis 146

6.3.2.2 Band colour composite and HSI transformation enhancement 152

6.3.3 Aban Ahmar (study area 3) 157

6.3.3.1 Principal component (PCA) and band ratio analysis 157

6.3.3.2 Band colour composite and HSI transformation enhancement 163

6.3.4 Aban Asmar (study area 4) 168

6.3.4.1 Band ratio analysis 168

6.3.4.2 False colour composite and HSI transformation enhancement 170

6.4 Summary and conclusion 175

CHAPTER 7: DIGITAL CLASSIFICATION TECHNIQUES:CONCEPT AND RESULTS

7.1 Introduction 180

7.2 Digital classification in geology 182

7.3 Classification strategies 183

7.4 Classification algorithms 184

7.4.1 The unsupervised maximum likelihood method 184

7.4.1.1 Clustering 184

7.4.1.2 Maximum likelihood 186

7.4.2 Watershed method 187

7.5 Accuracy assessment 195

7.6 Method of investigation 198

7.7 Results 200

7.7.1 Silsilah ring complex test area 201

7.7.2 Jabal ar Raha test area 214

7.8 Summary and conclusion 224

CHAPTER 8: CONCLUSIONS AND SUGGESTIONS FOR FUTURE WORK

8.1 Conclusions 226

8.2 Suggestions for future work 230

REFERENCES 233

LIST OF FIGURES

2.1	Map showing the location of the Arabian Shield.	14
2.2	Distribution of various rocks in the Arabian Shield.	15
2.3	Location map of the four test areas.	17
2.4	Diagram representing the geological evolution of rock units in the northeastern Arabian Shield.	18
2.5	Geologic map of Silsilah ring complex, test area 1 .	22
2.6	Field photograph showing the Hadhir aplite (Ha) on top of Fawwarah alkali-feldspar granite (Fag).	23
2.7	Geologic map of Jabal ar Raha, test area 2.	28
2.8	Geologic map of Aban Ahmar, test area 3.	33
2.9	Field photograph showing the relatively flat peneplain and the sand dune field that are exposed west of Aban Ahmar test area.	36
2.10	Field photograph showing the saline encrustations (Sabkha deposits).	36
2.11	Geologic map of Aban Asmar, test area 4 .	38
3.1	Electromagnetic wave with the electric (E) and magnetic (M) components orthogonal to each other .	43
3.2	The electromagnetic spectrum, the diagram shows parts that are important in remote sensing.	44
3.3	Colour .	48
3.4	The main atmospheric windows throughout the electromagnetic spectrum .	48
3.5	a) Specular reflection from a smooth surface; b) defused (Lambartian) reflection from rough surface; c) semi-defused reflection (natural bodies).	51
3.6	Reflection spectra of ferric-iron-bearing minerals showing decrease in reflectivity towards the blue, caused by charge transfer effect .	53

3.7 Reflection spectra of particulate samples of different materials, all of which display sharp absorption edge effect. 53

3.8 Spectra of minerals that contain ferrous ions in different crystal fields. All the absorption features are due to the crystal field effect. 55

3.9 Reflectance spectra of different hydroxyles and carbonate minerals that show different absorption features caused by the vibration process: a) clay minerals; b) water bearing minerals; c) carbonates . 55

3.10 Spectral reflectance showing the effect of adding varying amounts of magnetite to olivine, causing a reduction in reflectivity . 62

3.11 Reflectance spectra of different igneous rocks, arranged in order of decreasing acidity from top to bottom. 62

4.1 Distribution of Landsat ground receiving stations. 69

4.2 Landsat-4 and -5 sun-synchronous orbit. 71

4.3 Scanning arrangement of MSS on board Landsat-1, -2 and -3. On Landsat-4 and -5 the altitude is 705 km and the scan angle is 14.9. 71

4.4 Thematic mapper optical system. 74

4.5 Data format of Landsat tape: (a) band sequential (BSQ); (b) band interleaved (BIL). 77

5.1 TM band-1 image of Silsilah ring complex : (a) is the original image with its corresponding histogram (b). 89

5.2 A simple linear contrast stretch of histogram in Figure 5.1(b). 92

5.3 (a) histogram equalised stretch of Figure 5.1(b). 92

5.4 The effect of (Laplacian add back) edge enhancement technique (b), on the principle component image of Aban Ahmar test area. 97

5.5 Red-green-blue colour cube . 99

5.6 The steps of principal component transformation; see text for explanation . 106

5.7 Hue-saturation-intensity (HSI) hexcone. 106

6.1 Flow diagram of the processing steps used for canonical analysis. 117

6.2 Principal component colour composite (PCC) image resulting from the principal component transformation of the six reflected TM bands of Silsilah ring complex, in which PC3, PC2 and PC1 were displayed as red, green and blue respectively. 130

6.3 Colour ratio composite (CRC) image of Silsilah ring complex in which TM 5/4, TM 5/1 and TM 5/7 band ratios were displayed as red, green and blue respectively. 130

6.4 Images (a) to (e) represent the gray level images of the individual canonical components of Silsilah ring complex. 140

6.5 Canonical component colour composite of Silsilah ring complex, in which canonical components` 1, 2 and 3, were displayed as red, green anbluerespectively.142

6.6 Band colour composite (CRC) image of Silsilah ring complex in which TM Band-7, TM Band-4 and TM band-1 were displayed as red, green and blue respectively. 144

6.7 The colour composite image of Figure 6.6 after hue-saturation-intensity enhancement. 144

6.8 Principal component colour composite (PCC) image resulting from the principal component transformation of the six reflected TM bands of Jabal ar Raha ring complex, in which PC3, PC2 and PC1 were displayed as red, green and blue respectively. 150

6.9 Colour ratio composite (CRC) image of Jabal ar Raha ring complex in which TM 5/4, TM 5/1 and TM 5/7 band ratios were displayed as red, green and blue respectively. 150

6.10	Band colour composite (CRC) image of Jabal ar Raha ring complex in which TM Band-7, TM Band-4 and TM band-1 were displayed as red, green and blue respectively.	155
6.11	The colour composite image of Figure 6.10 after hue-saturation-intensity enhancement.	155
6.12	An enlarged (zoom in) part of image in Figure 6.11.	156
6.13	Principal component colour composite (PCC) image resulting from the principal component transformation of the six reflected TM bands of Aban Ahmar ring complex, in which PC3, PC2 and PC1 were displayed as red, green and blue respectively.	161
6.14	Colour ratio composite (CRC) image of Aban Ahmar ring complex in which TM 5/4, TM 5/1 and TM 5/7 band ratios were displayed as red, green and blue respectively.	161
6.15	Colour composite image of Aban Ahmar, in which TM Band-7, TM Band-4 and TM band-1 were displayed as red, green and blue respectively.	165
6.16	The colour composite image of Figure 6.15 after hue-saturation-intensity enhancement.	167
6.17	Colour ratio composite (CRC) image of Aban Asmar ring complex in which TM 5/4, TM 5/1 and TM 5/7 band ratios were displayed as red, green and blue respectively.	172
6.18	Colour composite image of Aban Asmar, in which TM Band-7, TM Band-4 and TM band-1 were displayed as red, green and blue respectively.	172
6.19	The colour composite image of Figure 6.18 after hue-saturation-intensity enhancement.	173
7.1	a) one-dimensional histogram of band A; b) one-dimensional histogram of band B; c) two-dimensional histogram of bands A and B.	185
7.2	Clustering by the minimum distance to mean algorithm.	186
7.3	Two bands (A and B) feature space with three clusters.	188

7.4	The L structuring element in one of its 6 possible orientations.	193
7.5	(a-f) Theoretical description of the watershed method .	194
7.6	Flow diagram of the procedures used for watershed classification.	196
7.7	Density sliced, digital classified image (map), produced by the watershed algorithm for Silsilah ring complex.	215
7.8	Density sliced, digital classified image (map), produced by the watershed algorithm for Jabal ar Raha.	225

LIST OF TABLES

4.1 Landsat series of satellite, general characteristics. 67

4.2 Landsat MSS and TM sensor specification . 68

6.1 Statistics of Silsilah ring complex area where table (a) describes the correlation matrix between the six TM reflected bands. Table (b) describes the variance, eigenvalues and eigenvectors for each principal component denoted here as (C1 to C6) in which the percentage variance indicates the amount of variance that was picked by each component which is also expressed by the eigenvalue. The relative loading of each band for each component is shown. Table (c) gives the component loading summary. 124

6.2 Summary of colour associated with main lithologies in the colour ratio composite of Silsilah ring complex (Figure 6.3). 132

6.3 Correlation matrix between major element chemical composition of various rock types and the five canonical images (C1 to C5). 135

6.4 Major element chemical composition for the main rock units in Silsilah ring complex. 135

6.5. Statistics of Jabal ar Raha test area where table (a) describes the correlation coefficient between the 6 TM reflected bands. Table (b) describes the variance, eigenvalues and eigenvectors for each principal component in which the percentage variance indicates the amount of variance that was picked

by each component, and the table gives the relative loading of each band in each component. Table (c) gives the component loading summary. 147

6.6. Summary of colour associated with main lithologies in the CRC image of Jabal ar Raha (Figure 6.9). 151

6.7. Statistics of Aban Ahmar test area where table (a) describes the correlation coefficient between the 6 TM reflected bands. Table (b) describes the variance, eigenvalues and eigenvectors for each principal component in which the percentage variance indicates the amount of variance that was picked by each component which is also expressed by the eigenvalue. The eigenvector indicates the relative loading of each band in each component. Table (c) gives the component loading summary. 159

6.8. Summary of colour associated with main lithologies in the colour ratio composite of Figure 6.14. 162

6.9. Correlation coefficient matrix between the six TM reflected bands of Aban Asmar test area. 171

6.10. Summary of colour associated with main lithologies in the colour ratio composite (Figure 6.17). 171

7.1 (a and b) Confusion matrix produced using the original six reflected TM bands (B1-6) as an input for the maximum likelihood algorithm. 204

7.2 (a and b) Confusion matrix of the watershed classification using the best three classified images produced from the original six reflected TM bands (B1-6); see text for explanation. 206

7.3 (a and b) Confusion matrix produced using three hue images originated from each three adjacent bands of the

reflected TM data as an input for the maximum likelihood classifier. 207

7.4 (a and b) Confusion matrix produced using the same combination in table (7.3) as an input for the watershed classifier. 209

7.5 (a and b) Confusion matrix produced using combinations developed by this study of two hue images originated from the best three principal components and the best three band-ratios (HP 3-2-1) and (HR 5/4-5/1-5/7) as an input for the maximum likelihood classification algorithm. 212

7.6 (a and b) Confusion matrix produced using the same combination as in table (7.5) as an input for the watershed classification. 212

7.7 (a and b) Confusion matrix produced using combinations developed by this study of three hue images originated from the best three bands (HB 7-4-1), the best three principal components (HP 3-2-1) and the best three band ratios (HR 5/4-5/1-5/7) as an input for the maximum likelihood classifier. 213

7.8 (a and b) Confusion matrix produced using the same combination as in table (7.7) as an input for the watershed classification. 214

7.9 (a and b) Confusion matrix produced using three hue images originated from each three adjacent bands of the reflected TM data as an input for the maximum likelihood classifier. 220

7.10 (a and b) Confusion matrix produced using the same combination as in table (7.9) as an input for the watershed classifier. 221

7.11 (a and b) Confusion matrix produced using combinations developed by this study of two hue images originated from the best three principal components (HP 3-2-1) and the best three bands (HB 7-4-1) as an input for the maximum likelihood classifier. 221

7.12 (a and b) Confusion matrix produced from the same combination as in table (7.11) as an input for the watershed classifier. 222

7.13 (a and b) Confusion matrix produced using combinations developed by this study of three hue images originated from the best three bands (HB 7-4-1), the best three principal components (HP 3-2-1) and the best three band ratios (HR 5/4-5/1-5/7) as an input for the maximum likelihood classifier. 223

7.14 (a and b) Confusion matrix produced using the same combination as in table (7.13) as an input for the watershed classifier. 224

ABSTRACT

Satelite images have been used as a complementary information for geological studies. In order to realise the maximum potential of satillite imagery, then improvements are needed, both in the visual presentation of such images, and in their automatic classification , in order to reveal the rock differences. Methods of processing imagery, were evaluated (band ratio, principal components, decorrelated stretch and maximum likelihood) and new (canonical regression, hue-saturation-intensity HSI transform, with modified manipulation, and watershed) were evaluated with respect to their ability to reveal rock differences.

It was found that the HSI method gave the best results, both for visual presentation and automatic classifcation.This method has the ability to enhance both spectral and spatial information simultaneously without any data loss ,which is not the case in the other image enhancement methods (band ratio,principal components or decorrelation stretch).For automatic classification, the 'hue' images produced by the HSI transformation typically gave accurate (91%) classification of all the major rock types. Further, it was shown that the watershed method of classification was superior error rate= 9% to the maximum likelihood method (error rate 14%) for the same inputs. The new method of canonical regression was evaluated and although it was not very successful, the results were encouraging and it was concluded that this method may enable the estimation of the chemical composition of exposed rocks directly from satellite imagery.

CHAPTER ONE

INTRODUCTION

1.1 Development of remote sensing

1.2 Development in geological remote sensing

1.3 Study objectives

1.4 Test area selection

1.5 Structure of the thesis

1.1 Development of remote sensing

The collection of information about an object using a device some distance away from it is the simple and broad means of remote sensing. The remote sensing devices can be grouped according to the type of sensed force field (e.g., static or dynamic) and their modes of operation (Ulaby and Goetz, 1987). Due to the small amplitude of variation in the static field (e.g., gravity, magnetic), the effective altitudinal ranges of sensors measuring such variation usually do not exceed a few hundred meters; therefore they are mounted on low flying aircraft. Sonic sensors, such as those used to measure the depth of the ocean floor, cannot propagate in a vacuum; therefore they cannot be used from a satellite or high-flying aircraft. These restrictions make the electromagnetic sensors the only ones used for monitoring the earth from orbital altitudes. Therefore, a definition of modern remote sensing is restricted to the use of reflected and emitted electromagnetic energy (Goetz et al., 1983).

Electromagnetic sensors are grouped according to their wavelength range (see Chapter 3 for electromagnetic spectrum division) and their mode of operation. A passive sensor detects reflected sunlight or energy emitted from an object, whereas an active sensor supplies its own source of energy, directing it at an object and measuring the reflected energy. RADAR (RAdio Detection And Ranging) is an example of an active sensor, whereas the Thematic Mapper (TM) sensor, used in this study, is an example of the passive remote sensor. Since radar data was not used, the discussion will be confined to passive systems.

Remote sensing has mainly developed from aerial photography. Balloons at an altitude of about 80 meters were used, more than a century ago, to acquire photographs of large areas for topographic (geographic)

mapping. In the succeeding years a number of developments were made in photographic technology and in methods of acquiring these photographs. The advent of airplanes, in the very early years of this century, made aerial photography a very useful tool by providing a more stable and adaptable platform (Estes, 1978). The use of remote sensing techniques, at that time, was mainly limited to the analysis and interpretation of standard black and white aerial photographs (Holz, 1985). Remote sensing from space initially started during the period between 1946 and 1950, when small cameras were carried by captured V-2 rockets to a very high altitude (100 to 320 km). Since then numerous flights involving photography have been made by rockets, ballistic missiles, satellites and manned spacecraft. This has opened another dimension, and concept for remote sensing, by giving the opportunity to observe the earth from a high altitude, with very large areas included in this observation.

Earth observation by satellite-borne sensors initially started in 1960 (Ulaby and Goetz, 1987). The first space photograph of the earth's surface was transmitted by Explorer-6, followed by the Mercury program (1961) which provided a number of excellent photographs (70mm colour) from an automatic camera. Also during the 1960s a further development occurred, with the launch of the first meteorological satellite (TIROS-1) in 1960.

The successful results provided by the early unmanned meteorological satellites (TIROS/NOAA series), and the experiments of the manned spacecraft missions of Mercury, Gemini and Apollo, provided regional views, not easily gained through field or aerial photographic observations. This was accompanied by revolutionary developments in electronics and computers, which made digital image processing a real possibility.

NASA, with the cooperation of the U.S. government, initiated a program of launching a series of Earth Resource Technology satellites (ERTS). This resulted in a series of six orbiting satellites, the first of which was launched July 25, 1972 and renamed in 1975 Landsat-1. This series of satellites marked a new era in space applications that focused on the earth itself (Short, 1982). Landsat-1 represented the first unmanned satellite, specifically designed to collect data about the earth on a systematic, repetitive basis, with medium resolution and multispectral coverage. This satellite proved to be of great importance, as it gave remote sensing world wide recognition, through the "open skies" principle, without any political or copyright restriction. In addition, the cost was low compared to that of aerial photography for the same area. Since 1972, five Landsat satellites have been launched. The data used in this study were collected by the TM sensor on board the current Landsat-5 launched into orbit in March 1984. More discussion about this series of satellites and their on board sensors will be provided later in Chapter 4.

Between 1981 and the present, many short term space experiments have been conducted with, the re-usable space shuttle and aircraft. These experiments have investigated the use of many different sensor systems such as the Shuttle Imaging Radar (SIR-A and SIR-B), imaging spectrometers such as Airborn Imaging Spectrometer (AIS), and solid state electronic scanners such as Modular Optoelectronic Multispectral Scanner (MOMS). MOMS, was the first push-broom scanner system to be tested from space and was flown on space shuttle missions in 1983 and 1984 (Rothery and Francis, 1987). A similar scanner is also found in the French satellite, System Probatoire de l'Observation de la Terre (SPOT), launched into orbit in February 1986.

Digital image processing is concerned with the computer processing of images that are recorded in numerical form. Its general purpose is to enhance the visual appearance of the image, and extract some useful information from it, using mathematical equations in the form of computer programmes. The use of computers to process the image brings the advantage of computer flexibility and precision.

The advent of unmanned satellites, particularly the Landsat series of satellites in 1972, which provided repeatable world wide coverage of the earth's surface in digital format, and the rapid rise of electronics and computers, are regarded as the most important factors in developing remote sensing, and digital image processing technology. This technology permits the processing, analysis and display of huge amounts of information, recorded in different bands, and processes them simultaneously and in a short period of time (Schwengredt, 1983; Gonzales and Wintz, 1987; Sabin, 1987).

1.2 Development in Geological Remote Sensing

Geological use of remotely sensed data, in general, and in arid areas in particular, as a complementary technique for different geological studies, started with the use of black and white aerial photographs; stereo air photos in particular have been used since the 1930s (Goetz, 1989a). This concept extended to the use of space photographs, such as those provided from hand held cameras on Gemini and Apollo spacecraft in 1961. Mission GT-4 of the Mercury program in 1961, provided the first formal photographic experiment from space targeting geology.

Although the spectral bands of the MSS sensor on board Landsat-1 were designed primarily for agricultural studies, its data have

revolutionised the application of imagery to geological studies, by providing synoptic views of the earth's surface, in regions of the electromagnetic spectrum beyond, the aerial photographic film's sensitivity. The study and investigation of the early data of the Landsat series relied mainly on visual interpretation of their images. The rapid development of digital image processing enabled the use of computer and multispectral reflectance analysis, and much lithological and structural information was derived from the data collected by the Landsat series (e.g., Rowan et al., 1974, 1977; Rothery and Milton, 1981; Adams et al., 1982; Podwysocki et al., 1983; Kruse and Rains, 1984; Rothery, 1985; Bodechtel and Frei, 1992).

The possibility, offered by such systems, of providing spectral information beyond the visible part of the spectrum, required an understanding of the way that different objects (e.g, rocks and minerals) respond to, and interact in such spectral regions. Therefore extensive laboratory studies of reflectance spectra for different rocks and minerals, were carried out, mainly by Hunt and co-workers, starting in the early 1970s. Their studies and explanations were of value, and have been used since then, as a basis for discriminating between different minerals in the visible and infrared regions of the electromagnetic spectrum.

The launch of Landsat-4 in July 1982, brought into operation a more advanced sensor, the thematic mapper (TM), in which the geological community had specifically demanded the use of the seventh spectral band, centered at 2.2 μm wavelength (Chavez et al., 1983). A new decade of extensive remote sensing geological studies had started (Henderson and Rock, 1983) and since then, a number of geological studies have been conducted, using the TM sensor on board Landsats-4 and -5. Results, from laboratory and field spectra, indicate the importance of using high spectral

resolution sensors in the 0.4-2.5 μm bands. Therefore, several studies have used the data from finer spectral and spatial resolution sensors such as (AIS) to identify specific alteration mineral assemblages (e.g., Hutsinpiller and Taranik, 1986; Kruse ., 1988).

Other sensors such as Shuttle Imaging Radar (SIR) have produced very good results where, for example, the paleostream channels were located in the extremely dry western desert of Egypt (McCauley et al., 1982). However, sensors other than those on board orbiting satellites (MSS and TM), operated, only during short periods of time; the extent of the areas that they covered, and accessibility to their data are very limited.

1.3 Study objectives

There are mainly two basic approaches to geological remote sensing (Rothery, 1987). One is to produce a high quality image, that can be used by geologists to make important decisions about the available lithologies, their distribution and boundaries. The other approach is to give to the computer the task of dividing the image into areas of different spectral responses, which may be related to the lithology. This study explores both approaches with the aim of improving both of them; more precisely, this thesis was designed to tackle the following aims:

a) To test the different image enhancement techniques that are largely used in geological remote sensing (band ratio and principal component transformation) and the relatively new techniques that do not have the same popularity (decorrelation stretch and Hue-Saturation-Intensity or HSI transformation). The objective of such testing was to evaluate the best means of producing a hard copy image, that could present the information available, in a highly enhanced way, in terms of its spectral,

and spatial information, so that discrimination between different lithologies is optimal.

b) To test the canonical regression analysis technique, which is a new concept and strategy here aimed at relating, directly, the major chemical components of different lithologies, to their spectral signatures. After establishing a relation between the imagery and chemicals, for small training areas, the results could be generalised to large unknown areas.

c) To evaluate a new technique for the automatic and quantitative analysis of imagery. This technique is known as the 'watershed' algorithm (Watson, 1987). The first attempt to apply such an algorithm to a geological scene, is made in this thesis, and the degree of accuracy, will be compared with that achieved using what is, probably, the most widely used classification algorithm, the maximum likelihood algorithm. Furthermore, the effect of using pre-classification processing, as opposed to the original bands, will be tested. In particular, hue components will be investigated. These are produced by transforming the original data, from red-green-blue coordinates, to the hue-saturation-intensity coordinates. The objective was to increase the agreement between reference data and the classified image (classification accuracy).

1.4 Test area selection

Four test areas were selected in the arid, north eastern Arabian Shield as targets for this research. The selection of four test areas was made to show a more critical test for such techniques. The reasons for selecting such areas were: a) these test areas are well exposed and almost free of vegetation, and the soil is at a minimum, which enables the maximum use of spectral information as a means for lithologic discrimination and classification; b)

the excellent diversity and preservation of the lithology exposed in these areas; c) these areas are accessible for any field check needed; and d) the good amount of pre-existing geological information available for these areas, contained in previous geological reports and maps of DGMMR (Deputy Ministry for Mineral Resources, Saudi Arabia), provides a critical 'test bed' for the new techniques.

These four test areas were selected from two Landsat-5 TM quadrants acquired by the ground receiving station of the Remote Sensing Center, in Riyadh, Saudi Arabia, on 5 March 1990. Test areas 1 and 2 (Silsilah ring complex and Jabal ar Raha) are contained within Quadrant 1 of Landsat-5 TM scene of Path 168 and Row 042, whereas the other two test areas, Aban Ahmar and Aban Asmar, and a small part of test area 1, are contained in Quadrant 3 of the previous scene.

The size of each of the test areas 1 and 2 is 512 pixels by 512 lines. However, a small part of test area 1 is located in Quadrant 3; this test area was mosaiced to form one 512 x 512 pixel image.

The size of each of the test areas 3 and 4 is 1024 pixels by 1024 lines. The areas, that are of interest, in each of these two areas, are smaller than this size. However, this size has been chosen, since the digital image processing system used here can only display a full resolution of 512 pixels by 512 lines, whereas the areas of interest, the rocky parts of these two test areas, were about 750 x 750 pixels. Therefore it was decided to make the size of these areas 1024 x 1024 pixels and ignore the areas which are not of interest.

1.5 Structure of the thesis

This thesis is divided into eight chapters. The first chapter gives an introduction to the thesis. Chapter 2 gives a brief review of the physiography and general geology of the four test areas chosen for this research, in order to make the reader familiar with the location and types of rocks present, and their distribution throughout the test areas.

To use effectively and to understand the images obtained from a satellite sensor, that collects reflected electromagnetic radiation data in multispectral mode, an understanding of the nature and properties of this radiation, its division (electromagnetic spectrum), and the way that this radiation interacts with matter, is fundamental. Therefore, a brief review of such information is given in Chapter 3. However, this review is restricted to information related to this research.

Chapter 4 discusses briefly the Landsat series of satellites and its sensors. It also gives a brief description of the types of format, usually found, in the computer compatible tapes, that form the media for the satellite data used in this study, and also the image processing systems that were used in this study, and were available in the Remote Sensing Laboratory, Stirling University.

Chapter 5 contains a simple description of digital image pre-processing (haze correction), and processing techniques; in this study these processing techniques include different methods for image enhancement, e.g. contrast enhancement and spatial filtering. The more complex operations of image transformation of multi-band image sets such as principal component analysis, image ratio, canonical analysis, decorrelation stretch and hue-saturation-intensity transformation are also discussed.

Chapter 6 is divided into two main sections. The first section describes the general methodology, that was followed in applying the image enhancement techniques, whereas the second main section discusses the results that were obtained from such techniques in each of the four selected test areas.

Chapter 7 gives a brief description of the digital classification algorithms, followed by an evaluation of the results from applying such techniques, and an assessment of their relative accuracy. Chapter 8 contains the conclusions and recommendations for future work.

CHAPTER TWO

TEST AREAS LOCATION AND GENERAL GEOLOGY

2.1 Introduction

2.2 Geological setting

2.3 Test areas
- 2.3.1 Silsilah ring complex (test area 1)
- 2.3.2 Jabal ar Raha (test area 2)
- 2.3.3 Aban Ahmar (test area 3)
- 2.3.4 Aban Asmar (test area 4)

2.1 Introduction

The Precambrian rock units of the Arabian Shield (where the four test areas of this work were located), consist predominantly of late Proterozoic rocks, exposed in the western and southern parts of the Arabian Peninsula (Figure 2.1). Approximately 727,000 square kilometres of this basement is located in Saudi Arabia. Of this, 117,000 square kilometres is wholly or partly obscured by Cenozoic (Tertiary and Quaternary) basaltic lava fields that resulted from volcanism associated with the axial rifting of the Arabian-Nubian shield and the Cenozoic opening of the Red Sea axis (Drysdall et al., 1986). The north, east and southeast sides of the Precambrian basement, are unconformably covered by Phanerozoic Sedimentary successions, and the southwest side is bounded by the Cenozoic formations exposed in the coastal plain of the Red Sea.

Very little was known about the geology of Saudi Arabia before the start of the search for oil in the early 1930's, when a comprehensive geologic exploration activity took place in the east of the country, where the first test to yield oil was made on March 4, 1938 (Power et al., 1966). In 1954, the Saudi government, U.S. Department of State and the Arabian-American Oil Company (ARAMCO) came to a cooperative agreement which culminated in the publication of a series of 21 geologic and geographic maps with a scale of 1:500,000. Each of these maps cover an area of 3° longitude and 4° latitude (quadrangles). The first of these quadrangles was published in July 1956. The agreement was completed in 1963 with the publication of 1:500,000-scale geologic and geographic maps of the Arabian Peninsula.

The economic interest of the igneous and metamorphic rocks of the Arabian Shield lies in their mineral content, where the history of mining and prospecting dates back some 3,000 years (Smith et al., 1984). The

numerous and widespread ancient workings, found throughout the shield, document the widespread and intensive prospecting for gold and copper minerals. Geologic mapping of the igneous and metamorphic rocks of the Arabian Shield in the western part of the country did not have the same attention as did the eastern sedimentary basin. Geologic research began in the mid 1940's with localized studies by G. F. Brown between 1944 and 1946. A broad reconnaissance mapping and photo interpretation at 1:500,000 scale was made by the early 1960's. Systematic reconnaissance mapping and mineral occurrence studies began in the Arabian Shield by the mid 1970's, on behalf of the Ministry of Petroleum and Mineral Resources, at a scale of 1:100,000. These maps were then compiled in the 1980's to produce 1:250,000 scale geologic and geographic maps.

The test areas in this research were first mapped as part of the 1:500,000-scale geologic map of Wadi ar Rimah quadrangle (Bramkamp et al., 1963). A detail mapping with a scale of 1:100,000 was not completed until 1985 (Muller, 1975; Du Bray, 1983, 1984, 1986, 1988; Cole, 1981, 1985; Cole and Bohannon, 1985) and these were then compiled by Williams et al. (1986) and Cole (1988) to produce 1:250,000 scale geologic maps. These maps and accompanying reports were the main geologic references in this study. However, a detailed geologic description of the test areas is beyond the scope of this study. This chapter aims to give a brief description of the location and general geology of the selected test areas, which is summarised from the geological reports (above) published by the Directorate General of Mineral Resources, Saudi Arabia, and listed in the reference section at the end of the thesis.

2.2 Geological setting

The part of the Arabian Shield, located in Saudi Arabia Figure (2.2), consists of a volcano-sedimentary succession and associated plutonic complexes, that have been deformed, metamorphosed and intruded by numerous, predominantly granitic plutons (Drysdall et al., 1986,). The four test areas selected for this research are located at the eastern margin of the north-eastern Arabian Shield (Figure 2.3), which is underlain by late Proterozoic rocks, except for small relicts of the once-continuous cover of Cambrian-lower Ordovician Saq sandstone. Quaternary deposits of colluvial gravel and talus alluvial gravel and sand, eolian sand, and rare lacustrine silt are widespread, but are typically thin and discontinuous.

The Proterozoic rocks of the northern Arabian Shield are among the youngest in the Arabian-Nubian Craton and formed during the interval 700 to 570 Ma (Cole and Hedge, 1986). Chemical and isotopic evidence (Cole and Bohannon, 1985) indicate that no significant quantity of continental or evolved crust existed in this region prior to 700 Ma. The oldest rocks probably formed at about 700 Ma, and the youngest proterozoic rocks formed about 570 million years ago. The geologic and tectonic process, that formed the northeastern Arabian Shield, include four major rock-forming events (Cole, 1985; Cole and Hedge, 1986), which provide the skeleton for describing and interpreting the stratigraphy and structure of the region (Figure 2.4), and can be summarised as follows:

1. The oldest layered and intrusive rocks formed by a partial melting of subducted oceanic lithosphere, with a southwest dipping convergent plate tectonic boundary, active from about 700 to 670 Ma (Cole, 1985). This produced the new continental crust. This subduction ceased at about 670 Ma and was followed by regional orogenic deformation and erosion, and

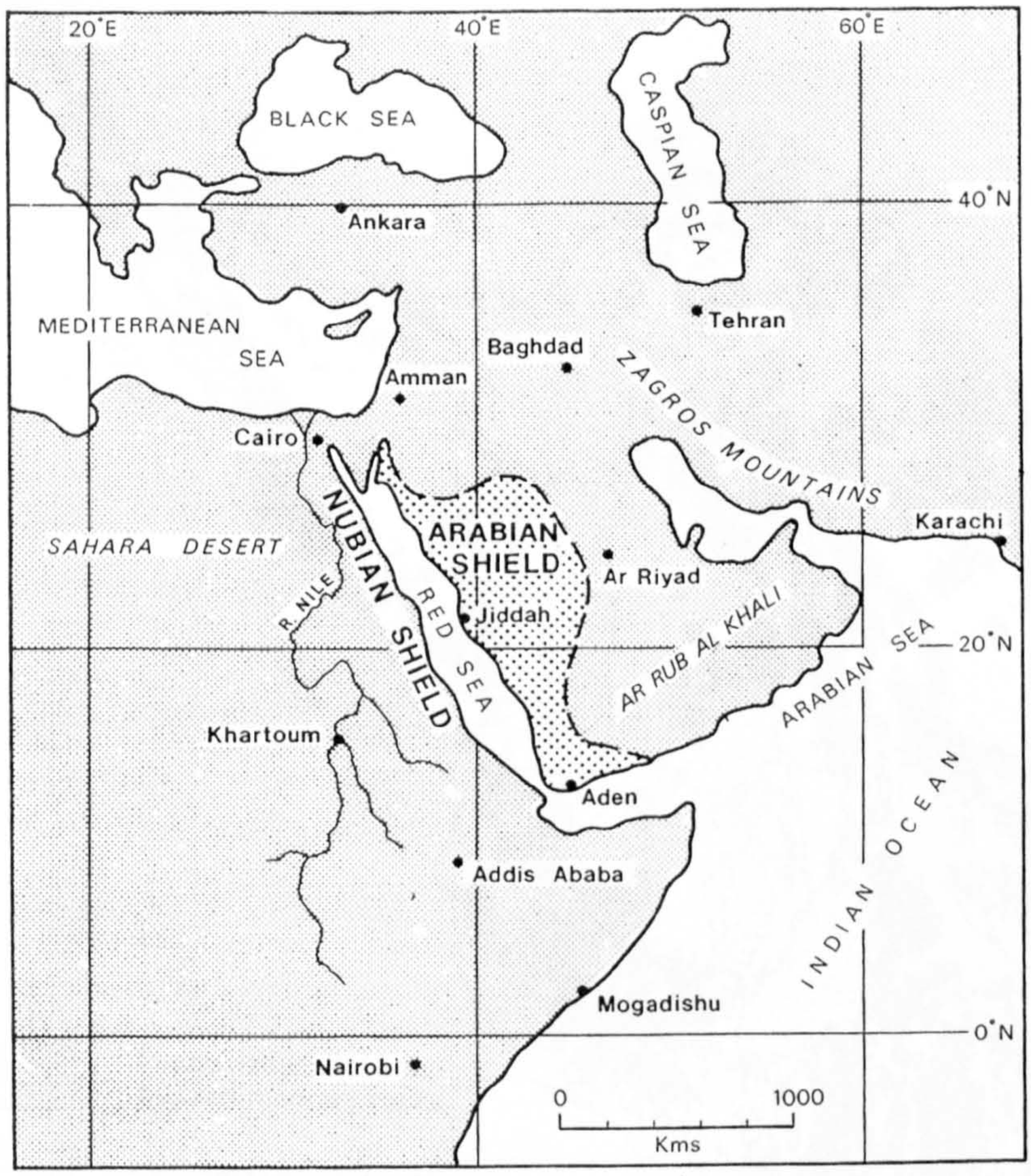

Figure 2.1 Map showing the location of the Arabian Shield.

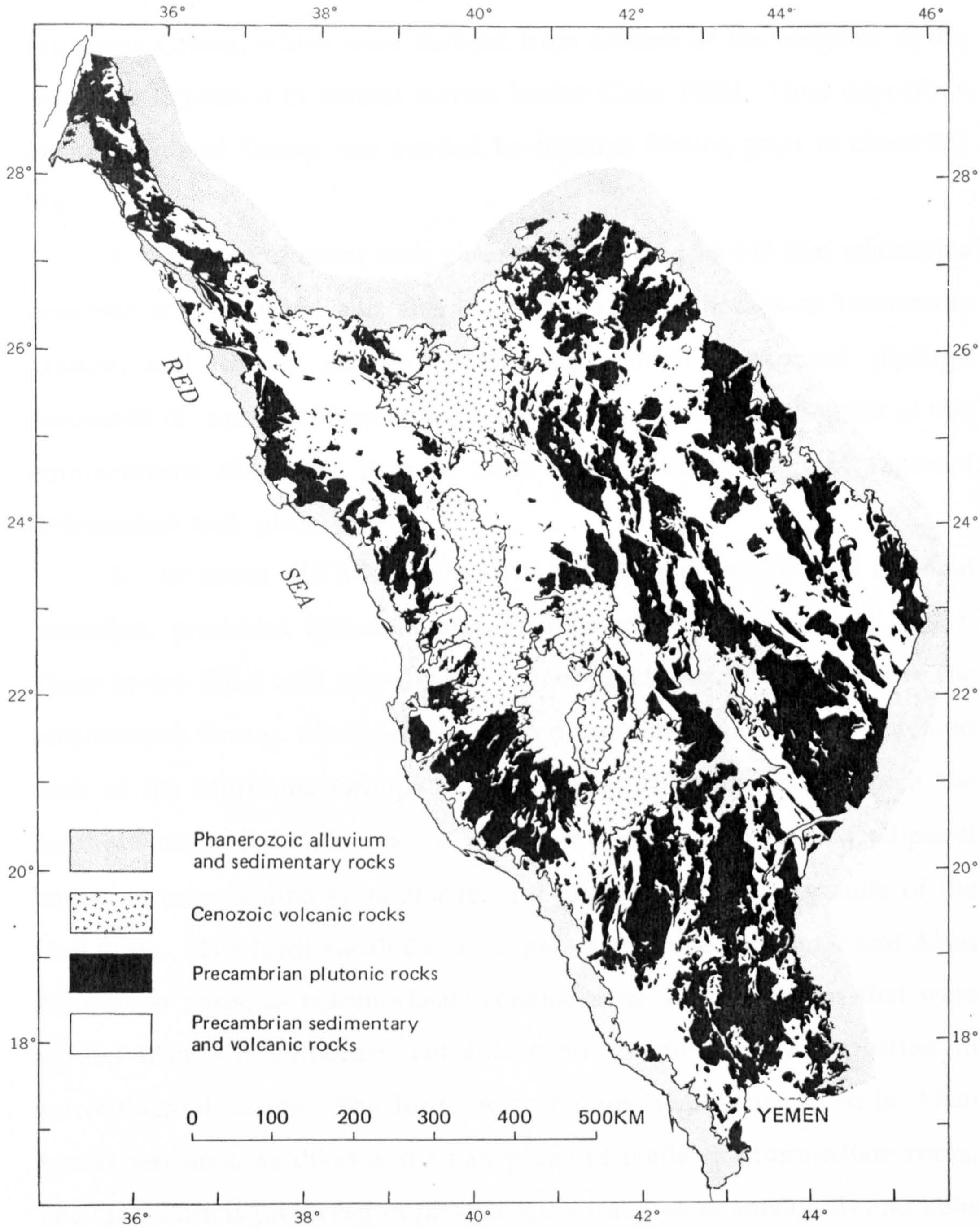

Figure 2.2. Distribution of various rocks in the Arabian Shield.

this crust was regionally folded, thickened and metamorphosed (Cole, 1988). These rocks are unconformably overlain by thick clastic deposits of the Murdama Group, which were derived from erosion of the orogenic uplift, and were deposited in several marine basins (Cole, 1988). Final deposition of the Murdama Group was marked by regional folding prior to about 655 Ma.

2. The second event took place between 655 and 645 Ma, where this neocrust was intruded and stabilised by batholith bodies of leucocratic granite, and formed the Khishaybi suite, which is exposed through thousands of square kilometres in this part of the shield. As a result of this emplacement the crust became more rigid and subsequent regional deformation took place.

3. At about 640 Ma, a period of widespread erosion and regional extension, produced epicontinental, shallow marine and suberial basins. These basins filled with calc-alkaline volcanic and intrusive materials of the Jurdhawiyah Group, which were deposited unconformably above the folded beds of the Murdama Group. Between about 620 and 615 Ma, both the Jurdhawiyah and Khishibi were widely intruded by numerous elliptical bodies of calc-alkaline granodiorite, and related diorite and granite of the Idah Suite. The Jurdhawiah Group is preserved in Aban Ahmar and Aban Asmar test areas, as volcanoclastic conglomerate and sandstone, that were eroded from contemporary volcanic centres, and rapidly deposited in epicontinental basins. The Jurdhawiah Group is preserved also in Aban Asmar test area, as dikes and small plugs of mafic to intermediate rocks. The Idah Suite is preserved in Jabal ar Raha test area as small hills and nobs of meta-gabbro and carbonate rocks. No layered or intrusive rocks are

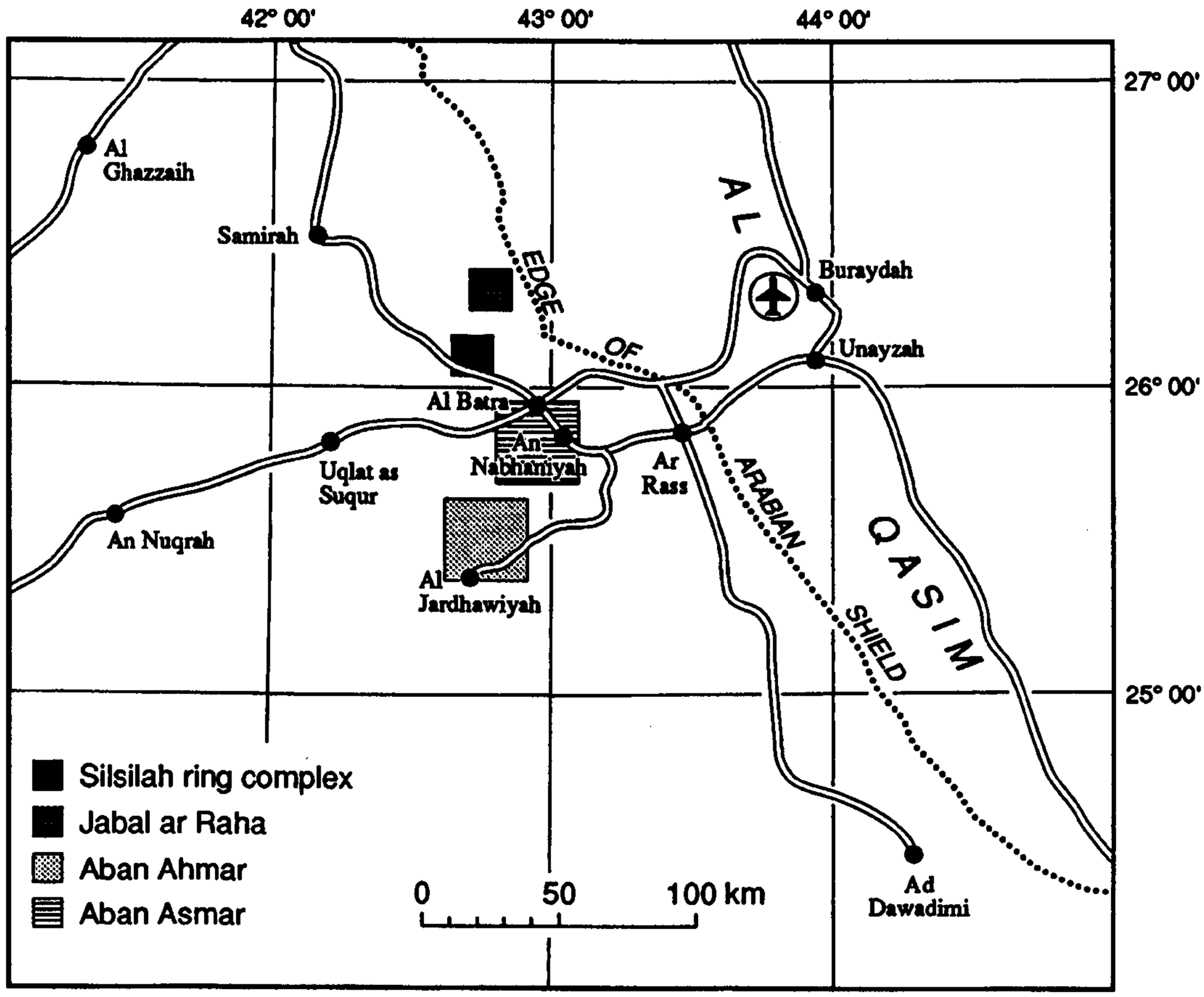

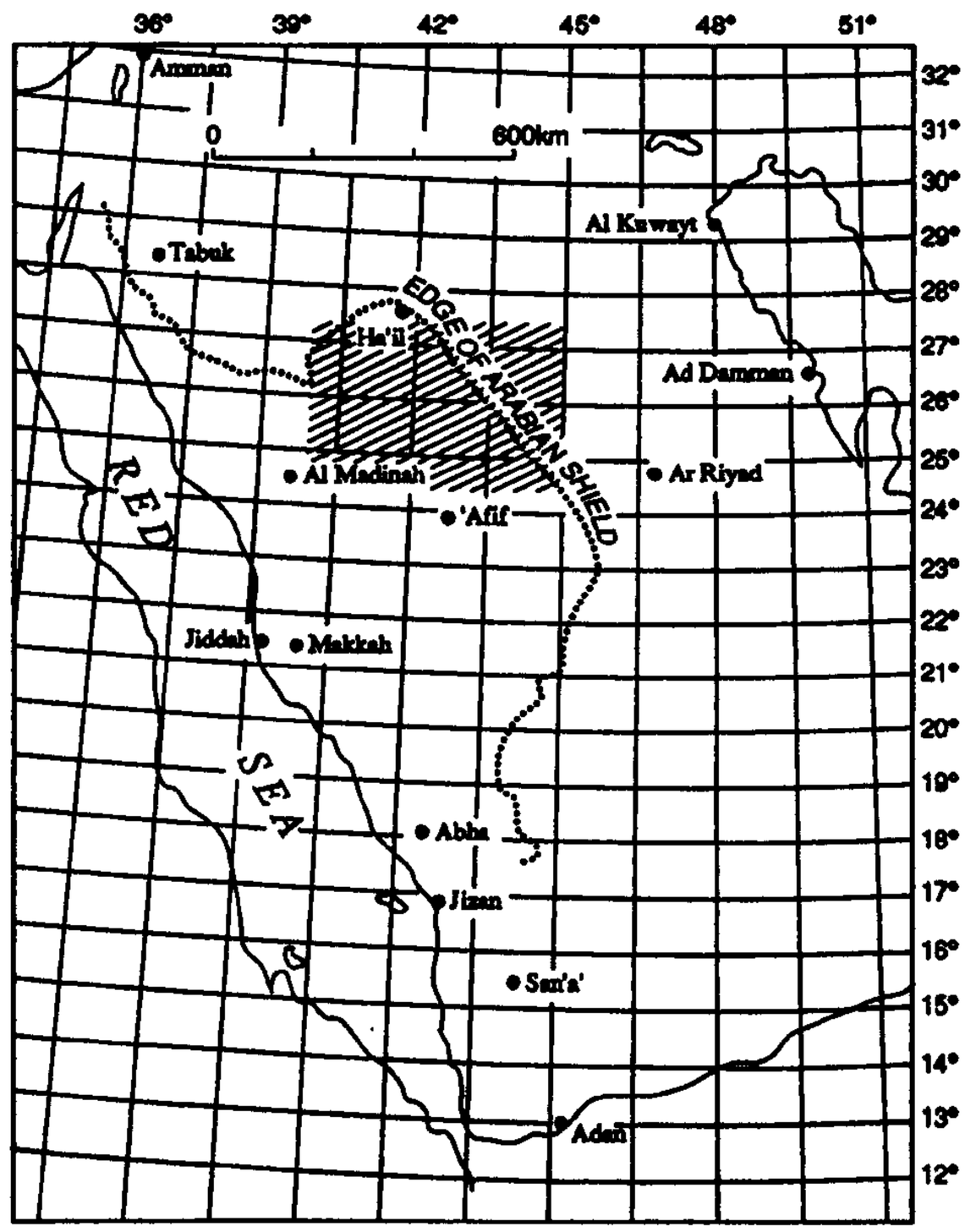

Figure 2.3 Location map of the four test areas.

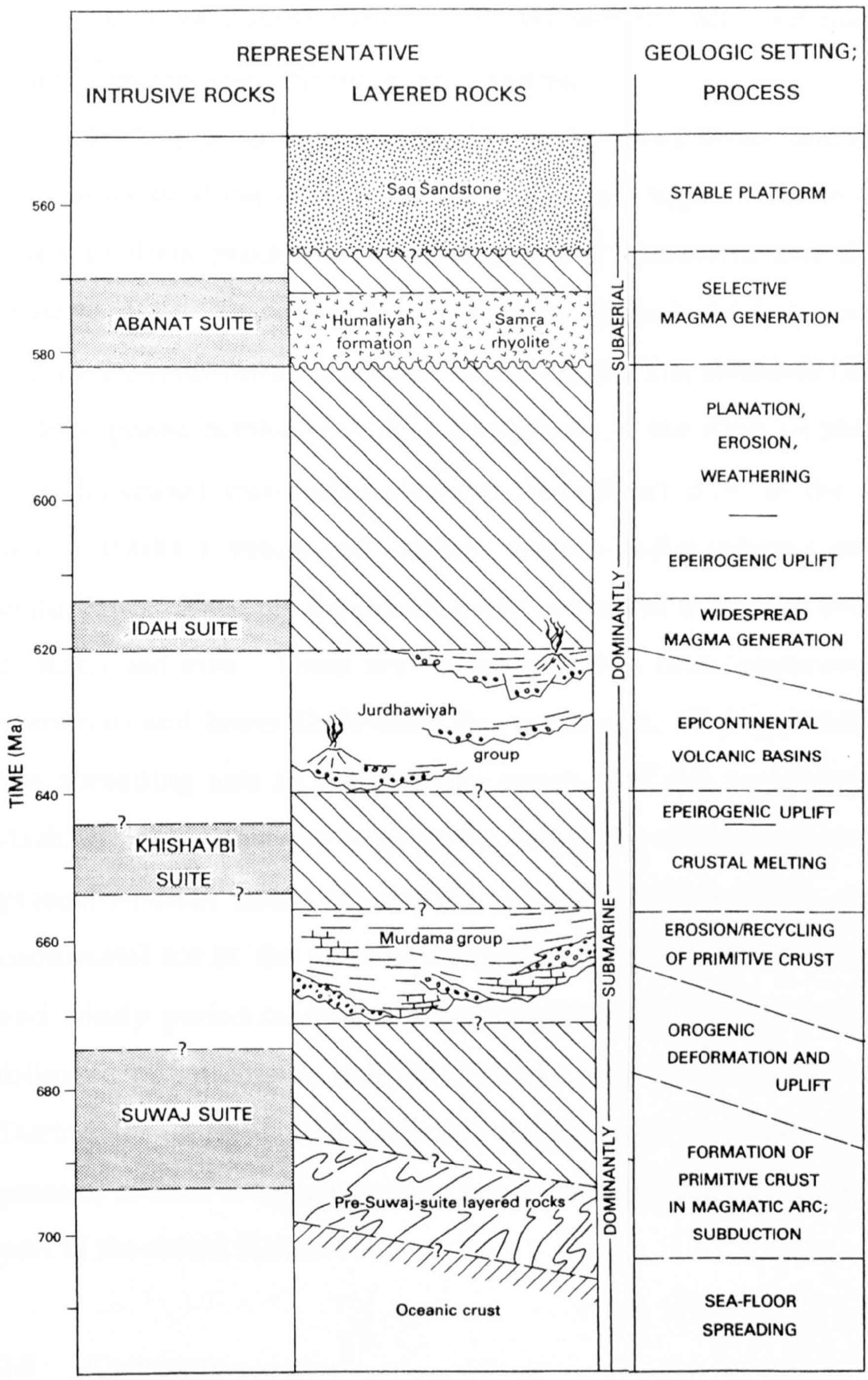

Figure 2.4. Diagram representing the geological evolution of rock units in the northeastern Arabian Shield (after Cole, 1990).

known to have formed between 615 Ma and 585 Ma, and this period was marked by considerable uplift and erosion.

4. Beginning at about 585 Ma, widespread minor bodies of evolved granite rocks of the Abanat suite intruded to a higher level in the crust and many of them produced coeval deposits of leucocritic and differentiation granitic rocks. This event is pervasive in all the test areas, and marked the end of the crust-forming process in the region. The sequence of sedimentary rocks exposed northeast, east and southeast of the Arabian Shield indicates that the craton was stable platform throughout most of the Phanerozoic, which marks a prolonged shallow marine sedimentation with no major disturbance. The only Palaeozoic rocks preserved in the test area are in Jabal ar Raha test area. These are remnants of the once continuous blanket of Cambrian and lower Ordovician Saq sandstone. The beginning of the Red Sea spreading axis in the Miocene epoch, and the associated drift of the Arabian peninsula away from Africa, led to the erosion and exposure of the present Arabian Shield (Cole,1990). The stage of maximum advance of the continental ice in the northern hemisphere, is correlated with a very arid and windy period in Arabia, which formed the great dune fields and was followed by successive and less extreme periods of dry and wet seasons. During the current arid cycle the sand dunes are largely inactive. At present, erosion is approximately balanced by depostion in the northeastern part of the shield (Cole, 1990).

2.3 Test areas

The four test areas, selected for this research, are located at the eastern edge of the northeastern Arabian Shield (Figure 2.3). The climate of this part of Saudi Arabia is described by Mashhady et al. (1986) as aridic

hyperthermic. It is characterised by hot summers, with maximum temperatures of about 45°C and minimum temperatures of about 24°C, and by cool winters with maximum temperatures of about 18°C and minimum temperatures of about 0°C. Marked diurnal temperature variations occur during most of the year. In general, there is no precipitation from June to September, and the highest precipitation occurs between January and March. The mean annual precipitation in the past ten years (Mashhady et al., 1986) is 110 mm with irregular distribution both in quantity and frequency. The four areas lie in a zone of weak weathering intensity. The physical weathering is the dominant type due to the high temperature and the lack of soil moisture .

2.3.1 Silsilah ring complex (test area 1)

This test area is located between latitude 26°03' and 26°11' North, and longitude 42°37' and 42°47' East (Figure 2.3). This test area is about 150 kilometres west southwest of Buraidah, near the northeastern limit of the exposed Arabian Shield. The area is about 16 x 16 square kilometres. It is composed of a prominent, circular ring-shaped topographic feature of about 12 kilometres in diameter (Figure 2.5) with an altitude range betwen 10 and 300 meteres above the surrounding pediment suraface, and with an average relief along the ring of about 100 metres. The drainage system traversing the area is a dendritic net, draining south to Wadi Ar Rimah. The principle settlement in this area is the village of al Fawwarah to the south, with about 1500 persons. The only paved road across this test area is the Qassim-Hail road. However, several desert tracks cut the area.

General geology

The following description of the geology (figure 2.5) is summarised from Du Bray (1983, 1984, 1988) and Williams et al. (1986). The oldest rock in this test area is a massively bedded, immature sandstone with minor interbedded siltstone, named in this area as Maraghan lithic greywacke (Mlg), which represents a major depositional basin (Murdama Group) in the northern Arabian shield (Du Bray, 1983). This rock was regionally metamorphosed to a lower green schist facies. The matrix is silt size intergrowths of clay minerals. The lithic fragments are felsite, grains of argillite, and fine grain volcanic clasts. The (Mlg) unit is intruded by (hence is older than) the igneous rocks that form the ring's structural feature. Du Bray (1988) states that the size and shape of the ring complx suggests that it represents a fraction of magma tapped from a large, subjacent magma chamber, through a set of closely spaced ring-shaped fractures. Four main rock units form this ring; they are (starting with the oldest) alkaline dacite (ad), commendite (com), Silsilah alkali granite (Sag), Hadhir aplite (Ha) and Fawwarah alkali-feldspar granite (Fag), of the Abanat Suite.

The alkaline dacite (ad) is a greyish black, very fine grained, subalkaline volcanic rock, which outcrops in the east and northeast of the ring complex (Figure 2.5) as dike-like bodies, and forms strongly weathered elongated bodies. This rock is composed of an intergranular to weakly trachytic intergrowth of plagioclase and opaque oxides (Du Bray, 1988). The (ad) is intruded by a fine grained porphyritic commendite (com) which contains abundant phenocrysts, up to 4mm long, of alkali-feldspar (60%) and outcrops at the eastern part of the ring in a dike-like form. Both (ad) and (com) units account for about 30% of the ring.

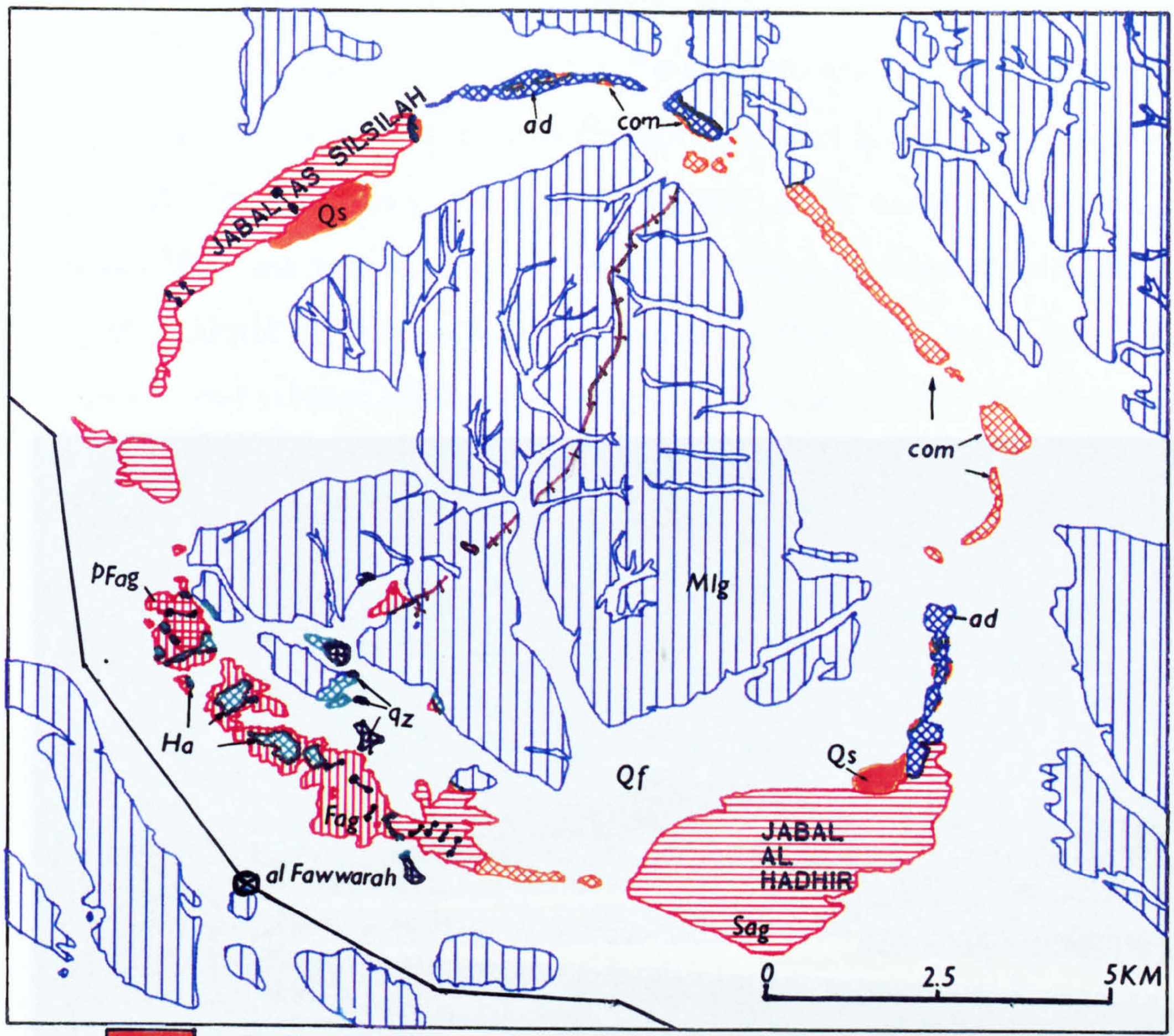

Qs Eolin Sand

Qf Alluvial fan and Apron deposits

quartz vein

Fag Fawwarah alkali-feldspar granite

qz quartz pegmatite

Ha Hadhir aplite

PFag proto Fawwarah alkali-feldspar granite

Sag Silsilah alkali granite

com Commendite

ad alkaline dacite

Mlg Maraghan lithic graywacke

Figure 2.5. Geologic map of Silsilah ring complex, test area 1 (after Du Bray, 1988).

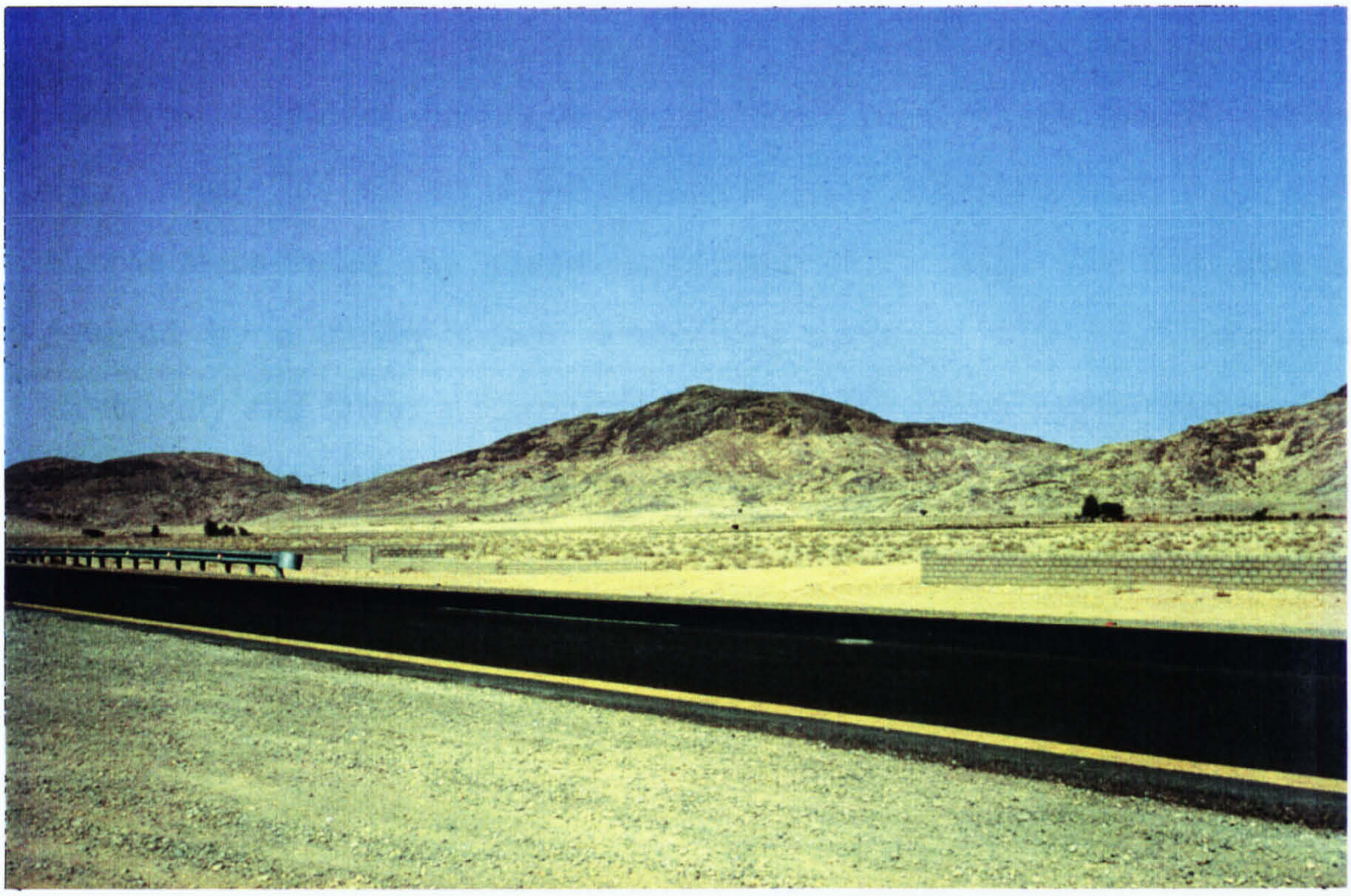

Figure 2.6. Field photograph showing the Hadhir aplite (Ha) on top of Fawwarah alkali-feldspar granite (Fag).

The Silsilah alkali granite (Sag) outcrops in the northwest and southeast of the ring, at Jabal as Silsilah and Jabal al Hadhir respectively, as greyish-red, medium grained alkali granite. In its contact with the Hadhir aplite (Ha), the (Sag) unit is weakly recrystallized and denterically altered for several hundred metres from its contact. The rock exposed at Jabal as Silsilah and Jabal al Hadhir is unaltered (Du Bray, 1988). The Hadhir aplite (Ha) is light grey, equigranular, and fine grained, and outcrops in the southwestern part of the ring as a nearly flat-lying sheet, less than 50 metres thick (Figure 2.6), on top of the Fawwarah alkali-feldspar granite (Fag), and also as slabs inside the southwestern limit of the ring. The (Ha) unit is covered by a dusky-brown weathering surface. The (Ha) weathers recessively and forms a minor component of the ring complx. Biotite and Fe-Li mica form scarce crystals as much as 1 mm long, and partly altered to opaque oxides from light tan to dark reddish brown.

The Fawwarah alkali-feldspar granite outcrops in the southwestern part of the ring as very light grey and medium grained rock. It is also exposed in two small isolated hills, located three and four kilometres inside the southwestern margin of the ring, where the granite intrudes (Mlg) unit inside the ring and is the youngest intrusive component of the ring complex. Fe-Li mica and rare light brown biotite are constituents of the Fawwarah alkali-feldspar granite. The proto Fawwarah alkali-feldspar granite (pFag) is lithologically identical to (Fag), and was initially mapped with that unit.

Bodies of massive milky-white quartz (qz) are exposed in a low hill within the ring structure, near its southwestern side. Quartz veins, ranging in width from 2 to 50 cm, penetrate all the units in this test area, particularly (Mlg), (Ha) and (Sag).

Superficial deposits

A moderately well sorted, sand size alluvium material (Qal) is presented in active Wadi channels, and also includes silt, pebbles and fine windblown materials. The areas around the high relief (inside and outside the ring) are characterised by deposits of alluvial fans (Qf) which are poorly sorted, angular materials ranging from silt to boulder size. The Eolian sand deposits (Qs) are found as two inactive sand bodies inside the ring north of Jabal al Hadhir and east of Jabal As Silsilah.

2.3.2 Jabal ar Raha (test area 2)

This test area is located northeast of test area 1 and covers an area of about 16 x 16 square kilometres between latitude 26°15' and 26°24' North and longitude 42°43' and 42°52' East (Figure 2.3) . There is no settlement in this area, either town or village; the nearest settlement is Buqayah village, 7 kilometres to the east with no more than a few hundred persons, and al Fawwarah about 30 kilometres southwest of the test area with about 1500 persons. The population in this area is very sparse and includes only two Bedouin encampments, whose economy is based on the raising of goats, sheep and camels. There is no paved road across this area, and the principal paved road is about 30 kilometres to the south (Qassim Hail road). The area can be reached from the Qassim Hail road near al Fawwarah by driving north for about one and half hours on desert tracks which turn sandy just south of the test area.

General geology

The rocks of the Jabal ar Raha can be divided into three groups: meta-sedimentary layered rocks, metavolcanic layered rocks, and mafic intrusive rocks. The geologic description of this test area is summarised from the reports by Du Bray (1983), Williams (1986) (Figure 2.7). The metasedimentary rocks (Murdama Group) consist of two units: the Qarnayn formation which crops out in the north-eastern part of the area as poorly sorted and extensively cleaved conglomerate (cg). It has a nearly homogenous population of sedimentary rock, much like that of sandstone matrix, but contains a few clasts of limestone, and fine grained volcanic rock and mafic plutonic rock. The matrix contains andesite, quartz, epidote, with mafic plutonic clast, particularly common in the upper layers of the conglomerate. This conglomerate is drained by well developed trellis drainage.

In the western and north-western part of the area, and also west of the conglomerate, the Qarnayn formation crops out as volcanoclastic greywacke, named by Du Bray (1983) as Qarnayn Lithic Greywacke (Qlg). This unit appears massive in outcrop and is poorly sorted, well-indurated, immature sandstone of volcanic province, characterised by well rounded and widely distributed pebbles (2 to 5 centimetres in diameter) of felsic to intermediate volcanic material. These pebbles are locally so numerous that the unit is weakly conglomeritic. Fine-grained and finally laminated felsic and pyratic volcanic ash is locally presented.

The second unit of the metasedimentary group is the Maraghan Lithic greywacke, which is very poorly exposed in the south-eastern corner of the area.

The carbonate (cr) rocks in this area are located, just north of Jabal ar Raha's north-eastern limit, as small pods and discontinuous podin-like

masses of marble, associated with meta-gabbro east of Jabal ar Raha. The marble is exposed as completely crystallised, bluish-grey, relatively pure carbonate rock. It is composed of calcite and trace amounts of hematite and quartz, or as structureless tan coloured material, that is distinctly vuggy, less pure, and contains trace amounts of sericite and possibly chlorite. These carbonate rocks are thought to be alteration product of plutonic rocks.

The mafic plutonic rocks in this area are divided into metagabbro and quartz monzodiorite. The metagabbro (mgb) crops out 2 kilometres east of Jabal ar Raha, as an isolated dark weathering hill of fine grained metagabbro at the eastern margin of the area, whereas the quartz monzodiorite, named as Shaila quartz monzodionite (Sqm), crops out as irregular shaped bodies of dark to medium grey, recessively weathered quartz monzodiorite in the central northern part of the area.

The meta-volcanic layered rocks exposed in the mid-southern half of the area are complexly interbedded, weakly metamorphosed volcanic rock of meta-rhyolite, meta-rhyolite tuff and meta-andesite which are approximately coeval. These meta-volcanic layered rocks are coeval to the rocks of Abanat suit.

The meta-rhyolite crops out as a "V" shape in the southern part of the area, and named as Raha meta-rhyolite (Rmr). This unit has a brick red weathering surface and contains salmon colour phenocrysts of microcline (as much as 5 millimetres long) partially altered to sericite at the northern edge of Jabal ar Raha. The meta-rhyolite tuff (mrt), is located near the centre of Jabal Ar Raha in an assemblage of felsic extrusive rocks. The biotite minerals in this unit are altered to chlorite. Glass structure and the remains of collapsed pumice blocks, are locally preserved. Much of this unit is stained reddish orange due to deuteric alteration.

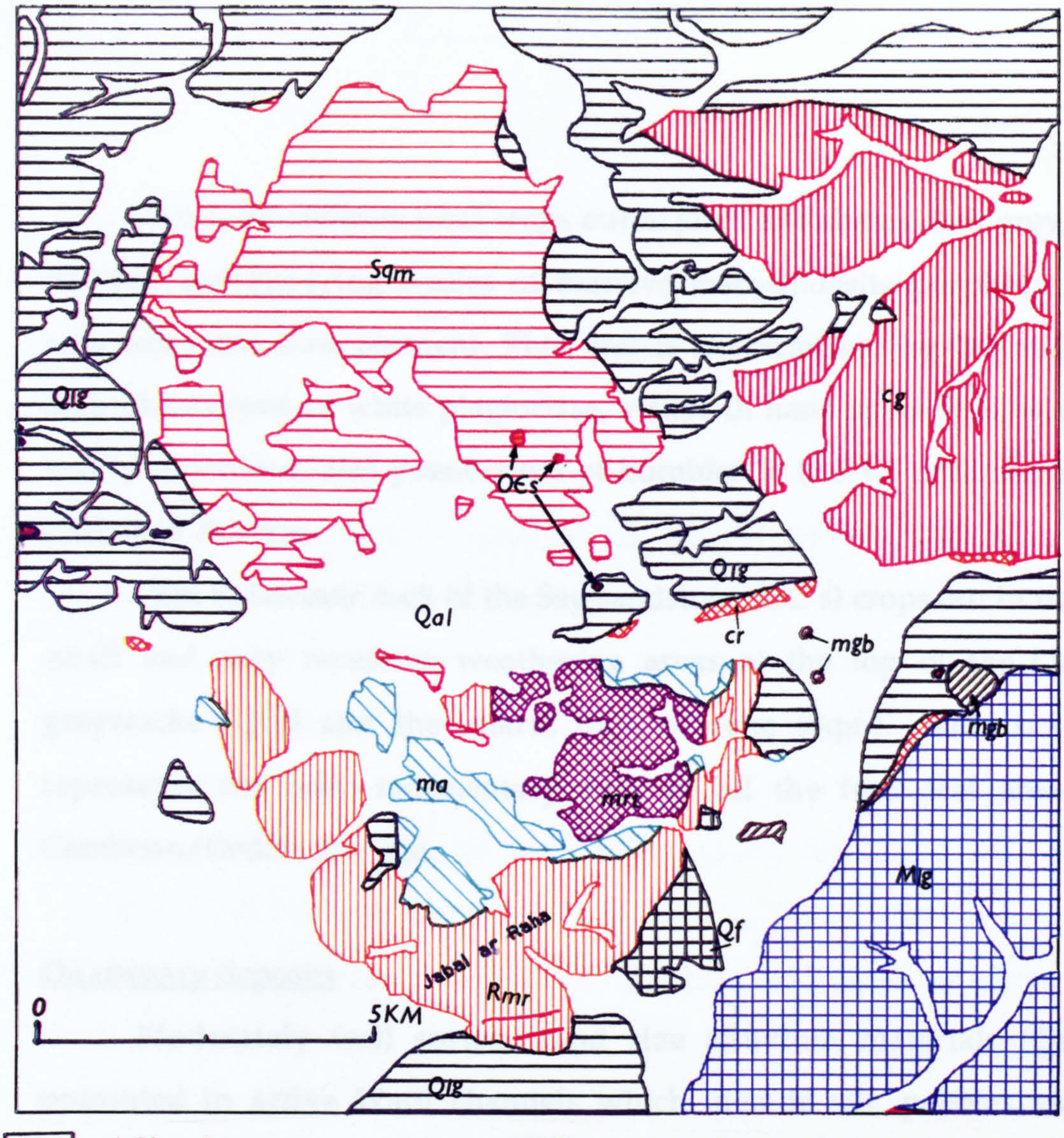

Qal Alluvium

Qf alluvial fan and apron deposits

OEs saq sandstone

ma meta-andesite

Rmr Raha meta-rhyolite

mrt meta-rhyolite tuff

Sqm Shaila quartz monzodiorite

mgb metagabbro

cr carbonates

Mlg Maraghan lithic graywacke

Qlg Qarnayn lithic graywacke

cg conglomerate

Figure 2.7. Geologic map of Jabal ar Raha, test area 2 (adapted from Du Bray, 1983).

The meta-andesite (ma) crops out at Jabal ar Raha as dark grey, small, isolated and flat-lying bodies of massive meta-andesite porphyry, which may represent flow remnant. This unit is characterised by 1-2 millimetre long phenocrysts of white plagioclase, visible in hand specimens, which are locally sericitized, also phenocrysts of hornblende (0.5-1.5 millimetres long) altered to chlorite.

The Palaeozoic rock of the Sag sandstone (OC s) crops out in two very small and very recessive weathering areas at the top of the Qarnayn greywacke (Qlg) and the quartz monzodiorite (Sqm). This sandstone represents the only sedimentary rock in all the four test areas of a Cambrian/Ordovician age.

Quaternary deposits

Moderately well sorted, sand size alluvium materials (Qal) are presented in active Wadi channels which include silt, pebbles and fine windblown materials. The alluvial fans (Qf) are restricted to aprons around Jabal Ar Raha which are poorly sorted, angular materials ranging from silt to boulder size.

2.3.3 Aban Ahmar (test area 4)

This area is located between latitude 25° 22' and 25° 37' and longitude 42° 39' and 42° 57' approximately (Figures 2.3 and 2.8), which covers an area of about 32 x 32 square kilometres. The area is relatively well populated with four villages (Figure 2.8) east of Aban al Ahmar mountain; Dulay Rashed, Jarrar, al Marmuthah and Mihayyidah and one village to the west of the mountain; Fayyadah with about 200 persons each. In addition to these villages there is a scattered Bedouin encampment around the Aban al

Ahmar mountain. The only paved road that cuts the test area is shown in Figure (2.8), with desert tracks circling the mountainous area.

The topography of the test area is characterised by a relatively flat peneplain covered by thin surfacial deposits of alluvium and eolian materials (Figure 2.9). The average altitude of the surface of the peneplain is about 700 metres and is sloping north and east and drained via drainage channels mainly to the mobile eolian sand fields (Nafud al Urayq west of the test area and Nafud al Maysariyah about two kilometres to the north of the test area) with a few channels drained directly to Wadi ar Rimah (to the north of this area). This peneplain surrounds the massive elongated mountainous terrain of Aban al Ahmar striking east-north-east direction whose summit is about 500 metres higher than the surrounding peneplain (1310 metres above sea level) and the ring shaped hills to the south-east of Aban al Ahmar.

General geology

The following description of the geology of the test area is summarised from the geologic reports by Muller (1975), Cole and Hedge (1986) and Cole (1985, 1988) (Figure 2.8). The area can be divided into four lithologic groups: the mafic metavolcanic rocks, mafic and intermediate plutonic rocks, calc-alkaline volcanic and contemporary volcanoclastic rocks, and peralkaline granitic rocks of Ahmar complex. The oldest rock in the area (pre-Suwaj Suite) is the mafic metavolcanic rocks of Dhiran-meta-andesite (Da). These rocks are poorly exposed as small eroded hills of dark green fractured and weakly schistose metavolcanic rocks west of Jibal Kihlah. This rock is recrystallised and rich in secondary quartz, chlorite, hornblende, calcite and sericite minerals.

The mafic and intermediate plutonic rocks include three types: the Khaytan quartz diorite (sqd), granodiorite (sgd) and granodiorite granophyre (sgg). Just south of Sinaf Aba-al Haddar, the Khaytan quartz diorite exposed as grey green, cataclastically foliated small and isolated knobs. Some minerals of this unit are altered to sericite, calcite and chlorite. The granodiorite is exposed as low hills of light grey rocks with variable composition that ranges from granodiorite to quartz monzodiorite with about 21% mafic minerals and moderate alteration. The granophyre outcrops as dark grey, heavily altered (chlorite, sericite and epidote) granodiorite porphyry, at Jibal Kihlah, west of Aban Ahmar mountain.

The calc-alkaline volcanic and contemporaneous volcanoclastic rocks include the layered rocks of the Jurdhawiyah group, which crop out along the east side of Aban al Ahmar as clastic and volcanic deposits, and as plugs and short dikes of dominantly andesitic rock. Isharat porphyry (pp) north of Mihayyidah, and also, as gabbro-norite north of the circular valley, west of Jarrar. The Jurdhawiyah Group includes Muqawqi andesite (Ja) which outcrops, mainly around the southern part of the Aban Ahmar, as dark green structureless to amygdaloidal flow rock and flow breccia.

The second unit of the Jurdhawiyah Group is the conglomerate (Jc) member, which consists of poorly sorted clasts of Muqawqi andesite, dacite and tuffacious materials (lapilli tuff), which crops out as ridges in the northeastern boundary of Aban al Ahmar. The alteration is variable and consists of chlorite, epidote and calcite.

The third unit is the sandstone member, which crops out as coarse grained, pebbly lenses of volcanic sandstone (Js), and forms the upper part of Jarrar formation east of Aban al Ahmar (Figure 2.8). This sandstone is composed mainly of andesite, similar to that in the conglomerate members.

The sandstone is cemented by chlorite, epidote and carbonates (calcite). Lapilli tuff (Jt) beds are also present as thick wedge-shaped deposits north of Jarrar, which consists of rhyodacite tuff breccia with pyroclasts of 10-40 centimetres in diameter. Lapilli tuff is variably altered by post depositional chlorite and clay minerals. Small plugs of Isharat porphyry and gabbro-norite intrude the rocks of the Jurdhawiah Group north-west and south-west of Jarrar. The gabbro-norite is exposed as dark bluish-grey, medium grained pyroxene gabbronorite and olivine gabbronorite southwest of Jarrar within the circular eroded valley (south of Mihayyidah). The Isharat porphyry (pp) is exposed as a small plug of andesite and minor dacite northwest of Jarrar, and was mapped by Cole (1985) as andesitic plugs and short dikes.

The Ahmar Complex crops out as an elongated zoned pluton (Abant Suit) striking east-north-east direction (Figure 2.8) which intrudes the previously described Jurdhawiyah Group, and the Dhiran meta-andesite. The core of the pluton consists of brick red, coarse to medium grained biotite perthit granite (apg) that has about 7% biotite. The grain size of the (apg) unit decreases to fine grain at the contact with the arfvedsonite-perthite granite (aag), and along the roof axis and is, in general, coloured by hematite. The outer carapace of the Ahmar complex consists of very coarse grained, tan to pale brown arfvedsonite-perthite granite (aag). This granite is discontinuous along the western margin. At Sinaf Aba al Haddar the arfvedsonite granite member is intruded by the rhyolite porphyry member (arp) which consists of brick red, sparsely porphyritic peralkaline rhyolite, and forms a thick discontinuous elliptical ring dike. Farther west (outside the test area) it is mostly buried under Nafud al 'Urayq sand body, and then

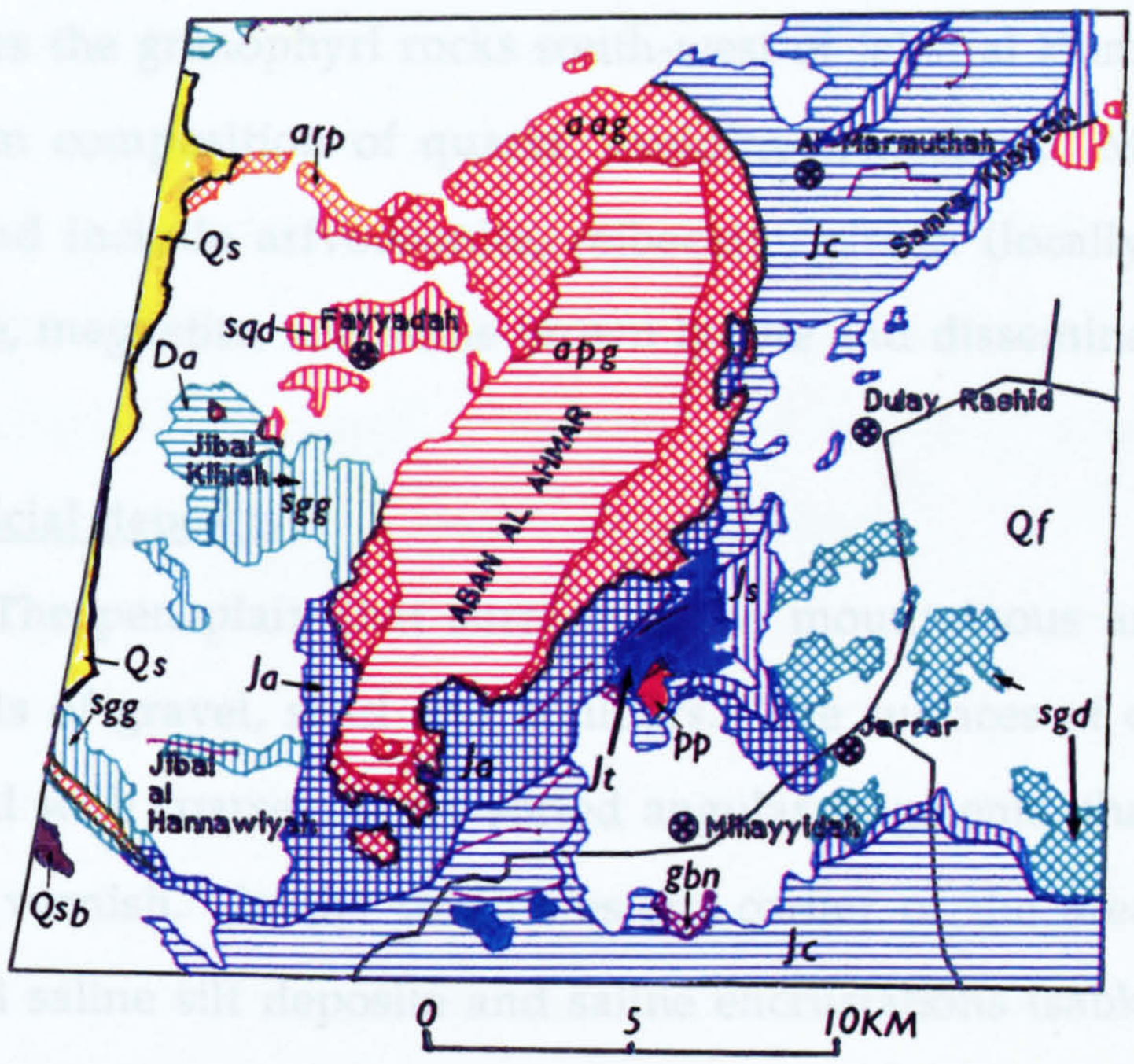

Qs	eolian sand
Qsb	sabkha deposits
Qf	alluvial fan and apron deposits
arp	rhyolite porphyry
aag	arfvedsonite granite
apg	perthite granite
gbn	gabbronorite
pp	Isharat porphyry
Js	sandstone
Jt	lapilli tuff
Jc	conglomerate
Ja	Muqawqi andesite
sgd	granodiorite
sgg	granophyre
sqd	Khaytan quartz diorite
Da	Dhiran meta-andesite

Figure 2.8. Geologic map of Aban Ahmar, test area 3 (adapted from Cole, 1988).

intrudes the granophyri rocks south-west of Jabal al Hannawiyah. It has a uniform composition of quartz, sanidine-orthoclase. Mafic minerals are rare and include arfvedsonite, reibeckite, zircon (locally very abundant), flourite, magnetite, and some brown biotite and disseminated hematite.

Superficial deposits

The peneplain that surrounds the mountainous area is covered by deposits of gravel, sand and boulders. The surfaces of other deposits are covered with coarse, poorly sorted angular fragments, that are coated with desert varnish. In the south-western corner of the area a small area of bedded saline silt deposite and saline encrustations (sabkha deposits "Qs") are present (Figure 2.10). It consists of carbonate and sulfate minerals that loosely cement silt-size eolian and ditrital materials. A very small part of the dune field of Nafud al Urayq presented in the western part of the area (Qs), consists mostly of a fine sand.

2.3.4 Aban Asmar (test area 4)

This test area is located between latitude 25° 40', 25° 55' N and longitude 42° 47' and 43° 04' E, and covers an area of about 32 x 32 square kilometres (Figure 2.3). Several roads cut this area and desert tracks circle the mountainous area. The area is relatively well populated with three small towns, An Nabhanyah, Albatra and Rawdat Qiradan, and also by scattered Bedouin encampments.

The topography of this area is characterised by a relatively flat peneplain, south-sloping surface, that drains to Wadi ar Rumah in the southern part, via the well developed dendiritic channels of Wadi Thadij and Wadi al Abaytir in the eastern part of the area, Shaib al Metla al

Ayman, which cuts the mountain of Aban al Asmar, and drains into a man made dam at the eastern margin of the mountainous area and Shaib al Metla al Alysar. The average altitude of this peneplain is about 750 metres above sea level, and it is widely covered by alluvium and eolian materials. This peneplain surrounds a mountainous terrain of Aban Alasmar where the altitude reaches 1243 metres above sea level.

General geology

The geologic description of this test area is summarised from the geologic reports by Cole and Bohannon (1985), Cole and Hedge (1986) and Cole (1988). The Proterozoic rocks of this area are divided into three groups. The oldest are the layered sedimentary and volcanic rocks of the Murdama and Jurdhawyah groups (Figure 2.4), which dominate the western part of the area, (Figure 2.11), and form a planar, south-sloping peneplain, cut by dendiritic channels east and west of Wadi Thadij, and form hills to the west of Aban al Asmar mountain.

The second group is the monzogranite of the Khishaybi suit (extensively weathered) and Samra rhyolite which forms the highest peak of Aban al Asmar, and is found to be younger than the Khishaybi and Jurdhawyah. The last group, is the intrusive units of the Asmar complex, which intrudes the Samra rhyolite, and outcrops in the north, south, and in an elongated body in the west side of the Samra rhyolite. Both the Samra rhyolite and Asmar complex belong to the Abanat Suite (Cole, 1985), and they are interpreted to be co-magmatic and coeval.

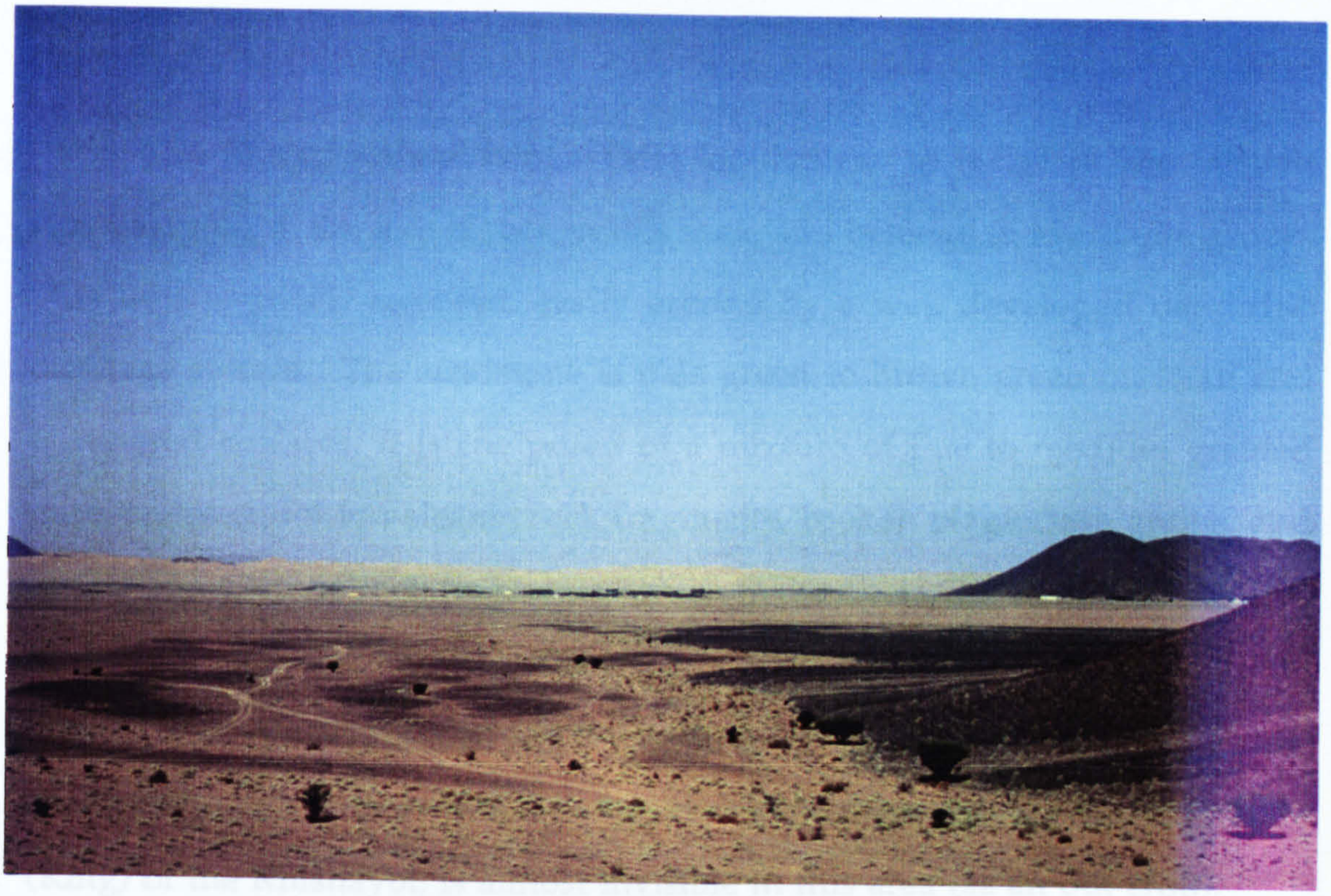

Figure 2.9. Field photograph showing the relatively flat peneplain and the sand dune field that are exposed west of Aban Ahmar test area.

Figure 2.10. Field photograph showing the saline encrustations (Sabkha deposits).

The Maraghan sandstone (Ms), equivalent to (Mlg) in the Silsilah ring complex, is the oldest rock in this area, and belongs to Murdama group. This unit is poorly exposed, easily eroded by a well developed dendiritic drainage system. The sandstone is pale green to brown green on fresh and weathered surfaces. It is composed of a mixture of fine to medium grained meta-andesite, felsic volcanic rock fragments, broken plagioclase grains, and quartz and granitic rock fragments, which make up 45, 35, 10 and 10 per cent of the rock, respectively. The alteration is widespread, with the calcite as the most common alteration products, and replaces the matrix and the clasts, and locally makes up as much as 50 per cent of the rock. The monzogranite (Kmg) of the Khishaybi, is almost invisible in this area (as an out crop).

The Jurdhawiyah group exposed to the east of the Maraghan sandstone, west of Aban al Asmar, are defined in this area by the Jarrar Formation, which is a texturally heterogeneous assemblage of volcanic clastic rocks, derived from erosion of primary Jurdhawiyah volcanic deposits. It consists of a conglomeritic member (Jc) and a sandstone member (Js). The conglomerate clasts consist of fresh andesite, dacite and tuff. The conglomerate is variably cemented by calcite and local chalcedony and post depositional growth of chlorite, actinolite, sphene and epidote. The sandstone member is pale green to pale brown, of volcanic rock fragments similar to that of the conglomerate member. Fresh hornblende, augite and magnetite are also common. Clasts of Maraghan sandstone are less common. The matrix is moderately cemented by chlorite, sparse calcite and minor epidote. The sandstone is exposed in this area as an elongated body striking north-west inside the conglomerate.

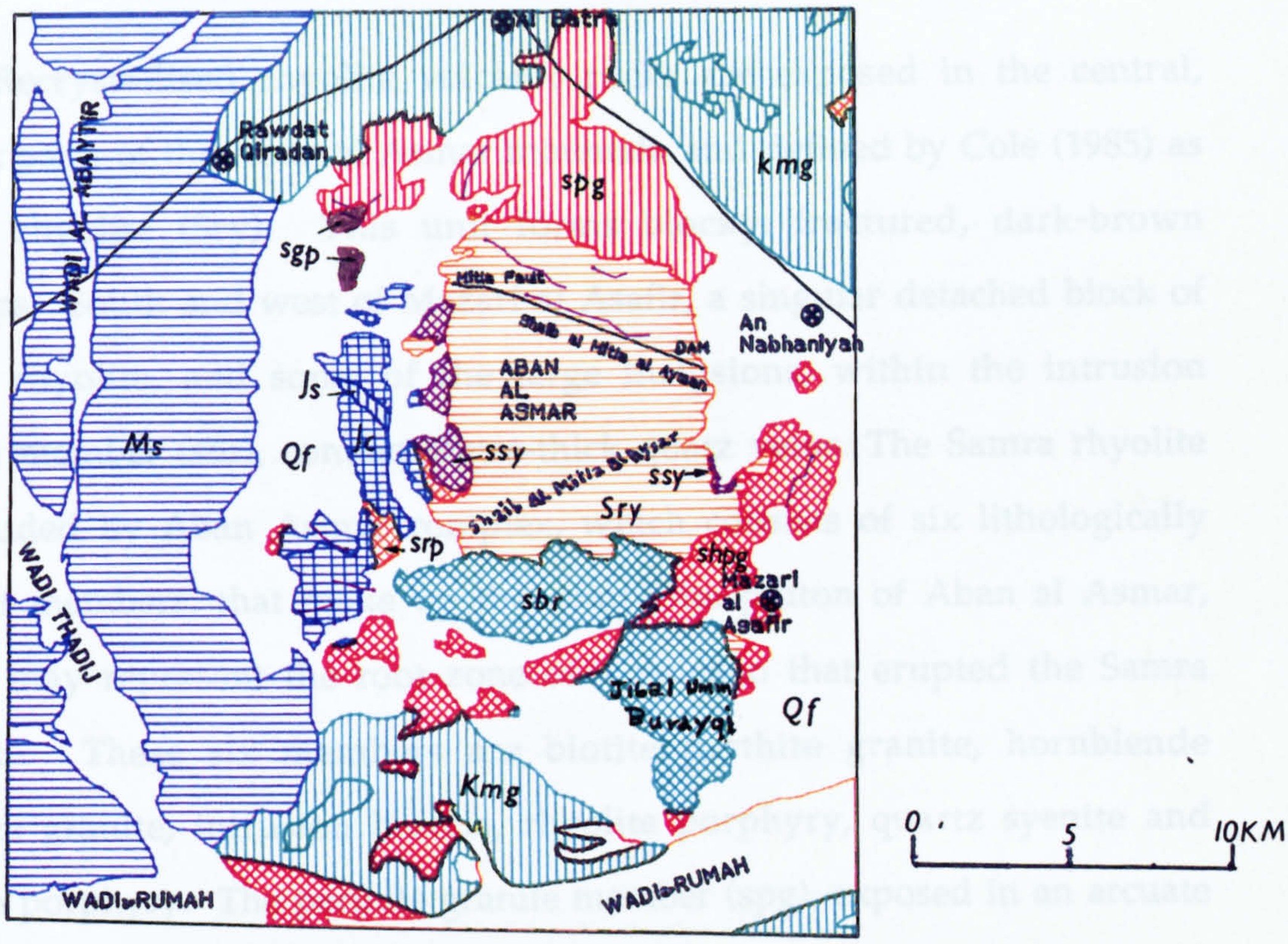

Qf alluvial fan and apron deposits

sgp granite porphyry

ssy quartz syenite

srp rhyolite porphyry

shpg hornblend perthite granite

spg biotite perthite granite

sbr introsion breccia

Sry Samra rhyolite

Js sandstone member

Jc conglomerate

Kmg monzogranit

Ms Maraghan sandstone

Figure 2.11. Geologic map of Aban Asmar, test area 4 (adapted from Cole, 1988).

Recrystallised rhyolite volcanic rocks are exposed in the central, highest parts of the Aban al Asmar mountain and defined by Cole (1985) as Samra rhyolite (Sry). This unit forms blocky, fractured, dark-brown outcrops. South and west of Mazari al Asafir, a singular detached block of Samra rhyolite, and some of the large inclusions, within the intrusion breccia member (sbr), contain metre-thick quatz veins. The Samra rhyolite is intruded by Aban Asmar complex, which consists of six lithologically distinct members, that make up the composite pluton of Aban al Asmar, which may represent the root zone of a volcano that erupted the Samra rhyolite. These six members are biotite perthite granite, hornblende perthite granite, intrusion breccia, rhyolite porphyry, quartz syenite and granite porphyry. The perthite granite member (spg), exposed in an arcuate mass at the northern end of the Asmar complex, is equigranular, coarse grained, tan to pale pink biotite perthite granite. It is very well exposed, and its contact with the Samra rhyolite is sharp, generally planar.

The hornblende perthite granite (shpg), exposed at the southern end of the Aban al Asmar, is very coarse-grained, equigranular, tan to pale pink, and orange biotite-hornblende perthite granite. It is mineralogically and texturally similar to the (spg) member, but contains minor amounts of dark green hornblende. The hornblende perthite granite is intruded by flat-lying sheets of the granite porphyries (sgp) and quatz syenite (ssy) west and north of Jibal umm Burayqi.

The intrusion breccia (sbr) member, exposed between the (shpg) and (sry). The (Sbr) consists of blocky slabs of Samra rhyolite (sry), enclosed by sub-horizontal sheets of the Hornblend Perthit granite member. The rhyolite porphyry member (srp) is exposed as irregular plugs of subvertical dikes of bright red, fine grained, moderately porphyritic rhyolite, that

intrudes country rocks along the western margin of the composite pluton at Aban al Asmar, and also intrudes the Samra rhyolite north of Mitla fault. Rhyolite porphyry is intruded by the quartz syenite member (ssy), but is not in contact with the granite members. The quartz syenite member (ssy), exposed as grey, richly porphyritic, medium grained biotite hornblende quartz syenite, forms a steep-sided stock in the wetern part of Aban al Asmar, and a gently dipping sheet north of Jibal umm Buraygi. This member intrudes (Sry), (shpg) and (srp) and is inferred to be younger than (spg). It is not in contact with (spg), but both were probably emplaced at the same time around the outer margins of the composite pluton at Aban al Asmar (Cole and Bohannon, 1985).

The granite porphyry member (sgp) is exposed as pale grey to pale pink, and is distinctively lighter in colour than other members of the complex. Leucocratic, sub-porphyritic to inequigranular biotite orthoclase granite and biotite syenogranite form a small north trending stock, and several thick dikes at the north-east corner of Aban al Asmar, and a northward dipping sheet three kilometres west of Jabal umm Buraygi. These various bodies intrude all other members of the Asmar complex except the quartz syenite (ssy), which is nowhere in contact.

Superficial deposits

Thin surfacial deposits of gravel, sand and boulders (Qf) are widespread in the plain areas and form fans and aprons around all the high peaks. The surface of the alluvial fans and apron deposits are covered with a large gravel derived from Jurdhawiyah group, Samra rhyolite and Abanat suite.

CHAPTER THREE

PHYSICAL PRINCIPLES OF REMOTE SENSING

3.1 Introduction

3.2 Electromagnetic radiation and spectrum
- 3.2.1 The visible region
- 3.2.2 The infrared region

3.3 Interaction of electromagnetic radiation with matter
- 3.3.1 Electron Transition
- 3.3.2 Vibration Transition

3.4 Interaction of electromagnetic radiation with earth's atmosphere
- 3.4.1 Scattering
- 3.4.2 Absorbtion

3.5 Interaction of EM radiation with rocks and minerals
- 3.5.1 Visible and NIR spectra
- 3.5.2 Mid IR spectra

3.6 Summary

3.1 Introduction

In remote sensing, the electromagnetic radiation (EMR) acts as a communication link between the sensor and the remotely located objects. The satellite sensor measures the amount of energy reflected from, or emitted by, the earth's surface that has passed through the earth's atmosphere. Hence, to effectively use such radiation and understand the results these sensors produce, an understanding of the nature, behaviour and the way this radiation interacts with matter (both earth's surface and atmosphere) is needed (Hunt, 1980; Hardy, 1981; Rees, 1990). In principle, remote sensing sensors could measure energy reflected or emitted from the earth's surface in any range of wavelength. However, the selective filtering of the earth's atmosphere (scattering and absorbtion by the atmospheric particulates), that lies between the sensor and the earth's surface, excludes certain wavelengths, and therefore limits the ability of the sensor to record information in these wavelengths.

This chapter presents some basic information about the properties of EMR and the way it interacts with matter. The discussion will be confined to those aspects of EMR relevant to this thesis.

3.2 Electromagnetic radiation and spectrum

The understanding of the physical basis of remote sensing begins with a study of electromagnetic radiation (EMR), which serves as a communication link between the satellite sensor, and the earth's surface. The EMR is a force field with electric and magnetic properties (orthogonal to each other) that ranges from metres to nanometers in its wavelength and travels in a sinusoidal fashion at the speed of light (Figure 3.1).

There are three basic attributes which define the electromagnetic radiation: wavelength (λ), distance from one crest of a wave to the next; wave frequency (ν), number of wave crests passing a fixed point in a specific period of time; and wave velocity (c), which is constant. The relation between these three measurements is:

$$c = \nu \lambda$$

in which wavelength and frequency have an inverse relation. Planck describes the electromagnetic radiation as a numerous tiny descrete packet of energy called a photon or quanta whose energy is given by

$$E = h\nu$$

where E is the photon energy (Jouls)
h is Planck's constant (6.626×10^{-34} Js)
ν is the frequency

In remote sensing, electromagnetic radiation is usually defined by its wavelength (Figure 3.2), which ranges from the very short wavelength of the gamma ray region, to the long wavelength of the radio wave region.

The wavelength regions which are of interest to remote sensing are the visible, near and mid infrared regions between 0.4 μm to 3 μm, thermal infrared region 3-14 μm and microwave region 1mm-1m. The regions in the EMS with wavelength shorter than the visible regions are not used in satellite remote sensing owing to the effect of scattering and

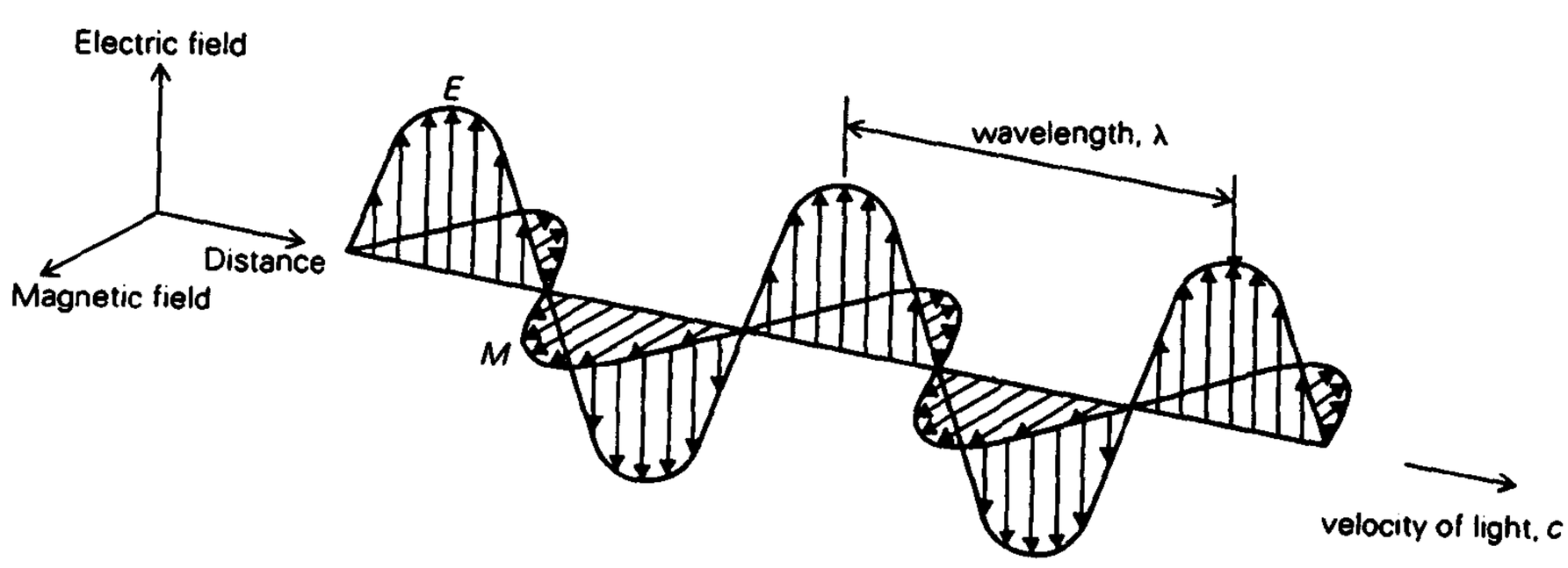

Figure 3.1. Electromagnetic wave with the electric (E) and magnetic (M) components orthogonal to each other (after Drury, 1987).

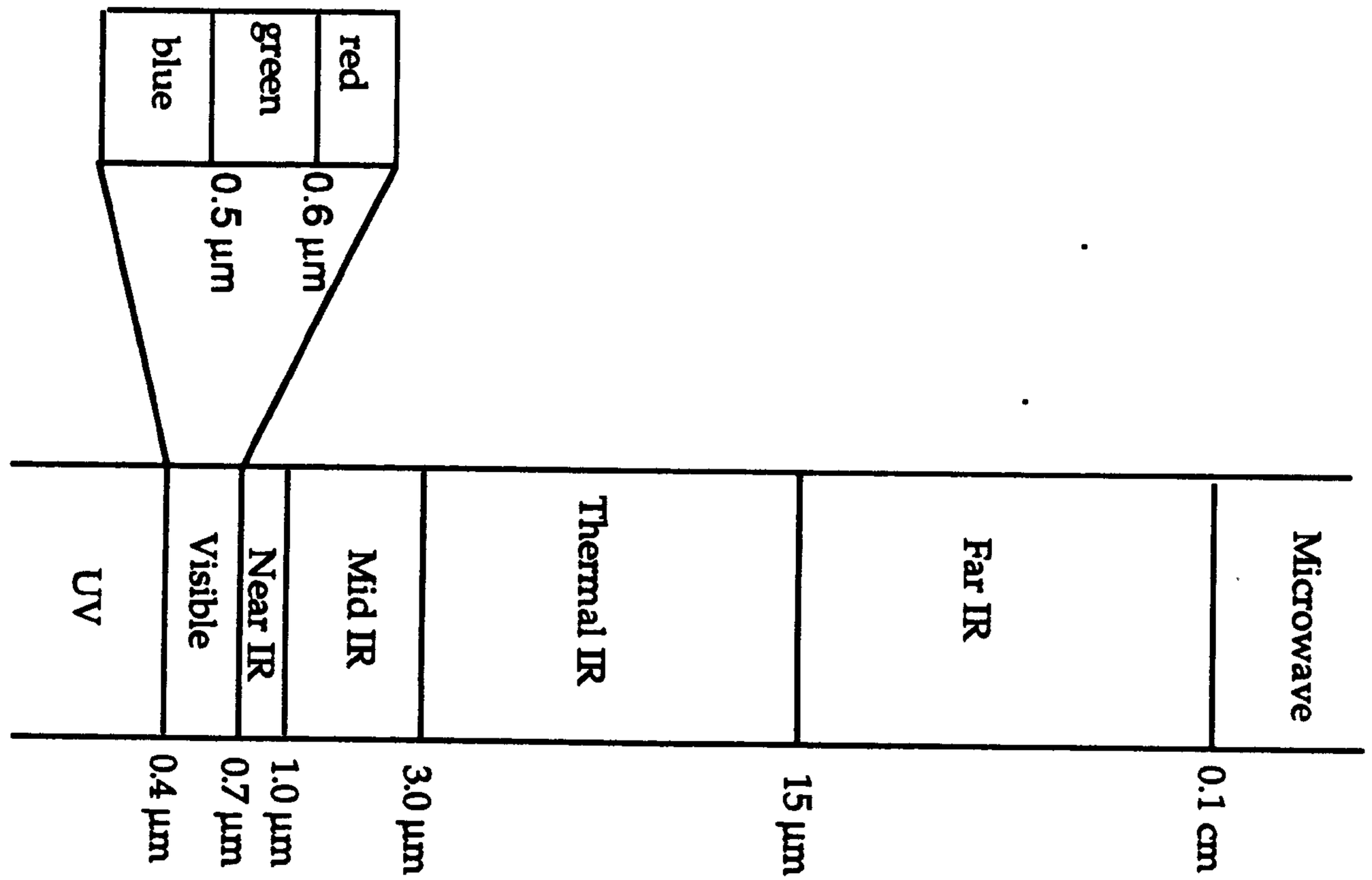

Figure 3.2. The electromagnetic spectrum, the diagram shows parts that are important in remote sensing.

absorption by the earth's atmosphere, and this will be discussed in later sections. Although the electromagnetic spectrum is divided into a number of regions, there are no sharp breaks between them.

3.2.1 The visible region

It constitutes a very small portion of the EMS with wavelength ranging between 0.4 μm to 0.7 μm. This region is defined by the sensitivity of the human visual system and that makes it the only well-defined region in the EMS (Campbell, 1987). This region is subdivided into three areas, blue, green and red, which correspond to the wavelengths 0.4 - 0.5μm, 0.5 - 0.6μm, and 0.6 to 0.7μm respectively. These three colours are named primary colours because no single one of them can be formed by mixing the other two, and all other colours can be formed by mixing them in appropriate portions (as will be described in Section 5.5).

In this region of the spectrum, the degree of sensitivity of the human eye to these three parts is not uniform, and has its peak of sensitivity at 0.55μm in the green (Mather, 1987). How the human eye detects these colours will be discussed in Section 5.5; however, an object's colour is defined by the interaction of this object with the incidence light. So if it, for instance, reflects the red light and absorbs the other two then we will see it as a red object and so on (Figure 3.3).

3.2.2 The infrared (IR) region

This region of the spectrum is very large relative to the visible region and divided into several parts. The part of the IR which is closest to the visible range and extends between 0.7 μm to 3 μm is divided into two sections, the near infrared (0.7 - 1.0 μm) and the mid infrared (1.0 - 3.0μm).

The part of the IR region that extends from 3.0 μm to 15 μm is called the Thermal IR region. In this region, radiation is emitted by the earth's surface and can be sensed by special sensors called Thermal Sensors. Much of the radiation in this area is absorbed by the atmosphere with principle windows at 3 - 5 μm and 8 - 14 μm wavelength (Figure 3.4)

How electromagnetic radiation generates and fluctuates is beyond the scope of this study. Useful reviews about the nature and physical principles of the EMR are given by for example Barret and Courtis (1982), Suits (1983), Elachi (1987) and Rees (1990). However, all matter above absolute zero (-273.15°C) will emit some form of radiation. The quantity of this radiation and its wavelength range is a complex function of the temperation of the body and its nature (Drury, 1987). The field of remote sensing is more concerned with how this radiation can be detected, reflected, or emitted. The source of the reflected radiation is invariably the sun and this radiation can be detected by systems, called "passive" systems, that sense the naturally available energy, whereas the systems that have their own source of energy to illuminate features of interest are termed "active" systems, such as RAdio Detection And Ranging systems (RADAR). This study will be concerned with the first type of system.

3.3 Interaction of electromagnetic radiation with matter

This section gives a simple review of the interaction mechanism of the EMR with matter, more detailed information can be found in Hunt (1980), Drury (1987), Elachi (1987) and Goetz (1989a). The interaction between EMR and the observed object is a very important factor in understanding and interpreting remotely sensed data.

When electromagnetic radiation is incident on an object, some of this energy will be reflected, some will be transmitted, and some will be absorbed. The conservation energy law states that:

$$Ei(\lambda) = Er(\lambda) + Ea(\lambda) + Et(\lambda)$$

where

$Ei(\lambda)$ = incident energy

$Er(\lambda)$ = reflected energy

$Ea(\lambda)$ = absorbed energy

$Et(\lambda)$ = transmitted energy

The reflected, transmitted, and absorbed components vary from one object to another and from one wavelength to another. These differences form the main skeleton for spectral remote sensing in multi-spectral measurements. The colour of any object we see when it is lit by the sun is the result of absorption or reflection of this continuous range (Figure 3.4). The same object may behave very differently if exposed to radiation of a different wavelength. For example, a glass might be transparent in one wavelength (visible) whereas in another wavelength (infrared) it appears opaque.

Roughness and orientation of the object also play an important role in the reflection process. Specular reflectors (Figure 3.5) are smooth surfaces that express a mirror like reflection, in which incident and reflection angles are equal. This happens when surface irregularities are smaller than the incident wavelength. Diffuse (or lambertian) surfaces are, on the other hand, rough surfaces which reflect uniformly in all directions. However, most of the earth surface is in between these two extremes. Whether a

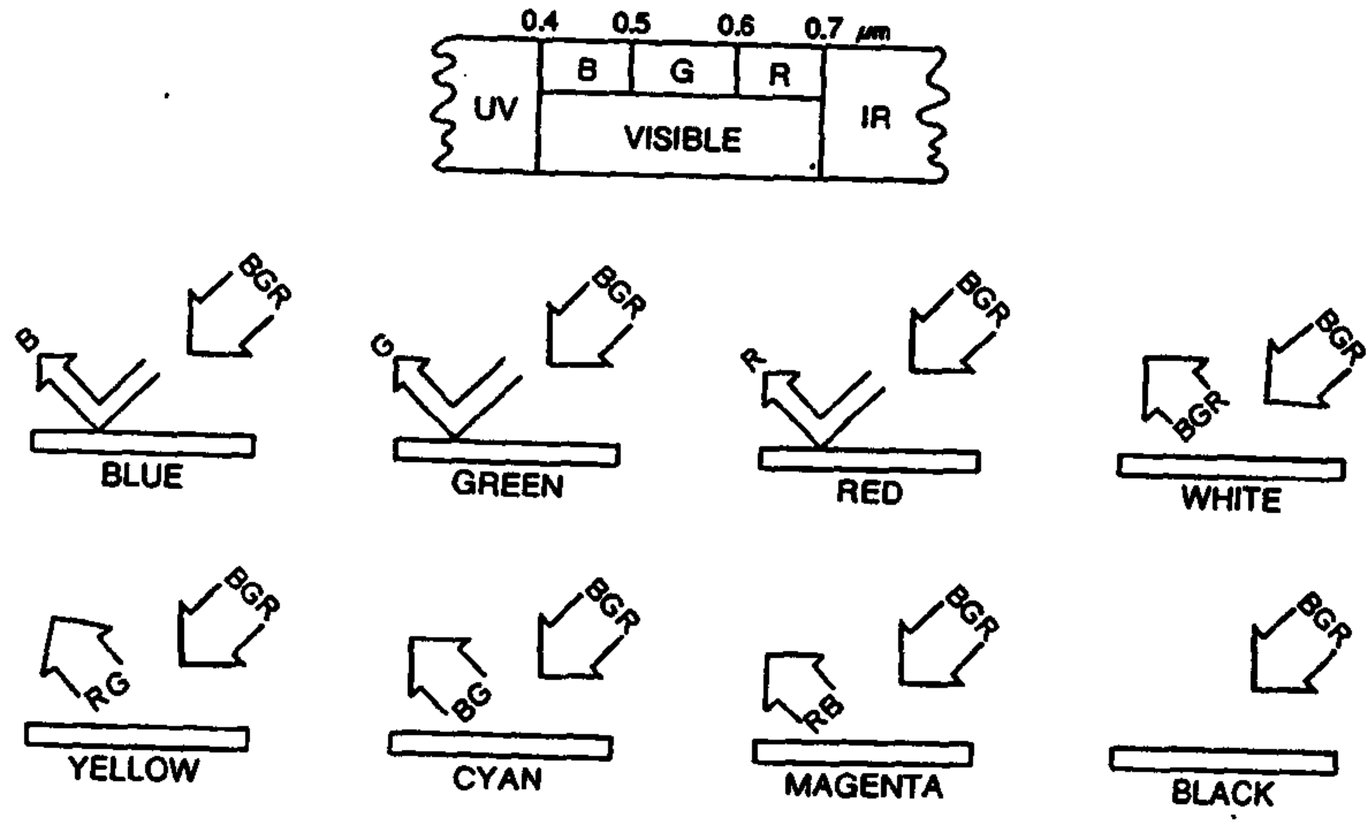

Figure 3.3. Colour (after Campbell, 1987).

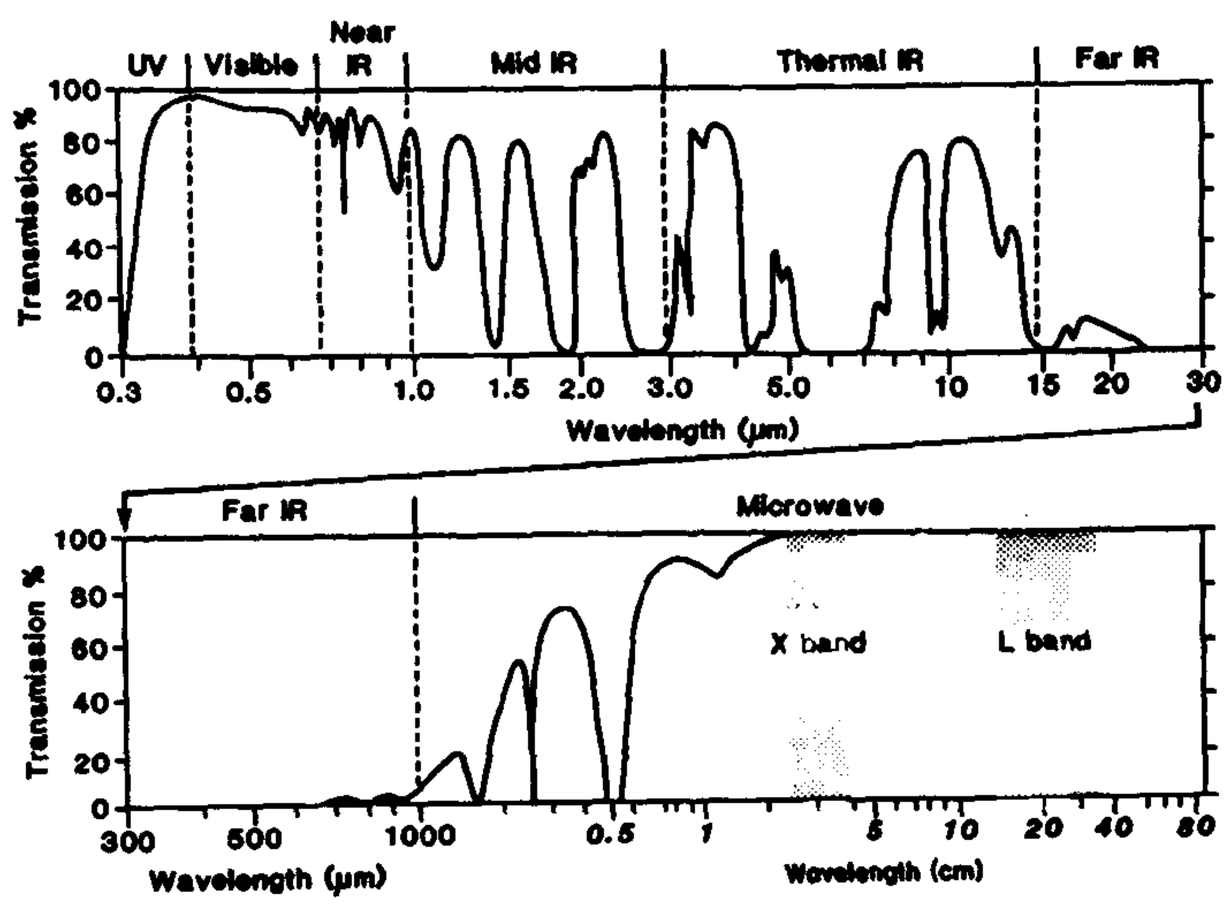

Figure 3.4. The main atmospheric windows throughout the electromagnetic spectrum (after Mather, 1987).

surface behaves as a smooth or rough surface depends on the wavelength involved. For example, a fine sand behaves like a rough surface in the visible range, whereas a very rough rock surface behaves like a smooth surface for radio waves. In satellite remote sensing we are more concerned with the diffuse reflectance since it contains spectral information about the colour of the reflecting surface (Lillisand and Kiefer, 1987). A useful expression of reflectivity of different surfaces is the reflection coefficient or albedo. Albedo is the ratio of energy reflected to energy incident on the surface. Dark and bright surfaces have low and high albedo respectively. In the visible region of EMS the wavelengths are very short, which leads to a diffuse reflection of most surfaces regardless of the incident angles (Barret and Curtis, 1982).

The part of the incident energy that is absorbed by the object elements causes an interaction between this incident energy (EMR) and the object's constituents. The energy state of an object is a function of the relative position and state of the cosntitutent particles at a given time. The total energy of an atomic molecular system is made up of the sum of three distinct types of energy states: electronic, vibrational and rotational (Hunt, 1980). Each of these states requires a different amount of energy for transition from one energy level to another (Gupta, 1991). Therefore, these mechanisms manifest themselves in different parts of the EMS (Figure 3.2). The electronic and vibrational transition processes create absorbtion bands in the visible,near and mid infrared regions, whereas the rotational processes occur at longer wavelengths (far infrared and microwave), and are restricted to gasses; therefore they will not be discussed further.

3.3.1 Electron transition

Electrons in an atom can only occupy a specific quantized orbit with a specific energy. The process associated with the transition of the electron from one energy level to another is called electron transition (Hunt, 1980). The most important electron transitions for remote sensing are associated with charge transfer, conduction band, and crystal field effects, which are observed predominantly in the short wavelength -- ultraviolet, visible, and near infrared regions of EMS due to the high energy required for their excitation.

The part of the energy that is absorbed will raise the energy level of electrons, causing migration from one atom to another. This process is known as charge transfer. The charge transfer between Fe and O_2 is the most commonly observed feature in the spectra of terrestrial minerals (Hunt, 1980). This feature is responsible for the steep increase in absorption towards the blue in the visible region, especially in the spectra of many weathered minerals (Figure 3.6).

In some semi-conductors (e.g., sulphides), almost all the photons with energy equivalent to the width of the forbeddin gab are absorbed (Gupta 1991). This gives rise to a sharp absorption edge in the visible or near infrared region of the EMS. This type of process is called conduction band process (examples of such absorption are given in Figure 3.7).

In molecules and many solids, the valence electrons of adjacent atoms form pairs, and these are the chemical bonds that hold atoms together. In the case of transition metal elements such as copper, chromium, cobalt, manganese and iron in particular, the partially filled inner shells in the atom hold unpaired electrons with excited states. These

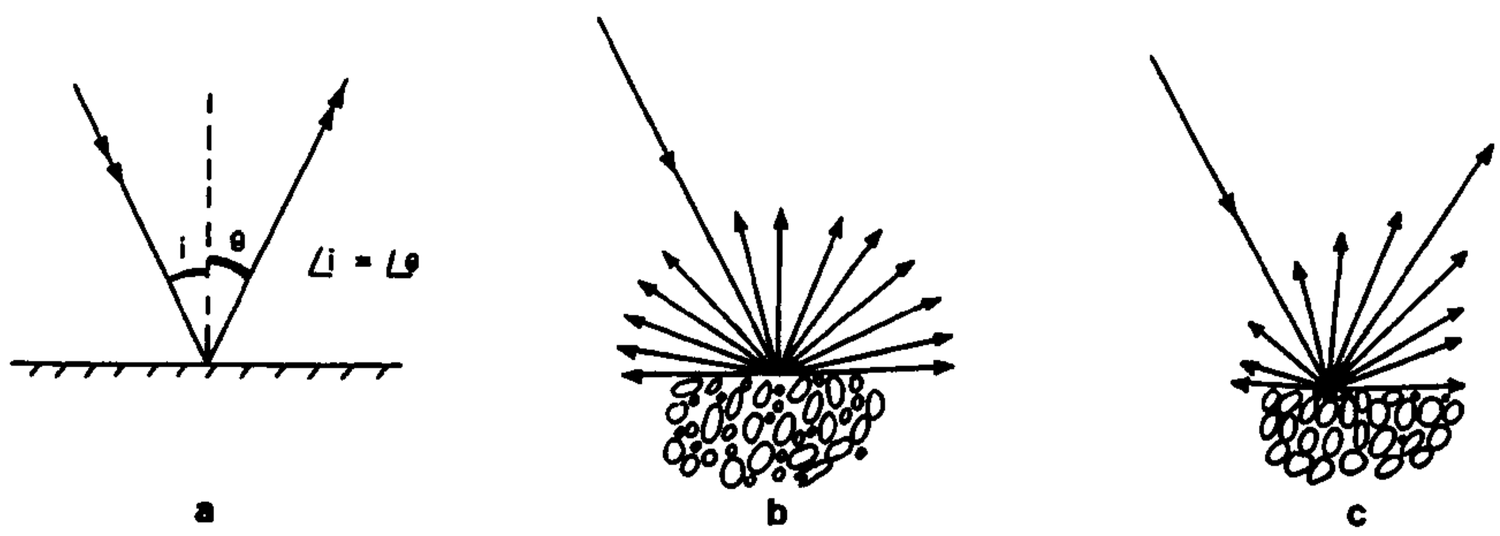

Figure 3.5. a) Specular reflection from a smooth surface;
b) defused (Lambartian) reflection from rough surface;
c) semi-defused reflection (natural bodies) (after Gupta, 1991).

excited states allow transitions, and consequently absorption, to take place. The energy associated with the transition lies in the visible region of the EM spectrum. However, the transitions, here are strongly affected by the electrostatic fields, that surround the atom, and which in turn are determined by the crystalline structure. As a result, different arrangements of energy levels for different crystals will produce different spectral effects for the same ion. This is called the crystal field effect; for example, ferrous ions will display absorption peaks at different wavelengths when located in different crystal fields (Figure 3.8).

3.3.2 Vibration process

This process is the result of bending and stretching of the chemical bonds. Spectral features for the vibration transition in geology occur in the mid and thermal IR parts of the EMS. In the mid infrared range the vibrational transitions are caused by overtone and combinations tones of the fundamental modes. The most common mineral group that provides absorption features in this region is the hydroxyle (OH) group.

The OH ion has one stretching fundamental which occurs near 2.77 μm, the exact location being dependent on the site in which the OH ions are located and the atom attached to it. In some cases the spectral features are doubled, indicating that the OH is in two slightly different locations or attached to two different minerals. For example, Al-OH and Mg-OH bending modes have fundamental wavelengths at 2.2 and 2.3 μm, respectively.

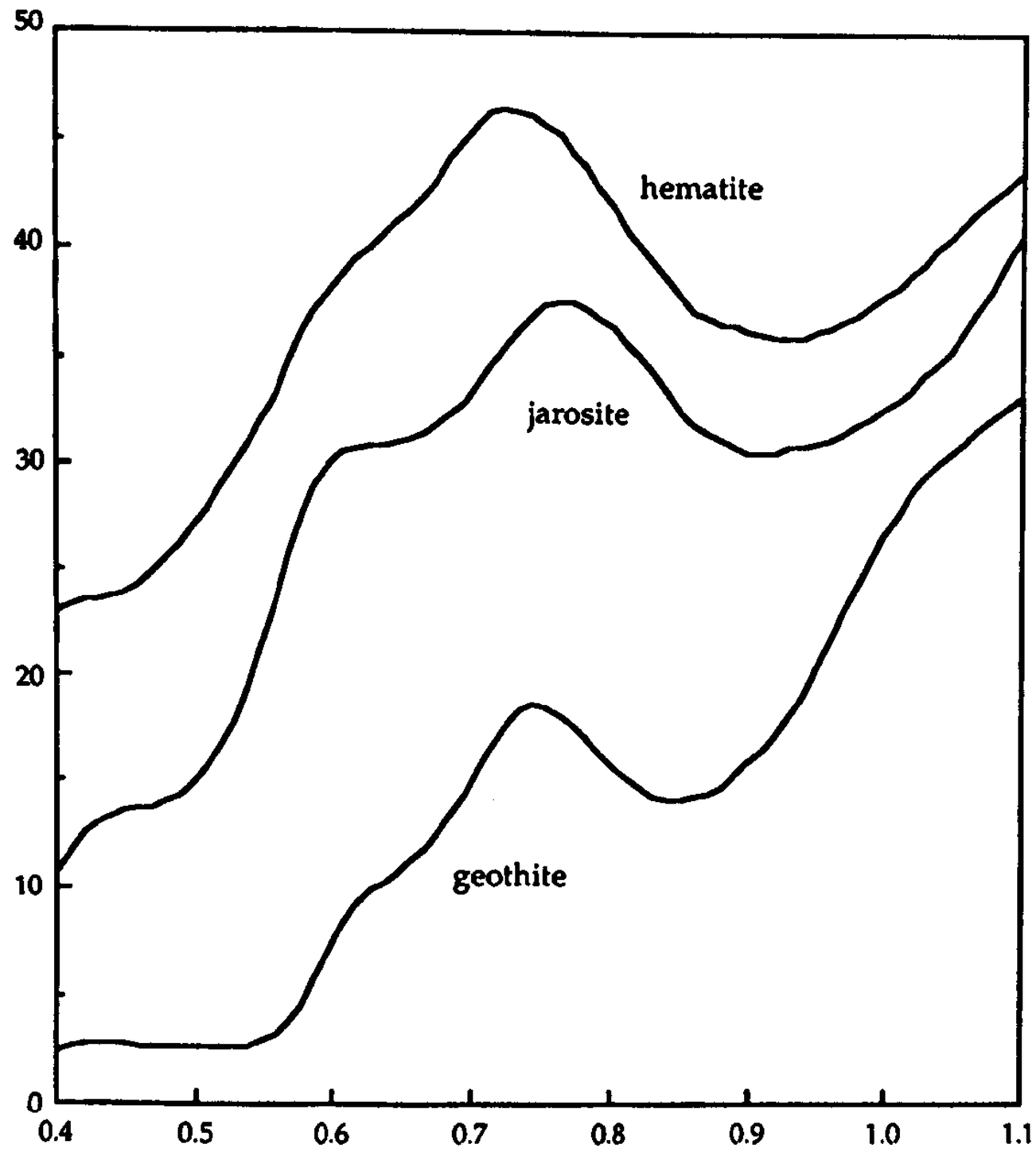

Figure 3.6. Reflection spectra of ferric-iron-bearing minerals showing a decrease in reflectivity towards the blue, caused by charge transfer effect (after Goetz, 1989).

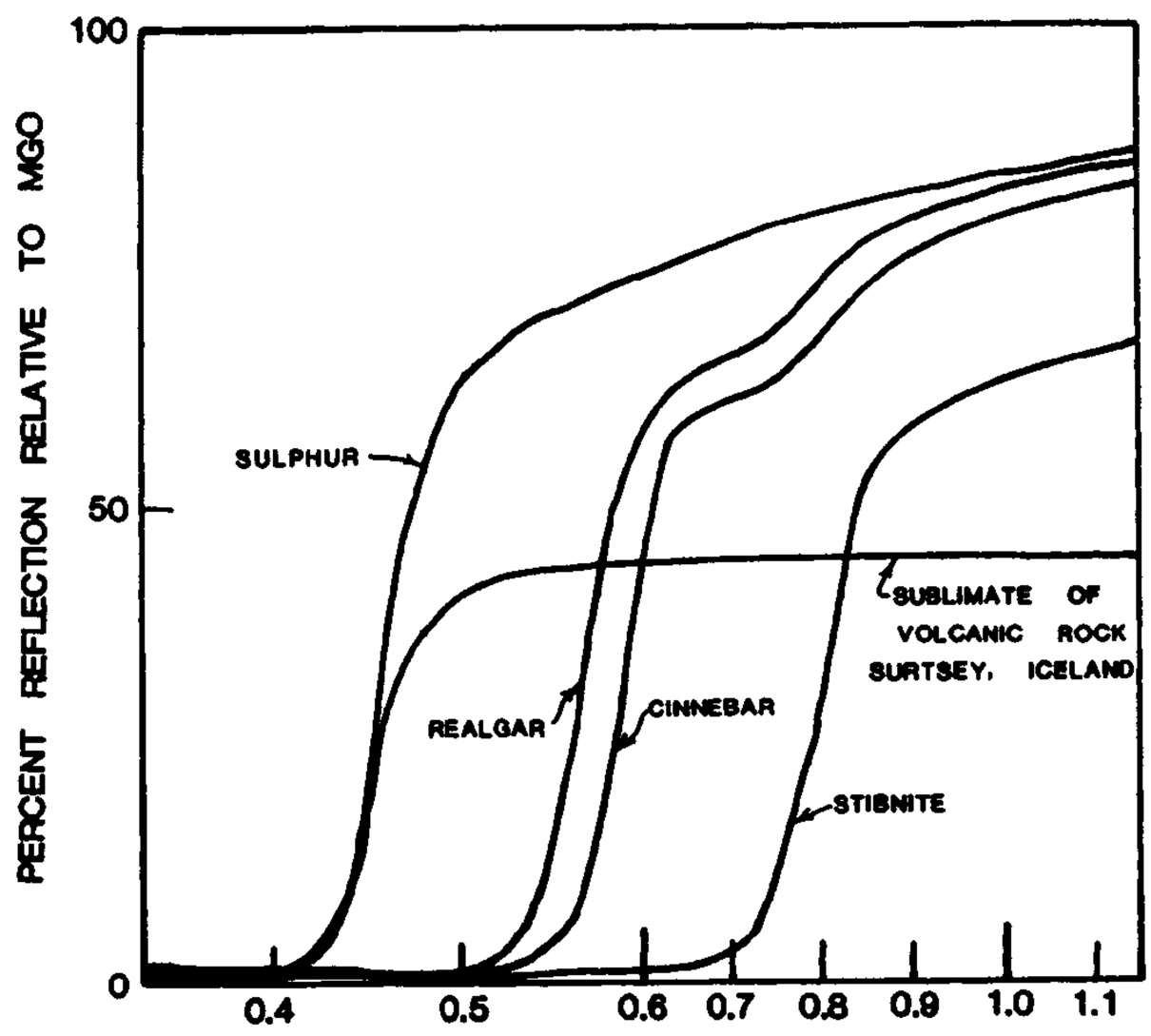

Figure 3.7. Reflection spectra of particulate samples of different materials, all of which display sharp absorption edge effect (after Hunt, 1980).

The carbonate minerals display similar features between 1.6 - 2.5 μm, and these are due to combinations and overtones of the fundamental vibrations of the CO_3 ion. Figure (3.9) shows the effect of the vibration process in different hydroxyles and carbonates.

Photons with just the right energy to excite one of the transition processes will be absorbed and so the light of the corresponding wavelength is not reflected. The absorption feature caused by a vibrational transition is relatively sharper than that caused by an electronic process (Rothery, 1987).

In this study both the interaction of the EMR with the atmosphere and with the earth's surface will be discussed; however, the discussion concerning the latter will be limited to minerals and rocks.

3.4 Interaction of electromagnetic radiation with the earth's atmosphere

Sensors that detect in the visible, near and mid infrared part of the spectrum are used to measure the radiation reflected by the earth's surface, and this radiation must pass through the atmosphere. The path length involved can vary according to the platform and the type of sensor used. For example, the radiation received by the six reflection bands of TM sensor, passes through the full thickness of the earth atmosphere twice on its journey from source to sensor, whereas a thermal aerial image senses energy emitted directly from the earth's surface and passes a single time through a relatively short atmospheric path. The interaction of EMR with the earth's atmosphere involves two processes, absorption and scattering; they both vary in their effect, according to wavelength (Anderson, 1985).

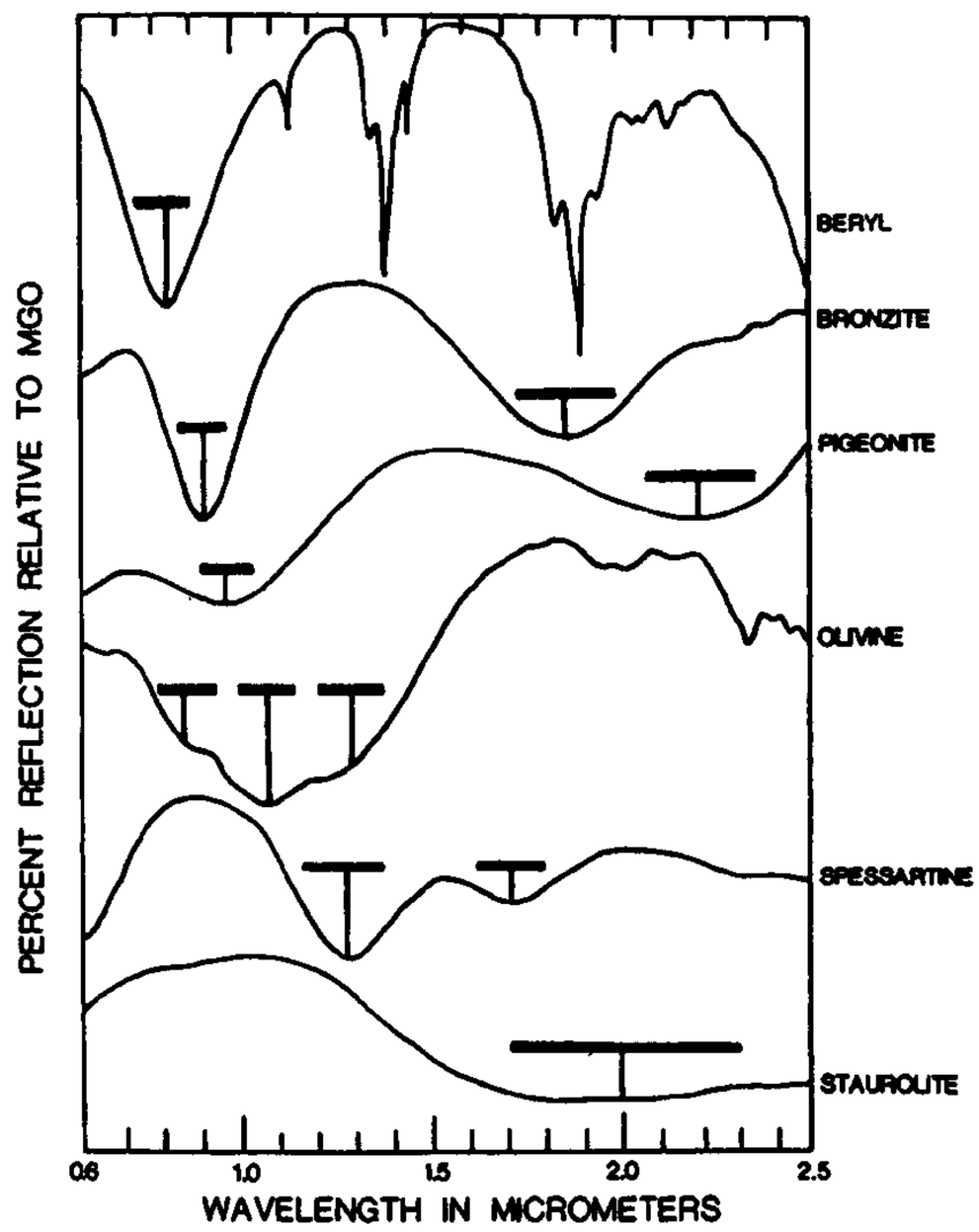

Figure 3.8. Spectra of minerals that contain ferrous ions in different crystal fields. All the absorption features are due to the crystal field effect (after Hunt, 1980).

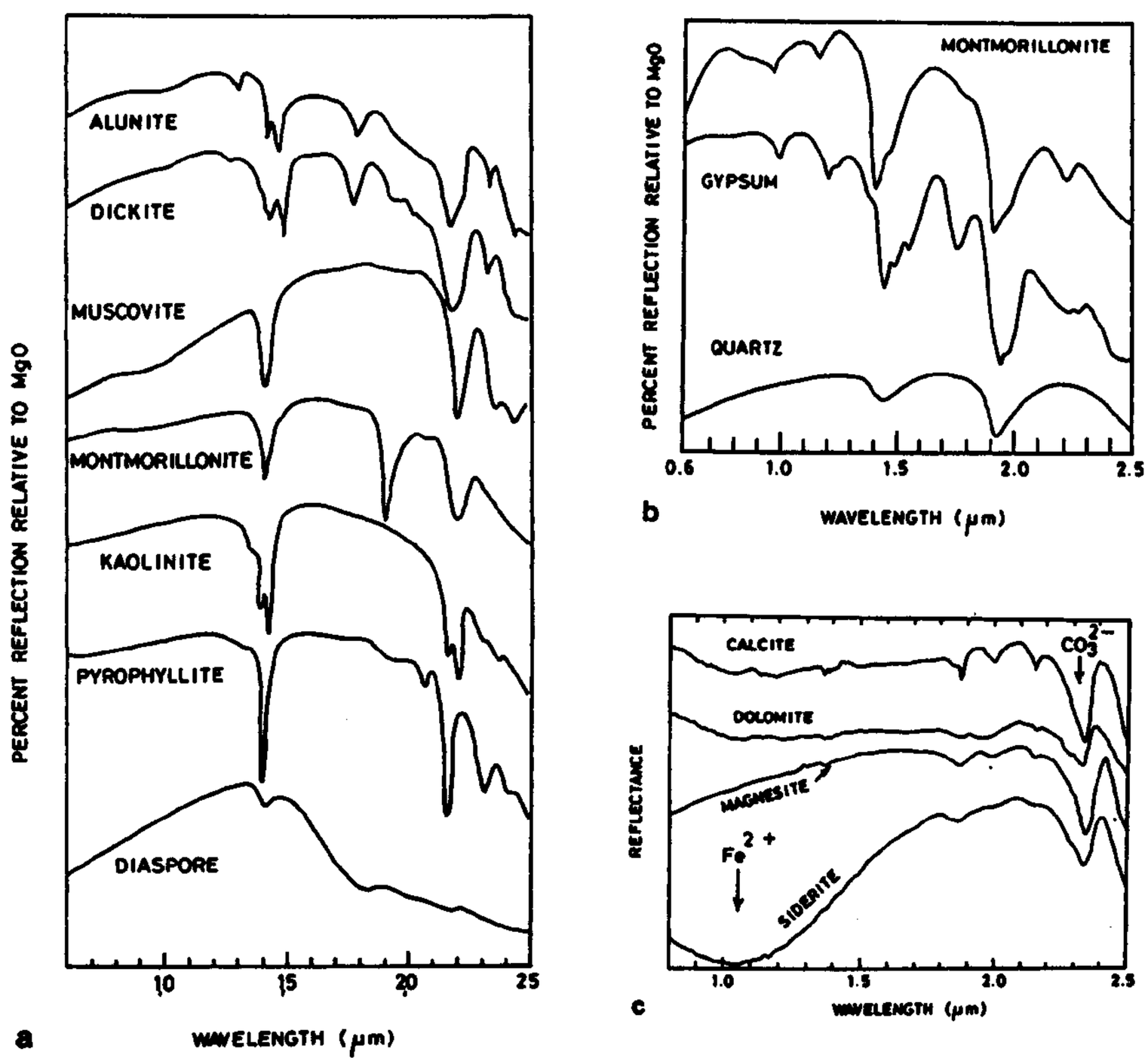

Figure 3.9. Reflectance spectra of different hydroxyles and carbonate minerals that show different absorption features caused by the vibration process: a) clay minerals; b) water bearing minerals; c) carbonates (after Gupta, 1990).

3.4.1 Scattering

Scattering can be defined as "multiple reflections of electromagnetic waves by particles or surfaces" (Sabins, 1987) which modify the direction and intensity of electromagnetic radiation. According to the size of the particles in the atmosphere, the scattering can be divided into three types: Rayleigh scattering, Mie scattering, and non selective scattering.

Rayleigh scattering occurs when the size of the effective atmospheric particles is smaller than the wavelength of radiation. The degree of scattering is inversely proportional to the fourth power of the wavelength, hence the shorter wave lengths are scattered more strongly by this scattering mechanism than the longer wavelengths (Drury, 1987; Mather, 1987). Rayleigh scattering is the main cause of haze in imagery, which reduces the contrast of the image.

In Mie scattering the size of effective atmospheric particles is approximately equal to the wavelength of radiation; water vapour and dust are the major causes of this type of scattering. It affects longer wavelengths compared to Rayleigh scattering.

Non selective scattering occurs when the size of the particles are much larger than the sensed wavelength radiation. Water droplets and dust cause this type of scattering, which affects all wavelengths equally, resulting in white fog or cloud.

3.4.2 Absorption

Unlike scattering, atmospheric absorption results in the effective loss of energy to the atmospheric constituents such as water vapour, carbon dioxide, ozone, nitrogen and oxygen. These constituents interact with the electromagnetic radiation by vibration and rotation transitions which cause

absorption of energy in specific wavelength regions. As shown in Figure 3.4, these regions appear narrow at the short wavelengths but increase in width toward the infrared and microwave regions. The regions of the electromagnetic spectrum, in which atmospheric absorption is low, are called atmospheric windows, and these are used to acquire remote sensing data.

From the above, it is clear that EMR is affected unavoidably, in many ways, by the atmosphere. The other components that affect electromagnetic radiation are the various types of feature that cover the earth's surface and cause radiation to be differentially reflected.

3.5 Interaction of EMR with rocks and minerals

Rocks are natural aggregates of one or more minerals. The study of rocks is based on methods drawn from mineralogy, geology, chemistry and physics, and the first step in their study requires an identification of the minerals present in them. The reflection and absorption spectra of rocks are a composite of the individual spectra of its constituent minerals. The spectra of minerals and rocks are dominated by either electronic or vibrational transition processes, since the rotation transition processes are restricted to gasses (Section 3.3). Laboratory studies of the visible, near and mid infrared spectra for minerals and rocks have received widespread attention in the literature (Hunt and Salisbury, 1970, 1971 and 1976 a and b; Hunt et al., 1971, 1974 ; Blom et al., 1980; Adams et al., 1982; Segal et al., 1986; Krohn, 1986; Whitney et al., 1983; Ross et al., 1989) where they have published visible, near and mid infrared spectra of a large number of minerals and rocks. These spectra are used as a guide by most geological remote sensing studies.

3.5.1 Visible and NIR spectra (0.4 - 1.0 μm) range

The spectra of geologic materials, in the visible and near infrared region of the electromagnetic spectrum, are dominated by the electronic transition process that were described earlier (Section 3.3). However, silicon, aluminium and oxygen, which are the major constituents of crustal rocks, do not have any electronic energy levels that show features in the visible and near infrared region of the spectrum. On the other hand, the less abundant transition elements of iron, copper, nickel, chromium, cobalt, manganese, vanadium, titanium and scandium have many excited states within this region of the electromagnetic spectrum (Elachi, 1987).

In the visible region the colour of an object could be a result of, either a specific absorption in this region, or an intense absorption in the adjacent wavelength region (near infrared or ultraviolet), where the absorption wing extends forward or backward into the visible. An example of this is olivine which has a green colour due to a major absorption band at 1.1 μm (NIR) and 0.4 μm (UV) (Hunt, 1980).

Electronic transitions within atoms usually require more energy than vibration transition within molecules, therefore the electronic transitions are characterised by short wavelength -- visible and near infrared absorption bands (0.4 - 1.1 μm) -- whereas the vibration transitions dominate the longer wavelength, mid and thermal infrared, regions (Podwysocki et al., 1986).

In the visible part of the EM spectrum, iron is the most important constituent and its effect is pervasive (Drury, 1987). Iron occurs widely on the earth's surface as a principal constituent of many materials; sometimes it partly replaces some of the elements, such as aluminium, magnesium

and silicon. Furthermore, iron ions can easily dissolve in water, which leads to an increase in their distribution in terristerial materials. The last two factors make iron a widespread element in most geological materials (Hunt, 1980).

The ferric ion displays a strong absorption band starting at the ultra-violet-blue region, due to charge transfer effect (Figure 3.6), and decreasing in absorption gradually toward the longer wavelength within the visible range. Iron ions also display absorption features at different wavelengths caused by the crystal field effect (Figure 3.8). Manganese also displays a strong absorption in the blue part of the spectrum. Examples of minerals that display absorption in the visible and near infrared region are iron minerals such as hematite, goethite and jarosite (Figure 3.6). Amphiboles and micas display absorption at about 1.0 μm caused by the presence of iron. Olivine displays a broad band in this region (Figure 3.10). Pyroxene minerals such as augite display an absorption feature at about 1.1 μm and 0.77 μm due to ferrous and ferric ions respectively (Hunt and Salisbury, 1970).

3.5.2 Mid infrared region (1.0 - 3.0 μm)

The absorption and reflection spectra within the region 1.0 - 3.0 μm is dominated by vibrational processes (Section 3.2.2). The most common active constituent is the hydroxyl ion (Hunt and Salisbury, 1971). The hydroxyl ion has a band near 2.7 μm, but its exact location depends on the site and the nature of the atom attached to it. Hydroxyl ions are commonly present in combination with aluminium and magnesium, e.g. Al-OH and Mg-OH in clays and hydrated silicates which cause a number of absorption features between 2.1 - 2.4 μm region. The Al-OH vibration band occurs at 2.2

μm, whereas the Mg-OH is at 2.3 μm. If both were present, such as in the case of kaolinite, then a double spectral feature would be noticed. The strongest absorption would occur at 2.3 μm and a weaker one at 2.2 μm. Figure 3.9a and b illustrates the different spectral features for different hydroxyle minerals. Areas that have been hydrothermally altered, usually contain clay (hydroxyl) minerals such as kaolinite, montmorillonite, muscovite and alunite. These minerals display strong absorption in the region between 2.1 - 2.4 μm (TM band 7), and have their peak reflectance at about 1.6 μm (TM band 5). Therefore these regions provide valuable information about the abundance of these minerals (Hunt, 1980).

Carbonates display similar absorption features between 1.6 and 2.5 μm due to overtones and combinations of the fundamental vibrations (Hunt, 1980). Carbonate minerals such as calcite, dolomite, magnesite and siderite display an absorption feature at 2.35 μm, which can be sensed by TM band 7. Siderite has an extra strong absorption feature at 1.1 μm caused by electronic transition in iron (Figure 3.9c).

From the above discussion, it can be summarised that the spectrum of a mineral is the result of the interaction between its constituent elements and the crystal field structure. Rocks are natural aggregates of different minerals. Therefore, the spectra of rocks depends on the spectra of the constituent minerals, their grain size and mixing, hence the interpretation of the spectra is very complicated. An example is shown in Figure 3.10, in which the addition of a small amount of an opaque or dark mineral (magnetite) to a reflecting mineral (olivine) reduces the overall reflectivity sharply. Representative laboratory spectra of some igneous rocks are shown in (Figure 3.11).

In addition, the curves, that show the spectral behaviour of the different minerals and rocks described earlier, were measured under laboratory conditions, and this reduces the complication caused by environmental factors such as atmospheric absorption and scattering. Another factor, is the breadth of the spectral bands detected by the satellite multispectral sensors, in which one band may cover the reflection by many different groups of minerals. For example, although TM band-7 is the best contributor to rock discrimination, its spectral breadth (2.0 - 2.35 μm) covers all carbonates and the hydroxyl minerals' spectral features (Figure 3.9a) and therefore prevents their precise identification. Another factor is the effect of weathering, which also presents a major problem in identifying rocks and minerals, from their spectral features (Watson, 1972; Settle, 1984). In particular, in desert areas a thin surface of manganese and iron oxides known as desert varnish frequently coats the rock surfaces (Adams et al., 1982). When the thickness of such a coat exceeds the maximum penetration of the radiation, 50 μm (Buckingham and Summer, 1983; Spatz et al., 1987 a and b), then, irrespective of its composition, it appears dark in the visible, near and mid infrared images. The effect and origin of this desert varnish are discussed in greater detail by Buckingham and Summer (1983) and Spatz et al. (1987b), (1989).

Because of the difficulties stated above, laboratory spectra should only be used as a guide in interpreting the spectral information acquired by the satellite systems and not as a definitive tool (Siegal and Gillespie, 1980). Despite all of the difficulties just stated, satellite images do provide a great amount of geological information (Siegel and Gillespie, 1980; Podwysocki et al., 1986; Drury, 1987; Rothery, 1987; Gupta, 1991). Pontual (1987) suggests

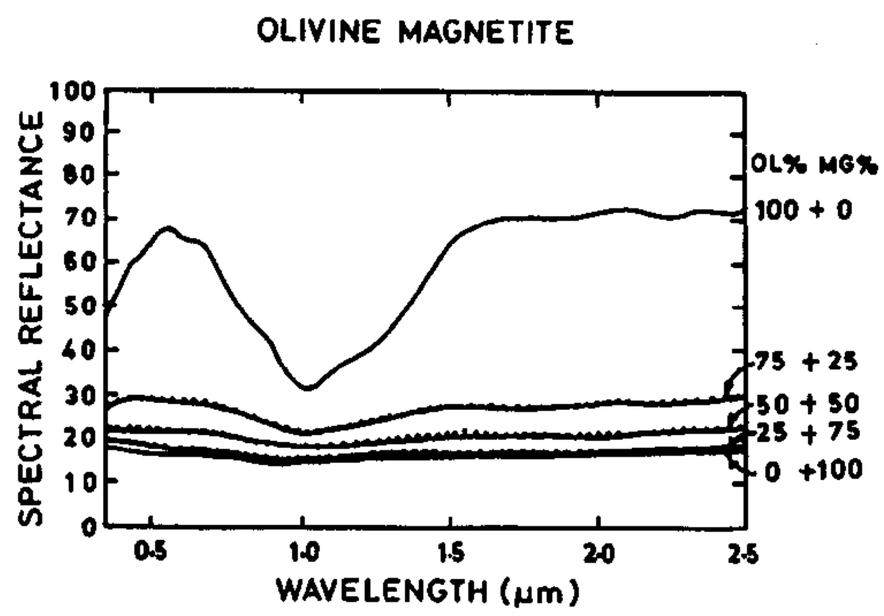

Figure 3.10. Spectral reflectance showing the effect of adding varying amounts of magnetite to olivine, causing a reduction in reflectivity (after Gupta, 1991).

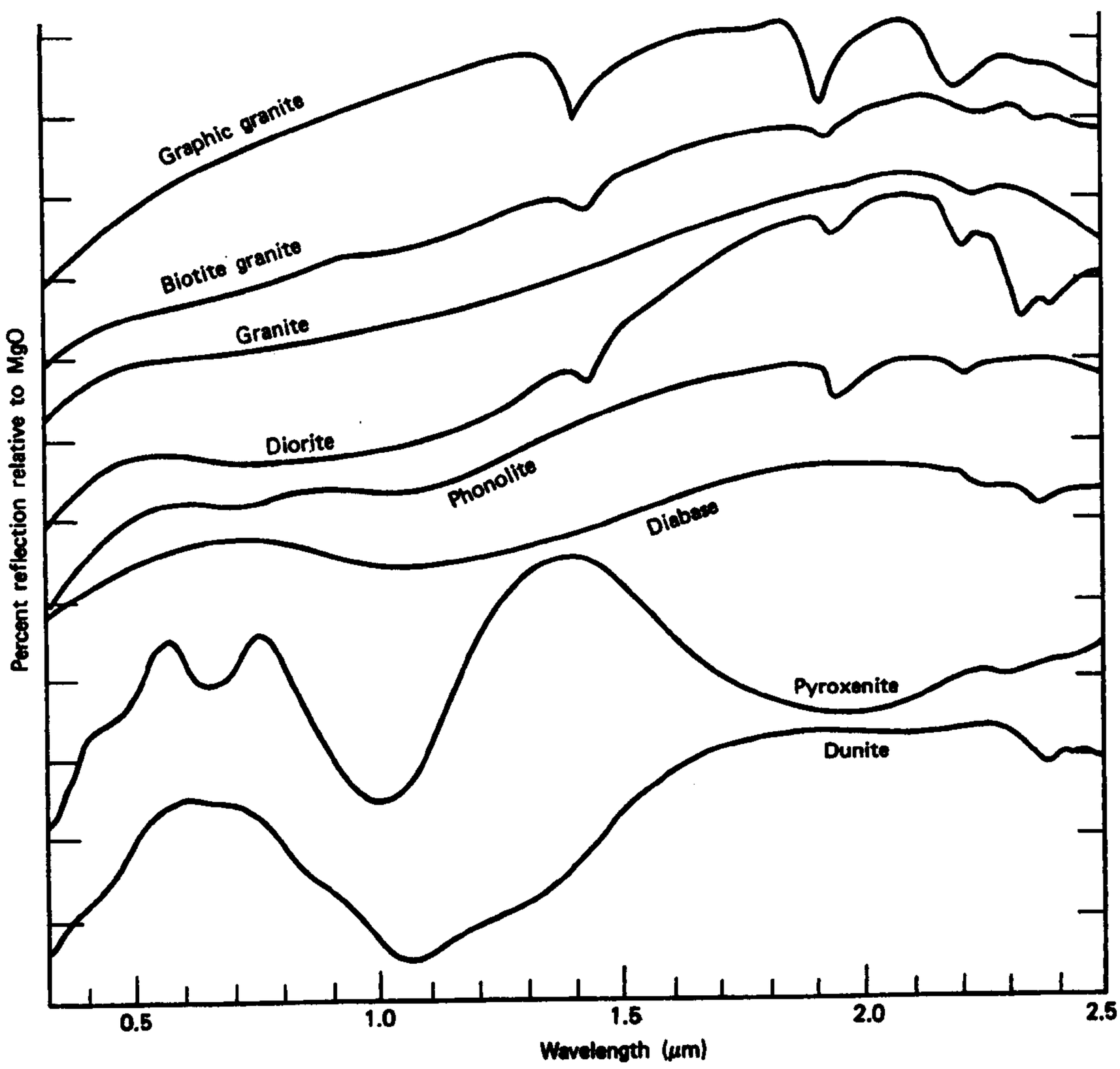

Figure 3.11. Reflectance spectra of different igneous rocks, arranged in order of decreasing acidity from top to bottom (after Abrams, 1980).

that the average weathering effects may be negligible over the 30 x 30 m^2 pixel area of the TM data because the rocks in arid areas, especially, weather to characteristic mineral assemblages which combine to give a distinctive spectrum.

3.6 Summary

In the first section of this chapter the basic information about the electromagnetic radiation was described. The information about the division of the electromagnetic spectrum that is related to this study, the visible, near and mid IR, were also described. This was followed by a description of the way in which electromagnetic radiation interacts with matter, and how it plays a major part in revealing information about an object. It has been demonstrated that, although the atmosphere plays a major role in restricting our ability to exploit and use the visible, near and mid-IR, we can still gather valuable information about these objects using the remaining windows.

The variation of reflected, transmitted and absorbed energy from one wavelength to another forms a valuable base for discriminating between different minerals and therefore different rock types. However, when dealing with real spectral features, that are derived from a satellite, additional complicating factors may intrude, which may change the apparent spectral reflectance of such minerals. When dealing with rocks, which are a natural aggregate of minerals, the situation becomes more complicated, and the net reflectance spectrum may be quite different from its constituents. However, as different mineral groups are present in different rock types, it is possible to describe broadly the spectral characteristics of rocks based on the spectra of their constituent minerals.

Hence, remote sensing data collected over arid and semi-arid areas, can provide a valuable amount of geological information.

CHAPTER FOUR

LANDSAT SATELLITE AND IMAGE PROCESSING SYSTEMS

4.1 Introduction

4.2 Landsat satellite programmes
- 4.2.1 Landsat MSS
- 4.2.2 Landsat TM

4.3 Computer compatable tape and data format

4.4 Digital processing systems
- 4.4.1 Microvax II
- 4.4.2 R-CHIPS software
- 4.4.3 IDRISI software

4.5 Preparation of the data

4.6 Summary

4.1 Introduction

Up until 1960, remote sensing data were mainly acquired from balloons, rockets or aeroplanes. By April 1960 a systematic orbital observation of the earth began by the launch of the first Television and Infrared Observation Satellite (TIROS-1), the first meteorological satellite. Since then a number of remote sensing satellites were launched. A detailed description of them can be found in Freden and Gordon (1983), Curran (1985), Jensen (1986), Richard (1986), Drury (1987), Lillisand and Kiefer (1987), Sabins (1987), Cracknel and Hayes (1991), Morelli (1992) and Morgan and Szejwach (1992).

One of the major developments in the field of earth's surface remote sensing was the launch in July 1972 of the first Earth Resource Technology Satellite (ERTS-1) which later was named Landsat-1. It and its successors have been widely used by geologists and geographers (Short, 1982; Drury, 1987; Sabins, 1987; Gupta 1991) and because of that, the Landsat series of satellites will be described in this chapter. In addition, the image processing systems used in this study will be briefly described.

4.2 Landsat satellite program

After about 10 years of planning and study by NASA, the first Landsat satellite, then called ERTS-1 (Earth Resource Technology Satellite-1) was launched on July 23, 1972 using a Thorn-Delta rocket. It was the first unmanned satellite system designed and operated solely for the study of land resources on a systematic, repetitive, medium resolution and multispectral basis (Mather, 1987). Landsat series operated under NASA up to 1983 when NOAA took that responsibility and in 1985 became under EOSAT Company. Five Landsat satellites have been launched since 1972;

they belong to two generations of technology with different platforms and orbital characteristics. Table (4.1) summarises these characteristics. One of the most significant features of this Landsat satellite programme was the decision to make all the data available to any one interested in it, at a reasonable price, and this has led to the establishment of a world-wide network of nationally and jointly-owned and operated receiving stations (Figure 4.1).

The first generation (Landsats-1 to -3) had identical orbit characteristics as summarised in Table (4.2). Their orbits were near polar, circular, repetitive, and sun synchronous. They covered most of the earth's surface (between 82°N and 82°S), and the circular orbit provided a relatively constant imagery scale. The sun synchronous orbit meant that it crossed the equator at approximately the same local sun time of about 9:30 a.m. The satellite altitude was about 918 kilometres (varying between 880 and 940 kilometres); they completed each orbit around the earth in about 103 minutes, resulting in 14 orbits a day, with a ground track speed of about 6.46 km/sec. Figure 4.2 shows the N to S ground traces for the satellite orbits for a single day. They cross the equator at 9° from normal.

Two image sensors were carried in this series (RBV and MSS). The Return Beam Vidicone (RBV) camera system on board Landsats-1 and -2 consists of three television-like cameras, that frame the same 185 x 185 km ground area simultaneously, with a nominal ground resolution of 80 m and spectral sensitivity of three bands: green (0.475 to 0.575 μm); red (0.58 to 0.68 μm); and near-infrared (0.69 to 0.83 μm) and named Bands 1, 2 and 3 respectively. The RBV cameras operate without the need for film; their images are exposed by a shutter device and stored on a photosensitive

Satellite	Launched	Retired	RBV bands	MSS bands	TM bands	Nominal altitude (km)	Orbit inclination	Orbit period (min)	Repeat cycle (days)	Equator crossing time
Landsat-1	23 July 1972	6 Jan 1978	1,2,3 (simultan. images)	4,5,6,7	None	918	99°	103	18	09 30
Landsat-2	22 Jan 1975	25 Feb 1982	" "	4,5,6,7	None	918	99°	103	18	09 30
										09 30
Landsat-3	5 Mar 1978	31 Mar 1983	A,B,C,D (one-band side by side images)	4,5,6,7,8*	None	918	99°	103	18	
Landsat-4	16 Jul 1982	—	None	1,2,3,4	1,2,3,4,5,6,7	705	98.2°	89.9	16	09 45
Landsat-5	1 Mar 1984	—	None	1,2,3,4	1,2,3,4,5,6,7	705	98.2°	89.9	16	09 45

* Band 8 (10.4-12.6mm) failed shortly after launch.

Table 4.1. Landsat series of satellite, general characteristics.

Band No. in Landsat-1, -2,-3	Band No. in Landsat-4,-5	Spectral range	Name	Ground resolution	Number of scan lines run concurrently	Quantization	Image format and comments
a) MSS - Landsat-1,-2,-3,-4,-5							
MSS-4	MSS-1	0.5-0.6 m	Green	79 x 79 m	6	6-bit	185 x 185 km
MSS-5	MSS-2	0.6-0.7 m	Red	spaced at 56 m	6	6-bit	images with 10% forward
MSS-6	MSS-3	0.7-0.8 m	Near-IR	intervals along scan	6	6-bit	overlap and 14% side
MSS-7	MSS-4	0.8-1.1 m	Near-IR	line	6	6-bit	overlap at the equator
MSS-8 (only on Landsat-3)		10.4-12.5 m	Thermal IR	120 x 120 m	4	Limited data available	increasing with latitude
b) TM - Landsat-4,-5							
	TM 1	0.45-0.52 m	Blue-green	30 m	16	8-bit	185 x 185 km
	TM 2	0.52-0.60 m	Green	30 m	16	8-bit	images with
	TM 3	0.63-0.69 m	Red	30 m	16	8-bit	10% forward
	TM 4	0.76-0.90 m	Near-IR	30 m	16	8-bit	overlap and
	TM 5	1.55-1.75 m	SWIR	30 m	16	8-bit	8% sidelap
	TM 7	2.08-2.35 m	SWIR	30 m	16	8-bit	at equator
	TM 6	10.4-12.5 m	Thermal IR	120 m	4	8-bit	increasing with latitude

Table 4.2. Landsat MSS and TM sensor specification (Gupta 1991).

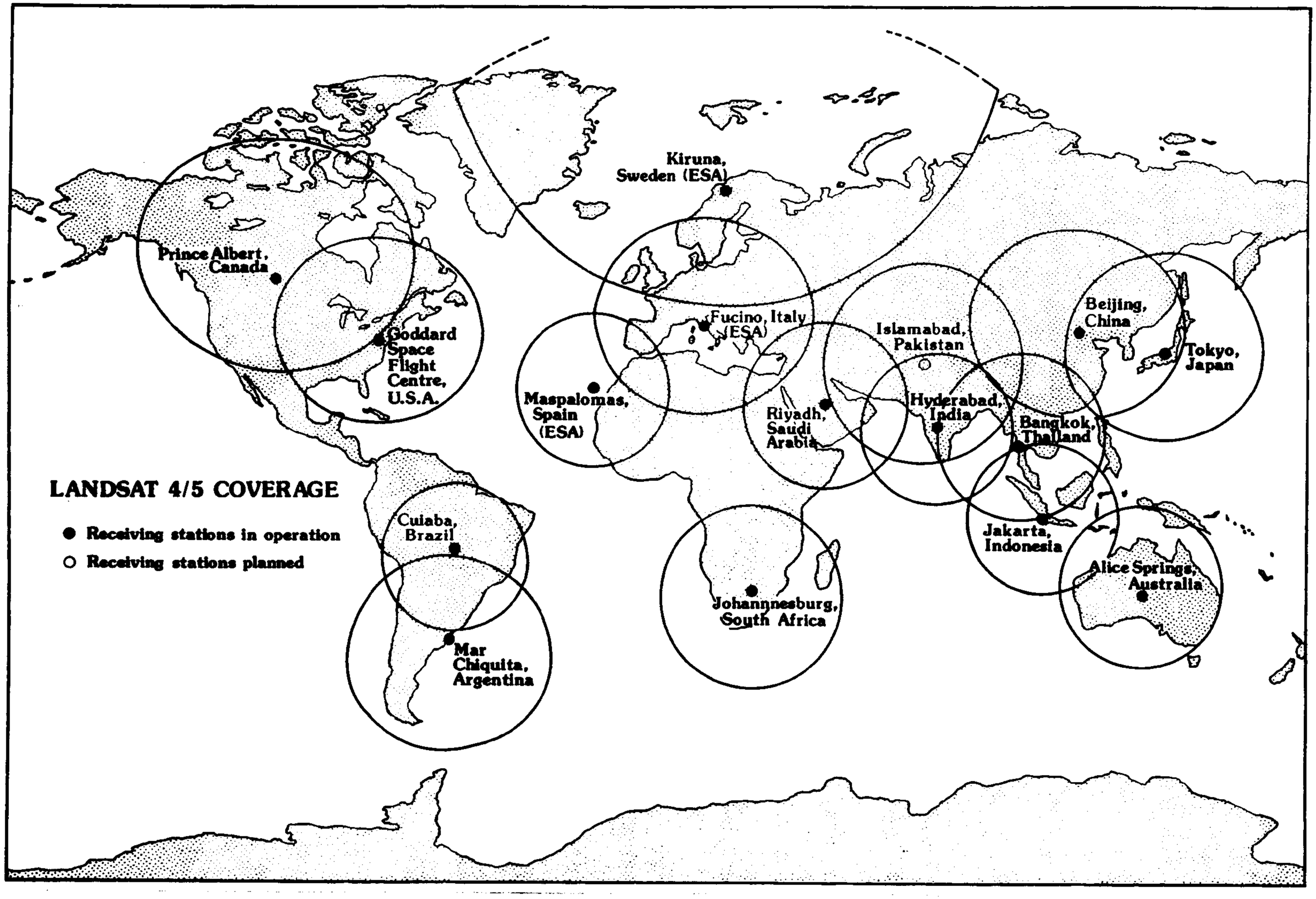

Figure 4.1. Distribution of Landsat ground receiving stations (after Drury, 1990).
• operational ° planned

surface which is then scanned by an electron beam to produce a video signal just like the television camera. The RBV system on board Landsat-3 provided much improved ground resolution of 30 m, using just one spectral band range between 0.5 to 0.75 μm, with two cameras aligned to view adjacent ground areas with 14 kilometres overlap, giving 183 x 93 km image.

The second generation of Landsat Series consists of two satellites, launched in July 16, 1982 and March 1, 1984 and named Landsat-4 and -5 respectively. They differ in their orbital characteristics in that, they have a lower altitude of 705 km (Table 4.1 and Figure 4.2), in order to achieve both higher resolution and shuttle recovery for refurbishing. The number of orbits per day was increased to 14.56, which gave a repeat cycle of 16 days, and crossed the equator at 9:45 a.m. local time. The imaging sensors carried on these satellites are MSS and Thematic Mapper (TM) (Table 4.2) and will be discussed in greater detail in sections 4.2.1 and 4.2.2.

Although it is TM data which has been used in this study, both the MSS and TM sensors will be described here, to show the improvement of TM compared to MSS both spectrally and spatially, which justifies using it in this study.

4.2.1 Landsat MSS

The MSS system is the only sensor which was available in the five Landsat satellites, it was the first satellite sensor in producing data in a digital format which made it possible to process the imagery using a computer, thus leading to their widespread use. From a geological point of view, the MSS system has revolutionised the geologist's view of the earth, in terms of synoptic views, and more importantly, by giving the

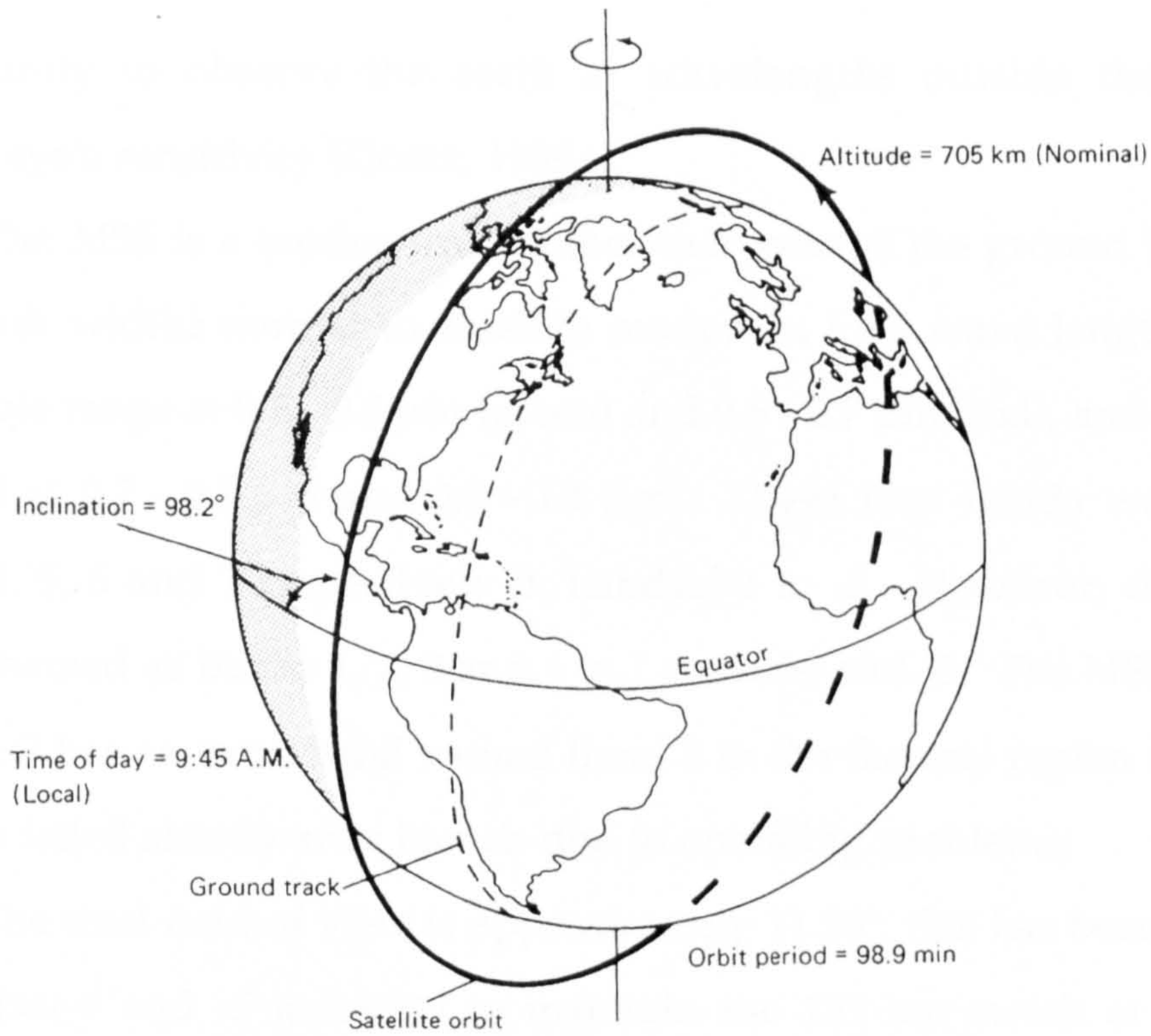

Figure 4.2. Landsat-4 and -5 sun-synchronous orbit (from Lillisand and Kiefer, 1987).

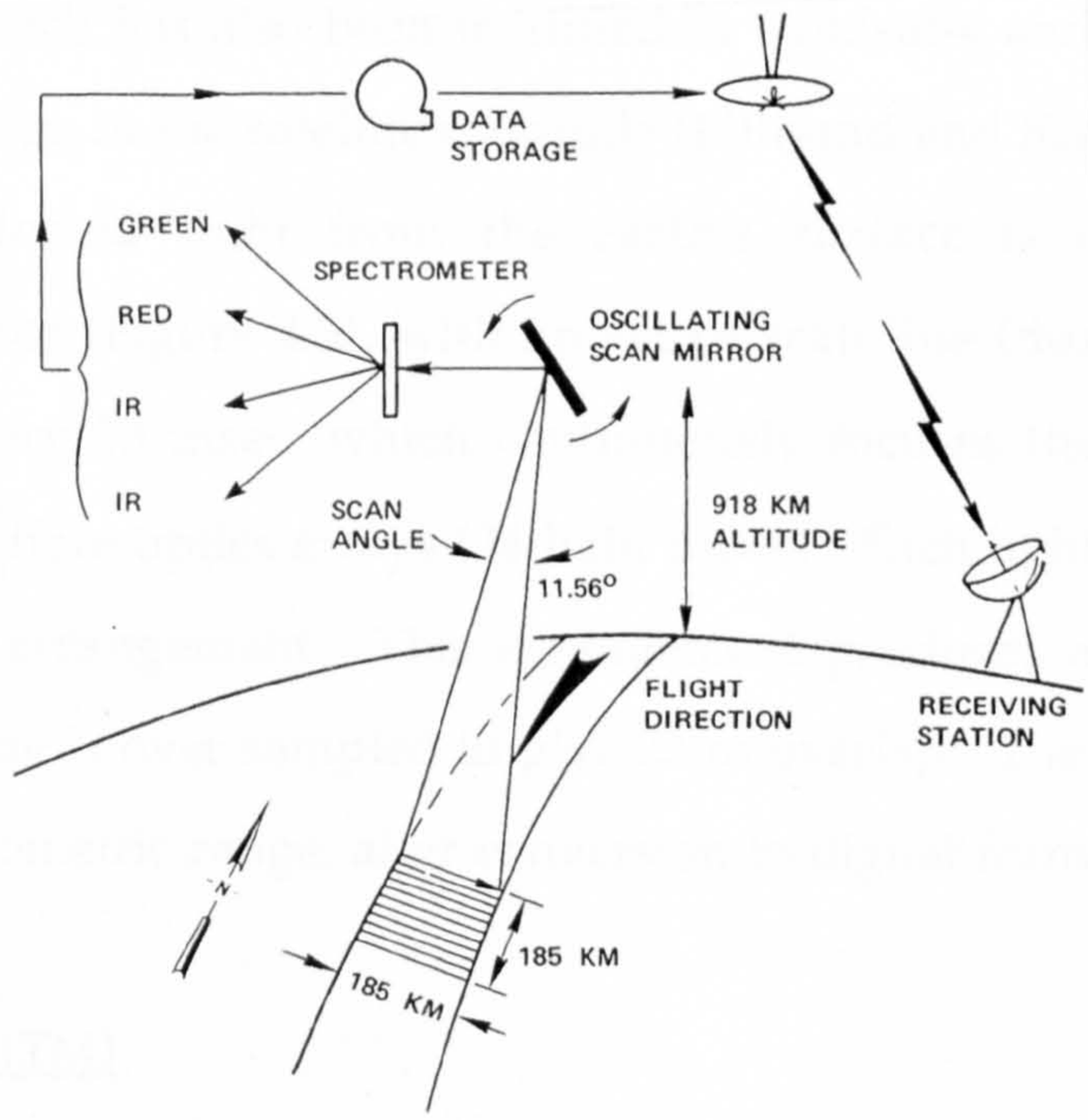

Figure 4.3. Scanning arrangement of MSS on board Landsat-1, -2 and -3. On Landsat-4 and -5 the altitude is 705 km and the scan angle is 14.9 (from Sabins, 1987).

opportunity to observe the earth at wavelengths outside the range of human eye's sensitivity (Goetz, 1989a).

The MSS is a mechanical scanner that sweeps the ground below (185 km swath width) normal to satellite motion in four wave lengths, two in the visible range at 0.5 - 0.6 μm (green) and 0.6 - 0.7 μm (red), and two in the Near IR at 0.7 - 0.8 μm and 0.8 - 1.1 μm. These four bands were named Bands 4, 5, 6 and 7 respectively in Landsat-1 to -3. However, these bands were renamed as Bands 1, 2, 3 and 4 in Landsat-4 and -5. The MSS on board Landsat-3 has an extra band named Band 8 in the thermal region (10.4 - 12.6 μm) but failed shortly after launch due to operating problems.

The total field of view is approximately 11.56°; this has been increased in Landsat-4 and -5 to 14.92° to maintain the 185 km swath at the lower altitude of 705 km (Figure 4.2). The instantaneous field of view (IFOV) is about 79 m, which has also been modified in Landsat-4 and -5 to 82 m due also to the change in the satellite's altitude (Lillisand and Kiefer 1987).

The reflected light from the earth's surface is directed by an oscillating mirror (Figure 4.3), with an active scan line (during the west to east phase) every 33 msec, which continuously focuses the ground image into a series of fibre optics arrays (24 light pipes). Each light pipe leads to a filter/detector arrangement. This arrangement produces a 6 line, 4 band image. Each line is over sampled to give 23 m overlap. The IFOV is 79 x 79 m and the radiometric range, after conversion to digital form, is 64 bits.

4.2.2 Landsat (TM)

Since it was carried out on board Landsat-4 (16 July 1982), the data collected by the TM sensor have gradually shifted the attention of the geological remote sensing community away from Landsat MSS data

(Rothery, 1987). The high spatial resolution capability of TM (30m for reflected bands) brings space-born remote sensing into the category similar to high altitude aerial photography (Haydn, 1983). The diversity of spectral bands on TM, which include part of the infrared, have proved to be more suitable than the MSS for lithological studies and offers a new capability for discriminating different objects (Abrams et al., 1983; Goetz et al., 1983; Haydn, 1983; Williams et al., 1983; Bernstein et al., 1984; Townsend, 1986; Rowan et al., 1987; Haack and Jampolar, 1987; Rothery, 1987; Abrams et al, 1988; Crosta and Moor, 1989).

The TM sensor carried by Landsat-4 and -5 is a highly advanced multispectral scanner that has new and more optimally placed spectral bands, finer spatial resolution and geometric design improvements relative to MSS (Williams et al., 1983). The TM has seven spectral bands covering the spectral region from 0.45 to 12.5 μm (Table 4.2). Three of them are in the spectral range of the MSS (green, red and reflected infrared) but with a narrower band width, which improves the spectral sensitivity, and four new spectral ranges. These include a 'blue' band, which makes it possible to produce natural colour images using the three bands in the visible region, and two bands in the infrared region. In fact Band-7 (2.08 to 2.35 μm) was added after the initial planning phase, at the request of the geological community (Richards, 1986). The fourth 'new band' was in the thermal infrared region. The wavelength and location of the TM bands were chosen to enhance the spectral differences of major earth's surface features.

Unlike the MSS, the TM scanning mirror collects data in both directions, with a sweep rate of 6.99 Hz (13.67 Hz in MSS) which gives a higher affective scan time for a given spot on the ground which, in turn,

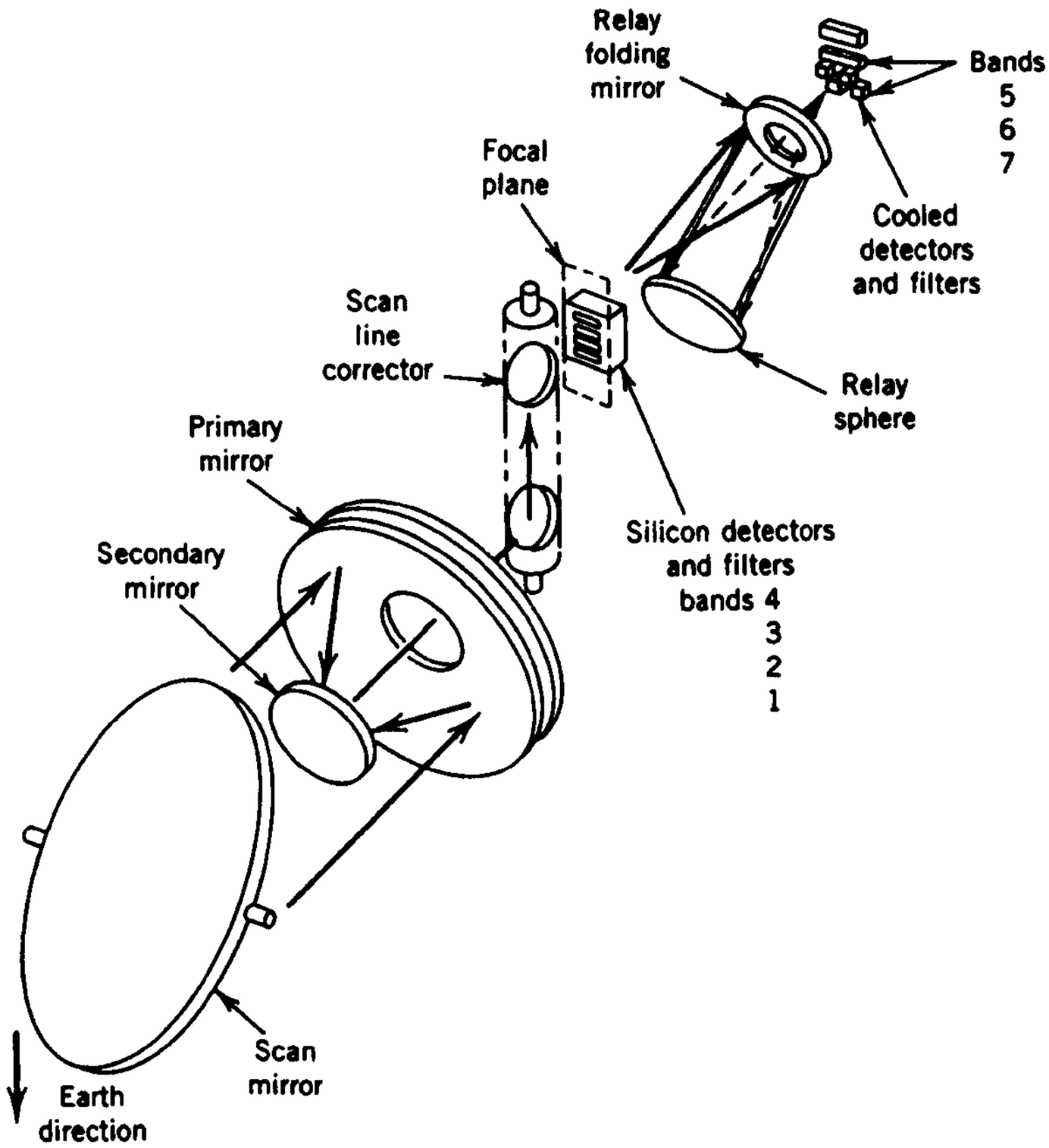

Figure 4.4. Thematic Mapper optical system (from Elachi, 1987).

improves the signal to noise performance, and makes it possible to achieve a higher spatial resolution of 30 m.

The TM sensor (Figure 4.4) has a scan line corrector, placed between the scan mirror and the detector, which rotates the TM line of sight backwards along the satellite direction in order to correct for the forward motion of space craft, and this produces a straight scan line perpendicular to the satellite motion.

The number of detectors was increased to 16 detectors for each of the 6 reflected bands and 4 detectors for the thermal band, and that implies that 16 lines for each reflected band and 4 lines for the thermal band are collected simultaneously with each sweep of the mirror. Instead of using fibre optics to transfer radiation to the detectors, the detectors are placed at the focal planes of the optical system. The detectors for bands 1 to 4 are located in the primary focal plane assembly whereas the detectors for bands 5 to 7 are located in the second focal plane assembly.

The radiometric quantisation level for the TM is improved from 64 to 256 which means small differences in reflection between objects can be measured. The data from the Landsat sensors is relayed, either directly, or over the Tracking and Data relay satellite (TDRS), to the ground receiving station. On the ground, the data are recorded temporarily on a High Density Digital Tape (HDDT), then the data are partially corrected, preprocessed and reformatted for supply to users in different forms; the most widely used is the computer compatible tape (CCT).

4.3 Computer Compatible Tape and Data Format

The medium used for the data in this study was the computer compatible tape (CCT). The CCT is a sequential storage medium. Nine

tracks parallel to the tape length are used to record the data. On the CCT, the data are organised into a number of files, e.g. header, which contain information about location, date, type and condition of sensor elevation, sun angle, etc. The image file contains the spectral data. Within the image file, the data for each pixel are stored as a byte across the tape in binary mode (8 bits, with a DN range 0-255), keeping the ninth bit free for parity checking. The density of bits along the tape can be 800, 1600, or 6250 bit per inch (bpi).

Due to the fact that no world-wide standard format has been agreed upon, the format of the tape needs to be known in order for the computer to read it. Once known, a suitable algorithm can be used to read the data to a computer disc. The most widely used formats are the Band Sequential (BSQ) format, and the band interleaved by line format (BIL).

In the BSQ format each band is written as one file, and the user can read each band separately and skip the unwanted bands. The structure of the data in a BSQ format is summarised in Figure 4.5a. In the (BIL) format the data for the bands are written line by line onto the tape as "Line 1 Band 1, Line 1Band 2" and so on (Figure 4.5b), which means that all the bands have to be read simultaneously or serially, which is useful if all the bands are to be used (Jensen, 1986). The format of the tapes used in this study was BSQ, with a data density of 6250 bpi.

4.4 Digital Processing Systems

Digital remote sensing data can be analysed using a digital image processing system. Many software and hardware image processing systems are available in the market starting from a very simple image processing software, which costs no more than a hundred pounds and can be run on a

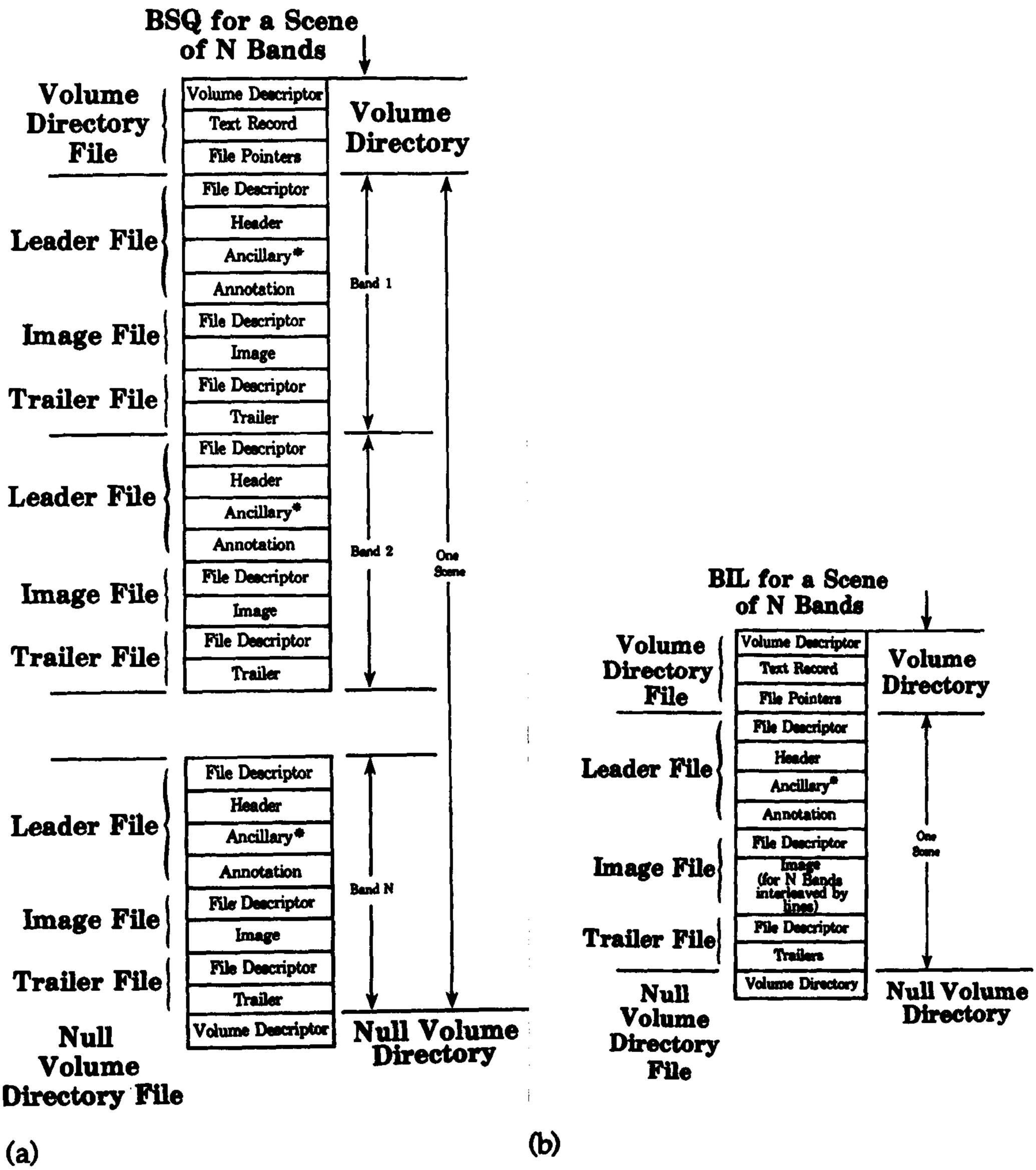

Figure 4.5 Data format of Landsat tape: (a) band sequential (BSQ); (b) band interleaved (BIL) (after Jensen, 1986).

personal computer, to a mainframe system with built-in software, which could cost hundreds of thousands of pounds. The choice of which to use depends on the scope, nature and volume of work and also the level of financial support available.

Several image processing software and hardware were either listed or described by Freden and Gordon (1983), Nicholas (1983), Jensen (1986), Mather (1987) and Harris (1987). A typical image processing system consists of four main components (Harris 1987): a magnetic tape drive to read the CCTs, a disk storage of data for fast access, a processing software and a colour monitor for display.

The remote sensing laboratory used at Stirling University consisted of a magnetic tape drive, a Microvax II on which there was software for data reading and processing, a personal computer with R-CHIPS software and a high resolution colour monitor which was connected to the Microvax. IDRISI software was available on another PC but not connected to the Microvax, and the data was transferred to a floppy disk in order to process them using IDRISI software. In addition to that, a digitising camera is available, and a Laserscan system.

4.4.1 Microvax II

The Microvax had a storage capacity of 380 megabytes for images and was connected by serial lines to three terminals, a 1600 bpi tape drive, PC computer and a digitisation camera. It had an image processing menu system which consisted of a list of program options designed and written by A.I. Watson. The reading of the digital data from the CCT tape drive and most of the image preparation and processing techniques used in this study, were made through this system.

4.4.2 R-CHIPS Software

R-CHIPS is an image processing software system. It combines a graphic display card with a user friendly menu system that enables the user to control and manipulate images on a high resolution graphic screen. The R-CHIPS menu interface was structured so that programs with similar functions were grouped together into thematic menus which are accessed from a main menu (i.e., a tree menu system). The image inspect menu was available from all the five thematic menus as the top option. Each of these options contained a series of sub menu systems. More information can be found in the R-CHIPS manual, Version 3.0.

4.4.3 IDRISI Software

IDRISI is a grid-based geographic analysis system that was designed to provide inexpensive access to computer-assisted geographic analysis technology and digital image processing.

IDRISI is a collection of almost 100 program modules that are linked by a unified menu system. These modules fall into three groups:

1. Core modules which provide utility of entry, storage, management, display and analysis of the data.

2. Ring module which provides extension of GIS or image processing modules.

3. Peripheral modules associated with data conversion utilities between IDRISI and other data formats.

The non standardised principal components analysis, found in the image processing ring module was used in this study.

4.5 Preparation of the data

The general procedures followed in order to get digital data as an image display on the colour monitor are as follows:

1. The computer compatible tapes (CCT), which contain the TM data used in this study, were brought from the Saudi Remote Sensing Center in Riyadh. They have a TM data density of 6250 BPI. However, the tape drive in the remote sensing lab in Stirling University could only read tapes with data density of 1600 BPI. Hence, the data was first taken to the computer centre in the University and copied to the main frame disc storage, and then two lots of three bands were transferred to two 1600 bpi CCT. (The thermal band was excluded because of its serious distortion.)

2. The 1600 (BPI) magnetic tapes were loaded in the remote sensing lab tape drive and the data was transferred to the Microvax disk storage using the program "ETAPE"available on the Microvax

3. A quick look of 512 x 512 pixels was then produced for the whole image using the option "TM QUICK LOOK" in the Microvax menu system. This program would display the whole quad by taking a sample of every eighth pixel and line. This image was then transferred to the R-CHIPS system for the selection of the test area.

4. The X and Y co-ordinates for the top left corner of the test area can then be taken to specify its location in the tape, using the Zoom and Roam options in the R-CHIPS menu system.

5. Using the option (Image Cut) from the Microvax image processing menu system, a sub scene of any size would be cut with full resolution, and stored on the storage disk. It could also be transferred to the R-CHIPS system for display or image manipulation. The image processing programs were run on both the Microvax and the R-CHIPS. IDRISI software was used

only to run the principal component analysis. A brief description of how each processing step was done will be given in later chapters. Once processed, the data was transferred to R-CHIPS system for image display on the colour monitor.

4.6 Summary

Landsat satellites have changed the view of many scientists (especially geographers and geologists) of the earth's surface in two ways: a) by providing synoptic views, and b) by providing a wider range of wavelengths. From the discussion in Section 4.2.2 it is obvious that the Landsat thematic mapper (TM) sensor is far superior to the Landsat multispectral scanner (MSS) in terms of its spectral, spatial and radiometric resolution, and therefore would provide more detailed information about objects on the earth's surface. Compared to other current satellite sensors, it may represent the best candidate to provide lithological information about the earth's surface.

Jaskolla and Henkel (1988) have demonstrated that, although multispectral SPOT data may have better spatial resolution (20m) than the TM data, the limited number of bands (three band only) and the high correlation of the spectral bands S1 and S2 (green and blue) of the multispectral SPOT data decrease strongly its usefulness in geological applications. This chapter has also reviewed the characteristics of the computer compatible tapes and the image processing systems used in this study, as well as the general procedures followed in the preparation of the data.

CHAPTER FIVE

DIGITAL IMAGE PROCESSING TECHNIQUES

5.1 Introduction

5.2 Pre-processing
- 5.2.1 Atmospheric correction

5.3 Contrast enhancement
- 5.3.1 Linear contrast stretch
- 5.3.2 Histogram equalise stretch
- 5.3.3 Balance contrast enhancement technique (BCET)

5.4 Spatial filtering

5.5 Colour composite and display

5.6 Band ratio

5.7 Principal component analysis (PCA)

5.8 Decorrelation stretch

5.9 Canonical transformation

5.10 Hue-Saturation-Intensity (HSI) transform

5.11 Summary

5.1 Introduction

As discussed earlier (Chapter 4) the satellite sensor produces data in a digital form. In general, one may define a digital image as a two dimensional array of n-tuples; each of these n-tuples represents the amount of light reflected in each band (n) from an area on the ground (IFOV, instantaneous field of view) (Schowengerdt, 1983). Manipulation of such images using a computer is called Digital Image Processing (Gillespie, 1980).

In general, multispectral information can best be accessed and analysed through digital and interactive processing techniques (Haydn, 1983). The use of digital format allows the user to transmit, store, retrieve and use the satellite image in a highly flexible way. Furthermore, unlike photographic images, digital images do not deteriorate with age. Applying the same processing program to the same image will produce exactly the same result, regardless of the number of times, or type of machine used, which is not always true of photographic products.

It is probably useful to mention that digital image processing did not originate with satellite remote sensing, and is not restricted to its data. Many other medically oriented applications, for example, were developed previously. However, the successful launch of Landsat-1 in 1972 marked the approximate start of increased interest in developing and using computer processing of digital images (Campbell, 1987).

Digital image processing is a very broad subject, and involves complex mathematical operations, which may include an equation or series of equations, written as computer programs, to be applied to the input images, when needed. The result of such operations, produces a new digital image, which may form the end product, or an intermediate product for further processing.

In this chapter, a simple description will be given for a number of digital image processing techniques, that were used in this study; a detailed mathematical description of such techniques is beyond the scope of this work. The end of this section contains a list of some of the references in this field to be referred to for detailed information. This chapter starts with the pre-processing operation, used to minimise the haze component produced in the satellite images by the atmosphere, as described previously (Section 3.4); it also describes the methodology and results of such operations. This is followed by a description of the different techniques for image enhancement, which include a) contrast enhancement -- different types of histogram stretching; b) selective enhancement of spatial information in the image (spatial filtering); and c) the more complex operations of image transformation on multi-band image sets such as the principal component analysis, image ratios, canonical analysis, decorrelation stretch and hue saturation-intensity transform

The equally important subject of image classification will be discussed in (chapter 7). A useful review of digital image processing can be found, for example, in Bernstein (1976), Mulder (1980), Estes et al (1983), Schowengerdt (1983), Bernstein et al (1984), Ekstrom (1984), Jensen (1986), Niblack (1986), Richards (1986), Lillisand and Kiefer (1987), Mather (1987), Gonzalez and Wintz (1987), Campbell (1987), Muller (1988), with discussion related to geological application in Gillespie et al. (1986), Drury (1987), Sabins (1987), Goetz (1989a), and Gupta (1991).

5.2 Pre-processing

5.2.1 Atmospheric correction

As discussed in section 3.4.1, atmospheric gases and particles scatter the shorter wavelengths of light more strongly (Drury, 1987; Mather, 1987). This scattering produces haze that has an additive effect on image brightness, and results in low image contrast. For Landsat TM data, Band 1 (0.45 - 0.52 μm, blue) has the highest scattering effect whereas Band 7 (2.8 - 2.35 μm, infra-red) has the least. If, for example, a band ratio technique (section 5.6) is performed to produce a ratio image, of band 7 over band 1 or vice versa, the value of the output ratio will not represent the true ratio. This is due to the fact that these two bands are not equally affected by scattering and therefore an atmospheric correction is needed to eliminate, or at least minimise, this effect.

Processing operations to correct for atmospheric scattering vary from 1) highly sophisticated techniques, such as a) using methods based upon efforts to model the physical behaviour of the radiation as it passes through the atmosphere, e.g. by modeling the physical process of scattering at the level of individual particles and molecules (Campbell, 1987); or b) procedures based on in situ field information, which enables the analyst to assess the atmospheric component, to 2) a more simple procedure such as identifying a dark object in the scene such as shadow caused by topographic variation (Berlin and Chavez, 1986). In a clear atmosphere, the reflection from such 'dark' objects should be very low, near zero reflectance, and the only source of energy directed from such areas is atmospheric scattering.

Normally, the data collected in the visible region (TM 1-3) have higher minimum values, caused by the high atmospheric scattering taking place in these wavelengths. By examining the histogram of such images the

lowest value in each band can be set to zero. Another procedure involves the application of regression methods of plotting pixel values for the least affected band, such as Landsat TM B7 against the values in the other bands (Crippen, 1986; Sabin, 1987).

Each of the previously described methods have their advantages and limitations. The first method (which uses the physical models or in situ field information) is more accurate, and could adjust to approximate true values observed under clear atmosphere. However, the physical modeling is very complex and requires detailed meteorological information, such as atmospheric humidity and concentration of atmospheric particles, which may be difficult to obtain in the necessary detail. Furthermore, the condition of the atmospheric change with the altitude, and the radiosound data that record changes with altitude, are routinely collected at only a few locations (Campbell, 1987). More important is that these methods cannot be applied to already collected data, where no information other than the digital data itself is available. With such conditions the dark obejct method may be the only option available.

However, Chavez (1988) pointed out that, in using the dark object method described above, difficulties may be encountered. The data may be over corrected in some or all bands due to the fact that haze values for each band are selected independently. To overcome this problem, he described a method called "improved dark object subtraction technique", which allows the user to select a relative scattering model, to predict the haze values for the spectral bands; hence the haze values will be wavelength-dependent and correlated with each other. This technique was used in this study. The basic steps of correcting the scattering effect on this data, using the improved dark object subtraction techniques, are as follows:

A frequency histogram print was generated using a large portion of the raw data (2048 pixel x 2048 line) for TM bands 1, 2, 3 using IDRISI software package. The histogram of these raw bands were found to be offset toward higher values, by some amount, due to scattering. The histogram print of band 1 was then checked to locate the starting haze value, where a relatively abrupt increase occurs in the number of pixels at a given grey level. The amplitude of the starting haze values was used to select a relative scattering model, which best represents the atmospheric conditions at the time of data collection, e.g. very clear, clear, moderate, hazy or very hazy.

The two well known relative scattering models are the Rayleigh and Mie models. As described in section (3.4.1) the Rayleigh models states that the degree of scattering is inversely proportional to the fourth power of the wavelength (λ^{-4}), therefore the shorter wavelength will be scattered more strongly than the longer wavelength. The Mie scattering model states that the relation between wavelength and relative scattering varies from λ° to λ^{-4}, where λ° describes total scattering such as complete cloud cover.

Chavez (1988) states that relative scattering occurs in clear atmosphere and seems to follow λ^{-2} to $\lambda^{-0.7}$ and not Rayleigh or Mie scattering, and in a hazy condition is approximately $\lambda^{-0.7}$ to $\lambda^{-0.5}$ and he supplied a relative scattering model as follows:

Atm. Condition	Relative Scattering Model
very clear	λ^{-4}
clear	λ^{-2}
moderate	λ^{-1}
hazy	$\lambda^{-0.7}$
very hazy	$\lambda^{-0.5}$

The relative scattering model for this area was found to be very clear (see Table 5 in previous reference), and this model was then used to predict the haze values for the other spectral bands, using the following equation (Chavez, 1988), and consulting the tables given by him.

$$DN_0 = B1 * Fi * Ni + Si$$

whereas DN_0 = output DN for band i

B1 = starting haze value for band 1

Fi = relative scattering model multiplication factor for band i (see Table 2 in previous reference)

Ni = Norm for band i (see Table 3 in previous reference)

Si = offset of band i (see Table 3 in previous reference)

Using the above equation and the tables supplied by Chavez (1988), starting haze value for band 2 was calculated as follows:

$$DN_2 = 56 * 0.56 * 0.51 + 2.44$$
$$= 18.4 \text{ or } \underline{18}$$

The same procedures were used for bands 3 and 4 for the four test areas, and the starting haze values for these two bands were found to be 12 and 6 respectively.

A programme called ADDSUB, available in the MicroVAX, was then used to subtract the haze values from each pixel of the TM bands-1, -2, -3 and -4. The amount of atmospheric scattering that occurs at TM bands -5 and -7 is very small, except for very hazy atmosphere, and can be considered negligible, and a haze DN value of zero can be used for bands -5 and -7 (Chavez, 1988).

5.3 Contrast enhancement

The Landsat satellite sensors were designed to be capable of detecting a wide range of terrain brightness, from oceans or black basalt plateau, to snow or desert areas. A very few individual scenes have brightness ranges that utilise the full sensitivity range of the sensor. Therefore, pixel values in Landsat scene commonly occupy a relatively small part of the possible range of image values (Figure 5.1a). The examination of the image histogram (Figure 5.1b) is a useful and necessary preliminary step for successful manipulation of image contrast. The image histogram describes the frequency of occurrence (along the vertical axis) of the grey levels (along the horizontal axis) in an image. From the previous figure, it can be seen that the pixel values occupy only a small area of the available range. This limited range causes the low contrast of the original image. Therefore the contrast enhancement techniques were used to stretch the data to occupy the full range of the grey levels available; this produced an image with greater range and shows greater contrast. Of the many methods available for contrast stretching the two most popular are the simple linear stretch, and the histogram equalisation stretch. A new method will also be described here, which was developed by Guo and Moore (1989).

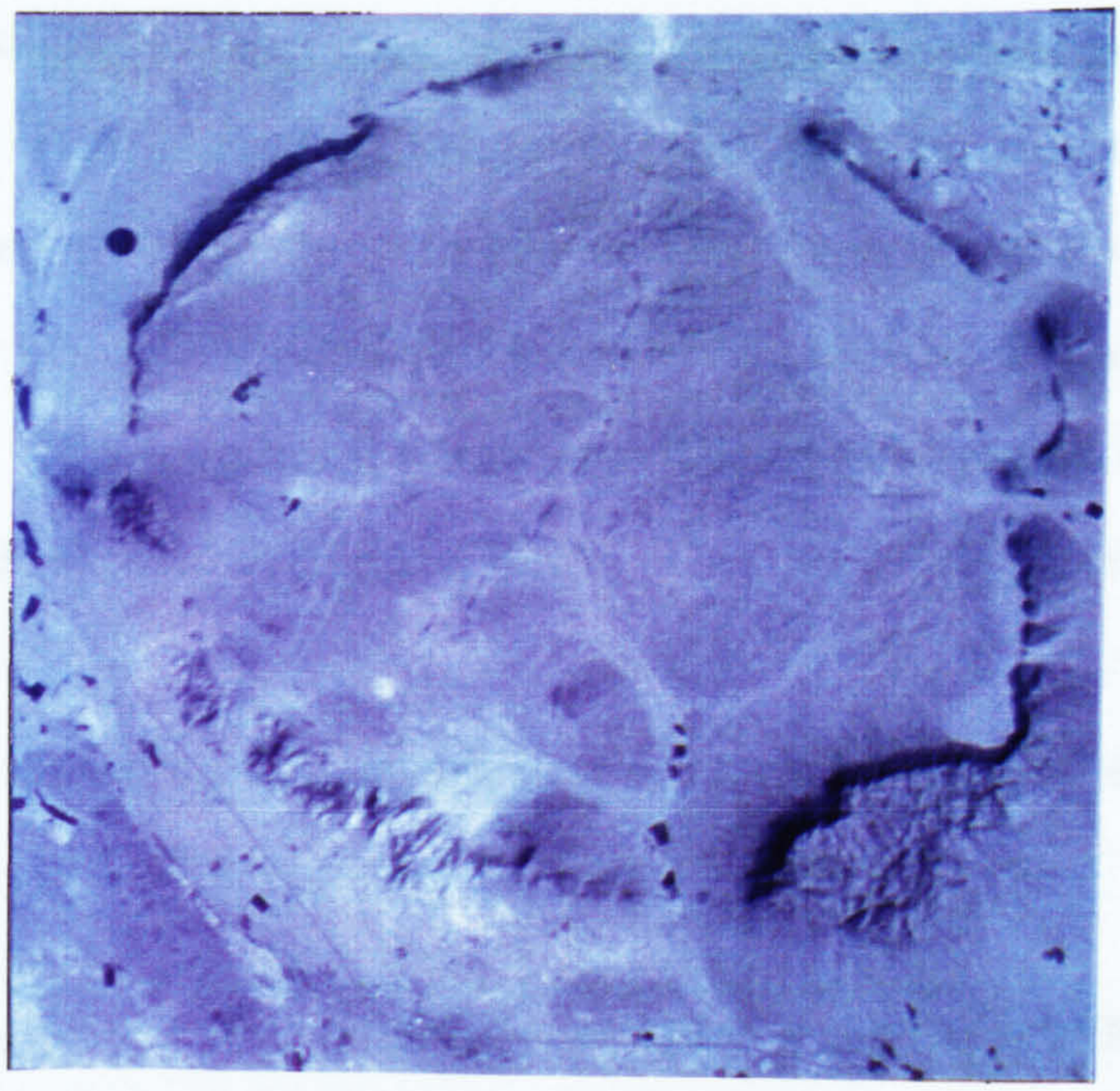

(a)

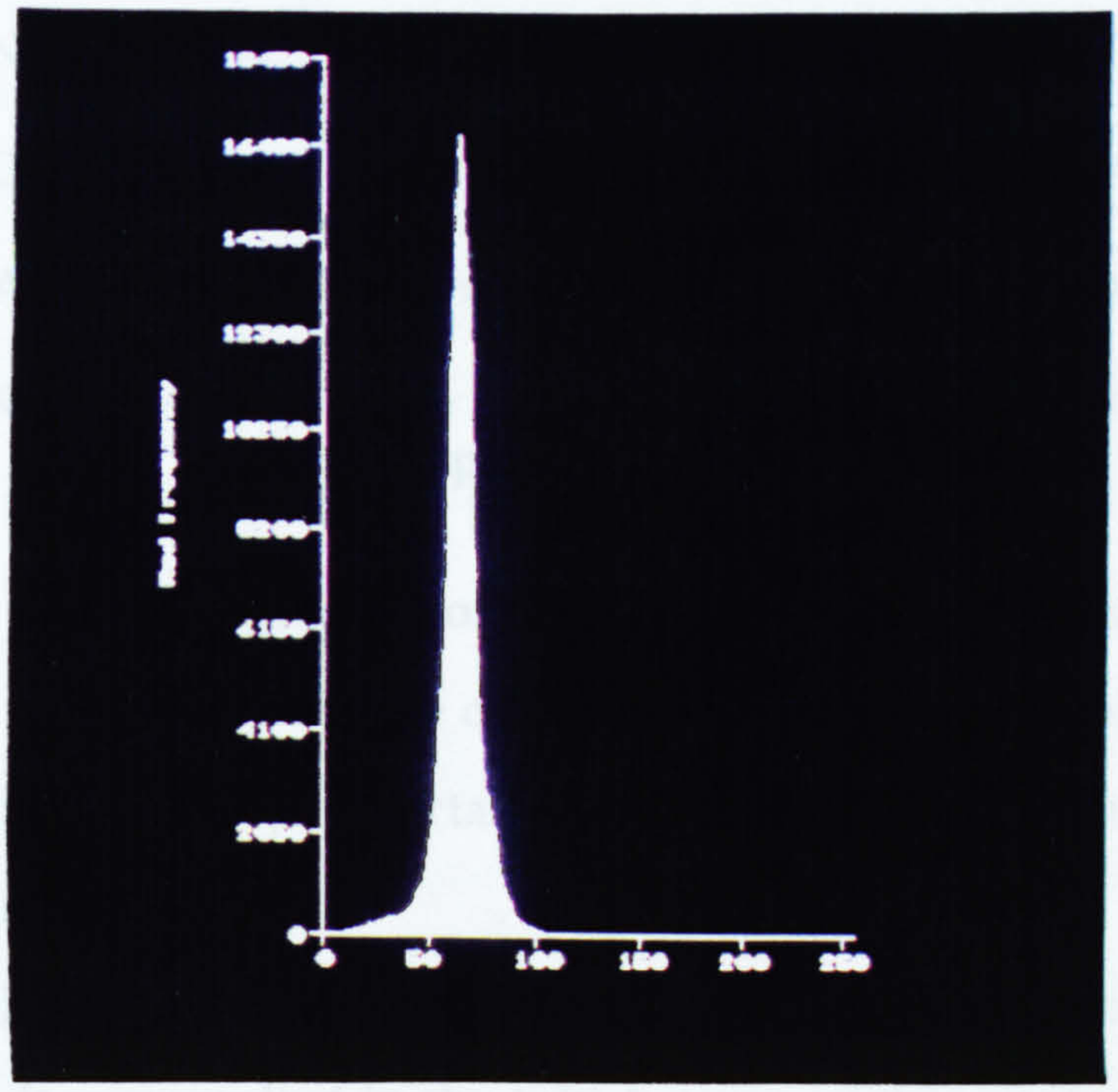

(b)

Figure 5.1: TM band-1 image of Silsilah ring complex: (a) is the original image with its corresponding histogram (b).

5.3.1 Linear contrast stretch

In this type, the range of input image values is expanded uniformly to fill the full dynamic range of the display device. This can be accomplished by assigning the low end of the original histogram to extreme black (zero DN value), and the value at the high end to extreme white (255 DN value). The remaining pixels are distributed linearly between these two extremes as shown in Figure (5.2). This leads to an image with greater contrast.

The linear stretch is applied to each pixel in the image using the equation:

$$DN_{out} = (DN_{in} - MIN / MAX - MIN)\, DN_r$$

where:

DN_{out}	=	output image digital number
DN_{in}	=	input image digital number
MIN	=	minimum value of input image
MAX	=	maximum value of input image
DN_r	=	the range of DN values that can be displayed (eg 255)

To achieve a greater contrast increase, some saturation at one or both extremes of the output range could be specified by the analysts, using a MIN and a MAX, that lies a certain percentage of pixels into the tails of the histogram.

This type of contrast stretch is found in most of the image processing systems. It was applied in the initial stages of this study for quick check of study areas and the "quick look" images using either the "MANUAL CONTRAST STRETCH" option on CHIPS to identify the minimum and

maximum values to be assigned, or by directly using the option "AUTOMATIC CONTRAST STRETCH", which stretched the data automatically with 2.5% saturation in both ends of the histogram.

5.3.2 Histogram equalise stretch

This is a more sophisticated method of contrast enhancement. The principle of this type of stretching, is that each histogram class (0-255) in the displayed image must contain an approximately equal number of DN values, and hence, after transformation, an almost uniform histogram results. Therefore, the high frequency DN values become more spaced, whereas the low frequency ones are amalgamated. The procedures for this type of stretching are described in great detail by Mather (1987) and Richards (1986). Histogram equalise stretch tends to reduce the contrast in both the very light and very dark areas in the image (Figure 5.3), and expands the middle grey level toward both ends of the output histogram. This is due to the gaussian (normal distribution) shape of most of the image histograms. This type of stretching was performed in this study, using the option "HISTOGRAM EQUALISED STRETCH" in CHIPS software menu system, which applied this type of stretching, automatically, without any input from the analyst.

5.3.3 Balance contrast enhancement technique (BCET)

The previously described linear contrast stretch, can stretch an image to a defined minimum and maximum, but may result in a colour bias if the average brightness in one band is significantly higher or lower than the other two bands of the colour composite image. The histogram equalize

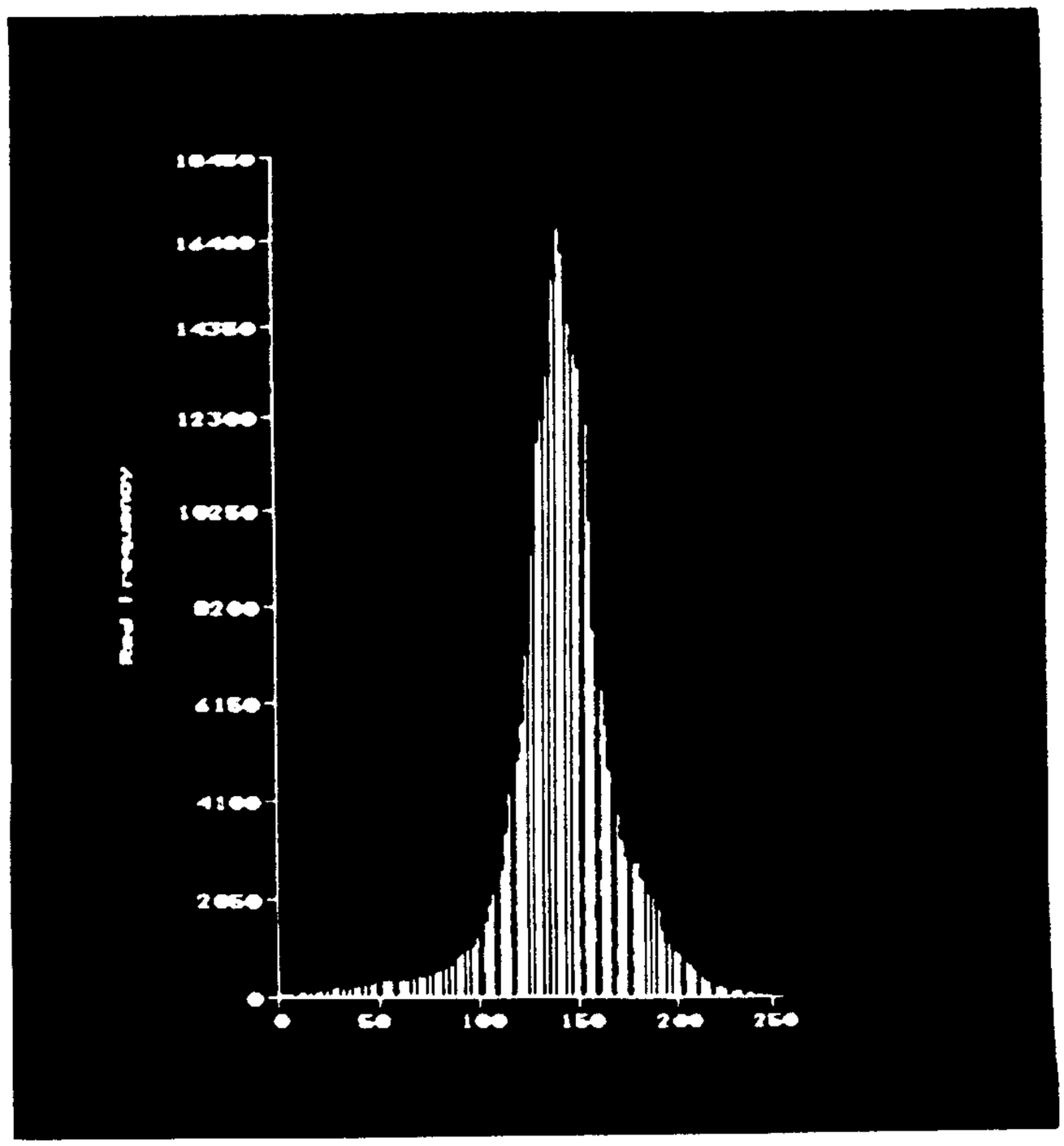

Figure 5.2: A simple linear contrast stretch of histogram in Figure 5.1(b).

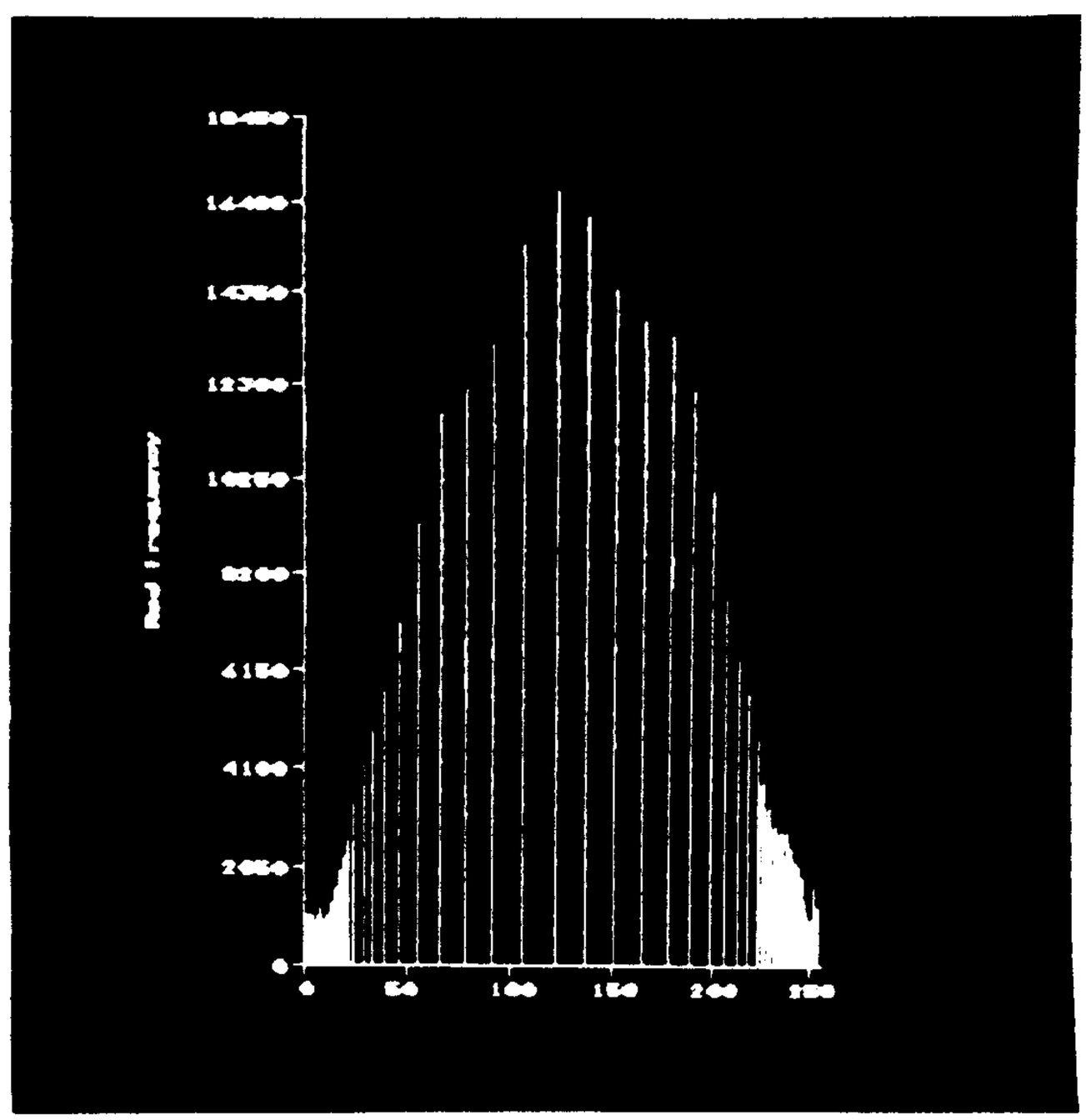

Figure 5.3: Histogram equalize stretch of Figure 5.1(b).

stretch could cause a change in the shape of the histogram which may cause loss of some information (Guo and Moore, 1989 and Guo 1991).

The previous references described a stretching technique called Balance Contrast Enhancement Technique (BCET). This is particularly useful for performing a stretch for a colour composite display, and can stretch the data, without causing colour bias, by stretching (or compressing) each band to a user defined maximum, minimum and mean. Thus the three bands used for colour composite can be transformed to have the same range and average brightness, which may not be the case for the ordinary linear contrast stretch. The BCET transformation increases monotonically the contrast within the value range used, therefore, unlike the histogram equalized stretch, it preserves the shape of the original histogram and maintains the structure of the image information.

The method is described in greater detail by the above reference. Two functions can be used to perform this technique, the parabola and the cubic functions. However, in this study the parabolic function is the only one that was used. In BCET, using parabolic function, a segment of the parabola curve derived from the original image is used as the point operation function which will stretch (compress) the data to a user defined value range and means, under the control of the monotonically increasing branch of the parabolic curve used for stretching. For more information about the mathematical equations and derivations, see Guo (1991). The program that performs this type of opeation was written (written comm. L. Guo, and pers. comm. A.I. Watson) for any PC.

5.4 Spatial filtering

The previously described enhancement methods enhance all the features in the image equally, using just independent pixel values. In spatial filtering, the enhancement of the pixel is made on the basis of grey levels in surrounding pixels. Therefore, spatial filtering is an area operation rather than point operation (Schowengerdt, 1983; Avery and Berlin, 1985). This allows the user to extract useful spatial frequency information from the imagery, by emphasising or de-emphasising information of various spatial frequencies (Curran, 1985).

Digital images normally contain low frequency as well as high frequency spatial information. The sum of these two make up the original image. The low frequency represents smooth areas of an image, such as open desert plain or water body, where grey level varies gradually over relatively larger numbers of pixels (low brightness variation). The high frequency is the opposite in which the brightness changes abruptly over relatively small areas (large brightness variation). These represent rough areas or the small details in the image, such as edges or boundaries between two lithologies with different compositions, or surfaces of different illumination due to topography effect, etc. Algorithms that perform spatial frequency enhancement are called filters, because they pass, or emphasis certain spatial frequencies and supress others.

Spatial filters, which are designed to pass high frequency information, enhancing the detail of an image, are called high pass filters or edge enhancers (Davis, 1975). Low pass filters are the opposite, in that they produce a smooth image, by suppressing the high spatial frequencies (Jensen, 1986). Spatial filtering is usually applied to an image by a sub array (box or window) of N by N pixels of odd dimensions centred on each pixel

in turn. The size of this window can be 3 x 3 , 5 x 5 , 7 x 7 , or 9 x 9 etc. To perform a spatial filtering of any size or value, the 3 x 3 window or box filter is placed over the top left corner of the original image. Each pixel is then multiplied by the corresponding value in the window. The nine resulting values for the filter are summed, and then combined with the central pixel of the window, which then replaces the original value of the central pixel. Once the output value for the filter has been calculated, the window moves one column (pixel) to the right and the operation is repeated until the window reaches the right margin of the image, where it will shift down one row, and back to the left margin of the image, and continue the same process, until all the image is processed.

As mentioned earlier, the filter can enhance the low frequency information or the high frequency information. However, linear features in the image form an important subject for a number of analysts such as geographers (man made linear features, e.g. roads and canals) and geologists (large and small scale lineament features). Such features can be enhanced using a high pass filter. The simplest means of high pass filtering is to subtract a low pass filtered image from the original image. The high pass filtering using a window can be designed as a non directional or directional filter. The non directional (Laplacian) filters are generally useful in edge and boundary detection in all directions, whereas the directional filters are used to detect lines with preferred orientation (Drury, 1987). The most comonly used high pass non directional filter is the Laplacian filter (Jensen, 1986; Mather, 1987; McCabe and Collins, 1985). Several Laplacian filters were described by many authors (Jensen, 1986; Drury, 1987; Sabins, 1987; Mather, 1987; Gupta 1991). The following filters (a-d) are shown here as an example.

	-1	-1	-1		0	-1	0
filter -a	-1	8	-1	filter -b	-1	4	-1
	-1	-1	-1		0	-1	0

	1	-2	1		0	-1	0
filter -c	-2	4	-2	filter -d	-1	5	-1
	1	-2	1		0	-1	0

Jensen (1987) found the Laplacian add-back window (filter -d) produced the best enhancement of high frequency detail for wetland and urban areas. In this study, this filter (Laplacian add-back) produced the best result as it sharpens the image to its limit without making it very noisy.

Figure 5.4(b) shows the advantage of such a filter. It shows the first principal component of Ahmar test area, in which the spatial features (structural and textural) were greatly enhanced in addition to sharpening the rock boundary, when compared to the original image as shown in Figure 5.4(a).

5.5 Colour composite and display

The human eye-brain system can only distinguish up to 30 grey levels in black and white images. On the other hand, it can easily distinguish over a million different colours (Gillespie, 1989); the limit is about 7 million (Drury, 1987). Therefore, the colour display is a more effective and practical way of presenting multispectral data (Gillespie, 1980). The detailed mechanisms by which we see colour are still not fully understood (Lillisand and Kiefer, 1987).

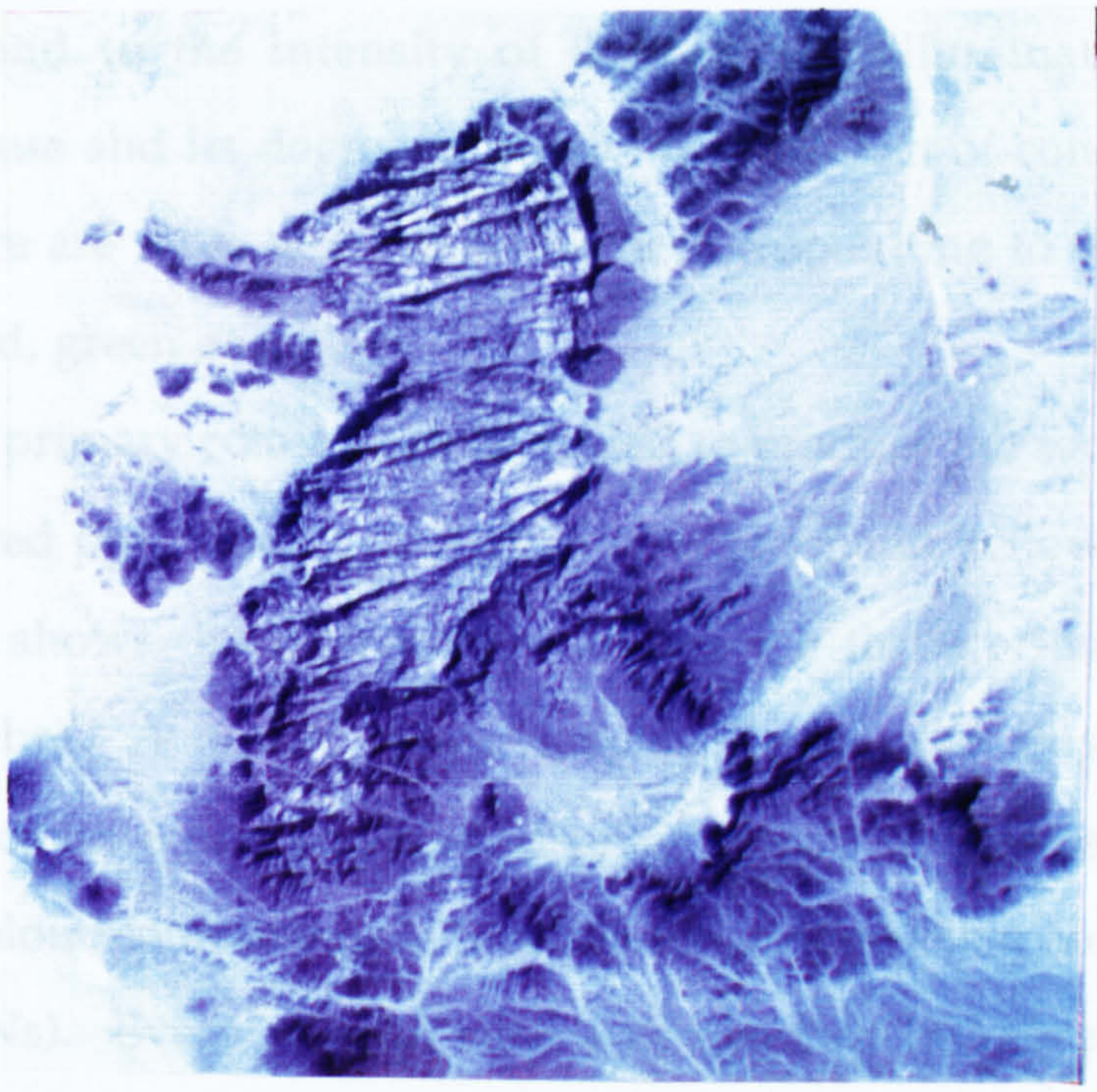

(a)

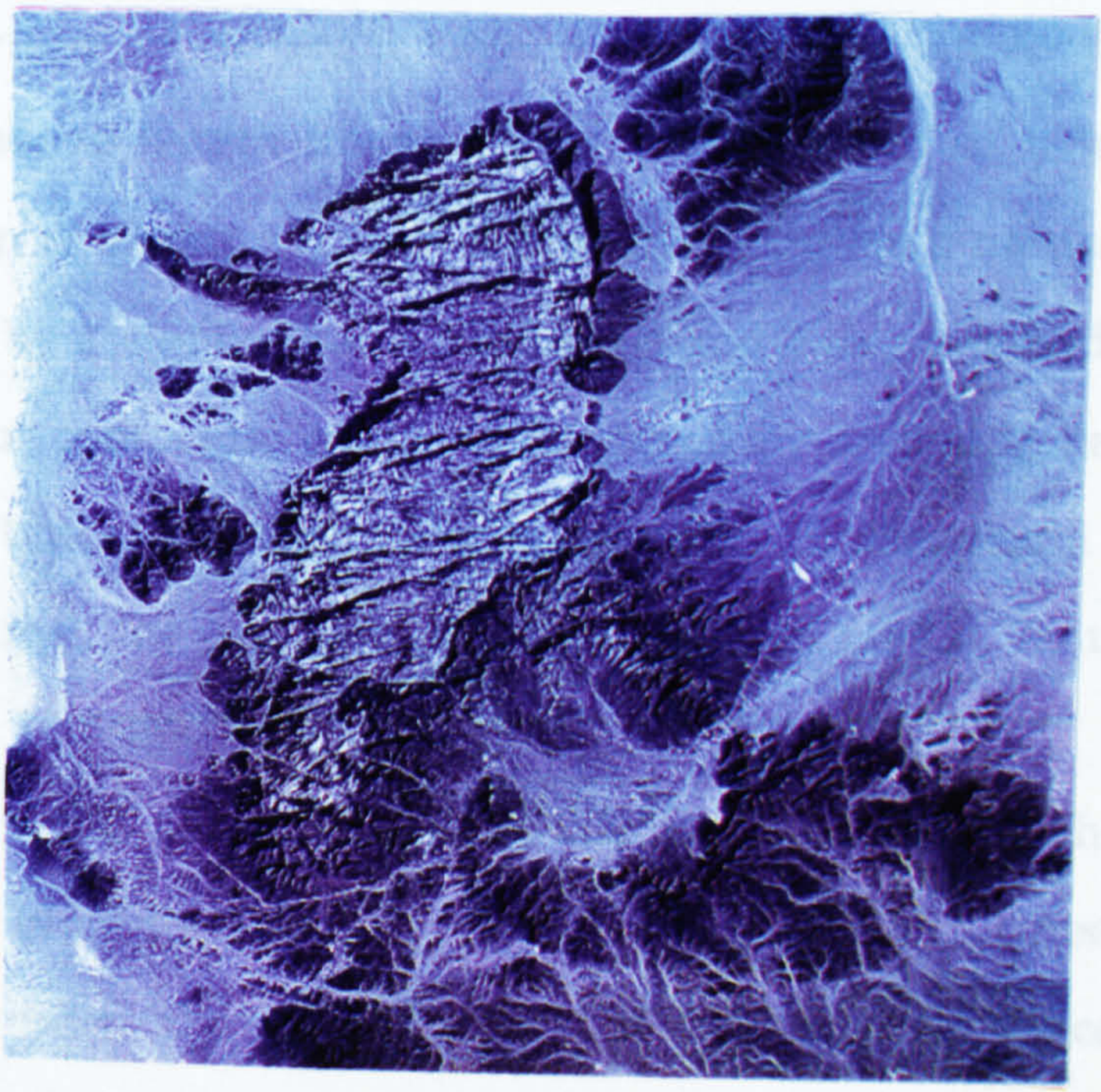

(b)

Figure 5.4: The effect of (laplacian add back) edge enhancement technique (b) on the first principal component image of Aban Ahmar study area (a).

The retina contains two types of photoreceptor cells; the rod-shaped cells respond to the intensity of light at low illumination, whereas the colour or hue and its degree of purity, is a product of cone-shaped receptor cells. There are three types of cones, each responding to one of the primary colours (red, green and blue).

The primary colours can be added to produce the secondary colours of magenta (red plus blue), cyan (green plus blue) and yellow (red plus green). Figure 5.5 shows the interrelation among the three primary colours (RGB Colour Cube). A typical colour display device uses this model of colour mixing. For an 8 bits per pixel display device, the range of DNs for each primary colour components is 0 to 255 (or 256^3 possible combinations of the R, G, B DNs). Every pixel in such a device may be represented by a three dimensional co-ordinate position, somewhere in the colour cube.

Colour displays give the opportunity of examining simultaneously the behaviour of different objects available in up to three images, e.g. different wave length image bands, ratio images or principal component images. In displaying colour composite TM data, a natural colour could be displayed by assigning band 1 to blue, band 2 to green and band 3 to red. A false colour composite could be displayed by assigning band 2, band 3 and band 4 to blue, green and red respectively. Further detail about this section can be found, for example, in Schowengerdt (1983), Drury (1987), Mather (1987) and Lillisand and Kiefer (1987).

Since the data can only be displayed using just three bands as red, green and blue the question arises concerning which three bands should be displayed from the six reflected TM bands, to produce the best colour composite. This can be achieved either by using visual selection of all the band combinations which can be created for six TM bands or by using image

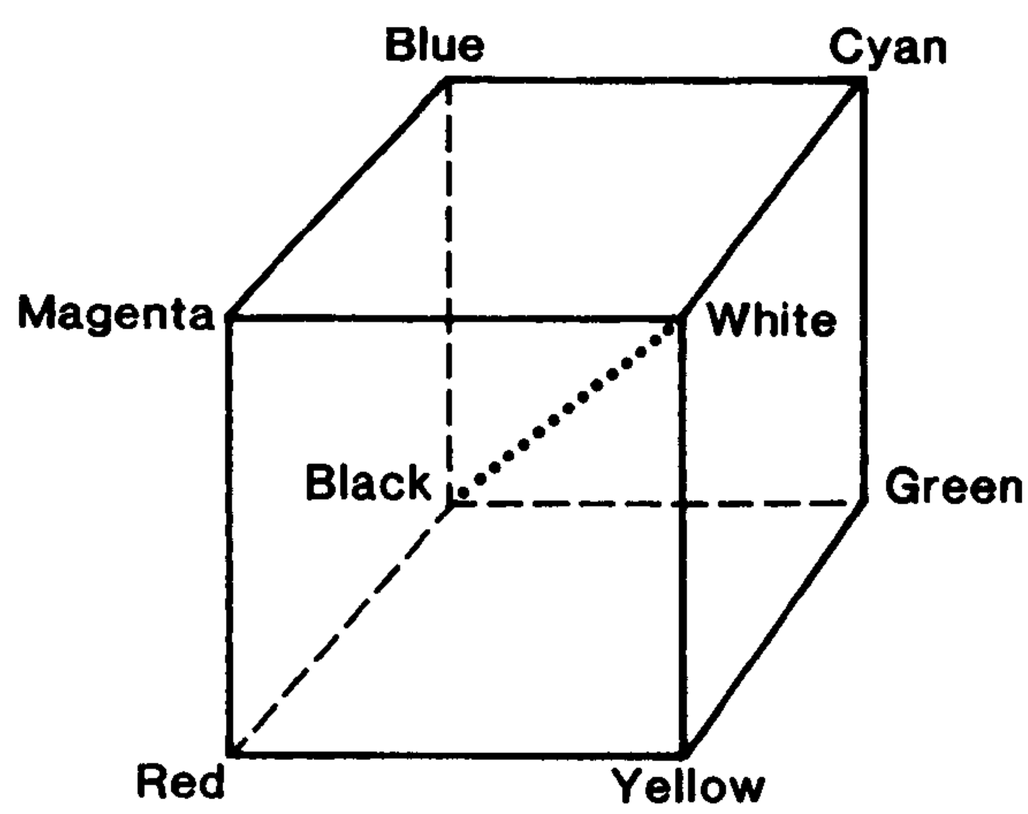

Figure 5.5. Red-green-blue colour cube (from Mather, 1987).

statistics such as image covariance, standard deviation and the correlation between images. Chavez, et al. (1982, 1984) devised a statistic method called Optimum Index Factor (OIF) to rank the best three ratio combinations for MSS, and the best three band combinations for TM. The OIF is based on the variance and the correlation among different bands and ratios. The index is calculated for each three band combination, by dividing the sum of the standard deviation of each combination by the sum of absolute value of the correlation coefficient:

$$OIF = \sum_{i=1}^{3} S D_i \; / \; \sum_{j=1}^{3} |CC_j|$$

where SD_i = standard deviation of band i

$|CC_j|$ = absolute value of the correlation coefficient between any two of the three bands (ratios)

Based on these statistics, the three band (ratio) combination that has the largest OIF value, has the most information with the least amount of duplication (as measured by correlation). Although OIF (as other statistical methods, Sheffield et al., 1985; Crippen, 1989) appears to be convenient and easily computed, and may provide useful band combination in a short time, the results do not always indicate precisely the geological information contained in an image (Greenbaum, 1987; Crosta and Moore, 1989) and frequently a visually selected set of bands is more useful (Hunt et al., 1986). In general, the best three band combinations include one from the visible bands (TM 1, 2 or 3) and one of the longer-wavelength, mid infrared bands (5 or 6) together with TM band 4 (Chavez et al., 1984; Jensen, 1986). Afterwards a decision has to be made for the colour of each band . The

strategies which were followed in this study to select the best bands will be described in chapter 6.

5.6 Band ratio

The division of one band by another is commonly known as band ratioing. This can be done by dividing each pixel in one of the bands by the corresponding pixel in the other band.

This type of enhancement was the first widely used technique in geological application of remote sensing data, (Rowan et al., 1974, 1977; Lyon, 1975), due to its ability of reducing the topographic effect, and enhancement of spectral differences.

The mathematical equation of the ratio function is:

$$BV_{i,j,r} = BV_{i,j,k} / BV_{i,j,l}$$

whereas,

$BV_{i,j,r}$	=	the output ratio value for pixel at row i column j
$BV_{i,j,k}$	=	the brightness value at the same location in band k
$BV_{i,j,l}$	=	the brightness at the same location in band l

Due to the fact that some input pixels can have brightness values of zero, therefore ratio values can then be equal to infinity. Furthermore, an integer value of less than 1 is common in the output ratio values, using the previous equation, which will compress much of the output ratio values between 0 and 1. Therefore, scaling of the output ratio values is needed in

order to relate them to the display device used, which ranges from 0 to 255. One way of doing this is by applying this equation:

$$BV_{i,j,r} = K \arctan (BV_{i,j,k} / BV_{i,j,l})$$

where K is the scaling factor that scales the ratio data to an appropriate integer range. If K is set to equal 162.34, the output ratio can then take any value between 0 and 255.

The number of ratio combinations available varies according to the source of digital data. The number of possible ratios that can be developed from N bands of data is N (N-1). Thus for Landsat TM data 6 (6-1) = 30 possible combinations.

The most common spectral ratio used in application of Landsat TM to geology is the ratio 5/7. This enhanced areas of hydrothermal alteration, whereas TM band ratios 5/4, 4/1, 5/1, 3/2, 3/1, 4/2 have been used for enhancing areas of Fe bearing minerals and Fe staining (Podwysocki et al., 1983; Laughlin and Taufiq, 1985; Brickey, 1986; Huckerby et al., 1986; Magee et al., 1986; Sultan et al., 1986; Kepper et al., 1986; Feldman and Taranik, 1986; Kruse, 1986; Elvidge, 1986; Spatz et al., 1987, 1989; Kaufman, 1988; and Amos and Greenbaum, 1989;).

Any three grey level ratio images can be combined to produce a colour ratio composite image, which further enhances the spectral reflectance difference. Ratio images also reduce differences in illumination conditions, which in turn minimise the topographic effect, so that ratio values for the same materials may be the same regardless of their topographical position (Rowan et al., 1974, 1977; Drury, 1987; Sabins, 1987; Lillisand and Kiefer, 1987; Mather, 1987).

Certain caution should be taken when generating and interpreting ratio images (Drury, 1987), such as removing haze effect (Segal, 1982), and also the fact that the ratio images are intensity blind. For example, basalt and marl have similar reflectance spectra, but basalt have low reflectivity and appear dark in all grey level images, whereas marl appears light. But in ratio images the two are often indistinguishable. In addition, Ratio images usually display a low contrast, and a low signal to noise ratio due to the removal of most of the original image variance (Goetz, 1989).

In this study, the ratio method was performed using CHIPS software, by choosing the option "RATIO TWO IMAGES", and then stating scaling factor so that the resultant grey scale ratio image can be displayed in the 8 bit screen. Choosing the best 3-colour composite ratios for display was done by visual examination of the grey scale ratio images, bearing in mind the previous studies using ratio techniques in arid areas (see Chapter 6 for further discussion).

5.7 Principal component analysis (PCA)

Colour images can be constructed by selecting three of the available six TM bands as red-green-blue in a colour screen. Even if the best three bands are chosen, either by visual inspection, or by statistical methods described in section 5.5, choosing only three bands out of six reflected TM bands might result in information contained in the remaining bands being overlooked.

Data compression, known as principal component analysis (PCA) (Jenson and Waltz, 1979; Canas and Barnett, 1985), also referred to as Karhunen-Loeve transformation, Eigenvector transformation and Hotelling transformation (Singh and Harrison, 1985), is a widely used

technique to accomplish dimensionality reduction of the data. This technique is based on the assumption, that the image varience may be used as a measurement of the information content of that data (Jenson and Waltz, 1979). It is a linear transformation which rotates and translates the original n-dimensional image vector (e.g. 6 TM bands) to a co-ordinate space with uncorrelated axes called principal components axis (image). Each of these components can be displayed, either as grey scale images or as a colour composite of red-green-blue.

The purpose of PC transformation is to define the dimensionality of the data, and to identify the principal axes of variability within the data, based on the variance and covariance of the data set. The variance is the measure of the scatter within one variable, whereas the covariance is the measure of the scatter between two variables. A detailed description of the statistical procedures used to derive PC transformation is beyond the scope of this work, and can be found in Jenson and Waltz (1979), Short (1982), Canas and Barnett (1985), Gillespie et al (1986), Richard (1986), Jensen (1986) or Mather (1987). Therefore, only a basic description of the technique will be given here.

The PC transformation (Figure 5.6a) started by shifting the original co-ordinates (x and y) by shifting (subtracting) the mean of the data (m_x, m_y) to zero. The next step is the rotation of the original co-ordinates axes to coincide with the direction of maximum and minimum variance in the data (Schowengerdt 1983). This new rotated axis is the first PC (Figure 5.6c). The second PC is the one at right angles to it. If the distribution is multidimensional (e.g., six TM bands) this operation continues to define orthogonal axes sequentially until all the variations are consumed. In other words, the total variance of the image consisting of the six bands is divided

in a way that the first component has the largest possible amount of the total variance; the second component has the next largest possible amount of the remaining variance and so on. For each pixel, new digital numbers are determined relative to each of the new co-ordinate axes (Jenson and Waltz, 1979; Drury, 1987). Thus it is expected that the first, second and third principal component images would contain more information than any three of the raw bands (Canas and Barnett, 1985). The PCA were performed in this study using the IDRIS software to produce six PC images for each test area.

PCA technique has been widely used in the geological application of remotely sensed data, to reduce dimensionality by, for example, Blodget et al. (1975), Settle (1984), Spatz et al. (1987), Amos and Greenbaum (1989), Chavez and Kwarteng (1989), Fraser (1990). However, caution must be taken in interpreting the results due to the fact that this transformation is scene dependent (Drury, 1987).

5.8 Decorrelation stretch

The decorrelation stretch technique has been introduced by Soha and Schwartz (1978). It is based on principal components analysis (Soha and Schwartz, 1978; Gillespie et al., 1986; Rothery, 1987, 1990). The steps of this method begin by applying principal component transformation to the original data, and then the components are stretched linearly to equalise their variance. These stretched PCs are then transformed back to the original co-ordinates, using the inverse of the PC transformation.

The reason for the second step was to exaggerate colour saturation and reduce the correlation between bands, whereas the last step has the advantage that the colour can be related to the spectral characteristics of the

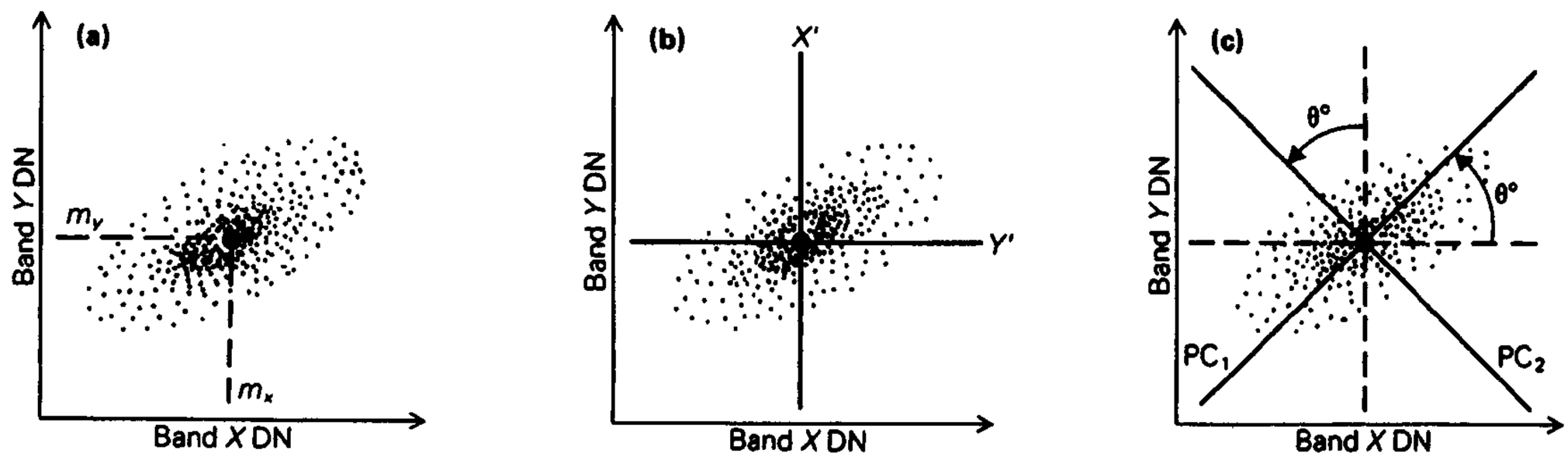

Figure 5.6. The steps of principal component transformation; see text for explanation (after Drury, 1987).

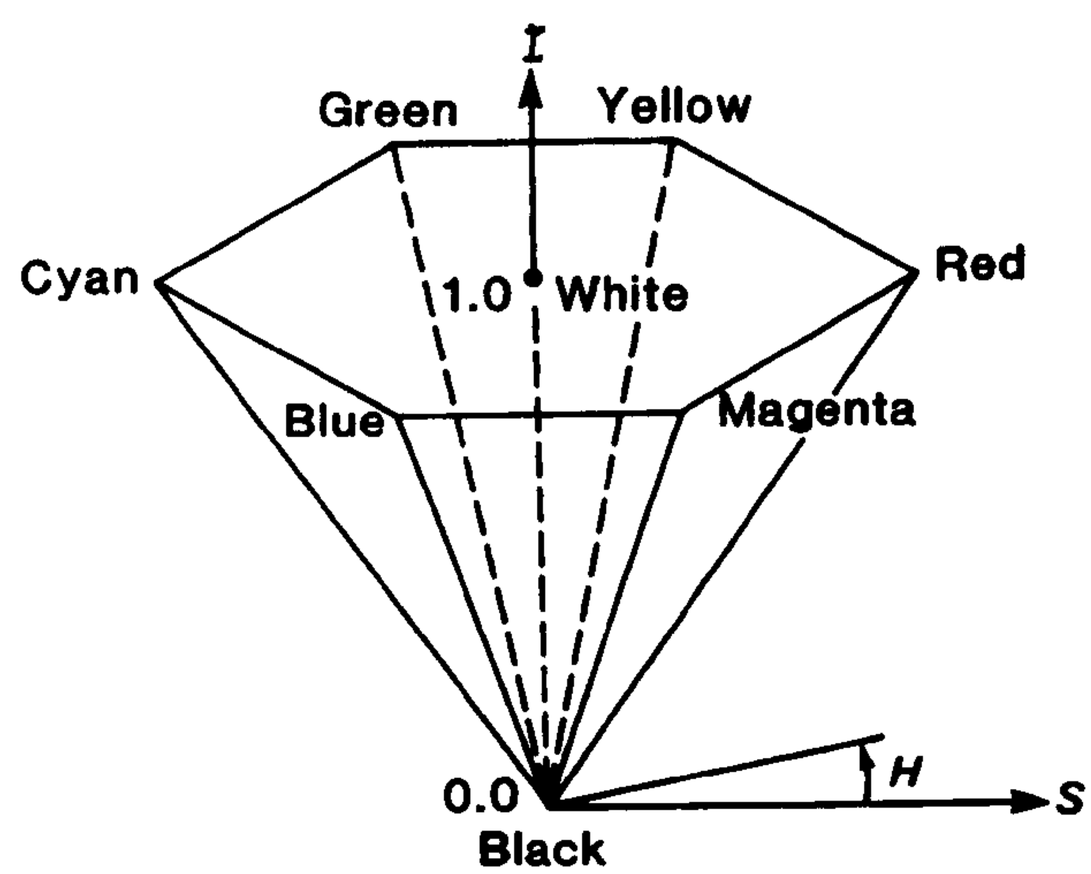

Figure 5.7. Hue-saturation-intensity (HSI) hexcone (after Mather, 1987).

materials in the images. This transformation has been described in great detail by the previously mentioned authors. This technique has been applied to rock discrimination (Abrams, 1986, et al., 1988; Gillespie et al., 1986; Rothery ,1987; Drury and Hunt, 1989; Al-Sari, 1990; Rothery and Hunt, 1990; and Puntual, 1990). The program for this technique (written comm. D. Rothery, and pers. comm. A. I. Watson), available in the MicroVAX menu system and called "DECORRELATION STRETCH", was based on Rothery (1987) and Rothery and Hunt (1990).

5.9 Canonical transformation

The principal components method of transformation produces an output that is not related (except accidentally) to the information of the input images. In the canonical transformation method, the transformation is related to the objectives of the study. In this study the TM bands are transformed to yield (in principal) the chemical composition of the rock. In general, canonical analysis enables a set of dependent variables to be related to a set of independent variables with the effect of maximising the correlation between certain linear combinations of the dependent and independent variables while minimising the correlation between these combinations.

Let us suppose that we have a set of variables x_1 (chemical composition of the rocks) and a set of values x_2 (raw DNs value). The variables (columns) of the data matrix are divided into sets, with r and q variables in each set; so that p, the total number of variables, equals r + q. The data matrix is then written as:

$$X = [x_1 \ , \ x_2]$$

$$nxp \quad nxr \quad nxq$$

in which x_1 = chemical percentage

x_2 = raw DN value

The variance-covariance matrix is written in partitioned form (hugget 1985) as:

$$S = \begin{bmatrix} A_{rr} \ , & C_{rq} \\ C'_{qr} \ , & B_{qq} \end{bmatrix}$$

whereas A_{rr} = covariance matrix between the x_1 variables (r) or "chemical percentage"

B_{qq} = covariance matrix between x_2 variables (q) or "DN values"

C_{rq} = covariance matrix between x_1 (r) variables or "chemical %" and x_2 (q) variables or "DN values"

C'_{rq} = transpose of C_{rq}

From this matrix, 'k' linear combinations of the form:

$$U_k = \sum_{i=1}^{r} l_{ki} \quad x_{1i}$$

$$V_k = \sum_{i=1}^{q} m_{ki} \quad x_{2i}$$

where l and m are weighting factors, $k = 1, 2 \ldots$

are sought, such that they have the property that the correlation between U_1 and V_1 is greatest, the correlation of U_2 and V_2 is next, and so on for all

possible pairs. In addition, each pair is independent of all others (i.e., orthogonal).

On performing the analysis, the number of independent linear combinations between the x_1 and x_2 is computed and tested statistically. Thus the number of significant components can be found, unlike the principal component method, where the number has to be guessed at. Further, if the number of independent combinations is greater than or equal to the number of x_1 variables, then it is possible to solve the set of simultaneous equations to yield direct estimates of the x_1 values from the x_2 values.

e.g., $l_{11} x_{11} + l_{12} x_{12} + l_{13} x_{13} + \ldots = m_{11} x_{21} + m_{12} x_{22} + \ldots$

$l_{21} x_{11} + l_{22} x_{12} + l_{23} x_{13} + \ldots = m_{21} x_{21} + m_{22} x_{22} + \ldots$

Since the x_2 values are known (in this case they are the DN values of a pixel) then the equations become:

$$l_{11} x_{11} + l_{12} x_{12} + \ldots l_{1r} x_{1r} = a_1$$

$$l_{21} x_{11} + l_{22} x_{12} + \ldots l_{2r} x_{1r} = a_1$$

$$l_{r1} x_{11} + l_{r2} x_{12} + \ldots l_{rr} x_{1r} = a_r$$

$$[a_1 = m_{11} x_{21} + m_{12} x_{22} + \ldots]$$

These equations can be solved for the x_1's. Thus, it is possible to predict the chemical composition of rocks, given imagery of the right quality.

The only application of this type of analysis in remote sensing, was to the problem of estimating the sediments and the chlorophyl concentration from SPOT imagery for a lake in Mexico (Chacon-Torres et al., 1992).

In this thesis the aim of using this transformation was to relate the DN values recorded by the reflected TM bands to the chemical composition of the rocks. The steps used to perform this analysis will be described in Section 6.2.2.

5.10 Hue-Saturation-Intensity (HSI) transform

Digital images are usually displayed as an additive colour composite using the RGB colour space (section 5.5). An alternative method is the use of Hue-Saturation-Intensity (HSI) model (Haydn, 1982; Gillespie et al., 1986), which refers to the parameter of human colour perception (Lillisand and Kiefer, 1987). An observer viewing a spot of colour can describe it relative to these three independent parameters (Buchanan and Pendegrass, 1980). The "hue" is the dominant wavelength of the colour (e.g., red, green or blue and their intermediate mixtures); "saturation" is the relative purity of the colour, or the amount of white light mixed with the hue; and "intensity" is the relative brightness. Any RGB image can be represented by three independent parameters which describe colour in terms of its hue (H), saturation (S) and intensity (I). These parameters will be perceived independently by the human eye, and can be individually manipulated (Haydn, 1982; Schowengerdt, 1983). Many algorithms have been developed for converting RGB tristimulus values to HSI and vice versa (e.g., Haydn et al., 1982; Siegal and Gillespie, 1980, 1986; Niblack, 1986; Mather, 1987). These methods differ mainly in the speed in calculating the intensity component of the transformation; in general they produce similar values for hue and saturation (Carper et al., 1990). The hexacon model (Figure 5.7) is one of these methods in which the hue is defined by the top edge with red at 0°, green at 120° and blue at 240°. Saturation is defined by the distance from the

vertical axes at the centre of the hexacon, and intensity is defined by the distance above the apex of the hexacon (Mather, 1987). Any point lying in the vertical axes will have no colour and a 0 saturation, the eye will perceive it as shades of grey that range from white to black, depending on the intensity.

The RGB-HSI transformation is useful as an intermediate step in digital image enhancement. For example, the intensity of an image can be stretched without causing any change to the hue and saturation images, or in merging data from different platforms with different spatial resolution (e.g., Landsat TM and AVHRR data). In this study the advantages of this technique will be discussed in greater detail in Chapters 6 and 7. This technique was used as an intermediate enhancement step for rock discrimination (Chapter 6) and the hue images were used in (Chapter 7) as an input for lithology classification. Detailed description of the relation between HSI and RGB colour space can be found in Buchanan and Pendegrass (1980).

The development and application of various HSI transformation and enhancement are under continuing research (Haydn, 1982, et al., 1982, 1983; Drury, 1987; Sabins, 1987; Goetz 1989a; Carper et al., 1990). Several authors have used it as an intermediate stage to enhance the visual interpretability of satellite data, that have the same spatial resolution (Haydn et al., 1982; Haydn, 1983; Curlis et al., 1986; Gillespie et al., 1986; Kaufmann and Pfeifer, 1986; Kaufmann, 1988) whereas others have used it for merging data that have different spatial resolutions (Haydn et al., 1982; Haydn, 1983; Kaufmann, 1984; Volk et al, 1986; Rothery and Francis, 1987; Carper et al., 1990). In this study the program which transforms the RGB image to HSI

images and vice versa (written comm. P. Mather, and pers. comm. A. I. Watson) was based on the subroutine that was discussed by Mather (1987).

5.11 Summary

Different methods of pre-processing and processing techniques were described in this chapter. These methods include the correction for the effect of atmospheric scattering based on approximate, dark object, methods. This was followed by a description of a number of contrast enhancement techniques, which are performed on a single band image or individual bands of multispectral image sets, to increase the contrast between different objects (lithologies). The methods of emphasising or de-emphasising certain frequency components (spatial filtering) of an image were also introduced. Operation on multiband images was also described. Two of these enhancement methods (ratio and principal component analysis) have been used extensively in geological studies, and provide valuable information that may not be found by using the original images. However, these methods have their limitations that may cause some loss of important information (e.g., textural information in ratio and spectral relation in principal component analysis). The HSI transformation was discussed and this method may reduce the two previously mentioned problems of both the ratio and PC transformation, and produce an optimal enhancement, when used as an intermediate step (section 6.2.4), or by directly using the hue component as classification inputs (chapter 7).

The canonical transformation has never been previously used to relate the pixel values of the satellite images to the chemical composition of various rock types. In principal, it may provide, from the imagery, a chemical description of the exposed lithology.

Digital image processing, however, is not limited to the methods described briefly in this chapter. The content of this chapter is restricted to the digital processing techniques that were required and performed in this study. The equally important subject of image classification will be described and applied in chapter 7.

CHAPTER SIX

LITHOLOGY DISCRIMINATION, METHODOLOGY AND RESULT

6.1 Introduction

6.2 Methodology
- 6.2.1 Principal component (PCA) and band ratio analysis
- 6.2.2 Canonical regression
- 6.2.3 Colour composite
- 6.2.4 Decorrelation stretch
- 6.2.5 Hue-Saturation-Intensity (HSI) transformation

6.3 Results
- 6.3.1 Silsilah ring complex (study area 1)
  - 6.3.1.1 Principal component (PCA) and band ratio analysis
  - 6.3.1.2 Canonical regression
  - 6.3.1.3 Band colour composite and HSI transformation enhancement
- 6.3.2 Jabal ar Raha (study area 2)
  - 6.3.2.1 Principal component (PCA) and band ratio analysis
  - 6.3.2.2 Band colour composite and HSI transformation enhancement
- 6.3.3 Aban Ahmar (study area 3)
  - 6.3.3.1 Principal component (PCA) and band ratio analysis
  - 6.3.3.2 Band colour composite and HSI transformation enhancement
- 6.3.4 Aban Asmar (study area 4)
  - 6.3.4.1 Band ratio analysis
  - 6.3.4.2 False colour composite and HSI transformation enhancement

6.4 Summary and conclusion

6.1 Introduction

One of the principal needs of remote sensing in geological studies is in discriminating different lithological units. In this chapter the results of applying the techniques described in the previous chapter to the problem of discrimination will be discussed. The techniques were applied to four test areas (described in Chapter 2) which have an excellent aggregate of different lithologies exposed in relatively small areas, and therefore provide an excellent area to test the various image processing techniques.

It is the aim of this chapter to evaluate the different techniques that have been used frequently for digital image enhancement (band ratio and principal component analysis), and compare them with the relatively new techniques that, as yet, do not have the same popularity (decorrelation stretch and HSI transformation). The Canonical regression analysis is also tested, with the aim of relating directly the major element chemical composition of the different lithologies, to their spectral signature. Although the aim of this chapter is to evaluate techniques, rather than carry out geologic investigation, it was decided to make a quick field check of the test areas, in order to ensure ground truth accuracy. Field check was carried out in November 1991, and several rock thin sections were made by the Geology Department, King Saud University, and were checked by J. Al-Alawi in the same department.

This chapter is divided into two main sections. The first section describes the methodology that was followed in applying the techniques, until an optimum result was reached. The second main section describes the results that were obtained in each area from the application of each technique. The results of techniques that did not produce an optimum discrimination in any of the test areas are not discussed.

6.2 Methodology

6.2.1 Principal component (PCA) and band ratio analysis

The PCA was performed in this study, with the IDRISI software package, using all the 6 reflected TM bands for each of the test areas. The program produced 6 principal component images. Because of the shift of the original coordinates caused by subtracting the means of the data, and the simple axis rotation used for transformation as described in section 5.7, some of the PC pixel values were negative. An option called "STRETCH" was used to project the image to 0-255 scale.

Tables 6.1, 6.5 and 6.7 describe the statistics involved in the production of PC images for three of the four test areas. The principal component results for the fourth test area (Aban Asmar) will not be discussed due to the low degree of discrimination achieved. The high degree of correlation found between the 6 TM bands in all the test areas, caused most of the information to be mapped in the first PCs. This can be seen, either from the percentage of variance accounted for by each component, or from the component loading summary table, that describes the amount of information mapped in each component from each band.

Ratio processing was performed on the CHIPS software by choosing the option "RATIO TWO IMAGES". The number of ratios that can be made from six reflected TM bands is somewhat large (30 ratios). Furthermore, to display these ratio images as ratio colour composites by combining three ratio images the number of combinations will be high.

The 'best' three-colour composite ratios for display were chosen by visual examination, bearing in mind the previous studies using ratio techniques in arid regions (section 5.4), and the spectral sensitivity of the various TM bands. Both the principal component and ratio images were stretched using the BCET stretch method. This step was taken to increase the contrast and minimised the noise, which both images suffer from, especially the ratio images.

6.2.2 Canonical regression

The main aim of using the canonical regression processing in this study (section 5.9) was to from a linear relation between the chemical composition of the various rock types and the digital number recorded in each of the six reflected bands of the TM data. This linear relation could then be stored in a canonical coefficient file and used to predict the chemical composition of unknown areas acquired by the TM sensor.

The processing of data by this technique includes various pre-processing stages. The following is a brief description of the steps that were followed (Figure 6.1). The first step was to locate the image coordinates of areas that had been chemically sampled and analysed by previous studies (Du Bray, 1983, 1988; Williams et al., 1986; Cole, 1988). Information for 210 samples was extracted from the published sources. Having identified the sites on the geological map. The next step was to extract the areas that cover those sites from the scene, in which 11 extracts (images) of 512 pixels by 512 lines were used. The corresponding x and y image coordinate was then found (visually). The average of nine pixels was taken for each site in each area, including the sample site pixel and its immediate surroundings, in order to ensure that representative values were obtained. Next, a VAX file

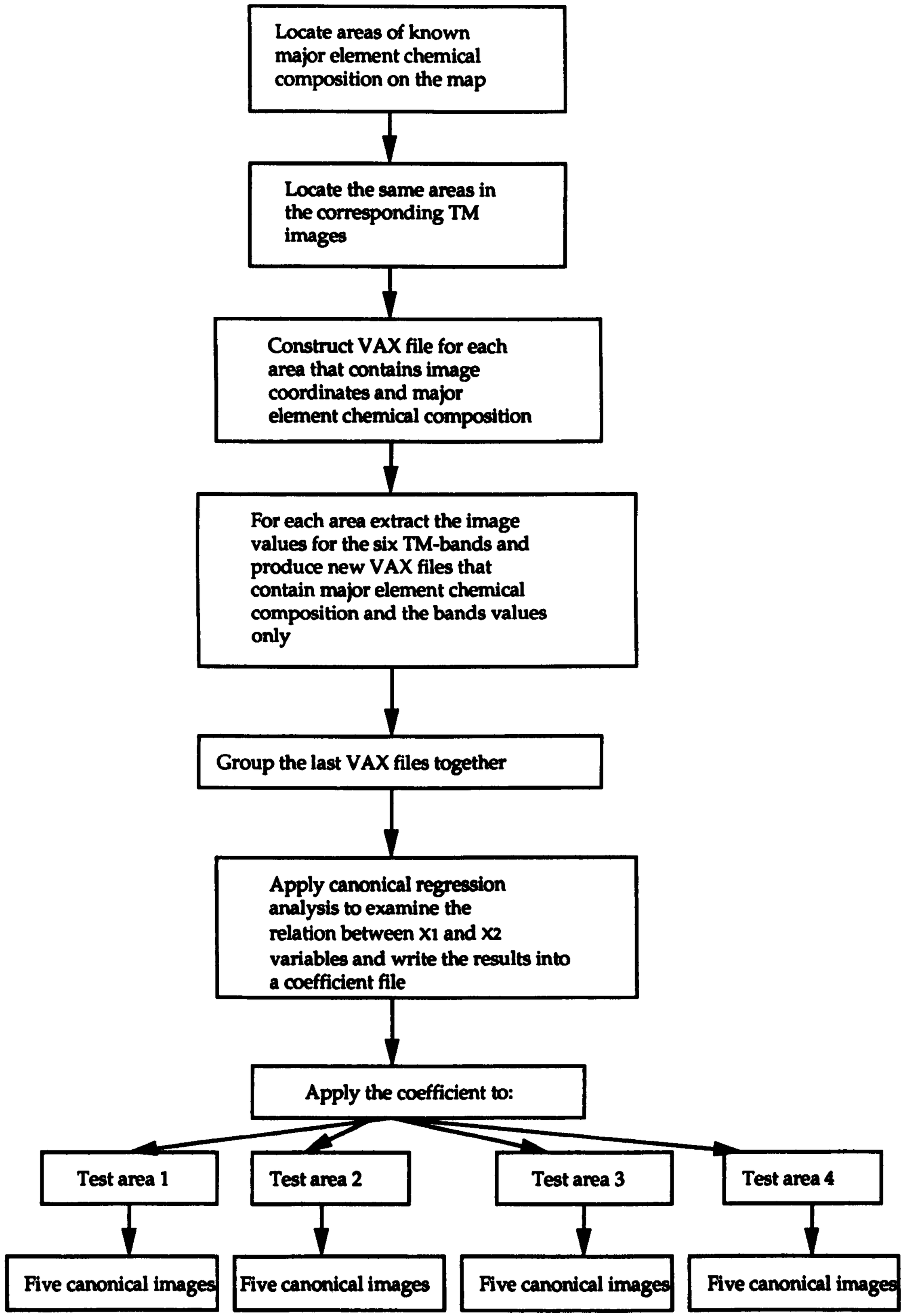

Figure 6.1. Flow diagram of the processing steps used for canonical analysis.

was constructed that contained these image coordinates and major chemical components of the samples (SiO_2, AL_2O_3, Fe_2O_3, FeO, MgO, CaO, Na_2O, K_2O, TiO_2, P_2O_5, and MnO).

The DN values of the six reflected TM bands for each 'sample' site were then extracted using one of the listed programmes made especially for the data used in this study. Therefore, for each of the areas (11 in all), a file was constructed that contained the chemicals as "x_1 variables" and the DN values for the six TM bands as "x_2 variables". These 11 files were then grouped into one VAX file.

A canonical regression analysis was then applied to the composite file. The program examines the linear relation between x_1 and x_2 variables and produce a canonical regression file that contains the number of components that are statistically significant and a canonical coefficient file that contains the coefficient matrix. The latter file was then applied to the six TM imges in order to transform the original data to the significant canonical component axes. This was done by choosing the option "CONSTRUCT THE CANONICAL IMAGE" from the canonical transform submenu in the MicroVAX. These canonical components could then be used in an attempt to predict the chemical composition of the rocks.

6.2.3 Colour composite

In this study six reflecting TM bands are available. The thermal band (Band 6) was excluded owing to its high degree of distortion. A decision has thus to be made about which three bands represent optimum spectral information to display.

The disadvantages of using a purely statistical method (section 5.5) to define the best three bands for colour display in geological studies are, that

these methods do not take into account the distinction between geologically significant variation, and the variations due to non geological factors (Rothery, 1987; Drury and Hunt, 1989). In this study selection was made using a combination of statistical investigation and visual inspection. The statistical investigation was made by examining the correlation matrix between TM bands to define the least correlated three bands that would display the most information (Hunt et al., 1986). The visual inspection was made by comparing each of the stretched TM band images, first as grey level images, and then as colour composites of three bands. The factor governing this assessment was the ability of individual bands to distinguish between different lithologies shown on the geologic maps (1:100,000 and 1:250,000) of the four test areas, bearing in mind the spectral reflectance characteristics of diferent minerals and rocks (section 3.5).

Using the latter procedure, it was found that the best three band colour composite that offered the best discrimination between various lithologies for the four test areas was as follows: TM band 7 displayed as red; TM band 4 displayed as green; and TM band 1 displayed as blue.

Statistically these three bands have the least correlation between them (Tables 6.4a, 6.6a, 6.8a and 6.10a). TM band 7 (2.8-2.35 μm) contains important information about hydroxyl minerals (Hunt et al., 1971; Goetz, 1989a). TM band 4 (0.76 - 0.90 μm) contains information on iron minerals (the Fe crystal field absorption) (Hunt, 1980) and has unique high reflectance of green vegetation. The presence of ferrous ions is best detected by a sharp absorption in TM band 1 (0.45 - 0.52 μm) (Drury 1987). Although this combination is placed tenth (by the OIF method) out of the 20 possible 3-band combinations from the six reflected TM bands, the combination of

these bands produces a better overall rock discrimination, than any of the combinations ranked better by OIF method.

This combination was different from the combinations of bands that other authors used (such as Sheffield, 1985; Rothery, 1987; Spatz et al., 1987). However, (Fielding, 1985; Kaufmann and Pfeiffer, 1986; Kaufmann, 1988; Davis and Berlin, 1989; Crippen, 1989; and Ferrari, 1992) found the same combination as the best for rock discrimination. Also Laughlin and Taufiq (1985) and Hunt et al. (1986) found a similar combination (displaying TM band 2 as blue instead of TM band 1).

6.2.4 Decorrelation stretch

The decorrelation stretch was applied in this study to the best three bands colour composite, (TM bands -7, -4 and -1), using a programme called DECORRELATION STRETCH (written comm. D. A. Rothery, and pers. comm. A. I. Watson) that was available on the Microvax. The programme transformed these three bands to three principal components. This step was followed by stretching these three components to fill the 8 bits range, and then transform them back to the original coordinates, using the inverse of PC transformation. However, the results of these techniques did not provide any significant improvement over the band colour composite, therefore its results will not be discussed.

6.2.5 Hue-Saturation-Intensity (HSI) transformation

A high degree of correlation that exists between different TM bands reduces the range of colour displayed. This is almost atypical behaviour for most geological scenes, owing to the relatively broad band width of the TM sensor (Drury, 1987), and the lack of strong absorption bands associated with

most rock surfaces (Kaufmann, 1988). Contrast stretching of the individual bands in the RGB coordinates by spreading out the histogram along the achromatic axis, while satisfactory in some cases, often fails to reduce this correlation and to fully utilise the available colour range (Soha and Schwartz, 1978). In addition, most of the rock types exhibit low intensity (dark appearance) in the image, which also tends to reduce colour variations.

Section 5.10 described the basic concept of the hue-saturation-intensity (HSI) transformation.In this section a description will be given to the transformation as an intermediate stage to reduce the correlation and improve the visual interpretability of atmospherically corrected TM images.

As discussed in section 5.10, any three-colour composite image in the red, green and blue (RGB) coordinates can be transformed into three independent parameters, which describe colour in terms of its hue (H), its saturation (S) and its intensity (I). These parameters are perceived independently by the human eye, and therefore each one of them can be manipulated without causing any interfering effects to any of the other two components. However, Gillespie et al. (1986) mentions that the stretching of the hue component in the HSI coordinates may cause hue distortion. He suggests that such distortion may be eliminated or effectively reduced by equalising the mean values of the original data before transformation to HSI coordinates. Kaufmann (1988) applied histogram equalised stretch to the original bands before transforming to HSI coordinates.

In this study the following strategies were employed to achieve the best results in reducing the two, previously mentioned problems which are widespread in most geological scenes, and also to produce a sharper image.

A balance contrast stretch (section 5.3.3) was applied to the best three-band colour composite. This implies that the three stretched images will have an equal range and means and hence should avoid any colour bias of one band over the others, and secure the equal contribution to the hues by the RGB components. The next step was to transform the data from RGB coordinates to HSI coordinates

In the HSI coordinates, saturation usually has a low value for TM data which implies a low degree of colour purity. This may due primarily to the high correlation between the bands (Gillespie et al., 1986). By increasing the saturation component, by shifting its histogram to a higher value within the 0-255 scale, a more saturated hue was achieved. The histogram shift was simply made by adding a visually estimated constant to each saturation value.

Since the intensity component is independent from both the hue and saturation, it was decided to replace it by the first principal component of the six reflected TM bands that were produced earlier (section 6.2.1). This first PC has the greatest contrast and reveals the albedo and topographic detail. Therefore, by using an edge enhanced filter (Laplacian add back, see section 5.4), it was anticipated that this would produce an image with high, sharp quality. As the (I) component is independent from the other two components, there will be no loss of spectral information, which may occur if the addback filter were applied to the RGB image.

Before transforming the data back to the RGB coordinate an increase to the intensity was made by shifting its histogram to a higher value, using the same procedures described earlier to shift the saturation component. This step was taken to enhance the hues in areas of low brightness (Haydn,

1982). The data were then transformed back to the RGB coordinates, and then transferred to the CHIPS system for display and evaluation.

6.3 Results

Four test areas selected for this study included the Silsilah ring complex, Jabal ar Raha, Aban Ahmar and Aban Asmar, with a size of 512 rows by 512 columns for the first two areas, and 1024 rows by 1024 columns for the other two areas. The location and geology of each of these test areas was briefly discussed earlier in chapter 2 . In this section, the discussion will be confined to the results of applying image processing techniques described earlier in chapter 5.

The discussion of the results of the canonical images will be confined to the Silsilah ring complex test area, due to the confusing results of this technique. The principal component results for the fourth test area (Aban Asmar) will not be discussed due to the low degree of discrimination compared to the ratio image. For information about the location of the different lithologies, see the geologic maps for the corresponding test area in chapter 2. A copy of these maps were put in a pocket at the end of this thesis for easy consultation.

6.3.1 Silsilah ring complex (test area 1)

6.3.1.1 Principal component (PCA) and band ratio analysis

The TM data show a high degree of correlation between different bands (six reflected bands) for this area (Table 6.1a). For example, the correlation of band 1 to band 2 and band 3 is 0.96 and 0.92 respectively. With this high degree of correlation, this area might be ideal for performing the PC analysis to produce a fewer uncorrelated set of components.

COR MATRIX	B1	B2	B3	B4	B5	B7
B1	1.00					
B2	0.96	1.00				
B3	0.92	0.98	1.00			
B4	0.79	0.88	0.90	1.00		
B5	0.87	0.93	0.95	0.90	1.00	
B7	0.82	0.89	0.92	0.82	0.95	1.00

(a)

COMPONENT	C1	C2	C3	C4	C5	C6
% var.	93.21	2.98	2.46	0.78	0.47	0.09
eigenval.	1254.44	40.12	33.10	10.51	6.39	1.20
B1	0.261	-0.228	-0.681	-0.219	0.537	-0.277
B2	0.229	-0.156	-0.305	0.063	-0.072	0.905
B3	0.425	-0.230	-0.277	0.363	-0.673	-0.320
B4	0.355	-0.620	0.542	0.260	0.355	-0.004
B5	0.628	0.215	0.264	-0.681	-0.155	0.002
B6	0.420	0.662	0.018	0.531	0.317	0.002

(b)

Table 6.1. See next page.

LOADING	C1	C2	C3	C4	C5	C6
B1	0.907	-0.141	-0.383	-0.069	0.132	-0.029
B2	0.958	-0.116	-0.207	0.024	-0.021	0.117
B3	0.978	-0.094	-0.103	0.076	-0.110	-0.022
B4	0.924	-0.288	0.229	0.062	0.065	-0.000
B5	0.991	0.060	0.067	-0.098	-0.017	0.000
B7	0.956	0.269	0.006	0.110	0.051	0.000

(c)

Table 6.1. Statistics of Silsilah ring complex area where table (a) describes the correlation matrix between the six TM reflected bands. Table (b) describes the variance, eigenvalues and eigenvectors for each principal component denoted here as (C1 to C6) in which the percentage variance indicates the amount of variance that was picked by each component which is also expressed by the eigenvalue. The relative loading of each band for each component is shown. Table (c) gives the component loading summary.

After performing the principal component analysis using the IDRISI software package, as was described earlier in section 6.2.1, six principal component images were produced. By examining the statistical tables that were produced (Table 6.1b) it was found that 93.21% of the total variance in the six reflected TM bands lay in the direction defined by the first PC only, and the rest of the variance (6.79%) was mapped for the other five PC images with each one having lower variance than its successor.

To display PC images as principal component colour composites which will enable the display of most of the information (98.65% of the variance if the first three components are used) in a single presentation. As each component contains information from all original bands, statistically it was obvious that the first three PC images will provide the best principal component colour composite (PCC). In addition, it has the best signal to noise ratio of all the PC images.

The eigenvalues and eigenvectors are shown in Table (6.1b). The eigenvalues give the length of the principal axis which is measured in terms of units of variance. The eigenvector describes the direction of the principal axis. For each of these eigenvectors a loading factor for the contribution of each band to each of the components is given. The previous table shows that PC1 has positive loading for all bands which presents it as almost an average of all of the bands.

PC2 contains high positive loading for band 7 (0.66) and smaller positive loading from band 5, with the rest of the bands having negative loading; therefore materials having greater contrast at bands 5 and 7 on one hand and bands 1 to 4 on the other hand will show opposite relations. This may suggest discrimination between iron rich material and hydroxyl rich material, as negative and positive contributions respectively.

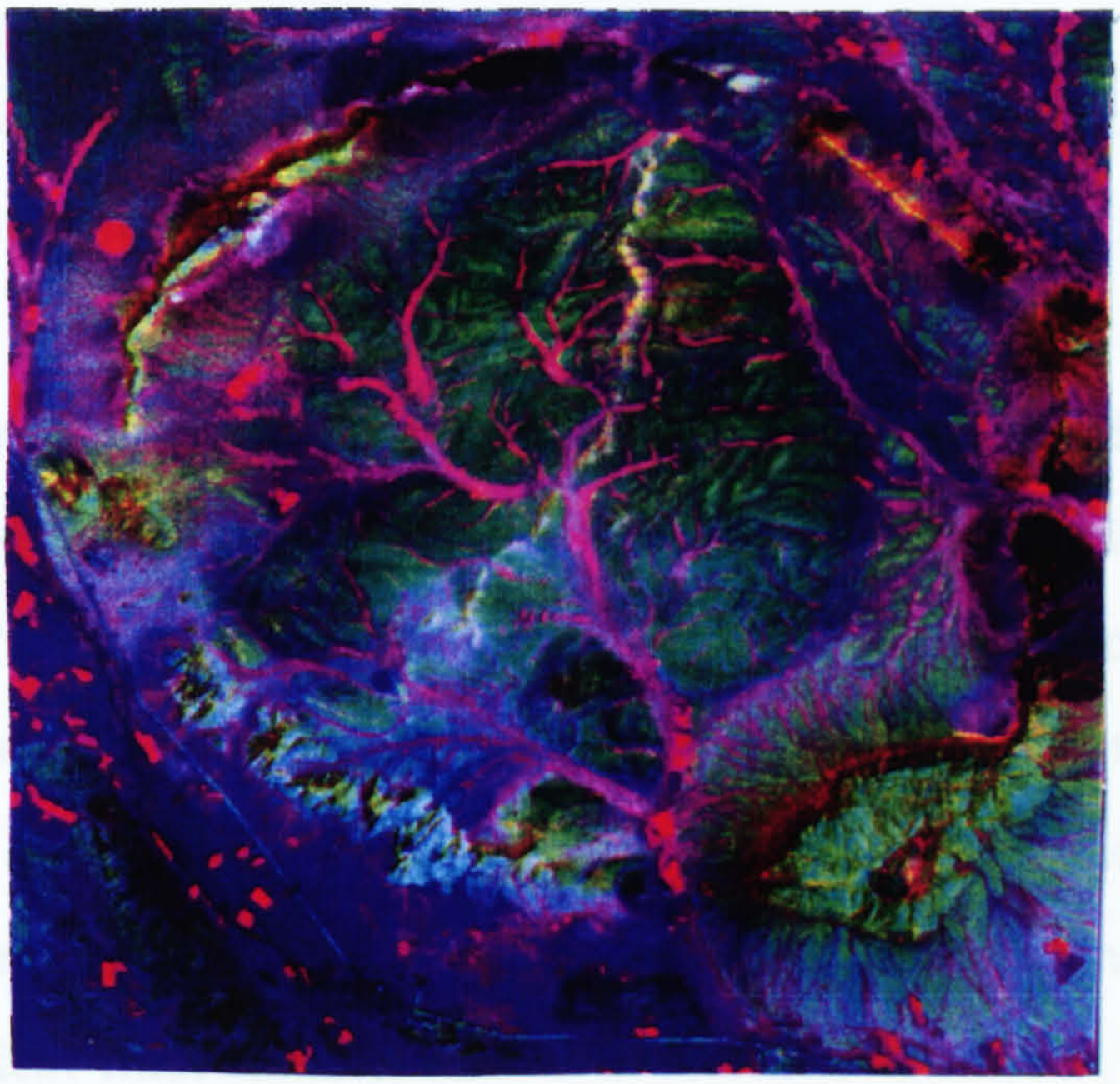

Figure 6.2: Principal component colour composite (PCC) image resulting from the principal component transformation of the six reflected TM bands of Silsilah ring complex, in which PC3, PC2 and PC1 were displayed as red, green and blue respectively.

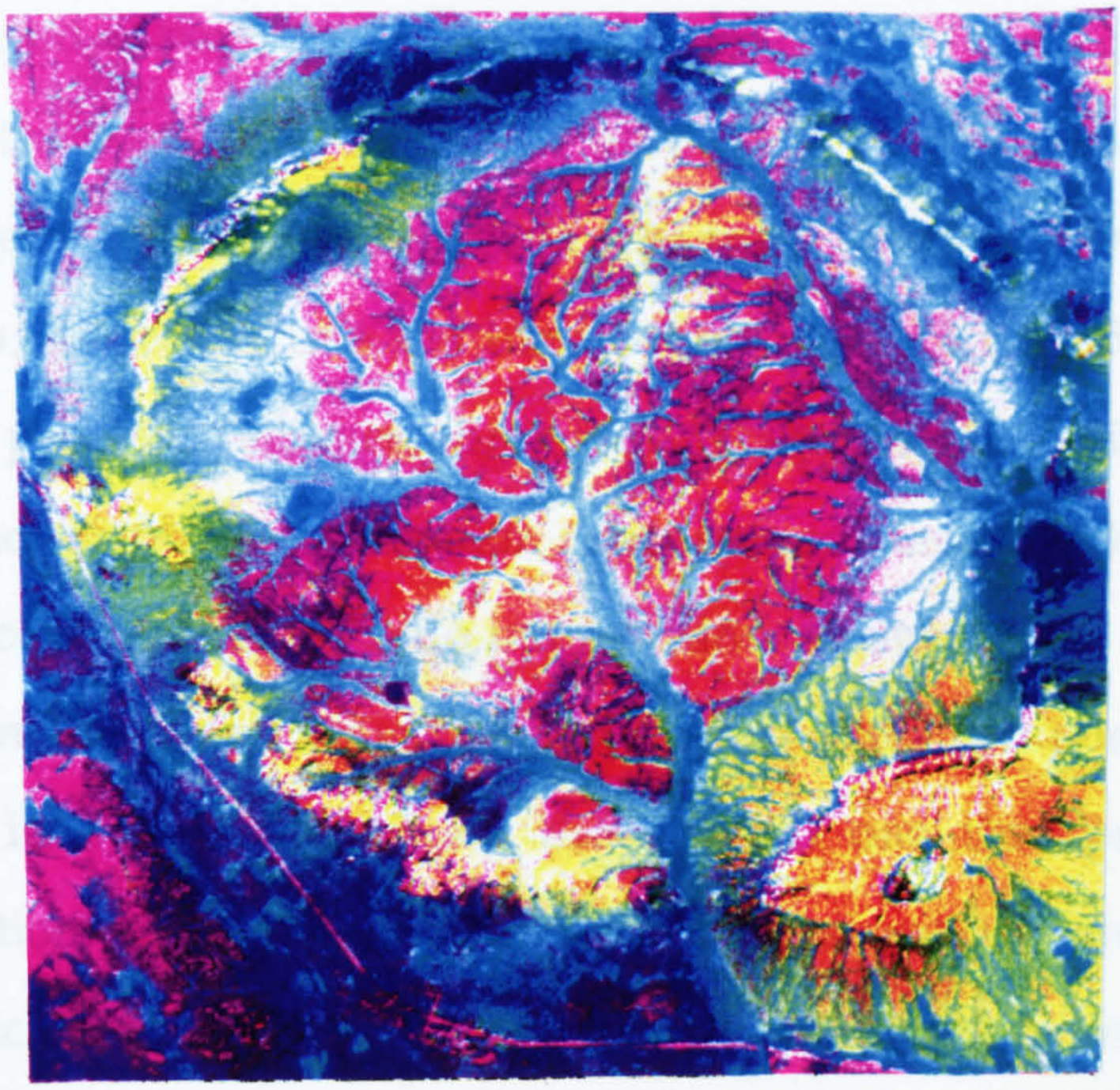

Figure 6.3: Colour ratio composite (CRC) image of Silsilah ring complex in which TM 5/4, TM 5/1 and TM 5/7 band ratios were displayed as red, green and blue respectively.

Vegetation, which has its highest reflectance in band 4, has intermediate and high positive eigenvector values in PC1 and PC3 respectively and high negative eigenvector values in PC2. This may suggest intermediate, low and high pixel values in PC1, PC2 and PC3 respectively. However, because of the very low variance associated with the lower order PCs (PC4, PC5 and PC6), they generally do not show much contrast and did not provide any additional information. However, these components sometimes show some distinction between certain materials, and it is sometimes necessary to check these images visually rather than relying on pure statistical information.

By examining each principal component image individually and as colour composites, it was found that the best three principal component images, that can be displayed as principal component colour composites (PCC) (Figure 6.2) were PC3, displayed as red, PC2, displayed as green, and PC1, displayed as blue.

For the band ratio technique only six of all the possible ratio images of the six reflected TM bands of this area were found to have good variation. These ratio images include TM band ratios 5/4, 5/3, 5/7, 5/1, 4/7 and 3/1. Like other processed images, three ratio images can be assigned to different colours and displayed as colour ratio composites (CRC) to combine the responses of each of these ratio in one colour image.

From the above ratio, various colour ratio composites (CRC) were produced in order to evaluate the optimal one that provides the best discrimination of the various lithologies. These ratios were stretched using BCET stretch technique, which enabled the reduction to some extent of the noise usually associated with ratio images. Ratio images that were chosen as the best were:

TM 5/1 This band ratio displays rocks having a higher amount of iron oxides as bright areas. However, vegetation areas are also bright in this band ratio. Areas that have high amounts of opaque minerals (e.g., magnetite) will have low values in band 5; therefore they will be displayed in this band ratio image as dark tone. This band ratio was also described by others, such as Huckerby et al. (1986), Magee et al. (1986), Sultan et al. (1986), and Kaufmann (1988), as the most reliable band ratio for enhancing iron oxides (e.g., limonite). Others such as Brickey (1986) and Kruse (1986) have used 3/1 band ratio for the same reason. However, Kaufmann (1988) mentioned that the 3/1 band ratio often fails due to the correlation between the two bands. In this study, it was found that the 5/1 band ratio looks better than 3/1 band ratio.

TM 5/4 Unlike the previous ratio, the vegetation and iron rich areas are inversely related. The rocks rich in iron bearing aluminosilicates (such as biotite) are displayed as bright areas, due to 0.85 μm (TM band 4) absorption, whereas the vegetation has high values in both TM band 4 and TM band 5 and appears dark. This ratio has also been used by other authors such as Magee et al. (1986), Brickey (1986), and Huckerby et al. (1986) for the same reasons.

TM 5/7 Hydroxyl and carbonate bearing minerals are affected by absorption in TM band 7 with respect to TM band 5 (Hunt and Salisbury, 1970, 1971; and Whitney et al., 1983). Therefore hydroxyl and carbonates show a high TM 5/7 band ratio value. This band ratio is widely used to enhance hydroxyls (Gupta, 1991; Goetz, 1989a), and was used previously by many authors to detect hydrothermally altered areas (Abrams et al., 1977, 1983; Podwysoki et al., 1983; Magee et al., 1986; Brickey, 1986; Amos and Greenbaum, 1989; Kruse, 1986; Fieldman and Taranick, 1986; Huckerby et al., 1986; Keeper et al., 1986; Sultan et al., 1986; Sabins, 1987; Drury, 1986; Elvidge, 1986).

Using the previously described ratio a colour ratio composite (CRC) was produced in which TM 5/4 band ratio images was displayed as red, TM 5/1 band ratio images was displayed as green and TM 5/7 band ratio images was displayed as blue.

Table (6.2) shows the colours associated with different lithologies on the colour ratio composite of Figure 6.3. In this (CRC) image, the main source of confusion was between parts of the alluvial deposition south and south west of the ring and the alkaline dacite (ad) (see Figure 2.5 for specific locations) in the eastern and northern parts of the ring structure, which both appear as blue colour, and cannot be distinguished. The reason for the confusion was described by Drury (1987); he mentioned that band ratioing suppressed differences in albedo in which lithology of low albedo, that appeared dark on all bands, and lithologies that have high albedo in all bands, often are indistinguishable in the ratio images. This has happened

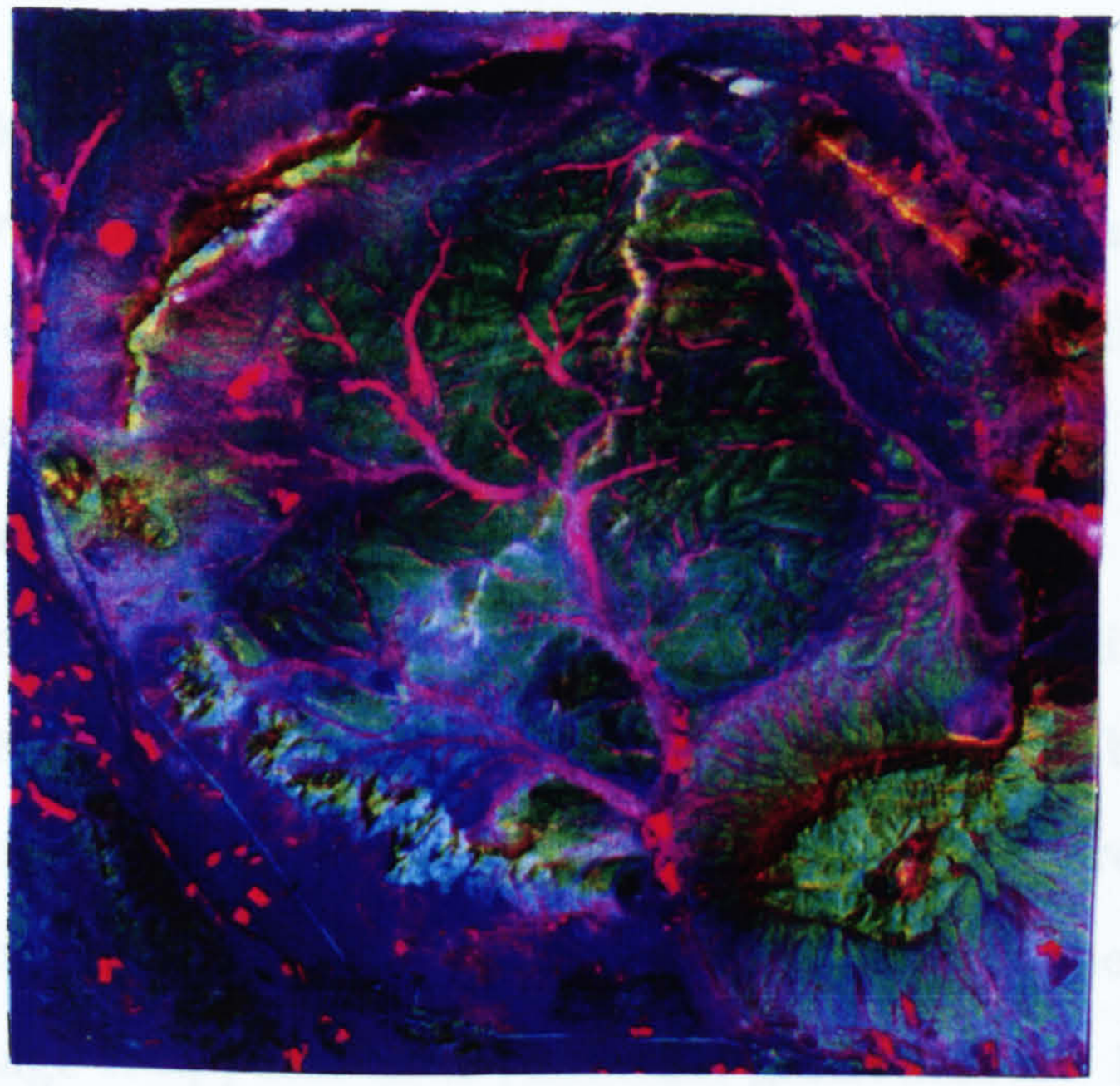

Figure 6.2: Principal component colour composite (PCC) image resulting from the principal component transformation of the six reflected TM bands of Silsilah ring complex, in which PC3, PC2 and PC1 were displayed as red, green and blue respectively.

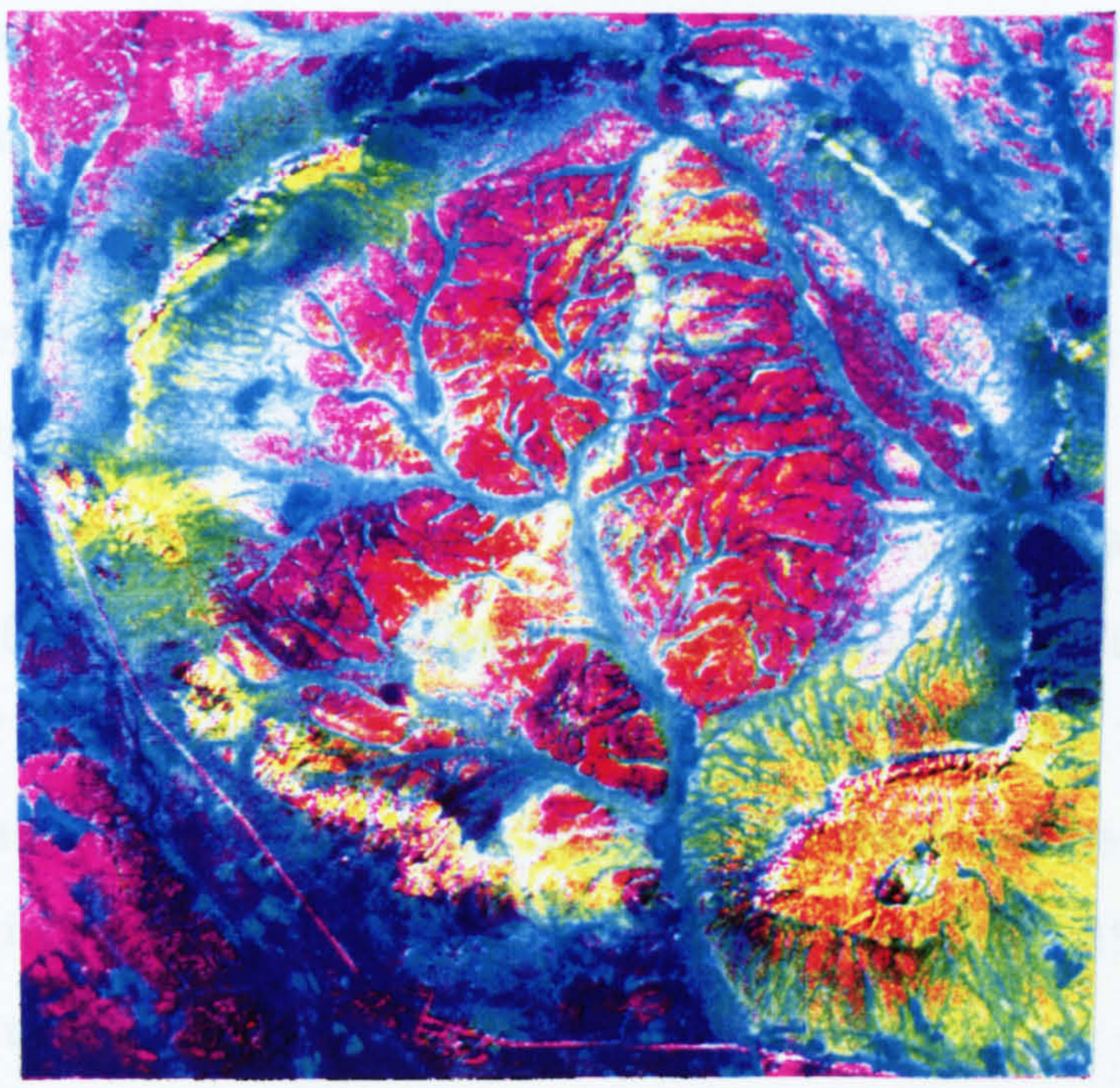

Figure 6.3: Colour ratio composite (CRC) image of Silsilah ring complex in which TM 5/4, TM 5/1 and TM 5/7 band ratios were displayed as red, green and blue respectively.

in this study, where the alkaline dacite have a low albedo and the alluvial deposits have a high albedo. However, this was not the case in the principal component colour composite (PCC) (Figure 6.2) where the alkaline dacite can be clearly discriminated by its dark brown colour, compared to the alluvial deposits which have a blue colour.

In contrast to the alkaline dacite, the Silsilah alkali granite (Sag) has the opposite composition, therefore it has the opposite band ratio values, which give it the yellow colour (high in red and green band ratios), especially in the outcrop in the south eastern part of the ring, whereas in the PCC image it appears as a yellowish green colour. However, for this rock type both images have more detail than the geologic maps; for example, in the CRC image the bright cyan colour in the centre of Jabal al Hadhir corresponds to an area, noted during the field trip as being less resistant and weathered more strongly, such that most of the rock surface was covered by weathering products (and soil) which gave it a different colour in the CRC image. In the middle of Jabal as Silsilah (north west of the ring) this rock appears as blueish green. These variations in colour that were noticed in the two locations within the Silsilah alkali granite can also be noticed in the PCC image.

The strongly weathered, low relief lithology Maraghan lithic greywacke (Mlg) that fills the inside of the ring, and also to the west, appears in the CRC as magenta colour (higher values in both the TM 5/4 and TM 5/7 band ratio images). This may be caused by the presence of clay minerals, and biotite in its matrix (which was reported by Du Bray, 1988). In the PCC image this unit appears as a dark green colour. The part of this unit, that was exposed inside the ring was not uniform, and was cut by dendritic, lightly vegetated channels that have cyan colour in the CRC image. These

	TM 5/4 band ratio image (red)	TM 5/1 band ratio image (green)	TM 5/7 band ratio image (blue)	Colour ratio composite (CRC)
Alkaline dacite	dark	dark	moderate	blue
Silsilah alkali granite and hadhir aplite	bright	moderate-bright	dark	yellow
Maraghan lithic graywacke	bright	dark	moderate	magenta
Commendite	moderate-bright	bright	moderate	bright white
Fawwarah alkali feldspar granite	bright	moderate-bright	dark	pale pink
Vegetation	dark	bright	bright	cyan

Table 6.2. Summary of colour associated with main lithologies in the colour ratio composite of Silsilah ring complex (Figure 6.3).

channels have light magenta colour in the PCC image, and also can be clearly discriminated. This unit was also cut by a number of small quartz veins which are shown as a yellow colour in the CRC. These were noticed during the field visit and were also reported by Du Bray (1983). These quartz veins are less noticeable in the PCC image compared to the CRC image.

The Maraghan lithic greywacke has also been cut by a NE-SW striking commendite dike, which also appears in another location as part of the ring structure (north east). This commendite (com) unit can be distinguished clearly in the CRC image by its bright colour, due to its high values in all three ratio images. This may be caused by the presence of iron as well as hydroxyl minerals. This unit also can be distinguished in the PCC image where its intensity and its yellow colour are evident. The Fawwarah alkali feldspar granite (Fag) appears as bright pink colour, which may be due to the presence of biotite, in small amounts, in its matrix, whereas in the PCC image it appears as a cyan colour. The sparsely vegetated (Veg) areas, inside and outside the ring structure, have a cyan colour in the CRC image, whereas in the PCC image they have a more discriminable red colour.

Sediments scattered around the high ground consist mainly of rock fragments that have fallen from these high areas (hence compositionally they are similar to these sources). However, due to the loss of textural information and the suppression of topography information, it was not easy to define the boundary of the rock area and separate it from the fragments surrounding it.

6.3.1.2 Canonical regression

The results of applying the canonical regression using the methodology described earlier in section 6.2.2 produced six components,

after the regression table produced was examined. The first three of these components were found to be highly significant; the following two components were within acceptable significant limits, whereas the sixth one was insignificant, and therefore it was rejected. The relation between the chemical composition percentage for the various rock types available, on one hand, and the canonical component images, on the other hand, was evaluated. This was made by submitting the chemical composition for each rock type, and its average DN value in the canonical images, to a statistics (correlation) package which would enable one to observe the effect of each chemical on the canonical images. (Table 6.3).

In the first canonical component, SiO_2 has the highest positive correlation values (Table 6.3) closely followed by the K_2O. This implies that for the first canonical component image the increase of these two chemical components leads to an increase in the DN values. Whereas the FeO, MgO and CaO have completely the opposite relationship with a high negative correlation followed by the MnO, P_2O_5, and TiO_2. This implies that the increase of these chemical component percentages in the rock leads to a decrease in the DN values of the first canonical image. This is also demonstrated in Figure 6.4a, which is the grey level image of the first canonical component.

From Table 6.4, the rock units that have high SiO_2 and K_2O percentages can be identified. Fawwarah alkali feldspar granite, Hadhir aplite, commendite and Silsilah alkali granite, (see figure 2.5 for the rock units locations), with compositions ranging from 74.7% $Si0_2$ and 5.14% K_20 for the Fawwarah alkali feldspar granite to 73.24% SiO_2 and 5.19 K_2O for Silsilah alkali granite are predicted to be bright, whereas the darkest rock unit in this image is predicted to be the alkaline dacite which has 53.2%

	SiO_2	AL_2O_3	Fe_2O_3	FeO	MgO	CaO	Na_2O	K_2O	TiO_2	P_2O_5	MnO
C1	0.890	-0.450	-0.450	-0.853	-0.926	-0.809	-0.257	0.783	-0.643	-0.628	-0.765
C2	-0.634	0.261	0.542	0.214	0.410	0.532	-0.032	-0.496	0.636	0.632	0.548
C3	-0.746	0.145	0.808	0.240	0.367	0.556	-0.126	-0.449	0.779	0.811	0.786
C4	-0.180	-0.097	0.149	0.130	0.155	0.147	-0.525	-0.104	0.147	0.220	0.109
C5	-0.264	0.266	-0.038	0.264	0.244	0.385	-0.052	-0.112	0.153	0.174	0.140

Table 6.3. Correlation matrix between major element chemical composition of various rock types and the five canonical images (C1 to C5).

	SiO_2	AL_2O_3	Fe_2O_3	FeO	MgO	CaO	Na_2O	K_2O	TiO_2	P_2O_5	MnO
Fawwarah alkali-feldspar granite	74.70	12.50	00.14	00.20	00.09	01.23	03.90	05.14	00.07	00.02	00.01
Silsilah alkali granite	73.24	12.90	01.87	00.92	00.12	00.74	04.84	05.19	00.26	00.05	00.06
Com-mendite	73.90	12.30	01.70	00.50	00.70	00.60	04.25	05.20	00.28	00.02	00.04
Alkaline dacite	53.20	14.00	10.60	01.28	01.50	04.19	04.64	02.65	01.89	00.65	00.15
Maraghan lithic graywacke	60.78	15.56	02.96	04.21	03.33	03.47	04.90	01.98	00.74	00.19	00.10

Table 6.4. Major element chemical composition for the main rock units in Silsilah ring complex.

SiO_2 and 2.65% K_2O. This rock and the Maraghan lithic greywacke has also the highest values of MgO, FeO, CaO, TiO_2 and P_2O_5, chemical elements percentage which have a high negative correlation with this canonical image.

In the second canonical component a moderate positive correlation was recorded for the following elements: TiO_2, P_2O_5, MnO, Fe_2O_3 and CaO, which means that the increase of these components leads to an increase in the DN values for this canonical image. Whereas the SiO_2, K_2O have completely the opposite correlation, which suggests that the increase of these two chemical elements will lead to a decrease in the DN values. Therefore, the information that can be drawn regarding the chemical composition from the second canonical image (Figure 6.4b) is that the light areas are the ones that have high TiO_2, P_2O_5, MnO, Fe_2O_3 and CaO such as the alkaline dacite, whereas the darker areas are the areas that have high SiO_2 and K_2O percentages, such as the Fawwarah alkali-feldspar granite and the Silsilah alkali granite. The Maraghan lithic greywacke has almost the same values in both the first and the second canonical images which may be due to its intermediate composition.

In the third canonical component (Figure 6.4c), the correlation matrix shows a high positive correlation with the Fe_2O_3, P_2O_5 and TiO_2 chemical elements, and high negative correlation with the SiO_2 and a moderate one with the K_2O. The positively correlated elements show their highest percentage in the alkaline dacite which also shows the lowest percentage regarding the SiO_2 element (53.2%). The low signal to noise ratio in this image reduces its usefulness. The amount of information that could be extracted from the fourth canonical image was again rather low but it did show the rock areas as dark and the sediments and vegetation as very bright

(Figure 6.4d). The fifth canonical image is visually degraded with low signal to noise ratio which looks as the negative of the fourth canonical image except for the vegetation which shows high values (Figure 6.4e).

A colour composite from the first three canonical images was made (Figure 6.5), where the first canonical image was displayed as red, the second as green, and the third as blue. From this colour composite image areas that are high in SiO_2 and K_2O are shown as red whereas areas that are high in the Fe_2O_3, MgO, CaO, TiO_2 and P_2O_5 are shown as cyan and blue.

Although this canonical transformation was applied to different areas to test its capability, only one test area showed interpretable results. However, it can be concluded that results obtained from this study are encouraging and the application of canonical regression with the methodology described here have some potential in combining Landsat TM-data with geochemical data.

Experience gained from the present study shows that the combination of data of widely different origin was a cumbersome and lengthy procedure, but by using the right data, it may turn out to be very useful in geochemical studies and mineral exploration. Therefore, further study needs to be made to fully justify the applicability of this technique by using, for example, data that are acquired by a higher spectral resolution system where there will be more spectral bands with a narrower band width, such as the Airborn Imaging Spectrometer (AIS). The AIS records data in 128 spectral bands with spectral resolution of 9.3 nm, and spectral coverage of 1.2-2.4 μm. Another system is the Airborn Visible and Infrared Imaging Spectrometer (AVIRIS) that collects data in 210 spectral bands in the spectral regions 0.4-2.4 μm with spectral resolution 9.8 nm, IFOV of 20m and swathe width of 11 km (Kingston and Crowley, 1989). Another

possibility is the High Resolution Imaging Spectrometer (HIRIS) which has a similar capability to AVIRIS, but covers three times larger swathe, and has 2-5 times greater radiometric sensitivity, with 129 channels covering the spectral range between 0.4 μm to 2.5 μm (Goetz, 1989). With the extra spectral information provided by these systems, it may be possible to create a data set that does contain enough components to reveal the chemistry of the rocks directly.

6.3.1.3 Band colour composite and HSI transformation enhancement

Figure (6.6) shows a colour composite of TM band-7 displayed as red, TM band-4 displayed as green, and TM band-1 displayed as blue. These three bands were stretched using a BCET technique (described earlier in section 5.3.3). Although this colour composite displays reasonable discrimination between different lithologies available in this test area, this enhanced image did not exploit fully the RGB colour space, due to the high degree of correlation that exists between the TM bands (Table 6.1a).

By transforming the image in Figure (6.6) from the RGB to the HSI coordinates and then using the manipulation, described earlier in section 6.2.5, for the saturation and intensity components, and then transforming the image back to RGB components, the end product was the image shown in Figure (6.7). It can be seen that the new image (Figure 6.7) has been enhanced spectrally as well as spatially. Lithological units having similar colour and texture can be clearly recognised, and dicriminated over the whole image. By comparing this image with the detailed geologic map that was produced by Du Bray (1988) as reference, the excellent degree of separability between rock types is obvious, and almost identical to the detailed geological map. Furthermore, the increase of intensity enhances

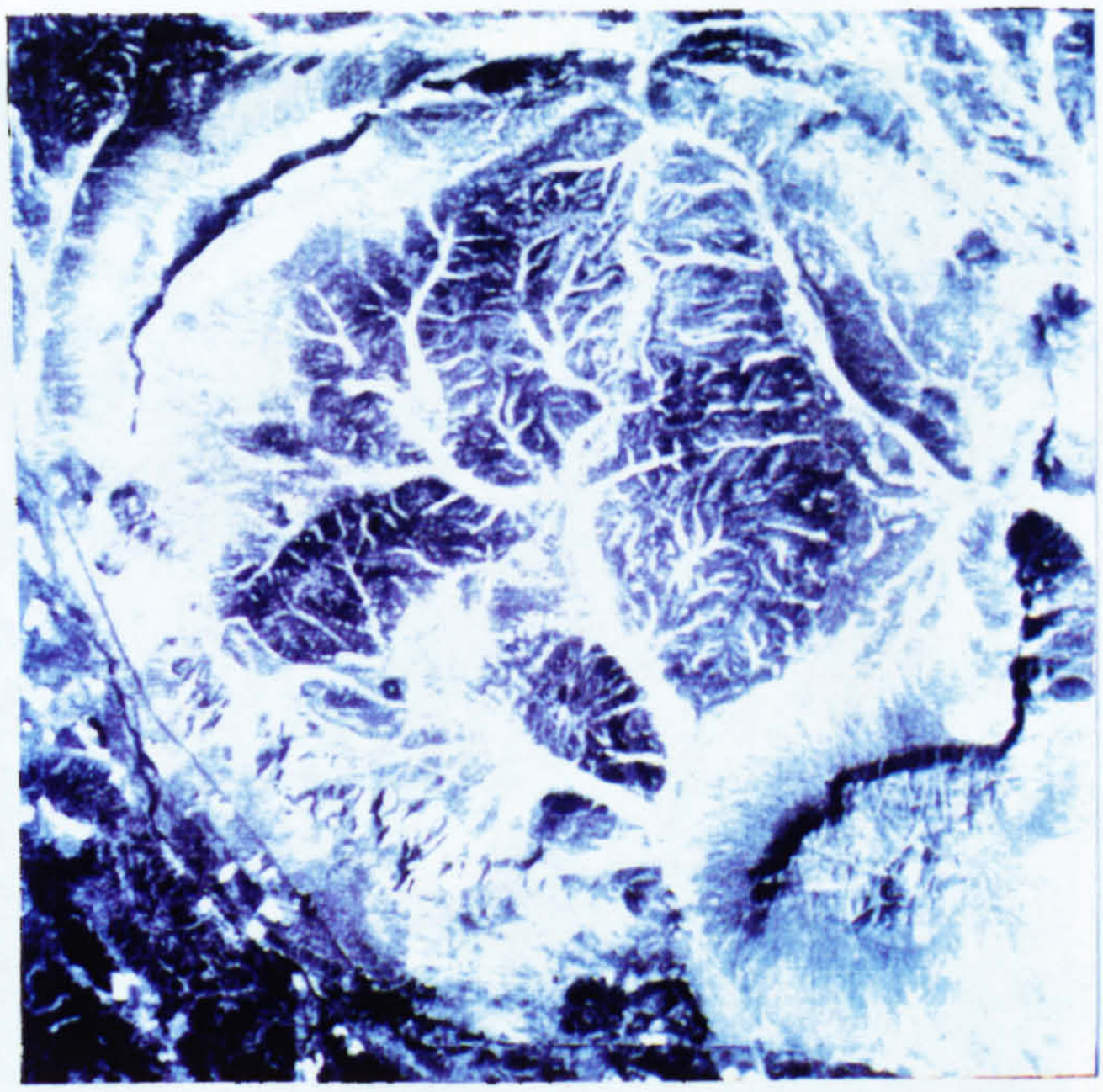

(a) First canonical component

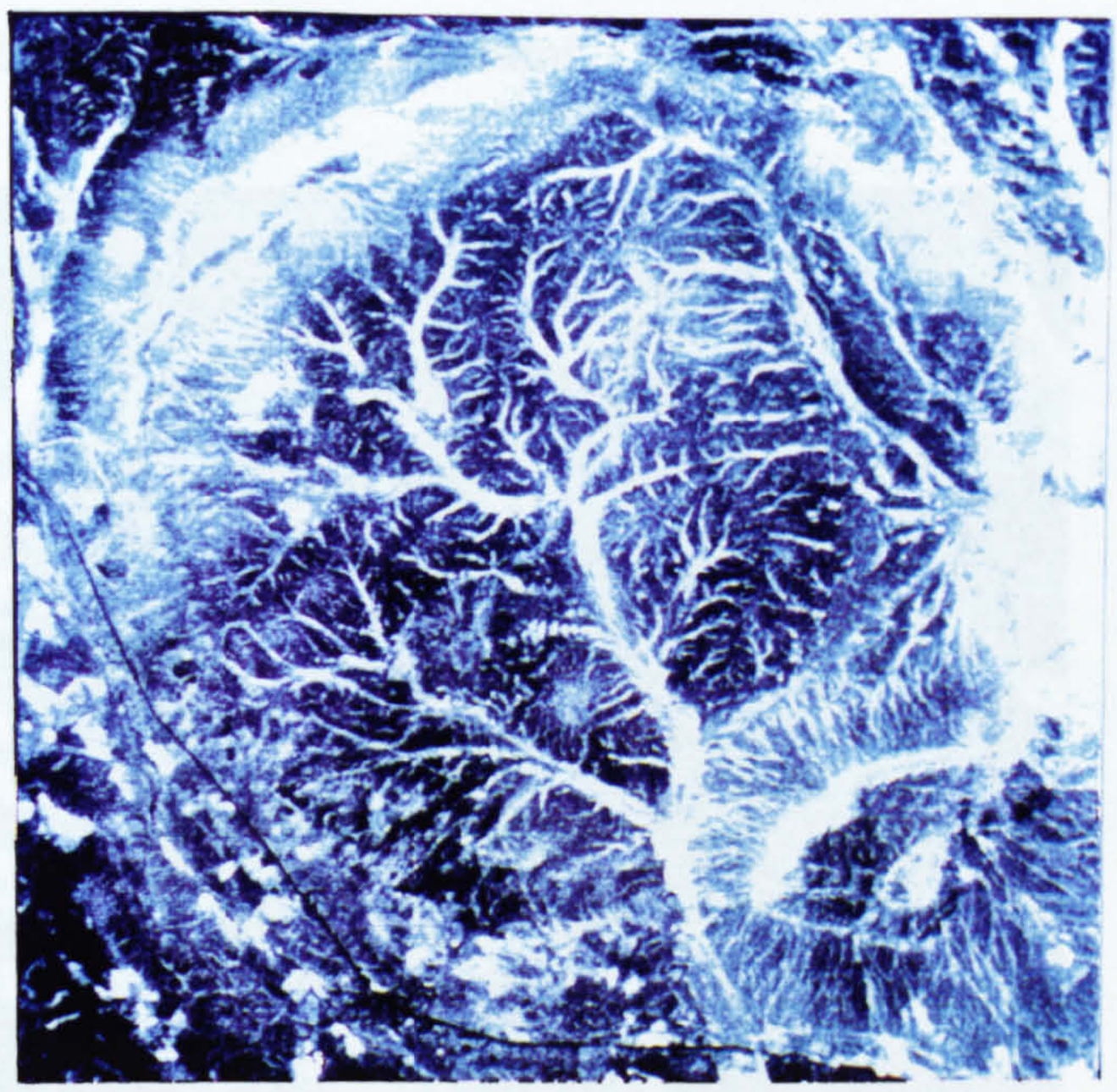

(b) Second canonical component

Figure 6.4: Images (a) - (e) represent the gray level images of the individual canonical components of Silsilah ring complex.

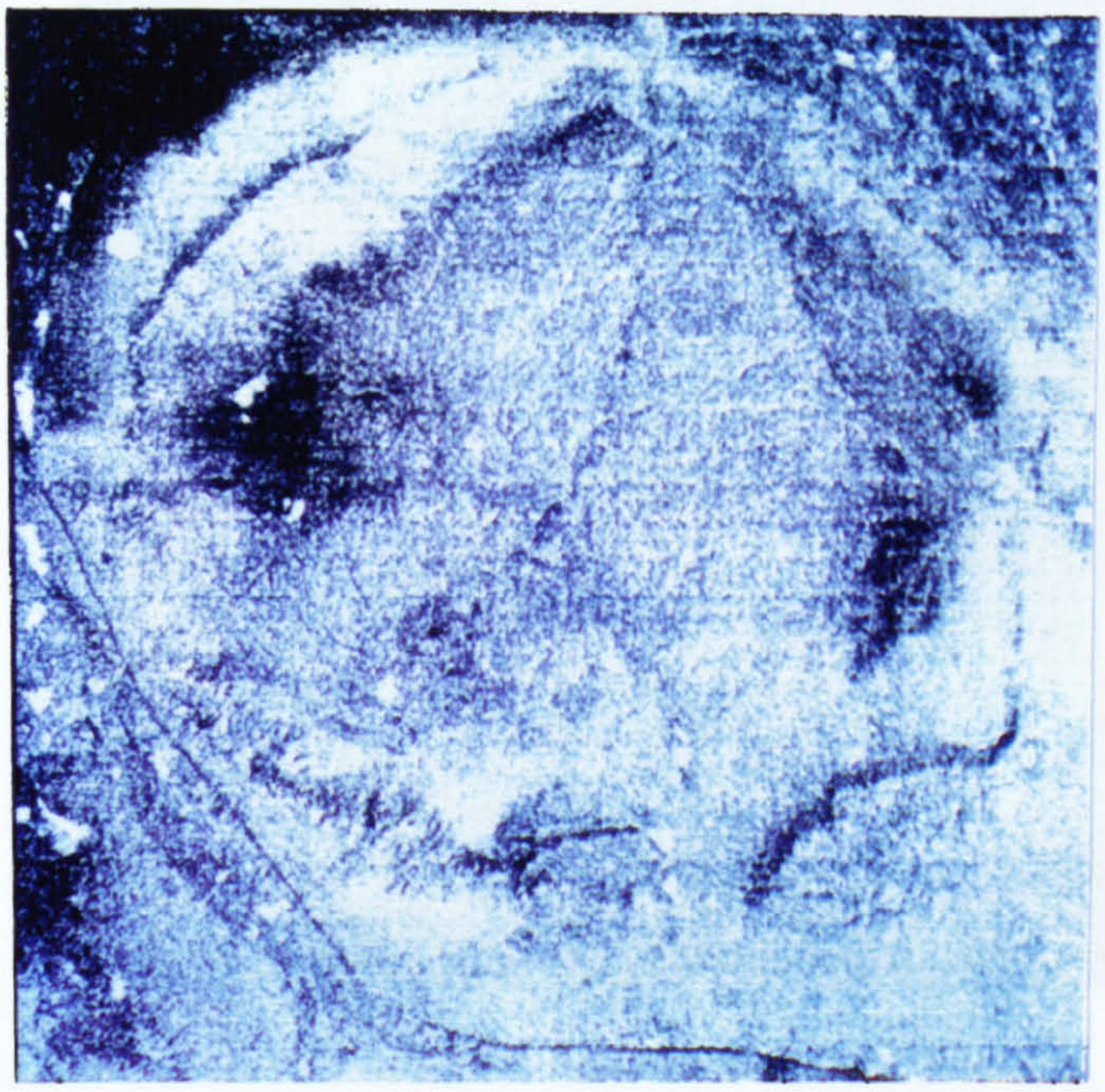

(c) Third canonical component

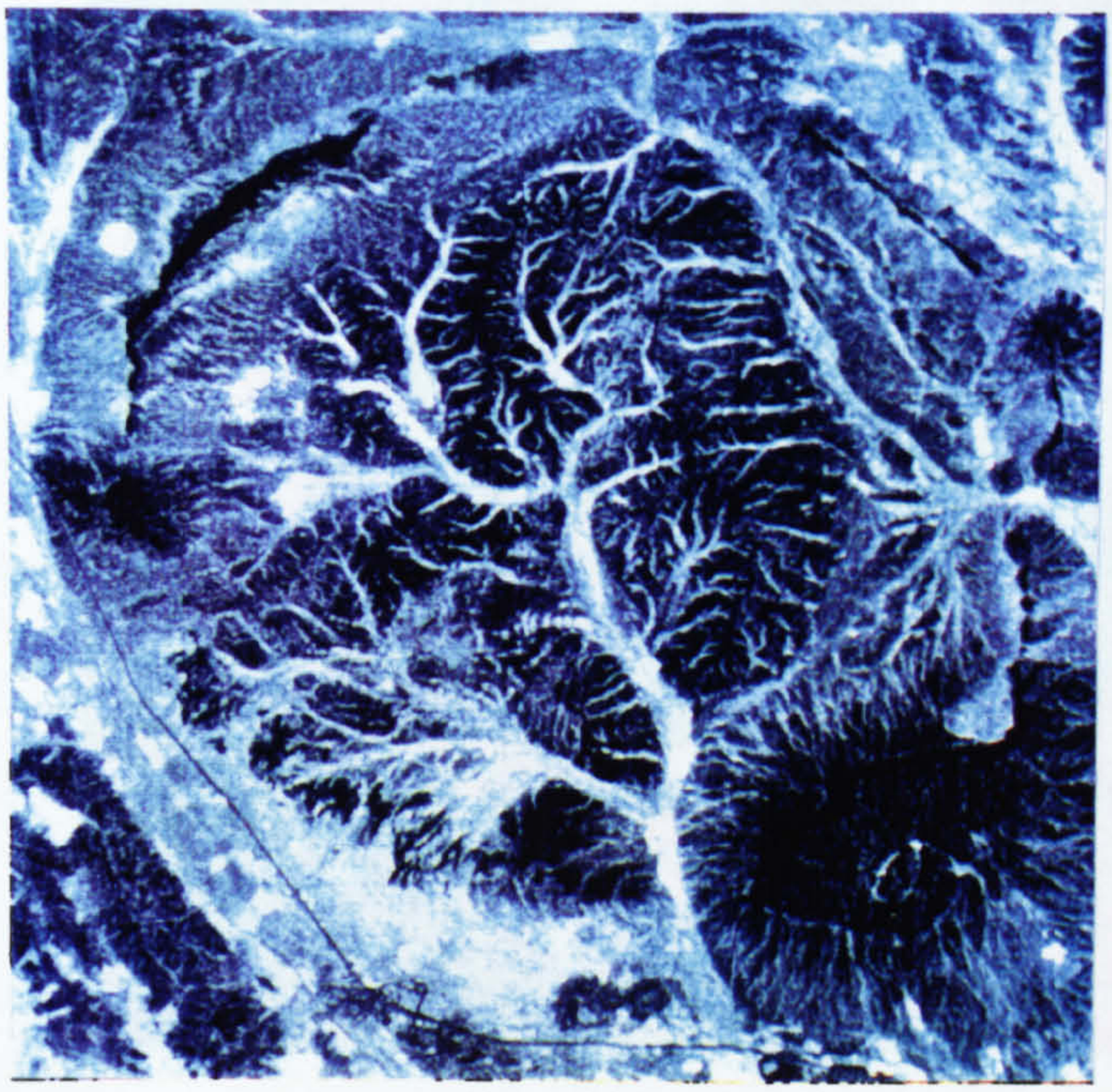

(d) Fourth canonical component

Figure 6.4: (Continued)

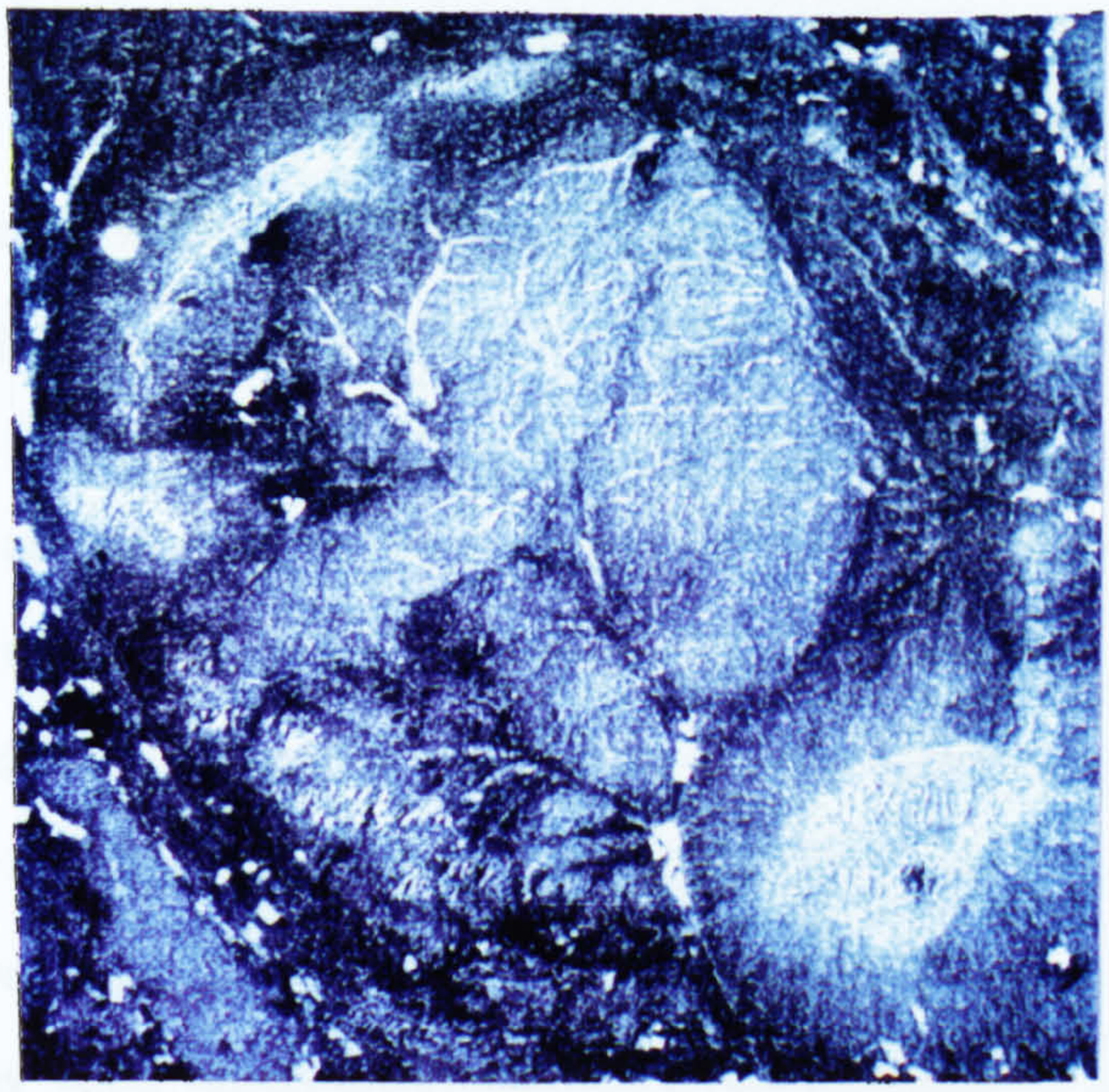

(e) Fifth canonical component

Figure 6.4: (Continued)

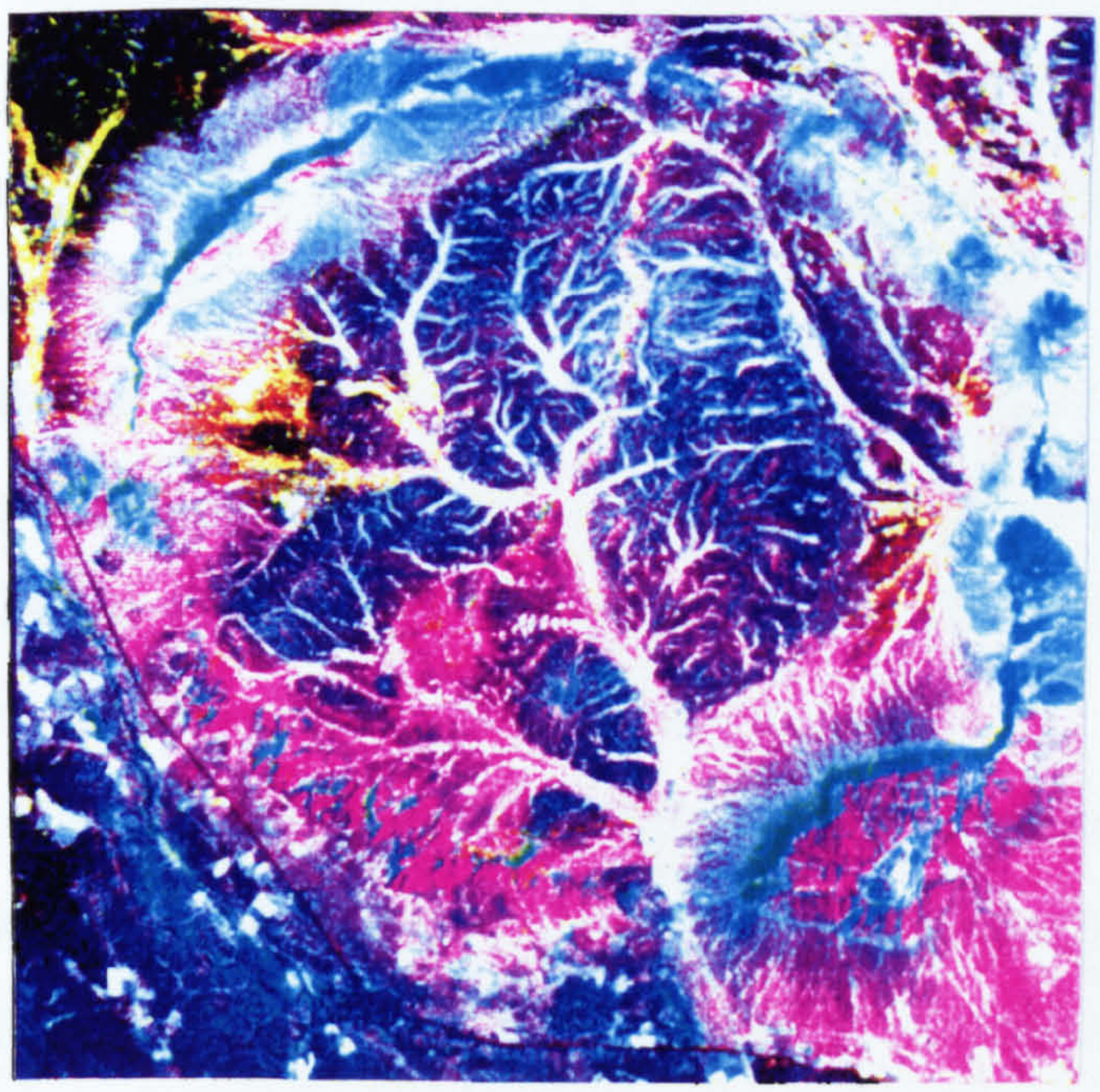

Figure 6.5: Canonical component colour composite of Silsilah ring complex in which canonical components 1, 2 and 3 were displayed as red, green and blue respectively.

the colour for the areas of low albedo (e.g., alkaline dacite). In addition, the sharpening filter that was used, has enhanced the rock texture, the drainage structure and the sharp contact between rock types. This image displays all the geologically relevant information in greater detail than any other composite.

The alkaline dacite, (see Figure 2.5 for rock unit locations) like all the ultramafic rocks, has a very low reflectance in the IR (TM band-7 and TM band-4) and slightly higher reflectance in the visible region (TM band-1) and therefore it appears as a blue colour. The lithic greywacke, in the area inside the ring complex, can be easily discriminated by its structure (where it has been cut by well developed dendritic drainage) or by its bluish magenta colour, caused by the abundance of clay minerals that cause absorption in the infrared band (TM band-7). The presence of ferruginous materials, in some areas, is indicated by the magenta colour, due to absorption by TM band-4. However, this unit appears more bluish in the northwest and southwest corners of the image, where there may be more clay minerals.

Fawwarah alkali feldspar granite can be discriminated by its slightly pinkish white colour, caused by high reflectivity of all TM bands, and this can be attributed to the fact that felsic rocks are highly reflective in all TM bands, exactly the opposite of mafic rocks (alkaline dacite). The presence of trace amounts of a very light brown Fe-Li mica (Du Bray, 1988) in this unit may have caused the slightly pinkish white colour.

The Silsilah alkali granite (Sag) can be divided into three types according to its appearance in this image: a) the highly jointed alkali granite at Jabal al Hadhir; b) recrystallised, fine grained and altered alkali granite at

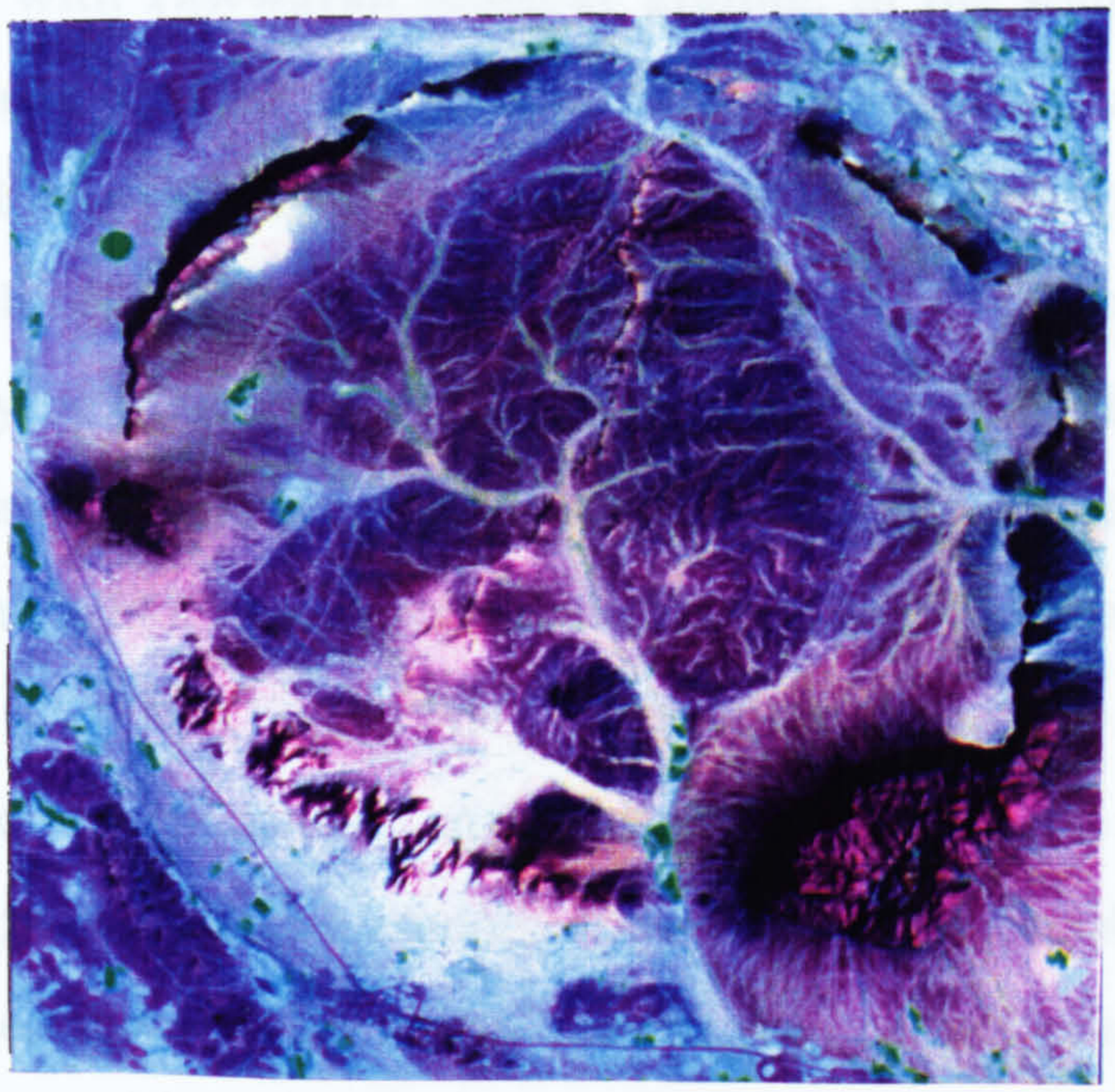

Figure 6.6: Band colour composite (BCC) image of Silsilah ring complex in which TM band-7, TM band-4 and TM band-1 were displayed as red, green and blue respectively.

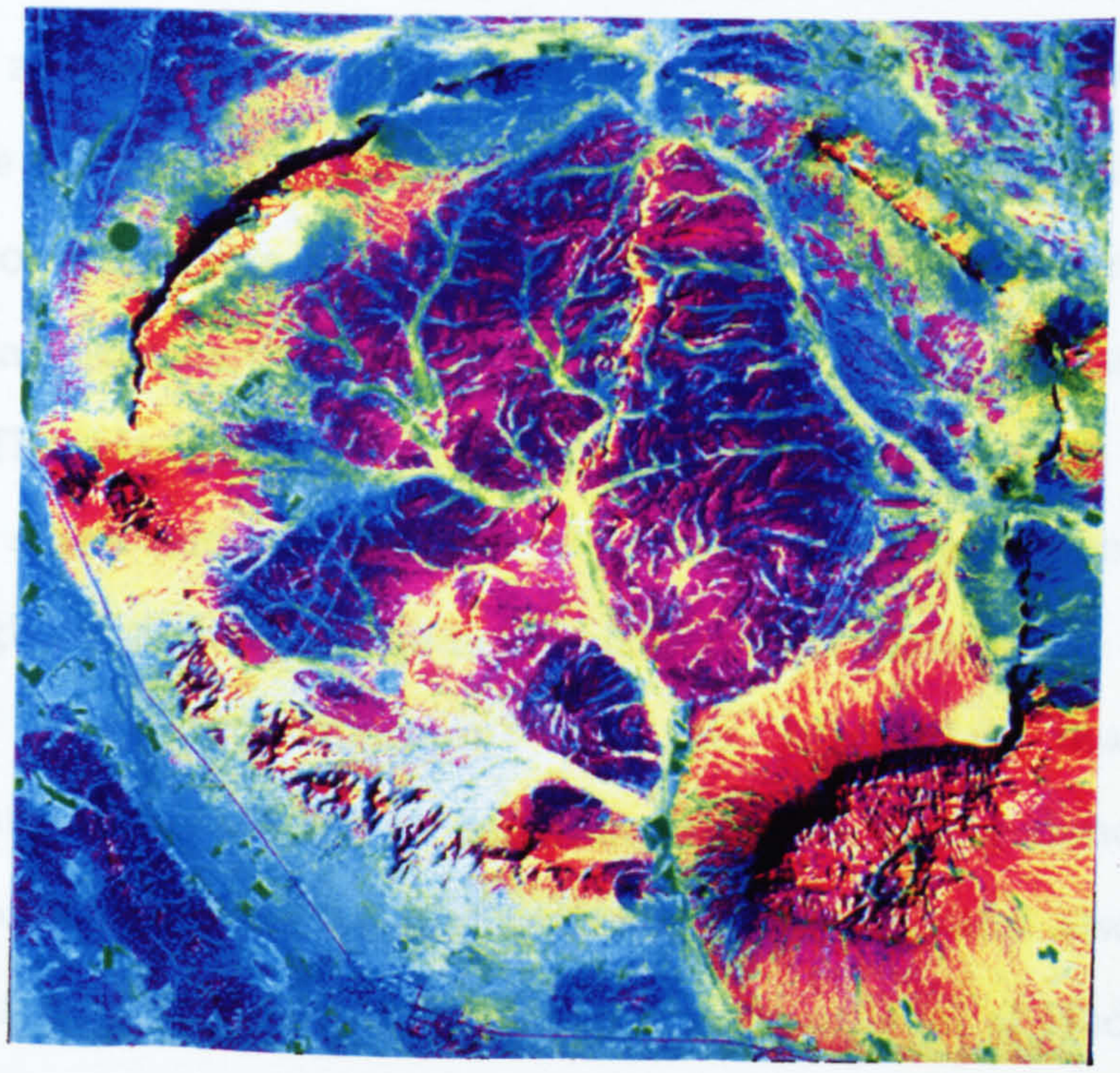

Figure 6.7: The colour composite image of Figure 6.6 after hue-saturation-intensity enhancement.

the contact with Fawwarah feldspar granite, in the southern part of the ring; and c) a smooth alkali granite in the north western part of the ring.

The highly jointed areas of Jabal al Hadhir are bluish red in colour due to the fall off in reflectance in TM bands 4 and 1 compared to TM band 7, which may be caused by the presence of iron oxides. The second type of the alkali granite (recrystallised) appears as a small unit at the contact with the Fawwarah alkali feldspar granite (Fag), with a degree of brightness in between the (Fag) and (Sag). The reduction in the amount of Fe oxides, and the increase of quartz content, may cause this type to have a brighter colour. The third type which has a smooth appearance in the north western part of the ring varied from bluish red to bluish green colour, possibly attributable to the presence of hydroxyl bearing minerals which cause a reduction in reflectivity of TM band-7.

For the commendite unit, the alteration of anorthoclase to sericite causes an absorption to band 7, which gives this rock the bluish green appearance in the slightly weathered areas. The commendite dike, inside the ring complex, has a reddish yellow colour, caused mainly by iron staining that reduces the reflectivity sharply in TM band-1, and also in TM band-4. The Hadhir aplite appears as light brown cap rock over the Fawwarah alkali feldspar granite. Vegetation has a green colour due to its distinct high reflectivity in the near infrared (TM band-4).

The edge enhancement of the intensity, made prior to transformation back to RGB coordinates, enhances the dendritic drainage structure which cuts the Maraghan lithic greywacke and also enhances the joints that are cutting the Silsilah alkali granite at Jabal al Hadhir.

6.3.2 Jabal ar Raha (test area 2)

6.3.2.1 Principal component and band ratio analysis

The TM bands in this test area exhibit a higher degree of correlation compared to the previous test area (Silsilah ring complex) as can be recognised in Table 6.5a. After applying the PC transformation for this area, as was expected from such a high degree of correlation, the first principal component axis mapped more variance than in the previous test area (Table 6.5b) and accounted for 97.03% of the total variance in the six reflected TM bands. The rest of the variance (2.97%) was mapped in the other five PC images. The loading factor for the contribution of each band to a component (eigenvector) is shown in Table (6.5b) and is very similar to the previous test area.

By examining each of the principal component images individually and as colour composites it was found that the best three PC images that can be displayed as PCC image was PC3 displayed as red, PC2 displayed as green, and PC1 displayed as blue (Figure 6.8). This is the same as was found for the first test area. These three components account for 99.41% of the total variance available in the six reflected TM bands acquired for this test area.

For the band ratio colour composite, the same procedure as described earlier led to the selection of TM 5/4 band ratio image to be displayed as red, TM 5/1 band ratio image to be displayed as green, and TM 5/7 band ratio image to be displayed as blue.

Table (6.6) shows the different colours associated with different lithologies found for this test area. In the colour ratio composite (Figure 6.9).

COR MATRIX	B1	B2	B3	B4	B5	B7
B1	1.00					
B2	0.97	1.00				
B3	0.94	0.99	1.00			
B4	0.93	0.97	0.99	1.00		
B5	0.90	0.95	0.97	0.98	1.00	
B7	0.88	0.94	0.96	0.96	0.98	1.00

(a)

COMPONENT	C1	C2	C3	C4	C5	C6
% var.	97.03	1.83	0.55	0.28	0.26	0.06
eigenval.	1977.07	37.24	11.25	5.62	5.28	1.16
B1	0.264	-0.702	0.054	0.568	-0.188	-0.272
B2	0.227	-0.301	0.051	-0.096	-0.143	0.908
B3	0.424	-0.261	0.084	-0.763	-0.246	-0.318
B4	0.388	-0.139	-0.120	-0.041	0.901	0.001
B5	0.616	0.433	-0.562	0.215	-0.263	0.002
B6	0.409	0.373	0.809	0.191	-0.001	-0.004

(b)

Table 6.5. See next page.

LOADING	C1	C2	C3	C4	C5	C6
B1	0.929	-0.338	0.014	0.106	-0.034	-0.023
B2	0.978	-0.177	0.016	-0.022	-0.031	0.094
B3	0.994	-0.084	0.014	-0.095	-0.029	-0.018
B4	0.990	-0.048	-0.023	-0.005	0.118	0.000
B5	0.991	0.095	-0.068	0.018	-0.021	0.000
B7	0.983	0.123	0.146	0.024	-0.000	-0.000

(c)

Table 6.5. Statistics of Jabal ar Raha test area where table (a) describes the correlation coefficient between the 6 TM reflected bands. Table (b) describes the variance, eigenvalues and eigenvectors for each principal component in which the percentage variance indicates the amount of variance that was picked by each component, and the table gives the relative loading of each band in each component. Table (c) gives the component loading summary.

The meta-andesite (ma) at location (A) in this figure appears as a dark blue colour (low values in TM 5/1 and TM 5/4 band ratios). This may be due to the presence of opaque oxides as accessory minerals and the low amount of iron oxides, or the presence of sericite and chlorite as alteration products, that cause a higher value in the TM 5/7 band. This unit appears in the PCC image as reddish brown. The units, that were mapped as meta-andesite at (B), are slightly different in the CRC image, which may be due to the presence of a number of rhyolite dikes that cut this unit, and were observed during the field visit to this area.

A similar colour was also found inside the conglomerate (cg) unit, which was not mapped previously, and could be of an andesitic composition. The conglomerate unit, that appears in the CRC image as magenta colour (mixture of red and blue), has a mixed composition (as described in chapter 2) of andesite as well as argillite and metamorphic epidote, which may account for its colour. This unit can be discriminated by its light brown colour in the PCC image.

The conglomerate is bounded to the west by the Qarnayn lithic greywacke which appears as an orange colour (mixture of red and green, with higher values in the red). The contact between these two units is gradational and complex as can be seen clearly in the colour ratio composite and was described in chapter 2. In the PCC image the Qarnayn lithic greywacke appears as greenish yellow and its gradational contact with the conglomerate can also be noticed.

South of this unit (in the southern half of the image) is a V shape unit of Raha meta-rhyolite that has bright colour in the CRC image (high values in both TM 5/4 and TM 5/1 band ratios), which may be due to the presence of Fe bearing minerals, whereas in the PCC image this unit has a

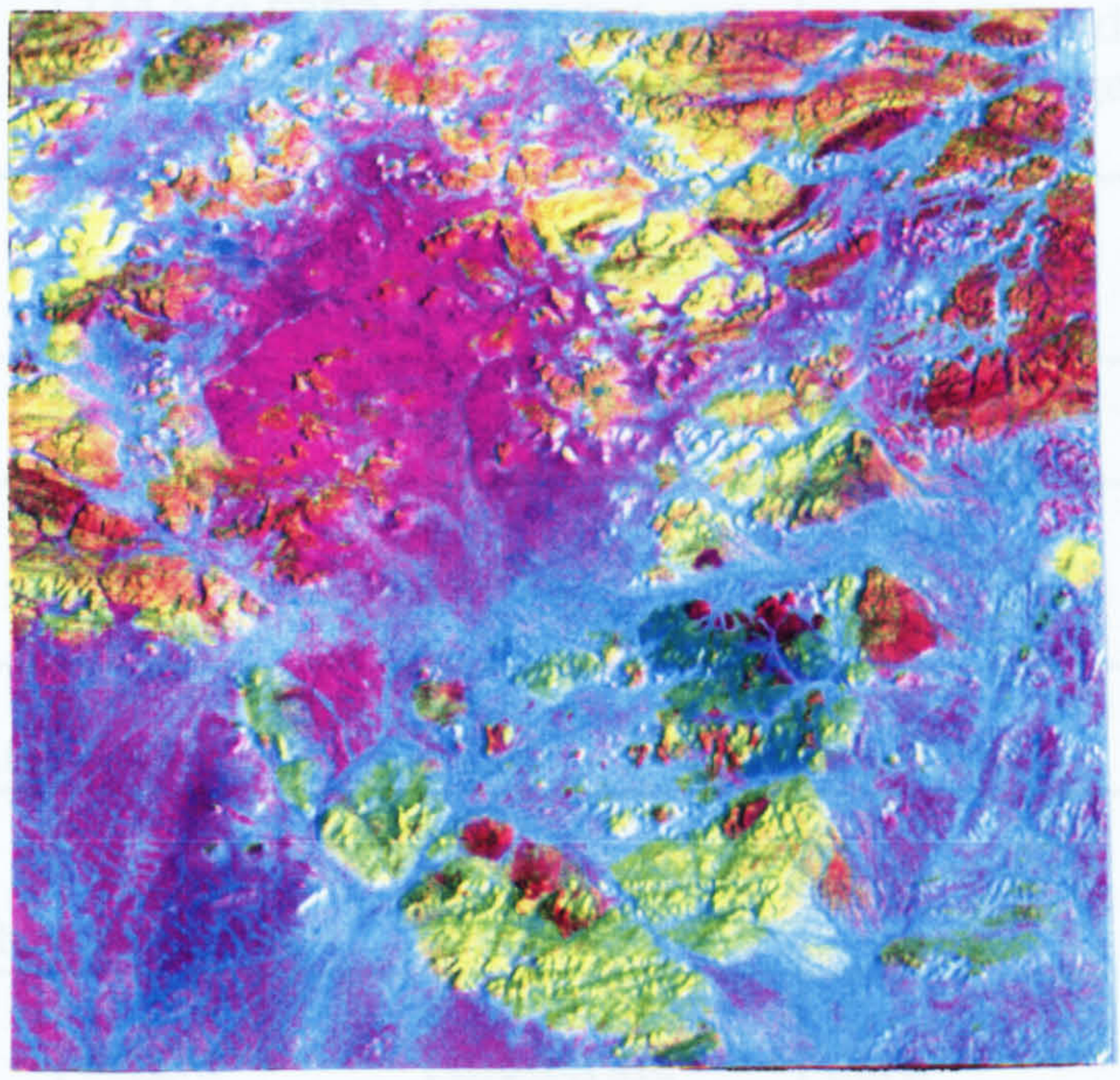

Figure 6.8: Principal component colour composite (PCC) image resulting from the principal component transformation of the six reflected TM bands of Jubal ar Raha in which PC3, PC2 and PC1 were displayed as red, green and blue respectively.

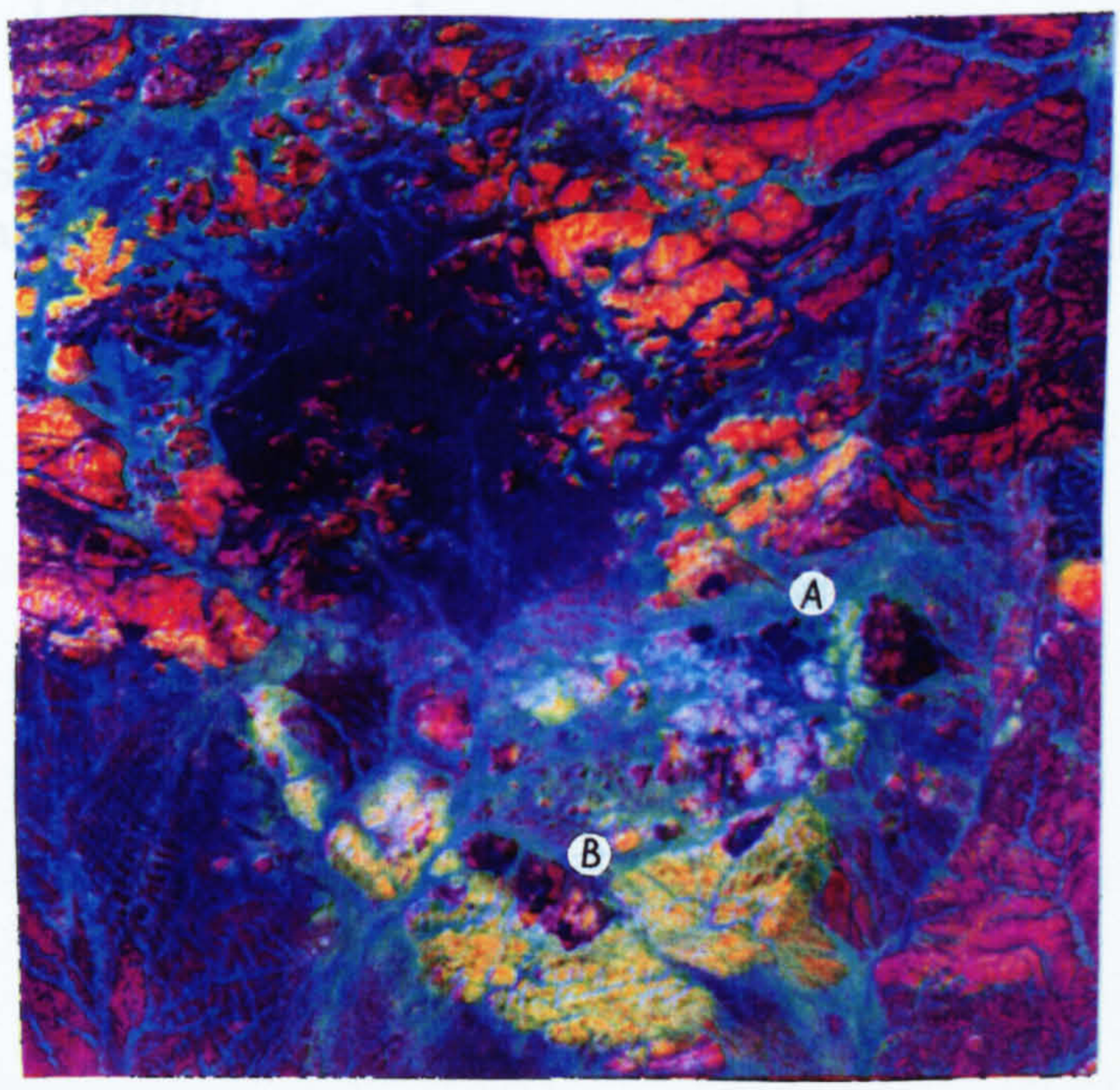

Figure 6.9: Colour ratio composite (CRC) image of Jabal ar Raha in which TM 5/4, TM 5/1 and TM 5/7 band ratios were displayed as red, green and blue respectively.

	TM 5/4 band ratio image (red)	TM 5/1 band ratio image (blue)	TM 5/7 band ratio image (green)	Colour Composite
Conglomte.	moderate-bright	dark	moderate	magenta
Carbonates	dark	dark	moderate	blue
Andisitic rocks	dark	dark	moderate	blue
Meta-andesite	dark	dark	moderate	blue
Raha meta-rhyolite	bright-moderate	bright	dark	yellow
Qarnayn lithic graywacke	bright	moderate	dark	orange
Meta gabbro	bright	moderate	dark	orange
Meta-rhyolite tuff	moderate-bright	bright	bright	cyan white

Table 6.6. Summary of colour associated with main lithologies in the CRC image of Jabal ar Raha (Figure 6.9).

yellowish green colour that looks slightly similar to Qarnayn lithic greywacke. Bounded to this unit is the metarhyolite tuff that can be distinguished by its bluish bright colour in the CRC image. Also the contact between this unit and the meta-andesite is clearly seen in the image. In the PCC image, this unit is more clearly observed by its green colour, and its contact with the meta-andesite can also be observed, but not as sharp as in the CRC.

The small carbonate unit to the north cannot be easily distinguished from the meta-andesite in both the PCC and CRC images. Also the meta gabbro cannot be discriminated from the Qarnayn lithic greywacke (qlg) which has the same orange colour; also the Shaila quartz monzodiorite cannot be discriminated from part of the (qlg), which has the same colour in both images.

6.3.3 Band colour composite and HSI transformation enhancement

Figure 6.10 shows a TM colour composite of band 7 displayed as red, band 4 displayed as green, and band 1 displayed as blue. These bands were stretched using a balance contrast enhancement technique. In this colour composite, although there is a reasonable discrimination between different lithologies, this image did not use the full RGB colour space, due to the reasons described earlier in section 6.2.5. By transforming these data from RGB coordinates to HSI coordinates, and using the manipulations that were described earlier in section 6.2.5, and then transforming the data back to the RGB coordinates for display, the colour composite image of Figure 6.11 was produced.

In this figure the improvement in the spectral as well as textural and structural information is very obvious, and the image becomes much easier

to interpret. The degree of colour separability between rock types has improved sharply, with more saturated colours, and shows more differentiation than can be predicted from the geologic map that was made by Du Bray (1983), and used here as reference. The sharp contact between some rock types is shown in greater detail, due to the replacement of the intensity by an edge-enhanced (sharpened) first principal component. An enlarged area of this image is shown in Figure 6.12 to demonstrate the HSI transform effect more clearly. For information about the location of various lithological units, consult the Geologic map in Figure (2.7).

In Figure 6.11, the Raha meta-rhyolite appears orange and this is caused by absorption, due to the presence of iron oxides in this unit. The meta-rhyolite tuff appears as green and this may be due to the presence of hydroxyl minerals, caused by hydrothermal alteration, and also due to the presence of iron oxides, that cause an absorption in the visible range of the electromagnetic spectrum (TM band 1). The variation in colour to the western part of this unit may be due to the presence of rhyolite dikes cutting this area.

The meta-andesite unit north of the meta-rhyolite tuff can be distinguished by its blue colour, indicating lower reflectance in TM band-7, that may be due to the presence of hydroxyl, caused by sericitisation of plagioclose, and also by some alteration of the hornblende to chlorite (Chapter 2), which leads to absorption of band-7, whereas absorption of band-4 may be due to the presence of hornblende (Hunt et al., 1973).

In the conglomerate (Cg) unit, the absorption in band-7 caused by the presence of argillite (mixture of clay minerals) as an alteration product and the absorption in band-4 caused by the presence of epidote (Hunt, 1973), gives this unit a dark blue appearance. The stretched pebble conglomerate

(spc) that appears as a blue lens inside the qlg unit was described by Du Bray (1983) as lithologically similar to the conglomerate east of the test area (Chapter 2), and it has also the same colour in Figure 6.11. The meta-andesite at (A) appear as bluish green. This may be due to the absorption in band-7 by hydroxyls formed during alteration, combined with a slight fall off to the blue (band-1), due possibly to ferric oxides; similar samples were described by Hunt et al. (1973). The meta-andesite unit at (B) was cut by a number of rhyolite dikes and numerous small quartz veins. These were observed during the field visit. The Qarnayn lithic greywacke unit appeared as red colour due to absorption in bands-1 and -4 which may be caused by the presence of iron oxides from the alteration of magnetite, which accounts for 5% of this unit (Du Bray, 1982).

The Shaila quartz monzodiorite (Sqm), although similar in colour to the conglomerate (Cg), could be discriminated by its more grayish blue colour and its textural differences, whereas the meta-andesite is more blue in colour than this unit. The flat area around the (Sqm) unit is distinctly different in its appearance in Landsat TM bands; it appears as bright in band-1 and decreases in its reflectivity gradually and reaches its minimum in Landsat TM infrared bands-5, -7. In the colour composite of Figure (6.11), it appears as blue which is probably due to the presence of hydroxyls. The strong red colour of the meta-gabbro exhibits some spectral features, described by Hunt et al. (1974) for Gabbro samples, in which the presence of iron oxides produced a strong fall in reflectance in both TM band-1 and TM band-4, and this may have caused its strong red colour. However, this rock cannot be discriminated in this area from Qarnayn lithic greywacke. The massive marble could be discriminated by its cyan colour (C) (absorption of band-7) caused by the carbonate minerals.

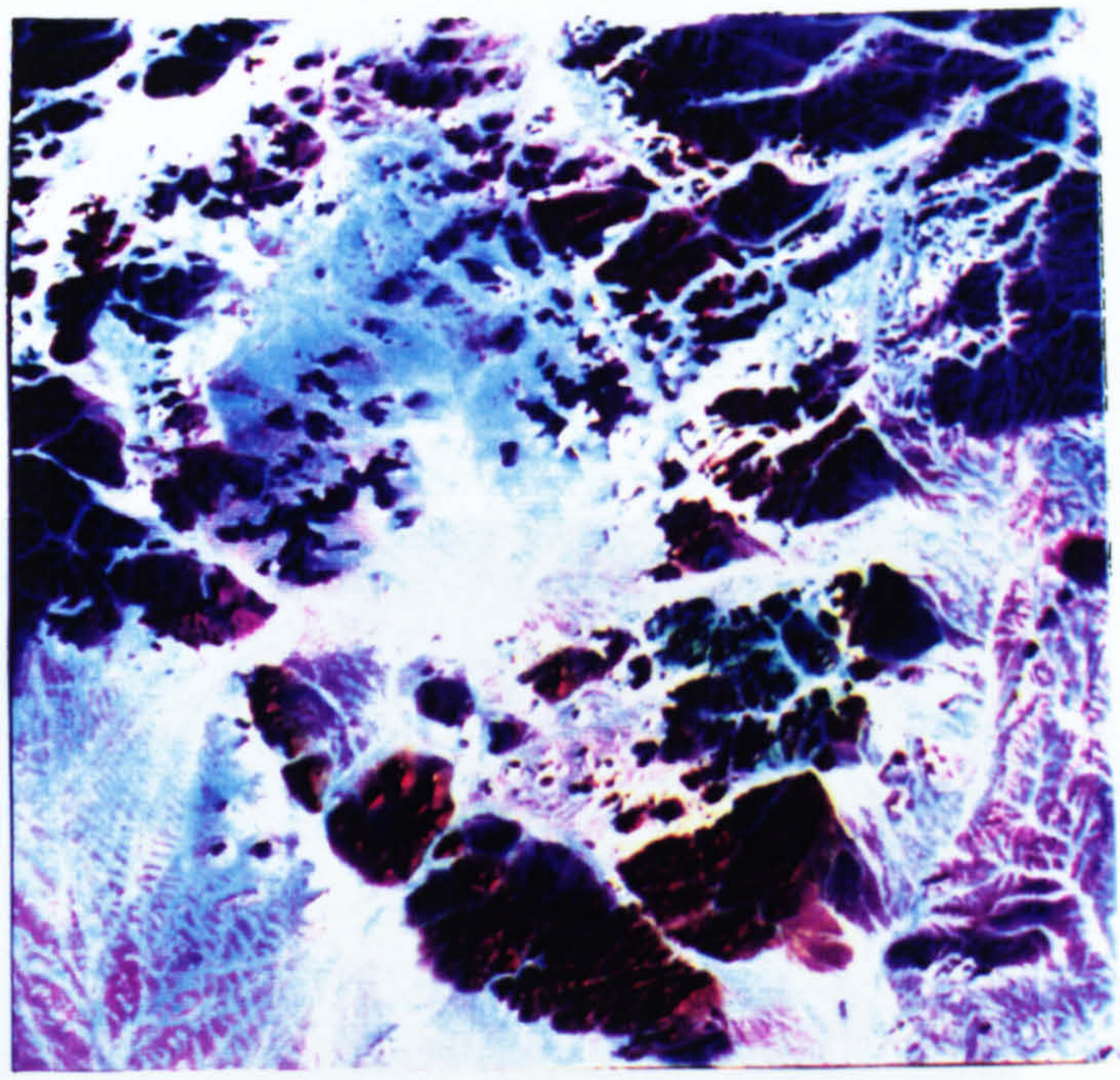

Figure 6.10: Colour composite image of Jabal ar Raha in which TM band-7, TM band-4 and TM band-1 were displayed as red, green and blue respectively.

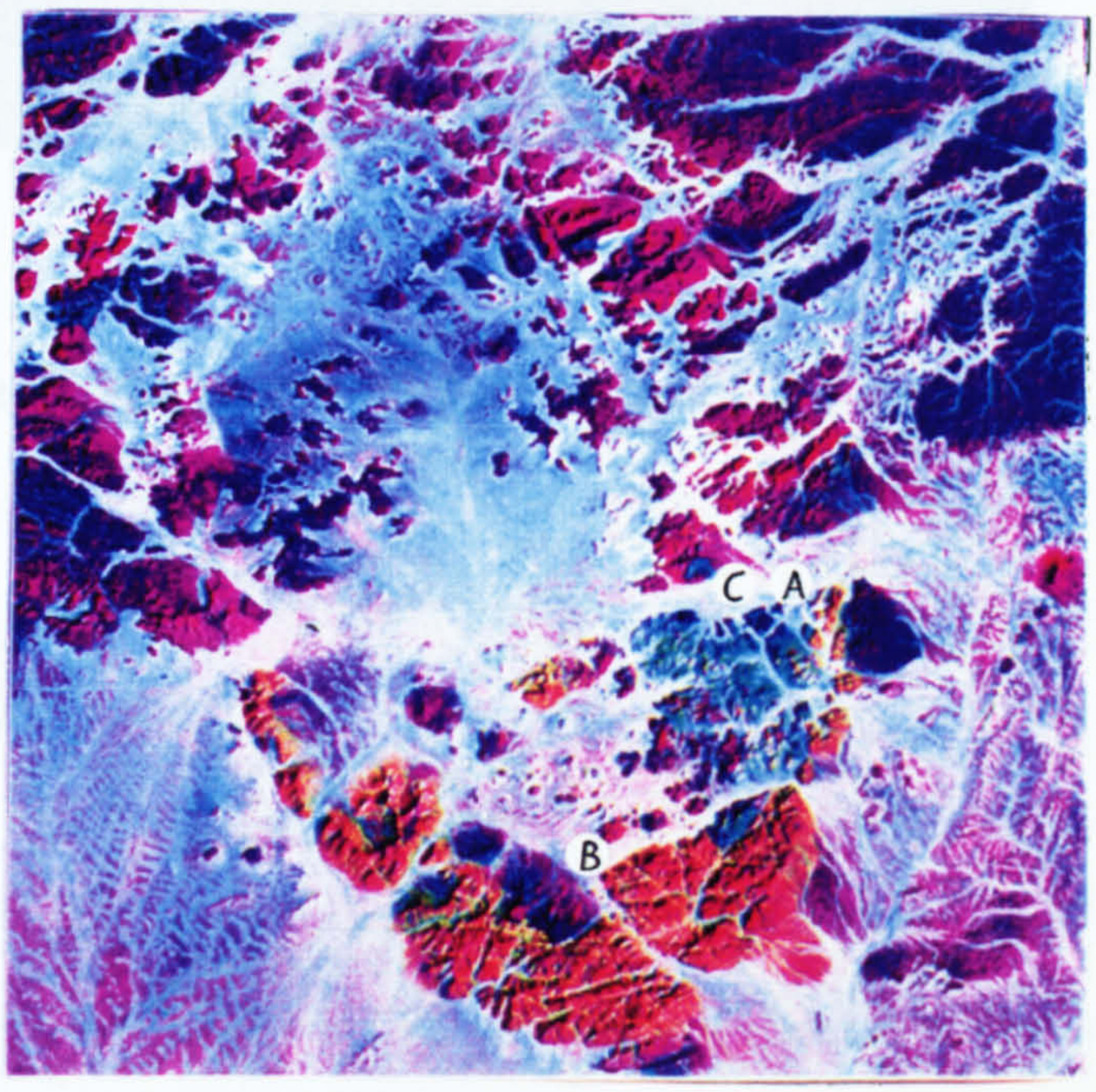

Figure 6.11: The colour composite image of Figure 6.10 after hue-saturation-intensity enhancement.

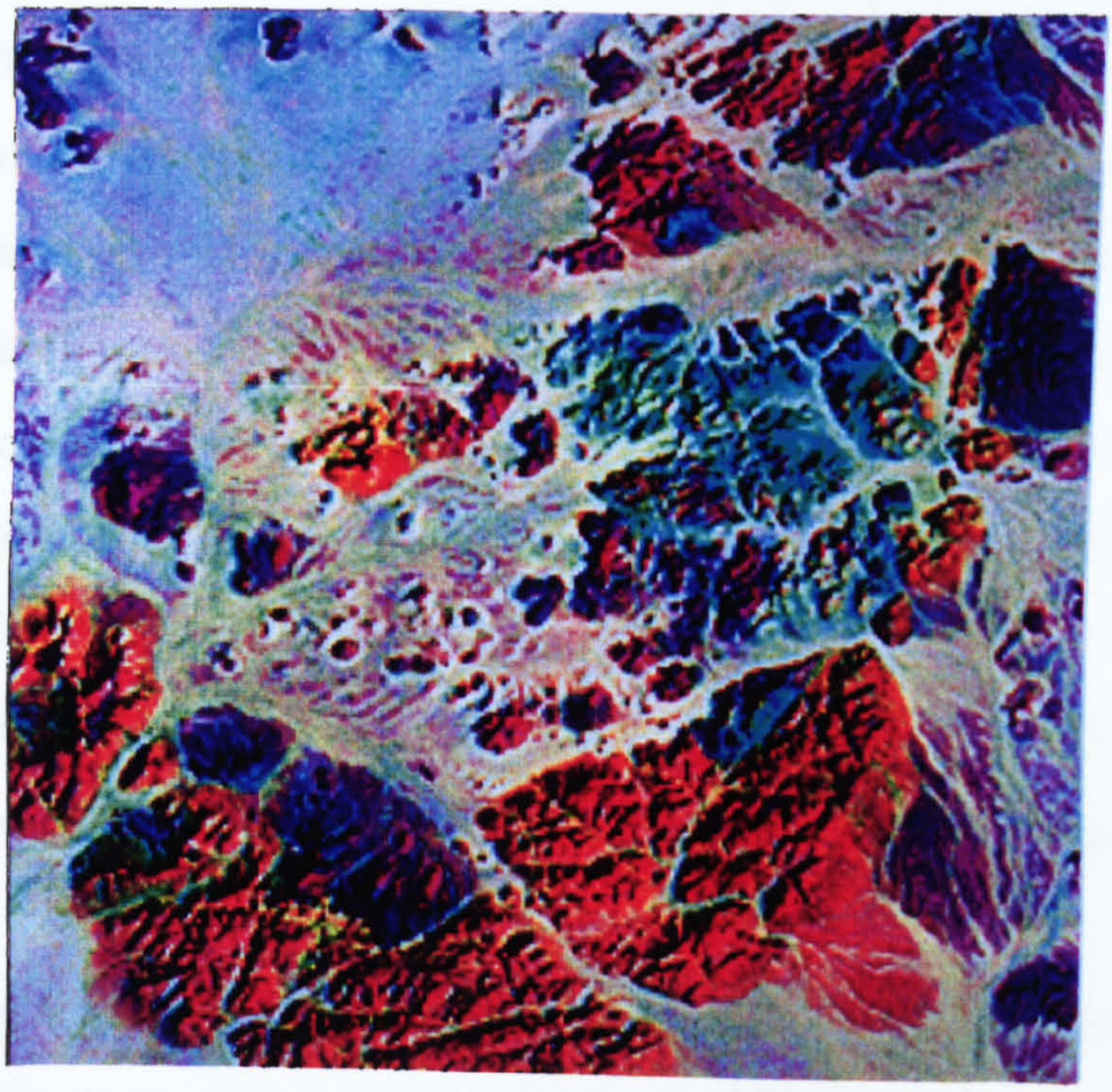

Figure 6.12: An enlarged (zoom in) part of image in Figure 6.11.

6.3.3 Aban Ahmar

6.3.3.1 Principal component and band ratio analysis

The degree of correlation between the reflected TM bands in this area (Table 6.7a) is again high (as in the previous test area). Table (6.7b) shows the percentage distribution of the total variance as mapped (after the PC transformation) for the six principal components in which 97.27% of the total variance was mapped by the first principal component axis, and progressively lower variance was mapped by each higher order principal component which also progressively had a higher noise component. The eigenvectors are shown in Table 6.7b, which also shows a similar response as in the previous two areas, especially the first three PCs in test area two.

The three best PC bands were displayed as before: PC3 as red, PC2 as green and PC1 as blue. These account for 99.43% of the total variance available in the six reflected TM bands acquired for this test area (Figure 6.13).

By applying the ratio enhancement to this test area, only six of the possible ratio images of the six reflected TM bands show a good variation betwen rock types. This include TM band ratio images 5/7, 5/1, 4/1, 4/2, 3/1 and 5/4. From these ratios, various colour ratio composites were produced. The colour ratio composite, which were chosen as the best to provide discrimination between the available lithologies, were the TM band 5/4 ratio image displayed as red, TM band 5/1 ratio image displayed as green, and TM band 5/7 ratio image displayed as blue (Figure 6.14 and Table 6.8).

In this image various lithologies can be discriminated (consult Figure 2.8 for their location), such as the perthite granite member (apg) which appears a yellowish green colour. This may be due to the relatively higher percentage of iron bearing aluminosilicate in this rock, such as biotite,

which accounts for up to 7% of the rock (Cole, 1988), and also the presence of iron oxides. These constituents may be responsible for its moderate value in TM 5/4 band ratio, and higher values in TM 5/1 band ratio that were displayed as red and green respectively, compared to the low values in TM 5/7 band ratio that was displayed as blue. This unit becomes more greenish toward the south, which may be due to the increase of the amount of the iron bearing aluminosilicate that increases the TM 5/4 ratio values displayed as green. In the PCC image, this unit has almost the same colour as in the CRC, but becomes more yellow towards the south.

In the arfvedsonite granite (aag) the presence of iron bearing aluminosilicate in its constituent (arfvedsonite) could be responsible for the moderate values of this rock in TM 5/4 band ratio (red) TM 5/1 band ratios (green). The very low values of 5/7 ratio displayed here as blue may be due to the fact that it is almost free of alteration. Therefore, this rock appears as orange colour. In the PCC image it appears as bright yellow. The other part of the (aag) unit to the west has more alteration minerals such as sericite and kaolinite, and possibly lesser amounts of arfvedsonite (confirmed by examining a thin section collected during the field visit). This may account for its greenish blue in the CRC image. In the PCC image this small unit appears more reddish.

The rhyolite porphyry (arp), exposed at Sinaf abal Haddar, appears in the CRC image as cyan colour (high in blue and green). This may be due to its high degree of alteration, and the presence of iron oxides (hematite),whereas the southern unit appears bright yellow colour. In the PCC image the (arp) unit at Sinaf abal Haddar has a green colour, whereas the southern unit has a yellowish colour.

COR MATRIX	B1	B2	B3	B4	B5	B7
B1	1.00					
B2	0.97	1.00				
B3	0.94	0.99	1.00			
B4	0.91	0.97	0.99	1.00		
B5	0.89	0.95	0.98	0.98	1.00	
B7	0.87	0.94	0.97	0.97	0.99	1.00

(a)

COMPONENT	C1	C2	C3	C4	C5	C6
% var.	97.27	1.85	0.31	0.26	0.23	0.09
eigenval.	3028.02	57.69	9.53	7.98	7.13	2.74
B1	0.251	-0.692	0.085	0.396	-0.168	-0.513
B2	0.221	-0.327	0.070	0.320	-0.123	0.849
B3	0.424	-0.284	0.137	-0.821	-0.207	0.048
B4	0.364	-0.124	-0.134	-0.021	0.912	0.008
B5	0.614	0.358	-0.619	0.157	-0.283	-0.071
B6	0.443	0.433	0.753	0.200	-0.001	-0.086

(b)

Table 6.7. See next page.

LOADING	C1	C2	C3	C4	C5	C6
B1	0.924	0.351	0.017	0.074	0.030	0.056
B2	0.985	0.200	0.017	0.073	0.026	0.113
B3	0.997	0.092	0.018	0.099	0.023	0.003
B4	0.991	0.046	0.020	0.002	0.120	0.000
B5	0.990	0.079	0.055	0.013	0.022	0.003
B7	0.986	0.133	0.093	0.022	0.000	0.005

(c)

Table 6.7. Statistics of Aban Ahmar test area where table (a) describes the correlation coefficient between the 6 TM reflected bands. Table (b) describes the variance, eigenvalues and eigenvectors for each principal component in which the percentage variance indicates the amount of variance that was picked by each component which is also expressed by the eigenvalue. The eigenvector indicates the relative loading of each band in each component. Table (c) gives the component loading summary.

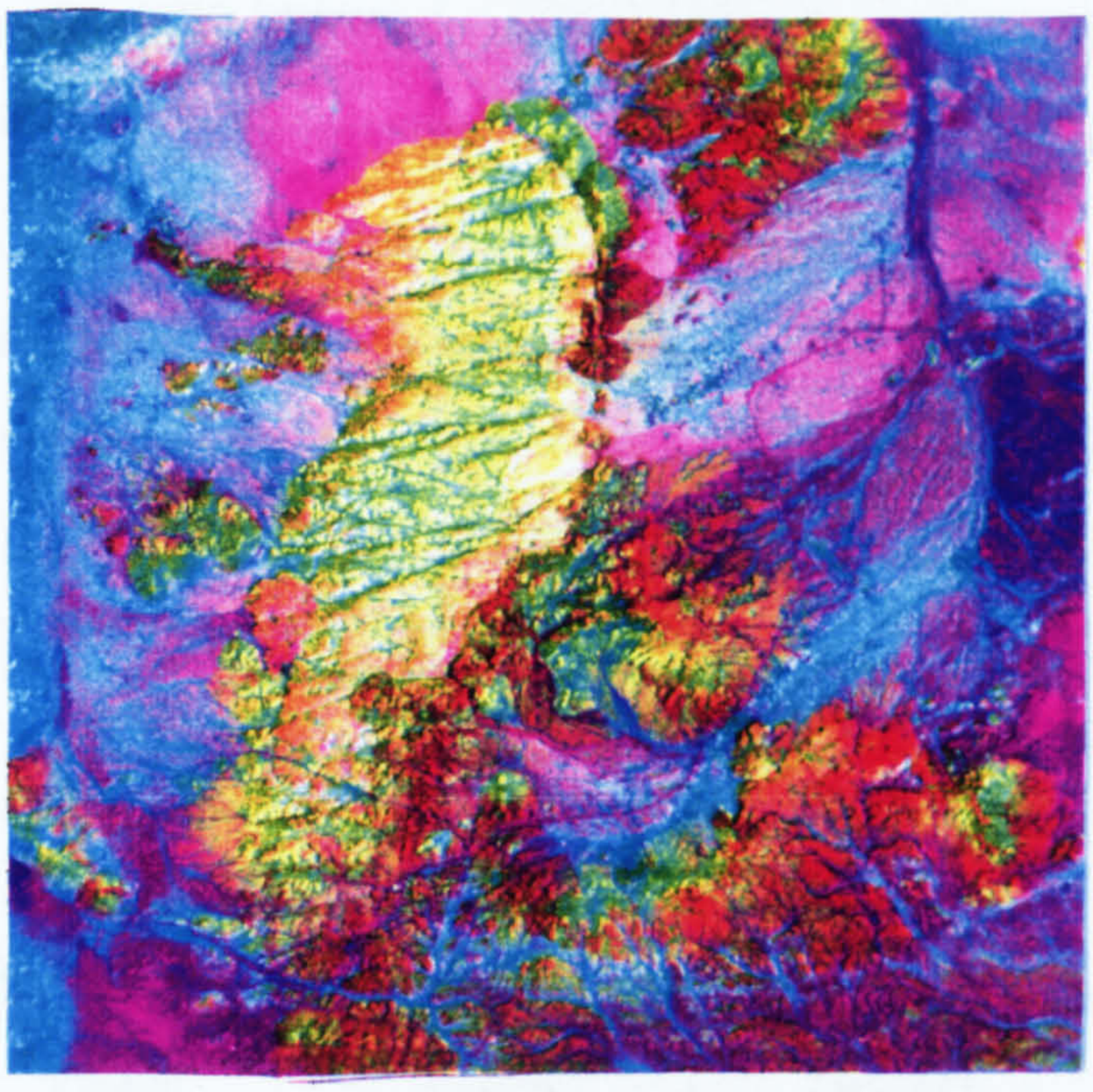

Figure 6.13: Principal component colour composite (PCC) image resulting from principal component transformation of the six reflected TM bands of Aban Ahmar, in which PC3, PC2 and PC1 were displayed as red, green and blue respectively.

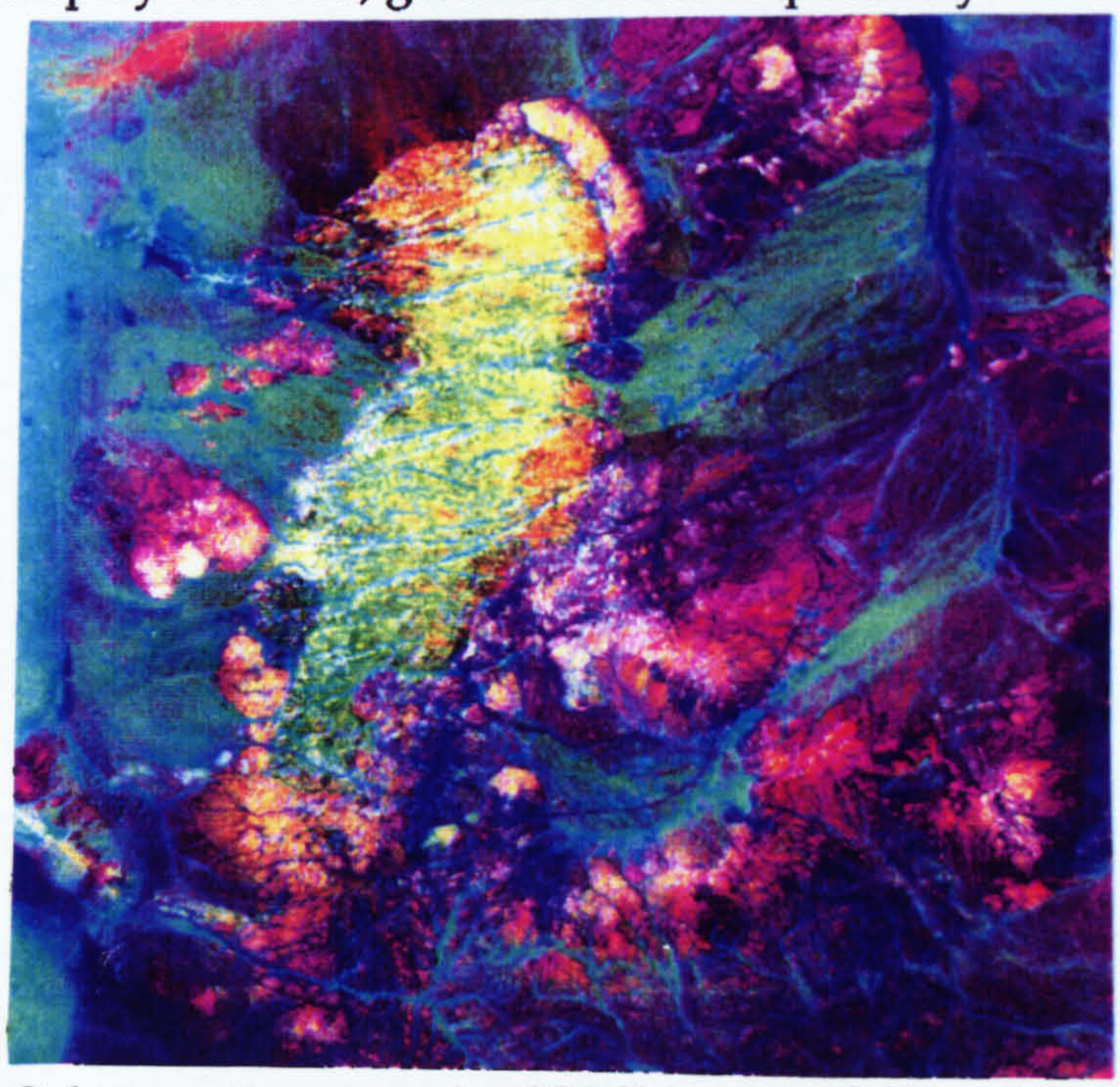

Figure 6.14: Colour ratio composite (CRC) image of Aban Ahmar in which TM 5/4, TM 5/1 and TM 5/7 band ratios were displayed as red, green and blue respectively.

	TM 5/4 band ratio image (red)	TM 5/1 band ratio image (blue)	TM 5/7 band ratio image (green)	Colour Composite
Perthite granite	moderate	bright	dark	yellowish green
Arfvedsonite granite	moderate	moderate	dark	yellow
Rhyolite porphyry	moderate	bright	moderate	cyan
Granophyre	bright	moderate-bright	moderate	reddish bright
Khaytan quartz diorite	bright	moderate	moderate	reddish bright
Sabkha	dark	dark	bright	dark blue

Table 6.8. Summary of colour associated with main lithologies in the colour ratio composite of Figure 6.14.

In the granophyre (sgg) unit the high percentage of iron oxides and iron bearing aluminosilicate (biotite), as well as the presence of alteration minerals (sericite), has given this unit a yellowish bright colour. In the PCC image it has a green colour.

The andesitic flow rock, flow breccia, and conglomerate units (Ja, Jc, Js and Jt) were mapped according to their stratigraphic positions and also by the clasts' size and microscopic texture. These differences cannot be traced by satellite sensor, such as the one used here; therefore the discrimination between these units was not possible.

The Sabkha area (evaporites) appears similar to part of the andesitic unit, due to the reasons that were described in section 6.3.1.1, with regard to the albedo differences. This is not the case, however, in the PCC image and the Sabkha deposits can be discriminated clearly by their dark blue colour.

6.3.3.2 Band colour composite and HSI transformation enhancement

A colour composite of TM band-7 displayed as red, TM band-4 displayed as green, and TM band-1 displayed as blue is shown in Figure 6.15. These bands were stretched using a BCET technique to enhance discrimination between different lithologies. Various rock types exhibit some degree of colour variation in this figure, but the intensity of these colours is somewhat degraded, and does not show the detailed variation that was described by the geologic map (Figure 2.8) made by Cole (1988). The degree of saturation in these colours is low due to the reasons described earlier in section 6.2.5. The data in Figure 6.15 were transferred from RGB to HSI coordinates after being manipulated as described previously in section 6.2.5 and then transformed back to the RGB coordinates for visual inspection. To display the detailed texture and structural information, and

the sharp boundary and contact between various units, that was enhanced by this transformation and manipulation, the image of this test area (1024 x 1024 pixels) was divided into four 512 x 512 pixel subscenes. This was made to enable a full resolution display (Figure 6.16). This step was not taken for the other images (PCC and CRC images) since they did not show any significant details.

In this image, the improvement in the spatial as well as spectral information is self-evident. The image becomes easier to interpret in terms of its rock variation, rock boundary and rock texture. The degree of similarity between the image and geological map used by Cole (1988), and used here as reference, is convincing (for comparison and rock units location see the geologic map, Figure 2.8).

For example, the perthite granite member can be discriminated by its very rough texture and structure, and its reddish yellow colour (absorption in band-1), which suggests the presence of iron oxides. The higher amount of iron minerals in the arfvedsonite granite (apg) gives this unit a pink colour, due to absorption in both bands 1 and 4, that were displayed as blue and green respectively; also this unit is slightly less rough in its texture. However, the (apg) unit appears as greenish colour, west of the perthite granite, in the southern half of the image. By examining a thin section that was made during the field visit in November 1991, it was found that the main difference was the presence of clay minerals (kaolinite and sericite), as an alteration product, in addition to hematite, which is present in both areas. This leads to more absorption for band-7and band-1.

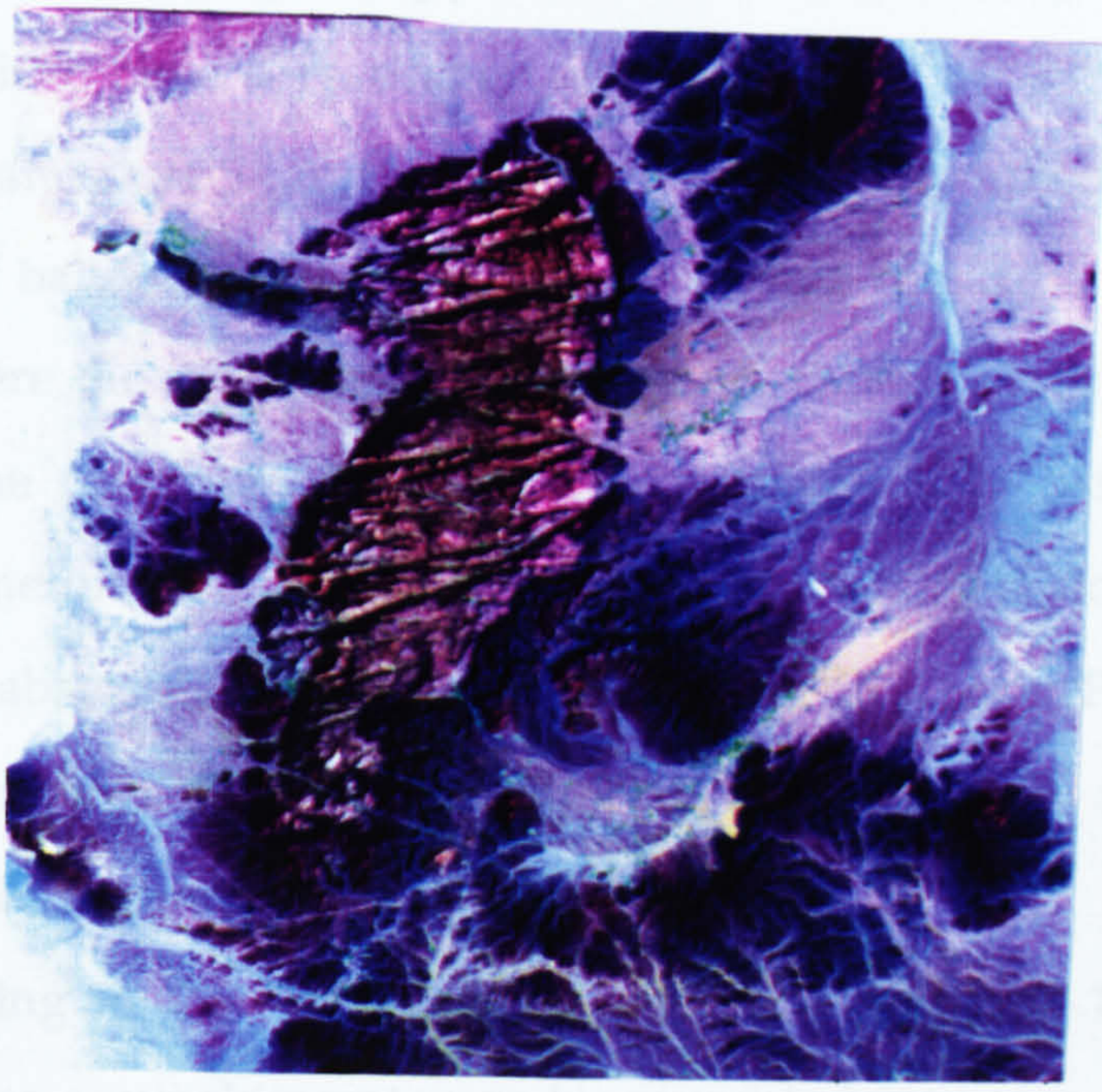

Figure 6.15: Colour composite image of Aban Ahmar, in which TM band-7, TM band-4 and TM band-1 were displayed as red, green and blue respectively.

The units mapped in the geologic map as rhyolite porphyry (arp) can be divided into two units in terms of the degree of alteration. The one at north west of Fayyadah can be discriminated by its green colour (absorption of bands-7 and -1 and slightly higher reflectance in band-4), that may be due to a combination of hydroxyl minerals formed by alteration, and the presence of hematite, which caused a sharp decrease in band 1 (confirmed by field observations). The small yellow area within this unit was observed in the field as an eolian sand dune that covers this area. The southern unit (west of Jibal al Hannawiyah) appears to have less hydroxyl minerals, which causes this unit to have deep orange red colour.

The granophyric unit (sgg) at Jibal Kihlah appear as deep red (absorption of bands-1 and -4). A similar sample was described by Hunt et al. (1973), where the high percentage of biotite caused absorption in bands 1 and 4, also the presence of augit caused absorption in band-4. Although Cole (1981) mentioned some alteration in this unit, it does not seem to show a high absorption in band-7. As in the CRC and PCC images, the andesitic flow rock, andesitic flow breccia, and the dacite units, cannot be separated easily in this image.

According to the enhanced TM shown in Figure 6.16, the unit that was mapped as a conglomerate can be separated into two, the red and the blue units. During the field trip a thin section was made for three samples, one from the blue and two from the red units. After examining the thin sections it was found that the main difference is the intense sericitization and kaolinization in the plagioclase of the sample taken from the blue area, plus the presence of some iron oxides, that cause more absorption in band 4 relative to band 1. The red unit is almost free of alteration and contains

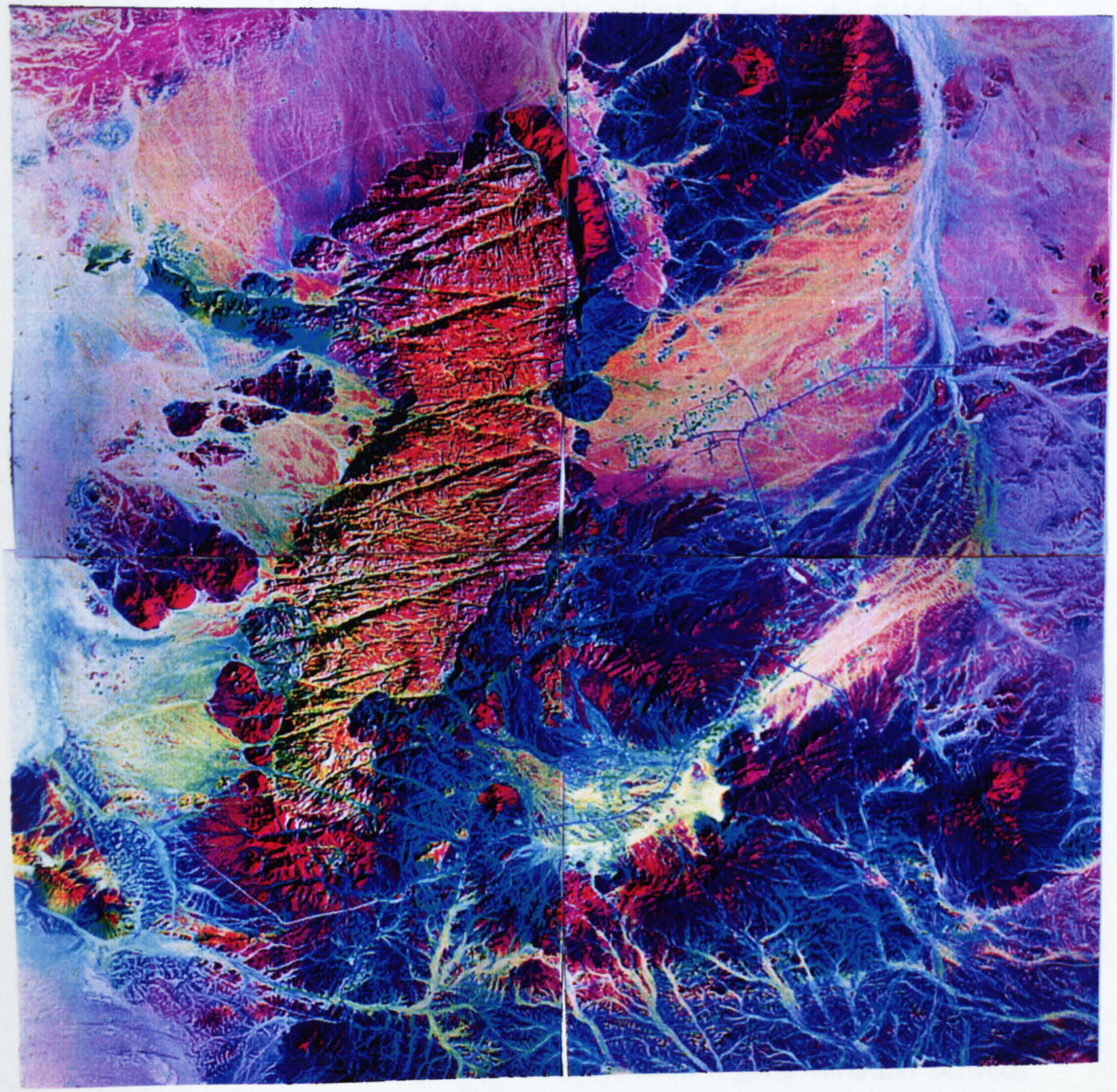

Figure 6.16: The colour composite image of Figure 6.15 after hue-saturation-intensity enhancement.

some magnetite and pyrite, that were altered to limonite, which caused the high absorption in bands 1 and 4. The unit mapped as andesite can be divided into two units, a blue and a red unit. A thin section, from the red unit, was made for one of the samples collected during the field visit. It showed that the epidote mineral forms a considerable amount of this unit, and hence reduced reflectivity in TM band-4. Also, a thick desert varnish covered the rock, and this caused a reduction in reflectance (absorption) in all the TM bands, but its effect in the IR bands, especially TM band-7, is less than the shorter wavelength bands. These two components may cause the red colour.

The area mapped as conglomerate unit north of Mihayyidah village, which apperas as orange colour, was checked in the field. The difference in its colour from the rest of the conglomerate may be due to a high amount of granite and rhyolite fragments as described by Cole (1981), and also the presence of small rhyolite dikes. The area mapped as Gabbronorite cannot be easily discriminated from others nearby.

Some of the rhyolite dikes, that intrude the andesitic flow rock and flow breccia, appear as yellow orange to orange colour west and north west of Mihayyidah. The Sabkha (evaporites) deposits can be recognised by their homogeneous cyan colour due to absorption of TM band 7 by carbonates.

6.3.4 Aban Asmar (test area 4)

6.3.4.1 Band ratio analysis

In this test area only six band ratios show a good variation between rock types. These are TM 5/1 , 5/3 , 5/4 , 5/7 , 4/1 and 4/7. As for previous test areas, a variety of ratio colour composites were made using the above ratios, in order to choose the best one that provides discrimination between

different lithologies. It was found that the best colour ratio composite was TM 5/4 band ratio image displayed as red, TM band 5/1 ratio image displayed as green, and TM band 5/7 ratio image displayed as blue, Figure (6.17). Table (6.10) summarises the different colours associated with different lithologies found in this test area (consult the geologic map in Figure (2.11) for rock units locations).

In this colour ratio composite the presence of iron oxides (e.g., hematite), and iron bearing aluminosilicates (biotite and hornblende), and the lack of alteration in both the biotite perthite granite (spg) and hornblende perthite granite (shpg) lithology units, may be responsible for the higher values in TM 5/4 band ratio, displayed as red and also in TM 5/1 band ratio, displayed as green, and low values in TM 5/7 band ratio, which gave these two units the yellow colour (mixture of red and green).

In the Samra rhyolite (Sry) unit the white areas are probably a sign of hydrothermal alteration. Whereas the bright cyan areas are the areas that have a relatively low 5/4 ratio, owing to a lower content of iron bearing aluminosilicates (such as biotite and hornblende), the darker cyan areas are caused by slightly lower value in ratio 5/1 than the bright cyan areas. This may be attributed to a lower content of iron oxides. The intrusion breccia (sbr) unit which is a mixture of both sry and shpg shows a mixture of blue, cyan and yellow. The quartz syenite (ssy) can be discriminated by its reddish yellow colour (low in TM 5/7 band ratio).

The conglomerate (Jc) east of the complex can be discriminated by its dark blue colour (low reflectance in TM 5/4 and 5/1 band ratio and high in TM 5/6 band ratio), which may be due to the presence of hydroxyl bearing minerals. The CRC also shows a magenta colour in the southern part of this unit, that may be caused by the abundance of rhyolite porphyry dikes

that cut this area (noticed during the field visit and also reported by Cole, 1988). The granite porphyry member (sgp) appears as a cyan colour and cannot be discriminated from some part of the rhyolite to the south of this unit. The dike of this unit, that cuts the conglomerate, appears as yellowish colour, and can be easily discriminated. The rhyolite porphyry (srp) unit appears as dark cyan colour and cannot be discriminated from the Jc unit.

6.3.4.2 False colour composite and HSI transformation enhancement

Figure (6.18) shows a false colour composite of TM band-7 displayed as red, TM band-4 displayed as green, and TM band-1 displayed as blue. These three bands were stretched using BCET stretch to enhance the visual appearance of the image. Due to the sharp differences in brightness between some lithologies (such as the granite and the Samra rhyolite), they can be discriminated in this image; however, rocks that have lower brightness have poor visual appearance in the image. The colour variation is poor, and the units that can be discriminated in the image are fewer than those found in the geologic map (Figure 2.11). By transforming the data in Figure (6.18) from the RGB to the HSI coordinates and then using the steps described earlier in section 6.2.5, and then transforming the data back to the RGB coordinate (Figure 6.19), the improvement in the data was obvious.

The increase in saturation and intensity enables the variation in the previously dark areas, especially the Asmar rhyolite unit, to be clearly seen (consult Figure 2.11 for rock units location). Some of these variations were not mapped in the geologic map used here as reference. For example, both biotite perthite granite (spg) and the hornblende perthite granite (shpg) appears as light red colour. This may be due to the fact that both rock units are compositionally and texturally the same (both are perthite granite),

COR MATRIX	B1	B2	B3	B4	B5	B7
B1	1.00					
B2	0.98	1.00				
B3	0.97	0.98	1.00			
B4	0.94	0.96	0.97	1.00		
B5	0.94	0.95	0.96	0.96	1.00	
B7	0.92	0.94	0.95	0.94	0.98	1.00

Table 6.9. Correlation coefficient matrix between the six TM reflected bands of Aban Asmar test area.

	TM 5/4 band ratio image (red)	TM 5/1 band ratio image (blue)	TM 5/7 band ratio image (green)	Colour Composite
Quartz Syenite	moderate-bright	dark	moderate	magenta
Samra rhyolite	moderate	bright	moderate-bright	white - bright to dark cyan
spg & shpg	bright	bright	dark	yellow
Intrusion breccia	moderate	moderate	moderate-bright	mixture of yellow, cyan and blue
Conglomerat e	dark	dark	bright	blue
Granite porphyry	moderate	bright	moderate-bright	cyan-blue

Table 6.10. Summary of colour associated with main lithologies in the colour ratio composite (Figure 6.17).

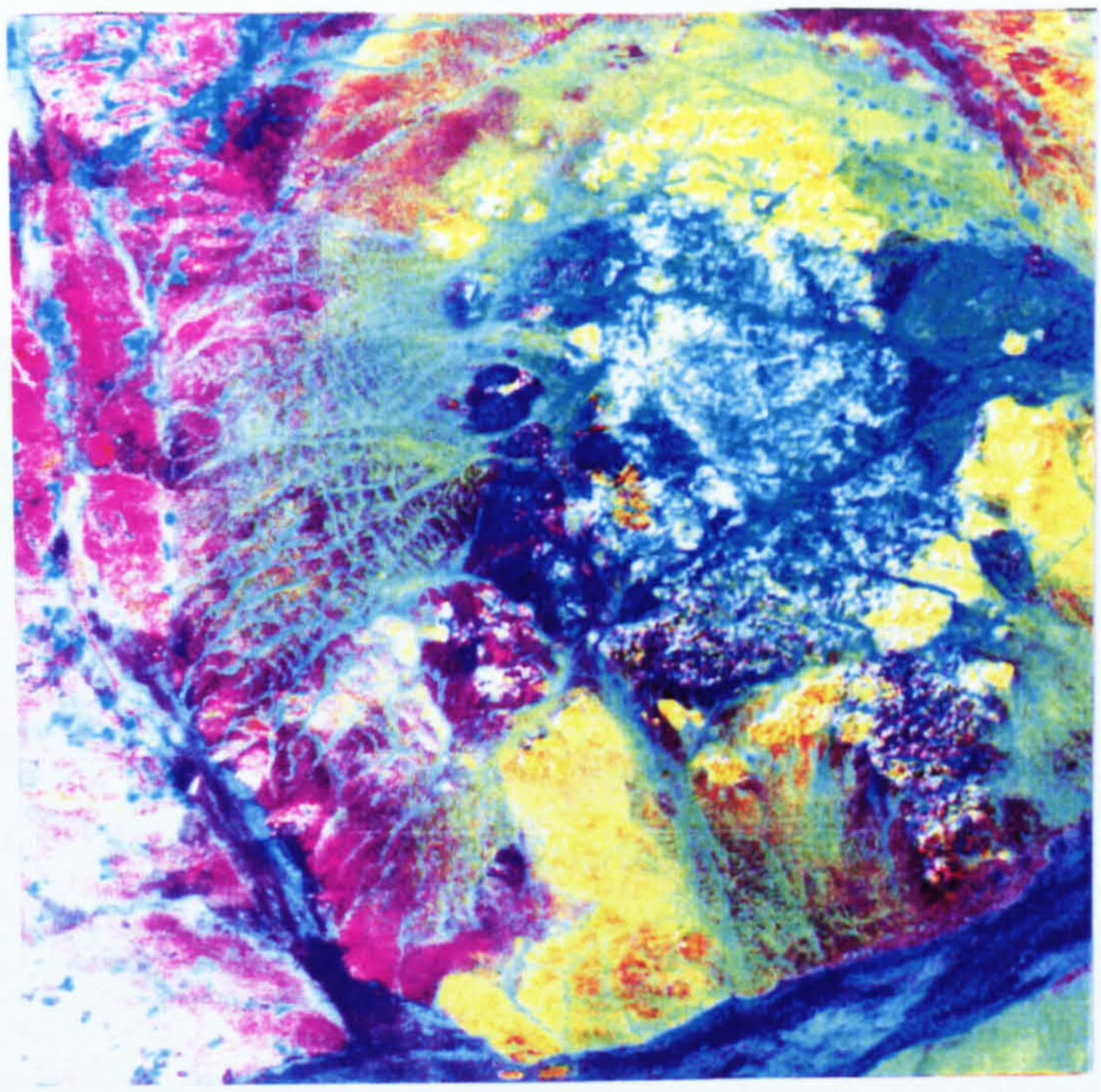

Figure 6.17: Colour ratio composite (CRC) image of Aban Asmar in which TM 5/4, TM 5/1 and TM 5/7 band ratios were displayed as red, green and blue respectively.

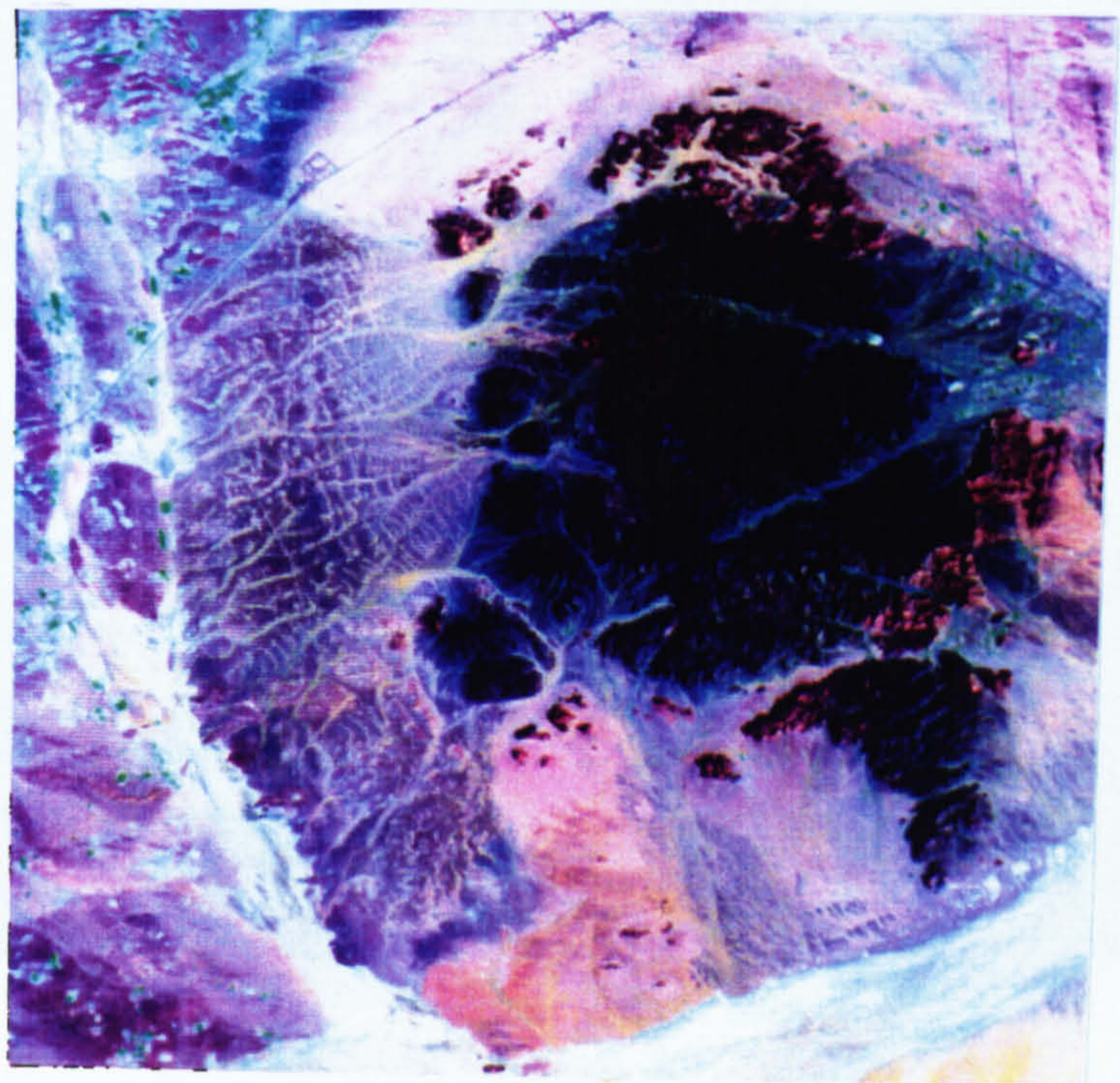

Figure 6.18: Colour composite image of Aban Asmar, in which TM band-7, TM band-4 and TM band-1 were displayed as red, green and blue respectively.

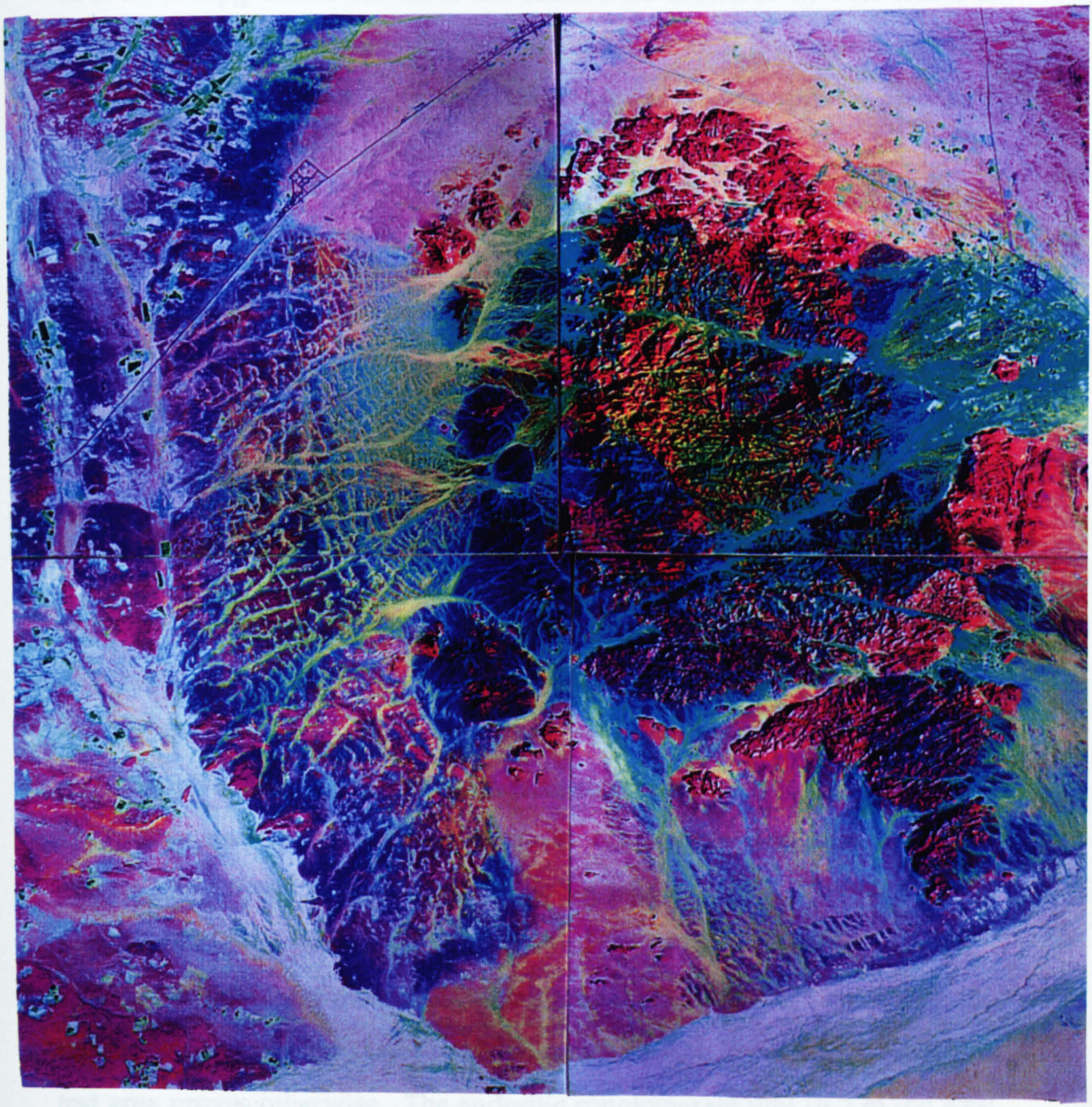

Figure 6.19: The colour composite image of Figure 6.18 after hue-saturation-intensity enhancement.

except that the hornblende unit contains minor and sparse dark green amphibole, and brown rather than green biotite (Cole, 1985). Its similarities were also confirmed in the field. The intrusion breccia units (sbr), which bound the shpg unit to the north and south were described by Cole (1985) as a mixutre of the hornblende perthite granite and the Samra rhyolite (section 2.3.4). Its colour in the HSI enhanced image appears also as a mixture of the colour of both units.

In the Samra rhyolite unit (sry) at the centre of Asmar complex, although it has been mapped as one unit, the image varies in its colour (red, green and blue) which suggests some differentiation. To check the source of this colour variation, a thin section were made for some of the rock samples, taken from the area that bounds Shaib al Mitla al Aysar, since other areas are almost impossible to reach. It was found that the sample taken from the green area has a high kaolinization (6% kaolinite and 1% sericite). It also has 3% of iron oxide as hematite staining. These two factors may cause the reduction in reflectivity in both TM band-1 which is displayed as blue and TM band-7 displayed as red and gives this unit its green colour in the image. Samples taken from the blue area have a more clay mineral content . The red areas were the least altered.

The quartz syenite member (ssy) can be discriminated from the granite units by its magenta colour, which may be due to the presence of augite and biotite, which reduce the reflectivity in band-4. Davis and Berlin (1989) conclude from their study of an area of the Arabian shield, that the granite and syenite could not be discriminated using TM data, whereas this test area proves otherwise. The andesitic conglomerate unit (JC) to the west of the complex has blue colour; the southern part of this unit shows more variation of red colour. This may be caused by the abundance of rhyolite

porphyry dikes that cut this area, which was reported by Cole (1988) and was also noticed during the field visit.

6.4 Summary and conclusion

In this chapter the results that were obtained by applying different image processing techniques to the images of four test areas were reviewed. These test areas were selected due to their excellent exposure and lack of vegetation, in addition to the diversity of rock types available. The purpose of this study was mainly to assess enhancement techniques (rather than a geologic investigation), and these techniques were applied to an area already studied geologically, so that the accuracy of interpretation can be assessed. In addition, where necessary and possible, field samples were taken to confirm the interpretations.

Results obtained from applying canonical regression analysis, although somewhat confusing, showed that this regression method has the potential for combining Landsat data with geochemical data. Experience gained from this study showed that it is to some extent a lengthy process, but the result may turn out to be very useful for various other studies, such as geochemical studies or mineral exploration. Owing to the limited number of spectral bands for Landsat TM, its full potential cannot be realised. This may produce more success by using remote sensing data with a higher spectral resolution and a higher number of spectral bands.

The results from the techniques that were used to produce a highly enhanced single image product for rock discrimination, show that from the six principal components, the best three for display were PC3, PC2 and PC1 displayed as red, green and blue respectively, whereas the best three TM-band ratios for display were band ratios 5/4, 5/1 and 5/7 displayed as red,

green and blue respectively. However, although the results of both ratio and principal component techniques, which are the most frequently used processing techniques for geological images, show some degree of discrimination between different lithologies, they are by no means the best. The ratio technique does enhance the appearance of rocks containing the hydroxyle and iron minerals. However, the ratio technique suffers from the disadvantage of suppressing of albedo and topographic relief. The suppression of topographic relief increases the difficulty of transferring the information from the CRC image to a topographic base map, or to locate the exact spatial distribution of the lithological units, since most of the surface expressions are lost. Furthermore, the theoretical basis of band ratio technique for eliminating shadow is made under the assumption that the objects have a Lambartian surface (reflect radiation equally in all directions), which is uncommon in nature (Drury, 1987; Liu and Moore, 1990). The high amount of noise is also a disadvantage in the CRC image.

In the case of principal component technique, despite the colourful results in some of the test areas, these colours are intractable and it is difficult to relate them to the spectral properties of the different lithologies available in the scene. This is mainly due to the fact that the different principal component images (PC axis) are created by weighted arithmetic combination of all the bands rather than for one band, which may increase the interpreter's confusion. In addition this technique uses the covariance matrix derived from the scene, which may lead to different colours of the same lithologies available in the different scenes, with increased confusion over topographically rugged areas (Drury, 1987; Rothery, 1987). In addition, most of the textural information is lost and the degree of signal to noise

ratio is low, and this degrades to some extent the interpretability of some of the images.

A simpler and more understandable way of interpreting the TM data is to choose three of the reflected TM bands for display as a colour composite, the choise being determined by the way the different target lithologies affect the chosen bands. This approach is certain to be superior to the statistical method of choosing the bands, for these ignore the significance of variations in lithological features, and therefore can only accidentally arrive at a 'good' choice. It was found, using such an approach, that the display of TM band-7, TM band-4 and TM band-1 as red, green and blue respectively gives the best band combination for overall lithological discrimination in the four test areas. However, the use of such colour composites is somewhat limited by the low degree of colour variation, which can be attributed to the high degree of correlation that generally exists between different (reflected) TM bands. Stretching of the original three band colour composite to fill the 8-bit range available for TM data, may increase the contrast slightly, but would not reduce the degree of correlation as was demonstrated earlier, and also discussed by other authors such as Soha and Schwartz (1978), Drury (1986), Gillespie et al. (1986), and Rothery (1987).

In contrast to some authors, e.g. Rothery (1987), who obtained good results using the decorrelation stretch, in this study the results of applying such techniques did not produce any significant results. Others, such as Davis and Berlin (1989), have used it as well for an area in the Arabian shield without any significant results. This may be due to the fact that the decorrelation stretch is based on principal component transform which, as described earlier, is based on the variance of the data, with less variance and

more noise distributed to the sucessively higher components. Stretching the principal components before transforming them back to the original coordinates (which is the basis of decorrelation stretch technique) will selectively enhance the noise. Ferrari (1992) suggests the use of a low pass filter to reduce the noise effect. However, this procedure does not guarantee the removal of such a component, and will negatively affect the spatial information.

As shown earlier, however, HSI transformation does provide a highly flexible and simple means of producing an excellent result based upon the original bands. The use of an alternative colour space (HSI colour space) to reduce the correlation, and enhance, simultaneously the spectral and spatial information in the scene, is an excellent, simple method, as clearly demonstrated by the results obtained in this study. The variation and purity of the colour were strongly enhanced, without any distortion to the original; in addition, the quality of spatial information was sharpened. This was made possible by transforming the RGB band colour composite (after equalizing the means using BCET stretch) into HSI colour space, which produced three new components that can be manipulated independently. In this study the saturation and intensity components were altered, whereas the hue was optimised by stretching the three original bands, so that they had equal means and ranges The saturation was altered by simple addition to higher values, to increase the colour purity. The intensity was controlled by an edge-enhanced first principal component, and also shifted to a higher range to provide a sharper image, and to enhance areas of low albedo. After these manipulations, in the HSI colour space, the data was transformed back to the RGB colour coordinates for display. From the results, it is clear that the HSI transform provides a

powerful technique in terms of its flexibility and quality of its product. It creates a superb output of an RGB band colour composite, without sacrificing any image content. Further, the results can be easily interpreted and provide the geologist, hydrologist or photogeologist, in a single colour image product, with the lithological, structural as well as textural (topography and drainage) information, clearly displayed. The HSI method with the methodology discussed in this chapter can also be used to enhance any other type of image to provide an enhanced colour product.

CHAPTER SEVEN

DIGITAL CLASSIFICATION TECHNIQUES: CONCEPT AND RESULTS

7.1 Introduction

7.2 Digital classification in geology

7.3 Classification strategies

7.4 Classification algorithms
- 7.4.1 The unsupervised maximum likelihood method
  - 7.4.1.1 Clustering
  - 7.4.1.2 Maximum likelihood
- 7.4.2 Watershed method

7.5 Accuracy assessment

7.6 Method of investigation

7.7 Results
- 7.7.1 Silsilah ring complex test area
- 7.7.2 Jabal ar Raha test area

7.8 Summary and conclusion

7.1 Introduction

In Chapters 5 and 6, the image processing techniques, that help the analyst in the qualitative, or visual interpretation of images, were described and evaluated. In this chapter, the techniques that help in the quantitative interpretation of the multispectral images, and the automatic classification of the pixels, will be described and tested. The main difference between the enhancement techniques, and the classification procedures, is that the enhancement techniques are designed by the analyst to enhance the visual interpretability of the data. Production of a map from these data is the duty of the analyst. Image classification, on the other hand, transfers this duty to the computer. This step is made to replace the uncertain interpretation of the analyst by a more quantitative and repeatable process.

Digital classification of images is the process that assigns each individual pixel in a digital image to a label or class based on its spectral properties. The logic is that in multispectral data, each pixel has a grey level in several spectral bands of the electromagnetic spectrum. Different categories will have different patterns that are unique enough to enable these categories to be distinguished from one another. Therefore, statistical techniques may be used to digitally classify the data based on these spectral features (Hutchinson, 1982). This process is carried out for all pixels in the image, dividing it into several homogeneous regions. The classified image, resulting from such a process, is presented as a thematic map, which can be density sliced to different colours, to show the geographical distribution of each class in the image. Once the classification procedure has been conducted, the final step is to check the degree of accuracy in the classified image compared to reference data.

Digital image classification is one of the most important image processing tasks in remote sensing. It could be used, either as a final product, or as one of several analytical procedures used to derive information from an image.

Two aims were set for this chapter. The first aim was to evaluate the degree of accuracy of a new unsupervised classification algorithm, named watershed algorithm. This algorithm was used for the first time by A.I. Watson (1987) for classification of agricultural scenes acquired by satellite sensor (see also Al-Dail, 1989). These studies revealed that the watershed algorithm is a better algorithm, in the degree of its accuracy, than any comparable method available. However, since this study is the first attempt at applying the watershed method to a geological scene, its accuracy will be compared to the maximum likelihood classifier, which is, probably, the most widely used method to classify multispectral images (Niblack, 1986), and which in many ways proves to be the best statistical algorithm (Short, 1984; Watson, 1987, 1992; Al-Dail, 1989; Booth and Oldfield, 1989). There are, of course, many other approaches and these can be found in Swain (1978), Short (1982), Schowengerdt (1983), Niblack (1986), Richards (1986), Campbell (1987)Jensen (1987), Mather (1987) and Lillisand and Kiefer (1987).

The second aim was to test the effect of using hue images as a classification input compared to the original bands. These hue images are produced by transforming the original data from RGB coordinates to hue-saturation-intensity coordinates

This chapter begins with a brief review of classification in geology, followed by classification strategies and a brief description of the classification algorithms used in this study and the method of assessing classification accuracy. This theoretical review is followed by an account of

the method of investigation used to perform the classification and its accuracy asessment, which is followed by the results that were obtained; the chapter ends with a summary and concluding remarks.

7.2 Digital classification in geology

Unlike in agricultural applications, where the digital classification techniques of remotely sensed data are common, in geology, digital classification of remotely sensed data is not a favoured technique (Siegal and Abrams, 1976; Abrams and Siegal, 1980; Goetz, 1989a) and has found a limited application in geological-lithological studies (Gupta, 1991). The limitation of the success of digital classification in geology is generally due to a number of factors (Siegal and Abrams, 1976; Abrams and Siegal, 1980), such as the heterogenity of geological units; the shadow effect, where large differences in the radiance values are caused by topographic variation in a terrain of a high relief; the presence of soil and eolian materials; and the vegetation cover.

Despite these obvious drawbacks, several studies have been reported regarding digital classification in geology using remote sensing data, such as Rothery and Melton (1981), Hutchinson (1982), Short (1984), Kaufman and Pfeifer (1986), Brickey (1986), McBird et al. (1986), Rowan et al. (1987), and Guo and Haigh (1990). These studies have used different strategies of pre classification processing and different statistical classification algorithms (e.g, minimum distance, parallel piped and maximum likelihood classfiers). However, apart from Short (1984) and Oldfield (1988), and to some extent Kaufmann and Pfeifer (1986), all the previously mentioned studies did not consider the accuracy of classification. Rather, they concentrated attention on the varying degrees of usefulness of such methods, which cannot be

seriously judged without considering the degree of agreement with the reference data. Therefore, this study will consider the assessment of the accuracy in more detail and with the objective of improving it. Short (1984) and Oldfield (1988), however, mention that the accuracy of Landsat MSS falls in the 40-60% accuracy range, relative to the maps made by traditional field and aerial studies, with about 10% improvement when using the TM data.

7.3 Classification strategies

In general, there are two strategies in performing the classification on remotely sensed data: a) the supervised strategy and b) the unsupervised strategy. The supervised approach requires the analyst to define a homogenous area in the image that is known to have a specific identity, in other words to define a certain objects in the image. These areas are called training areas. The analyst then supervises the classification process, by supplying to the computer algorithm the statistical identity of these areas, which will then guide the classifier in the labelling procedures, where it will compare the statistical identity of each pixel with each training area in the image set. Therefore, the selection of these areas forms the key step in the supervised strategies.

The unsupervised classification, on the other hand, does not require any assistance from the analyst and its algorithm can be applied directly to the data set. The data is first plotted in a feature space, which in effect is an n-dimensional histogram, where n is the number of bands. The algorithms divide the feature space into a natural grouping (cluster) in order to classify the images. The analyst then compares the classified image with reference data, in order to identify the nature of each cluster.

7.4 Classification algorithms

As mentioned earlier, this study is concerned with the unsupervised classification strategies. Two methods were used for classification: the maximum likelihood and the watershed.

7.4.1 The unsupervised maximum likelihood

The unsupervised maximum likelihood method used in this study started by applying clustering algorithm to produce a natural grouping (clusters) in the feature space, so that the mean and variance for each cluster can be found and used by the maximum likelihood to classify the data. Therefore, the following section will contain a brief description of the clustering and the maximum likelihood algorithm.

7.4.1.1 Clustering

Clustering within feature space, whose dimensionality depends on the numbers of bands, can produce better discrimination of features than the one-dimensional histogram taken separately. Figures 7.1(a) and (b) show a one dimensional histogram of two rock types (granite and basalt). These two rock types are found to be overlapped in both bands A and B; thus the rock types cannot be identified without error. In Figure 7.1(c), the feature space of a two dimensional histogram formed by bands A and B, in which one cluster represents granite and the other basalt. From this feature space, it is obvious that a simple decision boundary can be constructed that will allow reliable classification. However, this figure represents the ideal condition. In nature, the position of the objects in the feature space tends to be scattered, rather than form tight clusters. In these cases, the decision

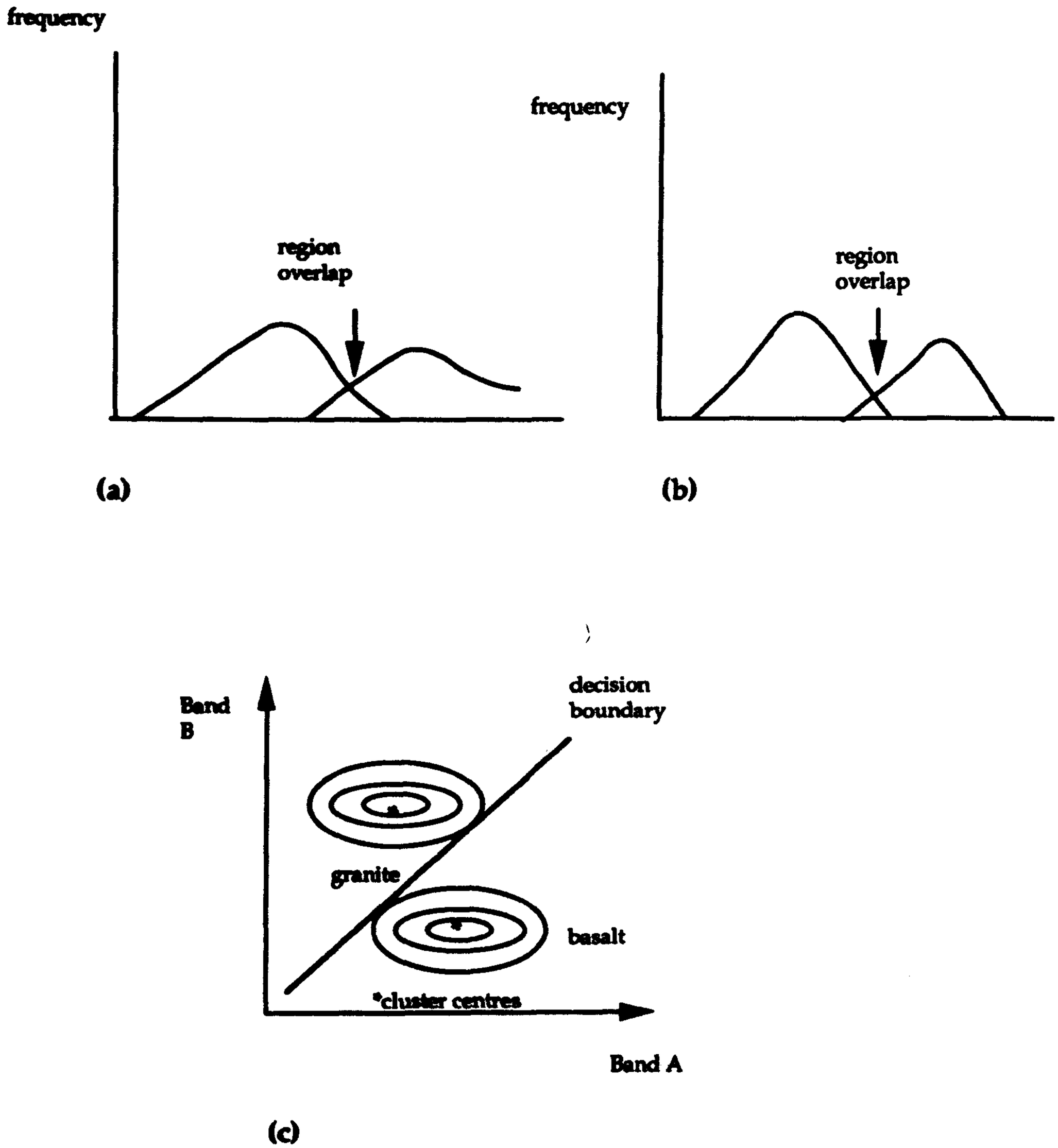

Figure 7.1. a) one-dimensional histogram of band A; b) one- dimensional histogram of band B; c) two-dimensional histogram of bands A and B.

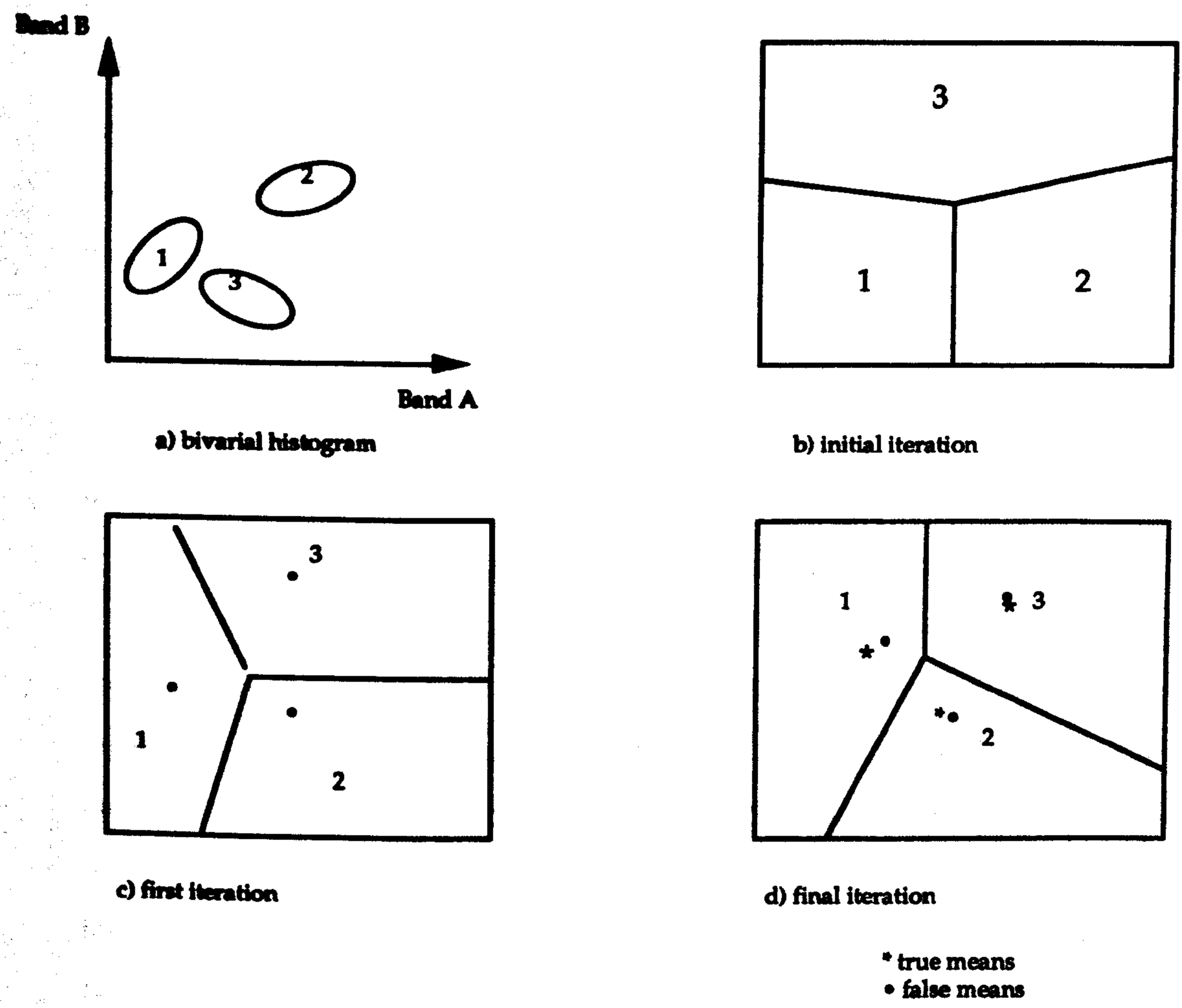

Figure 7.2: Clustering by the minimum distance to mean algorithm.

boundaries are difficult to define directly, and different methods are employed to determine class inclusion.

In most clustering algorithms the number of clusters must be submitted to the algorithm. The method starts by 1) guessing the initial cluster centres (means); these centres could be specified by the analyst. 2) The algorithm will then examine each pixel, one at a time, and assign it to the nearest cluster mean, usually using Euclidean distance measurement, until all pixels are assigned. This assignment will define the initial set of class boundaries (Figure 7.2b).

3) In the next step, the algorithms regenerate a new mean for each cluster, from the results of the previous clustering, and the pixels are reassigned to their nearest clusters. The cycle is repeated until there is no significant change detected in location of cluster means (Figure 7.2c).

However, in the final iteration (Figure 7.2d) the algorithm may not converge to the 'true' class mean. This is because the estimated cluster means are calculated from distribution that is truncated by the class partition (Schowengerdt, 1983), and an extra iteration may be required for convergence, if the estimated means are close to a decision boundary (see the previous references for more detail). In this study, the means and the covariance matrices of the clusters were used to classify the entire image, using the maximum likelihood algorithm, which will be described briefly in the following section.

7.4.1.2 Maximum likelihood algorithm

This type of classification assumes that the distributions within a feature space have a well defined shape (usually Gaussian). By using this

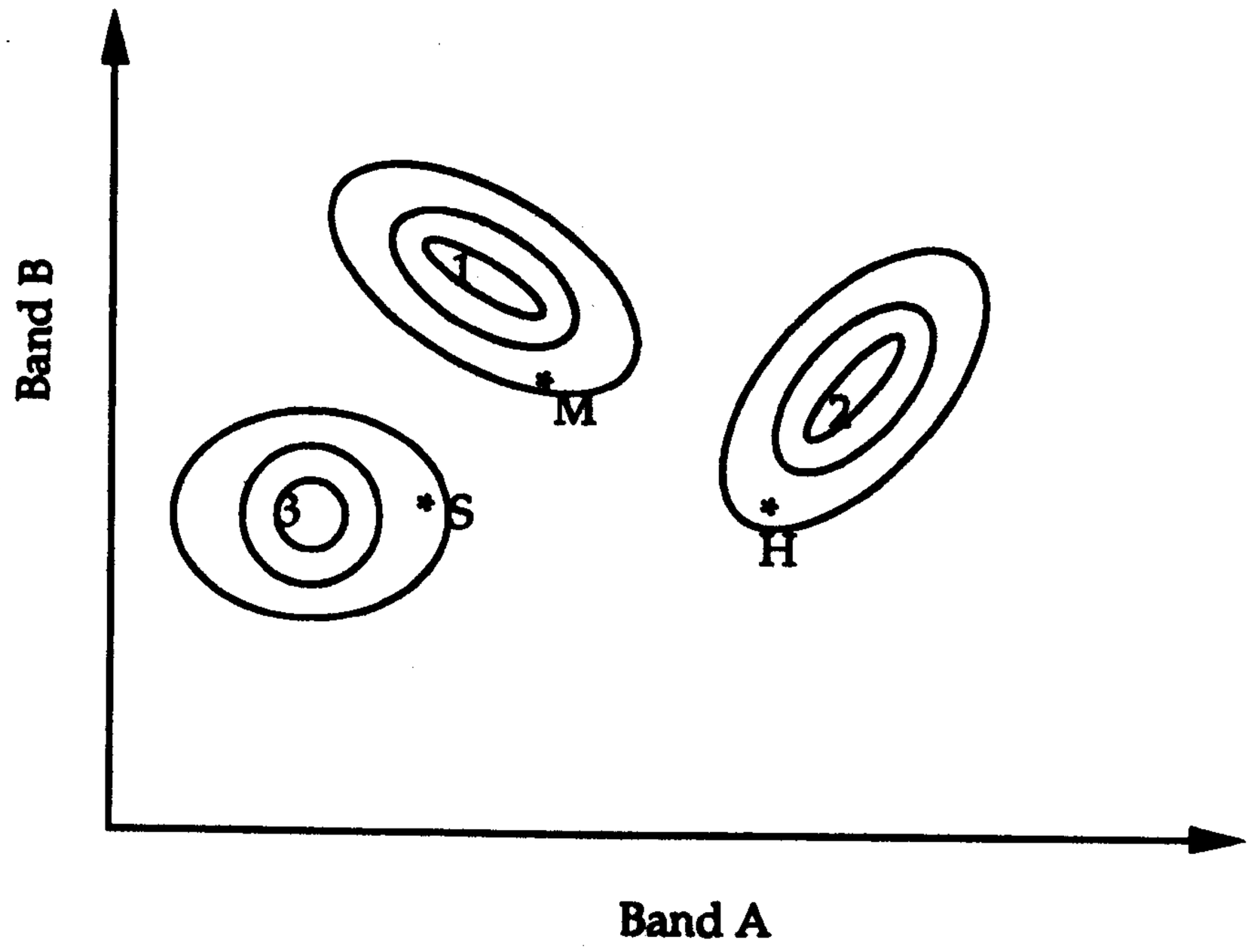

Figure 7.3. Two Bands (A) and (B) feature space with three clusters.

assumption, the distribution of a cluster in a feature space can be described by the mean vector and the covariance matrix.

Figure 7.3 shows a feature space of bands A and B with three clusters. Cluster 1 in the feature space shows a negative covariance. This means that high values in band B are associated with low values in band A, whereas cluster 2 shows a positive covariance, in which high values in band B are associated with high values in band A. Cluster 3 shows a near circular shape in which the band values are uncorrelated. The maximum likelihood algorithm uses the probability concept to assign pixels to classes. The algorithm calculates the probability of a pixel, represented by a point such as "M" in Figure (7.3), belonging to cluster 1, cluster 2 and so on, and then assigns the pixel "M" to the cluster with the highest probability and to which it 'most likely' belongs. These probability values are shown in Figure (7.3) as elliptical contours in clusters 1 and 2 and as concentric circles in cluster 3. These contours show the sensitivity of the likelihood classifier to covariance.

Watson (1987), Mather (1987) and Benic and Thomson (1992) pointed out that the concepts of the maximum likelihood method, are valid only under the assumption of the multi-variate normal distribution, which is not always true, since the intensity distribution to the classes to be merged are not necessarily Gaussian (normal distribution).

7.4.2 The watershed method

Unlike the traditionally used classification algorithms such as the maximum likelihood algorithm, the watershed method does not assume that the centre, size or shape of the grouping within the histogram is known in advance (Watson, 1987). The method is basically an image

segmentation algorithm that divides up an image, or feature space, on the basis of connectivity, into separate groups. The segmentation by the watershed was described by Beucher (1982) and Serra (1982). Its basic idea is to consider how water might flow over a complex surface, and thus provide an analogue to the problem of partitioning the feature space. The problem to be solved is to find the 'hills' on the two-dimensional histogram. These 'hills' correspond to the Gaussian probability distribution, but their shape and size is not predicted or assumed a priori. If the histogram is turned upside down, using the water flow analogue, then the new 'sinks' would correspond to the maximum, and the 'watershed' of each sink would be an estimate of the decision boundary between clusters. Hence, finding these 'watersheds' corresponds to the fundamental problems of finding proper positions of the feature space.

The process of finding the watershed involves the tracing 'backwards' or 'uphill' the flow of water reaching a 'sink'. Starting from a 'sink' (which is a maximum in the feature space), the adjacent points in the feature space are connected to the sink, provided that water would flow uniquely from these points to the sink. Having enlarged each sink, the process is repeated until points are reached, which would drain to two or more sinks. These by definition are the points that form a watershed. Provided that the process of 'connecting in' satisfies some strict topological requirements, it can be proved that if there are n sinks (or maxima) to be located, the watershed algorithm will find these n sinks automatically (Watson et al., 1992). Hence, one of the main problems of guessing the number of clusters is removed. In addition, the decision boundaries are found with a reasonable degree of accuracy.

The structuring element that is used to 'grow' each sink is the Golay L (Watson, 1987). It is applied repeatedly according to the rule that if, for example, (see Figure 7.4) points 3 and 4 belong to group X, and points 6 and 1 do not belong to any already defined group, then point 7 can be connected to group X, provided that point 7 has a height equal to or less than group X, otherwise it cannot be connected to group X. The groups grow around each sink until the whole two-dimensional histogram is scanned and labelled.

The watershed method is illustrated in Figure 7.5. Figure 7.5(a) shows the bivariate histogram of two bands, A and B, constructed on an hexagonal grid (on an hexagonal grid all the nearest neighbours are symmetrical and therefore connectivity is well defined, unlike a square grid for which the nearest neighbours are ambiguous and connectivity is not well defined) Watson (1992). Going 'up' or 'down' is equivalent, therefore the algorithm proceeds as follows. First the maximum points in the histogram (the sinks in the upside-down histogram) are located (Figure 7.5b). Then, reiteratively, points are added to a sink provided they satisfy the L structuring element rule (Fgure 7.5c, d, e). Once all the points are processed, then the groups can be uniquely labelled (Figure 7.5f). Thus, any pixel, having a particular combination of band values, can be labelled. The two band values are the two coordinates of the feature space; hence, knowing these values enables the postion within the feature space to be located. The final matrix (Figure 7.5f) can then be used as a look-up table to classify the original two-band image.

The watershed method was performed in this study using a series of programs available in the Microvax II and were applied successively to the data by choosing the option "WATERSHED CLASSIFICATION":

a) A program called SAM constructed a bivariate histogram by sampling each combination of the two of the multibands data together.

b) The HEX program (median filter) was then applied to remove isolated single points from the bivariate histogram to avoid trivial classes.

c) Then a program called MORPH divided up the smoothed histograms using the watershed algorithms as described earlier.

d) A program called LOOKUP took each two-band value for each pixel, and found the label in the MORPH table and put that label into the output image. The result will be a classified image (grey level) for each pair of bands. Figure (7.6) shows the flow diagram of the procedures used for this classfication algorithm.

The only drawback, to the use of this technique, in the classification of multispectral satellite images, is its restriction to two-dimensional histograms. If the number of bands exceeds two dimensions, then it will produce more than one classified image. For example, if the number of bands is three, the algorithm will look at each two of these three bands' histograms separately. It will then produce three look up tables, which can then be used to produce three classified images for bands 1 and 2, bands 1 and 3 and bands 2 and 3. So if the number of bands is six (as in the reflected TM bands) the algorithm will produce 15 look up tables. These can be used to produce 15 grey level classified images, whereas the maximum likelihood algorithm is capable of dealing with a multidimensional data, where it produces only one grey level image out of, for example, six TM bands.

In Watson (1987), several methods were proposed to reduce the dimensionality of the data. However, in this study a new and effective technique was tested, which reduces the dimensionality of the data, and at

```
. . . . .     . . . . .
. . 6 1 . .   . . 0 0 . .
. 5 7 2 .     .   ?   .
. . 4 3 . .   . . x x . .
. . . . .     . . . . .
```

Figure 7.4. The L structuring element in one of its 6 possible orientations.

Band B

		0		2		4		6		8		10	
	0	•	•	•	•	•	•	•	•	•	•	•	•
		•	1	1	1	•	•	1	1	1	•	•	•
Band A	2	•	2	2	1	1	1	1	1	1	1	•	•
		•	3	2	1	1	1	3	3	1	•	•	•
	4	•	•	3	1	1	1	2	2	•	•	•	•
		•	•	•	1	1	1	1	•	•	•	•	•
	6	•	•	•	•	•	•	•	•	•	•	•	•

a) the bivariate histogram

Band B

	•	•	•	•	•	•	•	•	•	•	•	•	
	•	•	•	•	•	•	•	•	•	•	•	•	
Band A	•	•	•	•	•	•	•	•	•	•	•	•	
	•	3	•	•	•	•	3	3	•	•	•	•	
	•	•	3	•	•	•	•	•	•	•	•	•	
	•	•	•	•	•	•	•	•	•	•	•	•	
	•	•	•	•	•	•	•	•	•	•	•	•	

b) the '3's provide the seed points and have been recognised as two separate peaks (sinks).

Band B

	•	•	•	•	•	•	•	•	•	•	•	•	
	•	•	•	•	•	•	•	•	•	•	•	•	
Band A	•	2	2	•	•	•	•	•	•	•	•	•	
	•	3	2	•	•	•	•	•	•	•	•	•	
	•	•	3	•	•	•	3	3	•	•	•	•	
	•	•	•	•	•	2	2	•	•	•	•	•	
	•	•	•	•	•	•	•	•	•	•	•	•	

c) the '2's are next connected to the '3's.

Figure 7.5 (a-f) Theoretical description of the watershed method (modified from Watson et al, 1992).

Band B

		0		2		4		6		8		10	
	0	•	•	•	•	•	•	•	•	•	•	•	•
		•	1	1	•	•	•	•	•	•	•	•	•
Band A	2	•	2	2	1	•	•	1	1	•	•	•	•
		•	3	2	1	•	1	3	3	1	•	•	•
	4	•	•	3	1	•	1	2	2	•	•	•	•
		•	•	1	•	•	1	•	•	•	•	•	•
	6	•	•	•	•	•	•	•	•	•	•	•	•

d) then the '1's are added, one at a time

•	•	•	•	•	•	•	•	•	•	•	•
•	1	1	1	•	•	1	1	1	•	•	•
•	2	2	1	1	•	1	1	1	1	•	•
•	3	2	1	•	1	3	3	1	•	•	•
•	•	3	1	•	1	2	2	•	•	•	•
•	•	•	•	•	1	1	•	•	•	•	•
•	•	•	•	•	•	•	•	•	•	•	•

(the watershed)

e) then the next shell of '1's. No more '1's can be found that satisfy the L condition, hence all the groups are defined.

•	•	•	•	•	•	•	•	•	•	•	•
•	c	c	c	•	•	d	d	d	•	•	•
•	c	c	c	c	•	d	d	d	d	•	•
•	c	c	c	•	d	d	d	d	•	•	•
•	•	c	c	•	d	d	d	•	•	•	•
•	•	•	•	•	d	d	d	•	•	•	•
•	•	•	•	•	•	•	•	•	•	•	•

f) finally the groups are labelled

Figure 7.5. (continued)

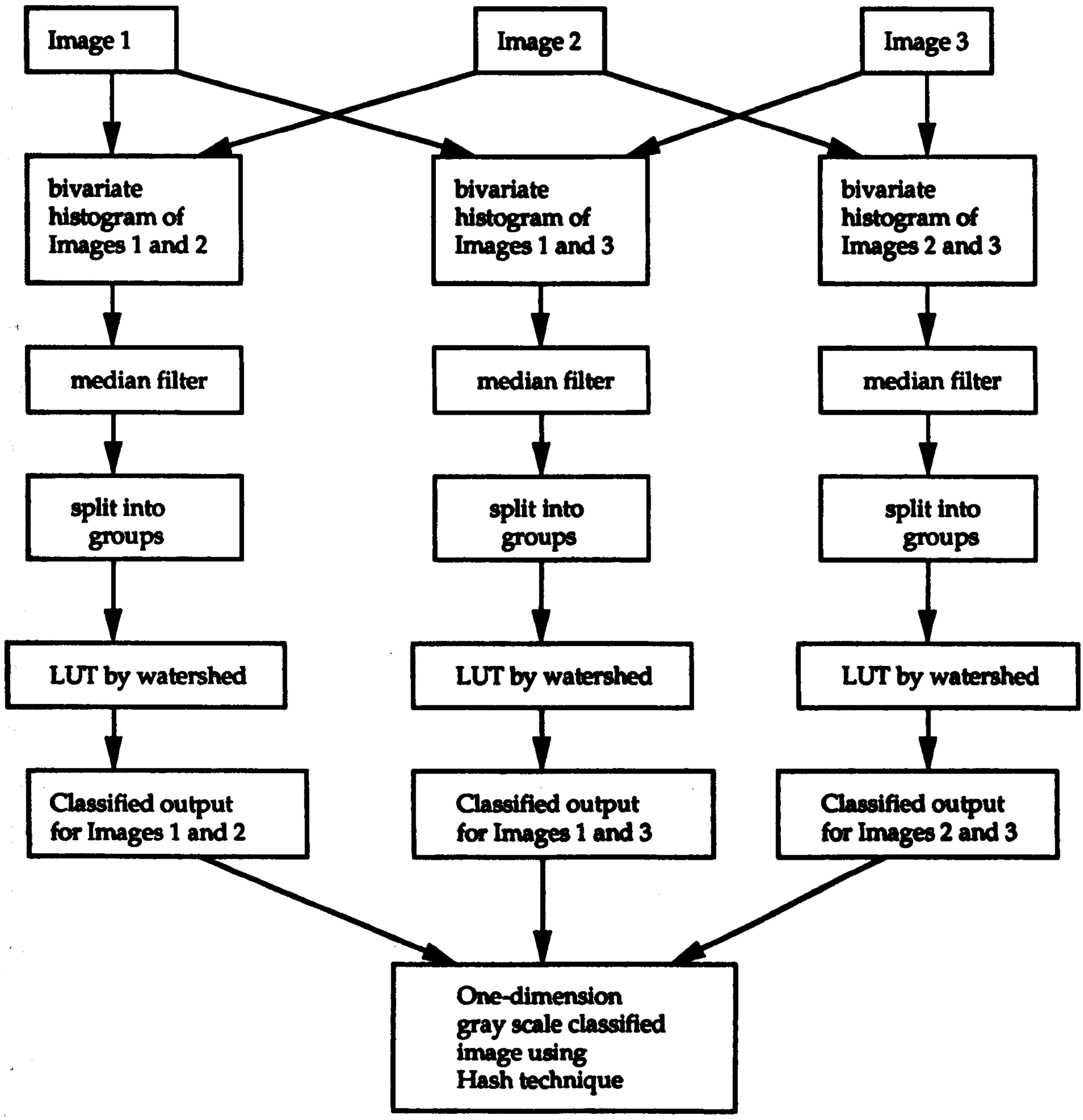

Figure 7.6. Flow diagram of the procedures used for watershed classification.

the same time improves the classification accuracy. In this study the reduction was achieved by transforming the RGB image (after BCET stretch) to an HSI image (as described in Sections 5.10 and 6.2.5) and selecting only the hue image as an input to the classification algorithm. The hue is independent from the brightness changes (or the intensity component) caused by shadowing, and seasonal solar elevation and azimuth variations (Magee et al., 1986). Therefore, it should not be affected by the shadow, and is only dependent on the three-band spectral signature of a pixel on the image (Liu and Moore, 1990). The second important advantage is that, computationally, it is more convenient to deal with a single hue value than the three RGB values. The concept of using hue images as an input for classification was previously applied by Liu and Haigh (1990) for a semi-arid area. They concluded that by using three hue images of each three of the adjacent seven TM bands (TM bands 7-6-5, 5-4-3 and 3-2-1) the shadow effect can be removed, whilst still preserving the relevant spectral information. In this study the idea was extended, and three hue components were extracted from three processed colour composite (best three band ratio images and three principal component images). As will be demonstrated in the results section, this development did improve the accuracy.

7.5 Accuracy assessment

After the classification had been performed, the agreement between the classified image and the reference data (classification accuracy) could be assessed. A complete accuracy check of a classification map has been described by Schwengredt (1983) and Lillisand and Kiefer (1987) as an unrealistic task that defeats the purpose of image classification in the first place. Rather, a representative test area should be used to assess the

classification accuracy. Lillisand and Kiefer (1987) have suggested using random sampling strategies, whereas Schowengerdt (1983) has proposed two strategies: 1) selection of homogeneous test areas specified by the analyst, or 2) selection of randomly located pixels or sites. In this study the first suggestion of Schowengerdt was adopted, and test areas were selected to include as many classes (rock types) as possible over as wide an area as possible.

These areas were selected using the option OVERLAY on the CHIPS software. This enables the user to draw filled polygons over the areas that are considered to be representative of class. Each of these overlays is associated with a number. At the end of this operation, an overlay image with different colour filled polygons is generated, which defines the test areas to be used in assessing the accuracy of classification.

The standard form of representing the degree of accuracy for the classification is the confusion (error) matrix, which is essential for any serious study of accuracy (Campbell, 1987; Mather, 1987; Dymond, 1992).

The matrix consists of a KxK array where K is the number of classes (Table 7.1b). The elements of this matrix refer to number of pixels, which the operator identifies from the reference data (ground truth) to be a member of class i, that were allocated to class j by the classifier. The values along the diagonal represent the number of correctly classified pixels, and their percentage is shown for each class in column (ii). The total number of correctly labelled pixels is the sum of the diagonal entries. The other elements of row i and column j show the number and distribution of incorrectly labelled pixels.

The errors of omission and commission are represented in columns (iii) and (iv) respectively. The error of omission results from a pixel, that is

of class i in reality, but was labelled by the classifier as members of some other classes. The error of commission results when a pixel that in reality is a member of some other class is assigned to class i by the classifier. The mean class accuracy was calculated by dividing the sum of the percentage for all the classes by the number of classes; in other words, it is the average of individual class accuracy. Whereas, the overall classification accuracy was calculated by dividing the total number of correctly classified pixels for all the classes by the total number of pixels that were defined by the operator (Mather, 1987). In this study, however, another matrix (Figure 7.1a) was used. This matrix contains the percentage that may show the variation in individual class accuracy more directly.

For more reliable estimates of the accuracy measurement, Jensen (1986) describes an equation for the calculation of the confidence limit (CL) in the classification accuracy. A similar equation has been proposed by Mather (1987). This equation is:

$$\text{Confidence Limit (CL)} = P - [1.645 \sqrt{(PQ/N)} + (50/N)]$$

whereas $P = \dfrac{\text{number of pixels correct}}{\text{total number of test pixels}} \times 100$

= the overall accuracy

Q = the failure percentage = $100 - P$

N = total number of test pixels

This equation was used to calculate the C.L. for the data in Tables 7.1 to 7.14. For example, if

$P = 90.8$, $Q = 100 - 90.8 = 9.2$ and $N = 3448$ then

$$C.L. = 90.8 - [\,1.645\ \sqrt{(90.8 \times 9.2/3448)} + (50/3448)\,]$$

$$= 90\%$$

This is the lower bound of the accuracy. The number of test pixels affects positively the confidence level; the larger the number of test pixels the greater the degree of confidence.

7.6 Methods of investigation

TM data of Silsilah ring complex and Jabal ar Raha test areas were selected to evaluate the classification algorithms described earlier in section (7.4). These two sites contain a wide variety of rocks; at the same time, geological maps and reports are available to define the ground truth.

All the six reflected TM bands were used. The classifications were performed into two sets of data:

1) The six reflected TM bands (original bands)

2) The processed bands, where a number of pre-classification manipulations and transformations were made to extract the greatest amount of information, reduce the data dimensionality as well as the shadow effect. Three hue components were extracted from the following:

a - The best combination of TM bands 7(R), 4(G) and 1(B). In addition, the hue component of the band combinations 7-5-4, 5-3-2, and 3-2-1 were also extracted.

b - The first three principal component images of the six reflected TM bands.

c - The best ratio colour composites (TM band ratios 5/4, 5/1, 5/7).

The images in sets 1 and 2 were used both to (i) test the accuracy of the two classification algorithms; the traditionally used maximum

likelihood algorithm and the watershed algorithm; (ii) at the same time, to test the results of using hue components as a classification input.

For each test area the following images were produced and will be designated hereafter by the symbols between brackets associated with each one.

- six original TM band images		(B 1-6)
- hue image for TM bands	7 - 4 - 1	(HB 7-4-1)
- " " "	7 - 5 - 4	(HB 7-5-4)
- " " "	5 - 3 - 2	(HB 5-3-2)
- " " "	3 - 2 - 1	(HB 3-2-1)
- hue image for best ratio colour composite		(HR 5/4-5/1-5/7)
- hue image for the first 3 PC		(HP 3-2-1)

The classification procedures (the maximum likelihood and the watershed classification algorithms) were applied to the following:

- the six reflected TM bands (original)	B1-6
- the two hue images	HP 3-2-1 and HR 5/4-5/1-5/7
- " "	HP 3-2-1 and HB 7-4-1
- " "	HR 5/4-5/1-5/7 and HB 7-4-1
- " "	HB 7-4-1 and HB 5-3-2
- " "	HB 7-5-4 and HB 3-2-1
- the three hue images	HP 3-2-1, HR 5/4-5/1-5/7, and HB 7-4-1
- " "	HB 7-4-1, HB 7-5-4, HB 5-3-2
- " "	HB 7-4-1, HB 6-5-4, HB 3-2-1
- " "	HB 7-5-4, HB 5-3-2, HB 3-2-1

The watershed algorithm (as discussed in section 7.4.2) analyses only two bands at a time, and if the input has more than two bands, it produces more than one classified image. To overcome this problem a program called HASHLIST (pers. com. A.I. Watson) was used. This program combined the classification labels from each of the input pairs, and produced a unique label. The maximum likelihood is a multi-dimensional classification algorithm, and produces only one label. These two classification techniques are available on the MicroVAX-II menu system in Stirling University's remote sensing laboratory.

7.7 Results

The accuracy of the algorithms (maximum likelihood and watershed) was tested using the methodology described earlier. Two test areas (Silsilah ring complx and Jabal ar Raha) were used to ensure a reasonable degree of representation. A total of 56 confusion matrices were constructed. Fourteen representative confusion matrices are shown in Tables 7.1 to 7.14. Each table contains two matrices. The rows in each of these matrices represent the classes in the classified image, whereas the columns represent the classes in the reference data. The values in the diagonal elements of matrix (a) are the percentage of correctly classified pixels, whereas in the second matrix (b) are the number of correctly classified pixels. The off diagonal elements are the error of commission or omission in percentage in matrix (a) and as number of pixels in matrix (b), (see section 7.5 for more details).

7.7.1 Silsilah ring complex

The rock units on this area were defined from reference data that include: a) the published geologic reports and maps (Du Bray, 1983, 1986 and 1988), and b) observation made during a field visit to the sites in November 1991. The classes are designated in the confusion matrix by the numbers as follows: eolian sand (1), Silsilah alkali granite (2), alkaline dacite (3), Hadhir aplite (4), Fawwarah alkali feldspar granite (5), Maraghan lithic graywack (6), vegetation (7), commendite (8), Proto-Fawwarah alkali-feldspar granite (9) and quartz (10). All the classification procedures described in the previous section were performed for this test area and evaluated. The following is a discussion of the results presented in Tables 7.1 to 7.8.

Using the original bands as an input for the maximum likelihood algorithm produced an overall accuracy of 66.1% with 64.78% confidence limit (Table 7.1). Only five out of ten classes were recognised by the algorithm. A recognisable class is defined, in this study, as the one that has a percentage of accuracy that equals or exceeds 50%. The accuracy range of these five classes starts from 60% for the alkali granite (2) to 98% for the alkali feldspar granite (5), with a mean class accuracy of 84% (for these five classes only). The mean class accuracy for all the classes is 45.2%. However, there are three classes that have been misclassified completely, which include the aplite (4), commendite (8) and quartz (10).

Reference Data Label	Classifier Label 1	2	3	4	5	6	7	8	9	10
1	27	0	0	0	73	0	0	0	0	0
2	0	60	0	0	0	40	0	0	0	0
3	0	0	89	0	0	2	9	0	0	0
4	0	44	3	0	0	52	0	0	1	0
5	2	0	0	0	98	0	0	0	0	0
6	0	4	0	0	0	96	0	0	0	0
7	0	0	22	0	0	2	77	0	0	0
8	0	1	34	0	0	57	8	0	0	0
9	2	28	7	0	0	58	1	0	5	0
10	0	0	0	0	100	0	0	0	0	0

	1	2	3	4	5	6	7	8	9	10	(i)	(ii)	(iii)	(iv)
1	65	0	0	0	177	0	0	0	0	0	242	27	177	7
2	0	312	0	0	0	210	0	0	2	0	524	60	212	115
3	0	0	475	0	0	9	47	0	0	0	531	89	56	180
4	0	46	3	0	0	54	0	0	1	0	104	0	104	0
5	5	0	0	0	269	0	0	0	0	0	274	98	5	326
6	0	34	0	0	0	816	0	0	0	0	850	96	34	473
7	0	0	94	0	0	7	336	0	0	0	437	77	101	65
8	0	2	75	0	0	125	17	0	0	0	219	0	219	0
9	2	33	8	0	0	68	1	0	6	0	118	5	112	3
10	0	0	0	0	149	0	0	0	0	0	149	0	149	0
											3448		1169	1169

(i) Number of pixels in class from ground reference data

(ii) Estimated class accuracy (%)

(iii) Errors of omission

(iv) Errors of commission

Mean class accuracy	MCA	=50.2%
Overall accuracy	OA	=66.1%
Confidence limit	CL	=64.78%

Table 7.1(a and b) Confusion matrix produced using the original six reflected TM bands (B1-6) as an input for the maximum likelihood algorithm.

Since the watershed method produced 15 classified images, for six input images (section 7.4.2), the best three classified images were chosen and gave, when combined, an overall accuracy of 74.7% with 73.5% confidence limit (Table 7.2). Five out of the ten classes were recognised with mean class accuracy of 90.8% and the accuracy range from 72% for the lithic greywacke class (6) to 100% for the vegetation class (7). Unlike the previous table, there is no complete misclassified class. The total errors of omission and commission were reduced from 1169 pixels to 871 pixels, and the mean class accuracy for the ten classes was 59.6%, compared with 45.2%.

Using the hue images, derived from different combinations of the original bands, as an input for the maximum likelihood algorithm increased the overall accuracy to 69.8% with 68.52% confidence limit (table 7.3). Six out of the ten classes were recognised with mean class accuracy of 82.5% (for these six classes) and the accuracy ranged from 51% for the commendite (8) to 99% for vegetation (7). One class was completely misclassified (quartz, 10) where 80% was confused with sand class (1). The mean class accuracy for the ten classes was 51.7% with total error of omission or commission of 1043 pixels.

By applying the watershed method for the previous set of images the overall accuracy increased sharply to 81.4% with 80.33% confidence limit (table 7.4). Seven classes were recognised, with a mean class accuracy (for these seven classes) of 83.9% and accuracy range from 57% for alkali feldspar granite (5) to 100% for vegetation (7), with no misclassified classes (the poorest was the quartz class (10) at 9%). The mean class accuracy was 65.2% and a total error of commission or omission of 640 pixels.

Using the combination of hue images derived from the best three bands, the best principal component images, and the best three band ratio

Classifier Label

Reference Data Label	1	2	3	4	5	6	7	8	9	10
1	48	0	0	0	52	0	0	0	0	0
2	0	91	0	0	0	9	0	0	0	0
3	0	0	99	0	0	0	0	1	0	0
4	0	70	1	10	0	18	0	1	0	0
5	6	0	0	0	92	0	0	0	0	2
6	0	28	0	0	0	72	0	0	0	0
7	0	0	0	0	0	0	100	0	0	0
8	0	7	37	1	0	15	0	39	1	0
9	0	57	6	2	0	22	0	3	11	0
10	0	0	0	0	66	0	0	0	0	34

	1	2	3	4	5	6	7	8	9	10	(i)	(ii)	(iii)	(iv)
1	117	0	0	0	125	0	0	0	0	0	242	48	125	17
2	0	478	0	0	0	45	0	0	1	0	524	91	46	397
3	0	0	527	0	0	1	0	3	0	0	531	99	4	90
4	0	73	1	10	0	19	0	1	0	0	104	10	94	4
5	17	0	0	0	252	0	0	0	0	5	274	92	22	224
6	0	242	0	0	0	608	0	0	0	0	850	72	242	123
7	0	0	0	0	0	0	437	0	0	0	437	100	0	0
8	0	15	82	2	0	32	0	85	3	0	219	39	134	7
9	0	67	7	2	0	26	0	3	13	0	118	11	105	4
10	0	0	0	0	99	0	0	0	0	50	149	34	99	5
											3448	871		871

MCA = 59.6%
OA = 74.7%
CL = 73.5%

Table 7.2(a and b) Confusion matrix of the watershed classification using the best three classified images produced from the original six reflected TM bands (B1-6); see text for explanation.

Classifier Label

Reference Data Label	1	2	3	4	5	6	7	8	9	10
1	93	1	0	0	6	0	0	0	0	0
2	8	86	0	1	0	4	0	0	1	0
3	0	1	87	0	0	1	0	10	0	0
4	25	61	0	8	0	3	0	2	2	0
5	47	39	0	0	11	3	0	0	0	0
6	0	19	1	0	0	79	0	1	0	0
7	0	0	1	0	0	0	99	0	0	0
8	16	5	16	0	1	7	3	51	1	0
9	10	28	2	2	3	30	0	14	13	0
10	80	12	1	0	0	0	4	3	0	0

	1	2	3	4	5	6	7	8	9	10	(i)	(ii)	(iii)	(iv)
1	226	2	0	0	14	0	0	0	0	0	242	93	16	364
2	43	451	0	5	0	19	0	2	4	0	524	86	73	400
3	0	5	463	2	1	5	0	55	0	0	531	87	68	50
4	26	63	0	8	0	3	0	2	2	0	104	8	96	9
5	129	106	0	0	29	9	0	0	1	0	274	11	245	22
6	0	163	8	0	2	668	1	8	0	0	850	79	182	87
7	0	0	3	0	0	0	434	0	0	0	437	99	3	13
8	35	10	36	0	2	16	6	111	3	0	219	51	108	88
9	12	33	2	2	3	35	0	16	15	0	118	13	103	10
10	119	18	1	0	0	0	6	5	0	0	149	0	149	0
											3448		1043	1043

MCA = 51.17%
OA = 69.8%
CL = 68.52%

Table 7.3(a and b) Confusion matrix produced using three hue images originated from each three adjacent bands of the reflected TM data as an input for the maximum likelihood classifier.

images, the accuracy increased sharply. For example, by using just the hue images for the principal component and ratio images (two input hue images only) the overall accuracy for the maximum likelihood was 79.8% with 78.69% confidence limit (table 7.5). Seven classes were recognised, with an accuracy ranging from 63% for commendite (8) to 100% for the Silsilah alkali granite (2), and mean class accuracy (for the seven classes) of 85.42%. Two classes were completely misclassified, which are the Hadhir aplite class (4), where 98% of it was confused with the alkali granite class (2), and the proto-Fawwarah alkali-feldspar granite (9), where 77% and 22% of it was confused with the sand and quartz classes, (1, 10) respectively. The mean class accuracy for the ten classes was 64.6%, with a total error of omission or commission of 697 pixels.

When the watershed method was applied to the same set, the overall accuracy was 80.8% with 79.72% confidence limit (table 7.6). Eight classes were recognised, with an accuracy ranging from 63% for alkali granite (2) to 100% for the lithic greywacke (6) and vegetation (7). One class was completely misclassified (class 9), where 82% and 15% were confused with the quartz and sand classes (10, 1) respectively. The mean class accuracy for the ten classes was 68.9%, with total error of omission and commission of 662 pixels.

When combining three hue images from the best three bands colour composite, band ratios, and principal component images, the maximum likelihood method produced its best results with an overall accuracy of 86.1% with 85.15% confidence limit (Table 7.7). Eight classes were recognised, with an accuracy ranging from 64% for commendite (8) to 99% for the lithic greywacke (6) and vegetation (7) and a mean class accuracy of 87.75% (for these eight classes). One class (aplite, 4) was misclassified

Classifier Label

Reference Data Label	1	2	3	4	5	6	7	8	9	10
1	80	1	0	0	2	0	14	2	0	0
2	3	92	1	0	1	2	0	1	1	0
3	0	0	91	0	0	2	1	5	1	0
4	6	55	0	25	4	3	0	1	7	0
5	4	5	0	0	57	2	28	0	1	2
6	0	0	2	0	0	97	0	0	0	0
7	0	0	0	0	0	0	100	0	0	0
8	7	3	12	0	0	3	1	70	2	0
9	3	22	17	2	3	14	0	8	31	1
10	2	1	1	0	4	0	82	1	0	9

	1	2	3	4	5	6	7	8	9	10	(i)	(ii)	(iii)	(iv)
1	193	2	0	0	6	0	35	6	0	0	242	80	49	57
2	18	480	3	1	3	9	2	3	5	0	524	92	44	108
3	0	0	485	0	0	10	5	26	3	2	531	91	46	67
4	6	57	0	26	4	3	0	1	7	0	104	25	78	5
5	11	15	0	1	157	6	77	0	2	5	274	57	117	27
6	0	0	15	0	3	828	0	1	3	0	850	97	22	50
7	0	0	0	0	0	0	435	2	0	0	437	100	2	244
8	15	7	27	1	1	6	3	154	4	1	219	70	65	49
9	4	26	20	2	4	16	0	9	36	1	118	31	82	24
10	3	1	2	0	6	0	122	1	0	14	149	9	135	9
											3448		640	640

MCA = 65.2%
OA = 81.4%
CL = 80.33%

Table 7.4(a and b) Confusion matrix produced using the same combination in table (7.3) as an input for the watershed classifier.

Reference Data Label \ Classifier Label	1	2	3	4	5	6	7	8	9	10
1	93	0	0	0	5	0	0	2	0	0
2	0	100	0	0	0	0	0	0	0	0
3	0	1	95	0	0	0	2	2	0	1
4	0	98	0	0	0	2	0	0	0	0
5	18	1	0	0	71	7	0	0	0	3
6	0	0	0	0	0	99	0	0	0	0
7	0	0	51	0	0	0	48	0	0	0
8	0	16	6	0	0	3	13	63	0	0
9	1	69	0	0	8	18	1	3	0	1
10	22	0	0	0	1	1	0	0	0	77

	1	2	3	4	5	6	7	8	9	10	(i)	(ii)	(iii)	(iv)
1	224	0	0	0	12	0	1	5	0	0	242	93	18	84
2	0	523	0	0	0	0	0	1	0	0	524	100	1	224
3	0	3	503	0	0	1	9	12	0	3	531	95	28	239
4	0	102	0	0	0	2	0	0	0	0	104	0	104	0
5	50	3	0	0	195	19	0	0	0	7	274	71	79	22
6	0	0	1	0	0	844	0	3	0	2	850	99	6	50
7	0	0	225	0	0	0	211	1	0	0	437	48	226	40
8	0	34	13	0	0	6	29	137	0	0	219	63	82	25
9	1	82	0	0	9	21	1	3	0	1	118	0	118	0
10	33	0	0	0	1	1	0	0	0	114	149	77	35	13
											3448		697	697

MCA = 64.6%
OA = 79.8%
CL = 78.69%

Table 7.5(a and b) Confusion matrix produced using combinations developed by this study of two hue images originated from the best three principalcomponents and the best three band-ratios (HP 3-2-1) and (HR 5/4-5/1-5/7) as an input for the maximum likelihood classification algorithm.

completely, 92% of it was confused with the alkali granite class. The mean class accuracy for the ten classes was 71.7%, with total error of omission or commission of 480 pixels.

By applying the watershed method for the same set it produced the best result with an overall accuracy of 90.8% with 90% confidence limit (table 7.8). Eight classes were recognised with mean classes accuracy of 91.9%. From Table 7.8 five of the ten classes were classified with a very high degree of accuracy (between 94% to 100%) which are the sand (1), alkali granite (2), alkaline dacite (3), lithic greywacke (6) and vegetation (7); whereas the commendite (8), quartz (10) and the alkali feldspar granite (5) have 83%, 83% and 78% respectively. The biggest misclassification was in the hadhir aplite class (4) where 84% of the class was confused with Silsilah alkali granite (2). However, although these two rocks were mapped as two different units, their surface appearances in the TM images are similar, which may be due to some extent to the weathering surface of these two rocks being similar (there is some iron oxide in both, that causes them to appear brown). The mean class accuracy for the ten classes was 78.6%, with total error of omission or commission of only 317 pixels. This set shows the highest accuracy, either in the confidence limit or as an overall or mean class accuracy, with the least error of commission or omission. A density sliced image "map" for the classified image is shown in Figure (7.8). Comparison of this figure with the published geologic map (Figure 2) indicates a very good agreement for most of the units. Greater disagreement occurs in the southwestern part of the ring, where there are greater amounts of misclassifications, in which most of the hadhir aplite unit for example was classified as alkali granite. The same thing occured to proto Fawwarah alkali feldspar granite unit but with slightly less severity.

Classifier Label

Reference Data Label	1	2	3	4	5	6	7	8	9	10
1	90	0	0	0	5	0	5	0	0	0
2	0	63	0	5	27	0	0	6	0	0
3	0	0	84	0	0	4	9	2	0	1
4	0	64	0	24	3	2	0	7	0	0
5	18	0	0	0	72	8	0	0	0	2
6	0	0	0	0	0	100	0	0	0	0
7	0	0	0	0	0	0	100	0	0	0
8	0	3	7	6	0	8	1	74	0	0
9	1	41	0	10	15	18	0	14	0	1
10	15	0	0	0	1	3	0	0	0	82

	1	2	3	4	5	6	7	8	9	10	(i)	(ii)	(iii)	(iv)
1	217	0	0	0	13	0	11	0	0	1	242	90	25	72
2	0	332	0	24	139	0	0	29	0	0	524	63	192	121
3	0	0	446	0	0	23	49	9	0	4	531	84	85	18
4	0	67	0	25	3	2	0	7	0	0	104	24	79	49
5	49	0	0	0	198	21	1	0	0	5	274	72	76	175
6	0	0	1	0	0	848	0	0	0	1	850	100	2	89
7	0	0	1	0	0	0	436	0	0	0	437	100	1	64
8	0	6	16	13	1	18	3	162	0	0	219	74	57	62
9	1	48	0	12	18	21	0	17	0	1	118	0	118	0
10	22	0	0	0	1	4	0	0	0	122	149	82	27	12
											3448		662	662

MCA = 68.9%
OA = 80.8%
CL = 79.72%

Table 7.6(a and b) Confusion matrix produced using the same combination as in table (7.5) as an input for the watershed classification.

Classifier Label

Reference Data Label	1	2	3	4	5	6	7	8	9	10
1	93	0	0	0	2	0	0	2	0	3
2	0	90	0	0	6	0	0	2	2	0
3	0	0	95	0	0	1	1	3	0	0
4	0	92	0	0	3	2	0	0	3	0
5	22	0	0	0	71	0	0	0	0	7
6	0	0	0	0	0	99	0	0	0	0
7	0	0	1	0	0	0	99	0	0	0
8	0	11	7	0	0	7	11	64	0	0
9	0	39	1	0	14	17	0	14	15	1
10	5	0	3	0	1	0	0	0	0	91

	1	2	3	4	5	6	7	8	9	10	(i)	(ii)	(iii)	(iv)
1	225	0	0	0	4	0	0	5	0	8	242	93	17	67
2	0	470	0	0	34	0	0	8	12	0	524	90	54	166
3	0	1	507	0	0	5	3	15	0	0	531	95	24	26
4	0	96	0	0	3	2	0	0	3	0	104	0	104	0
5	59	0	0	0	194	0	0	1	0	20	274	71	80	63
6	0	0	2	0	4	844	0	0	0	0	850	99	6	42
7	0	0	3	0	0	0	434	0	0	0	437	99	3	26
8	0	23	16	0	0	15	23	141	1	0	219	64	78	45
9	0	46	1	0	16	20	0	16	18	1	118	15	100	16
10	8	0	4	0	2	0	0	0	0	135	149	91	14	29
											3448	480	480	

MCA = 71.7%
OA = 86.1%
CL = 85.15%

Table 7.7(a and b) Confusion matrix produced using combinations developed by this study of three hue images originated from the best three bands (HB 7-4-1), the best three principal components (HP 3-2-1) and the best three band ratios (HR 5/4-5/1-5/7) as an input for the maximum likelihood classifier.

Classifier Label

Reference Data Label	1	2	3	4	5	6	7	8	9	10
1	94	0	0	0	5	0	0	0	0	1
2	0	99	0	0	0	0	0	0	0	0
3	0	0	99	0	0	0	0	1	0	0
4	0	84	0	15	0	0	0	0	1	0
5	12	8	0	0	78	0	0	0	0	1
6	0	0	0	0	0	100	0	0	0	0
7	0	0	1	0	0	0	99	0	0	0
8	0	4	9	0	0	1	1	83	2	0
9	0	36	0	3	3	14	0	7	36	0
10	13	0	0	0	3	1	0	0	0	83

	1	2	3	4	5	6	7	8	9	10	(i)	(ii)	(iii)	(iv)
1	227	0	0	0	13	0	0	0	0	2	242	94	15	51
2	0	519	0	2	0	0	0	1	2	0	524	99	5	162
3	0	0	525	0	0	0	0	6	0	0	531	99	6	24
4	0	87	0	16	0	0	0	0	1	0	104	15	88	7
5	32	23	0	0	215	0	0	0	0	4	274	78	59	21
6	0	0	0	0	0	848	0	1	1	0	850	100	2	20
7	0	0	4	0	0	0	433	0	0	0	437	99	4	2
8	0	9	20	1	0	2	2	181	4	0	219	83	38	16
9	0	43	0	4	3	17	0	8	43	0	118	36	75	8
10	19	0	0	0	5	1	0	0	0	124	149	83	25	6
											3448		317	317

MCA = 78.6%
OA = 90.8%
CL = 90.0%

Table 7.8(a and b) Confusion matrix produced using the same combination as in table (7.7) as an input for the watershed classification.

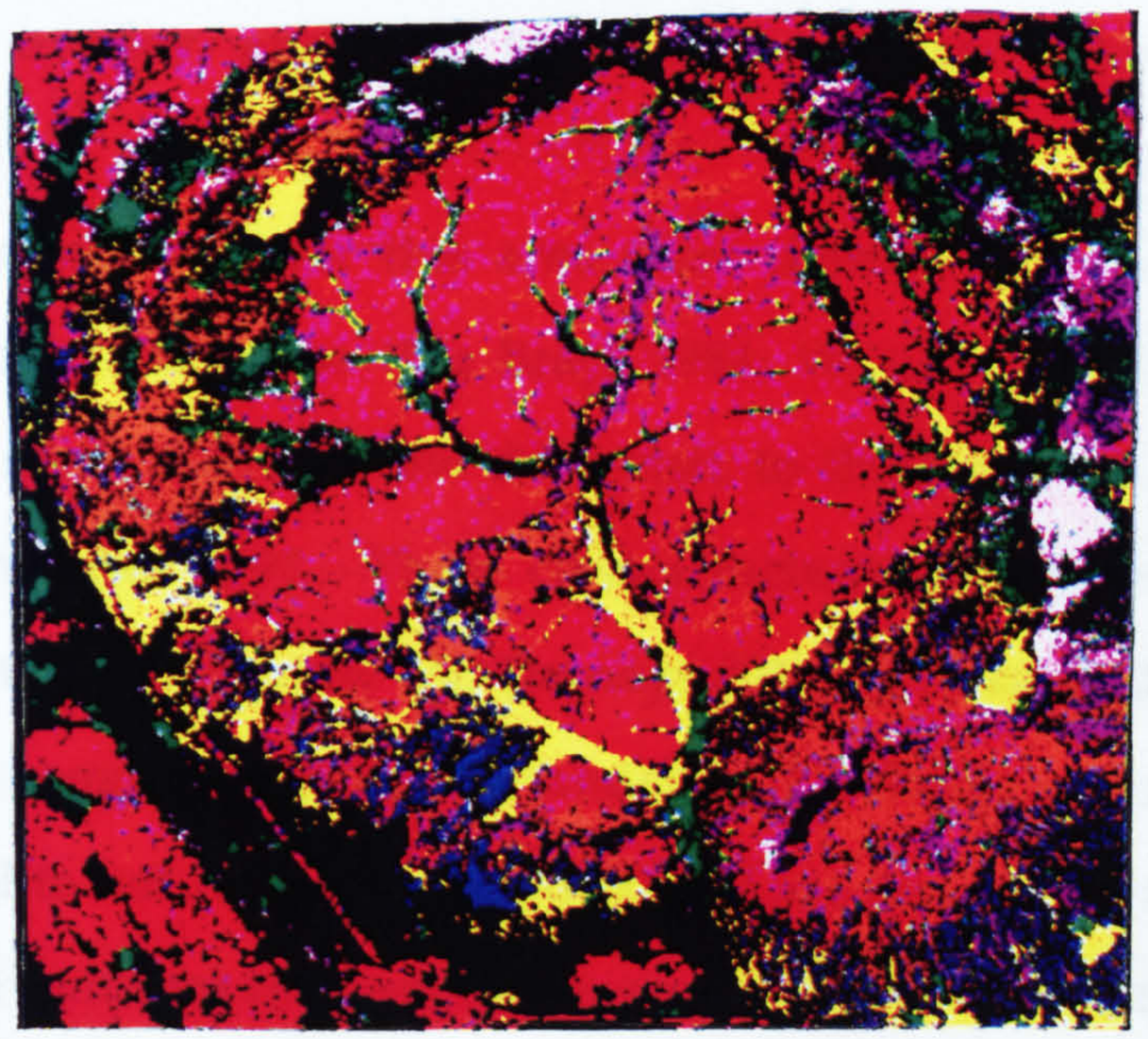

Figure 7.7. Density sliced, digital classified image (map), produced by the watershed algorithm for Silsilah ring complex.

Maraghan lithic greywacke at the centre of the ring complex was overmapped. Its area of occurrence increased to cover the paved road southwest of the ring complex, and part of the urban area.

7.7.2 Jabal ar Raha (test area 2)

The rocks available in this area are strongly weathered and separated into smaller areas filled by sediments and eolian sand. In order to eliminate the very small and insignificant areas, it was decided to mask these areas, by thresholding the intensity component image that was produced from RGB-HSI transformation, so that almost 95% of the sediment and insignificant rock areas were eliminated from the image. The masked areas were then saved as an overlay, and used to mask the images before applying the classification.

The classes used for this area were defined from a) the published geologic reports and maps (Du Bray, 1984; Williams et al., 1986), and b) observations made during a few days visit, to the test areas covered by this thesis, in November 1991. These classes include the following: carbonate rocks (1), Raha meta-rhyolite (2), Qarnayn lithic graywack (3), conglomerate (4), andesitic conglomerate (5), metandesite (6), Shaila quartz monzodiorite (7) meta-rhyolite tuff (8) meta-gabbro (9) and are designated in the Tables 7.9 to 7.14 by the numbers between brackets shown above. All the classification procedures described in section 7.5 were performed for this area. The results of applying both the maximum likelihood method and watershed method, to classify the nine categories by using original and processed images, are presented in Tables 7.9 to 7.14.

For this test area the overall accuracy of applying the maximum likelihood classifcation method for six original bands was very low (38.1%),

whereas by choosing the best three outputs of the watershed the overall accuracy was 49.8%. These two confusion matrices are not shown here, due to their very low accuracy.

By using the hue images for the different combinations of original bands, the overall accuracy of the maximum likelihood increased sharply to reach 70.7% with 69.31% confidence limit (Table 7.9). Five out of the nine classes were recognised with mean class accuracy of 85.8% (for the five classes) and an accuracy ranging from 68% for the conglomerate (4) to 98% for the meta-rhyolite class (2). Two of the nine classes were misclassified completely; these are the carbonates (1) and meta-gabbro (9). The mean class accuracy for the nine classes was 51.5% with total error of commission or omission of 860 pixels.

Using the watershed method for the previous set, the overall accuracy reached 81.4% with 80.21% confidence limit (Table 7.10). Seven classes were recognised with mean class accuracy of 79.3% and an accuracy range (for the seven classes) from 53% for the quartz monzodiorite class (7) to 97% for the meta-rhyolite (2). The mean class accuracy for the nine classes was 66.8%, with total error of omision or commission of 546 pixels.

By using the method introduced in this study, of combining the hue images of the best three bands with the hue images for principal component, and ratio images, the accuracy increases further. For example, by using two hue images only, as an input for the maximum likelihood algorithm (one principal component hue image, HP 3-2-1, and the hue image for the best three original bands, HB 7-4-1), the overall accuracy increased to 73.6% with 72.27% confidence limit (Table 7.11). In this table, six classes were recognised with mean class accuracy of 78%, with an accuracy that ranges from 53% for the meta-andesite class (6) to 93% for the

Classifier Label

Reference Data Label	1	2	3	4	5	6	7	8	9
1	0	8	0	0	69	22	0	0	0
2	0	98	1	0	0	0	0	1	0
3	0	17	81	2	0	0	0	0	0
4	0	6	21	68	2	0	2	0	0
5	0	0	0	2	93	4	0	0	0
6	0	3	1	4	67	15	2	7	0
7	0	12	13	25	27	3	19	1	0
8	0	3	0	2	0	5	0	89	0
9	0	30	70	0	0	0	0	0	0

	1	2	3	4	5	6	7	8	9	(i)	(ii)	(iii)	(iv)
1	0	3	0	0	25	8	0	0	0	36	0	36	0
2	0	864	5	3	0	0	0	9	0	881	98	17	220
3	0	106	501	12	0	0	0	0	0	619	81	118	225
4	0	28	95	302	9	2	9	1	0	446	68	144	103
5	0	0	0	4	190	9	0	1	0	204	93	14	236
6	0	6	1	8	122	28	4	13	0	182	15	154	37
7	0	35	37	73	80	10	57	2	0	294	19	237	13
8	0	5	0	3	0	8	0	133	0	149	89	16	26
9	0	37	87	0	0	0	0	0	0	124	0	124	0
										2935		860	860

MCA = 57.9%
OA = 70.7%
CL = 69.31%

Table 7.9(a and b) Confusion matrix produced using three hue images originated from each three adjacent bands of the reflected TM data as an input for the maximum likelihood classifier.

Classifier Label

Reference Data Label	1	2	3	4	5	6	7	8	9
1	14	8	0	0	31	42	6	0	0
2	0	97	2	0	0	0	0	2	0
3	0	6	90	2	0	0	0	0	2
4	0	1	9	85	1	0	4	0	0
5	0	0	0	1	75	18	5	0	0
6	1	1	0	4	19	64	9	1	0
7	0	2	7	14	14	9	53	0	0
8	0	3	0	0	0	6	0	91	0
9	0	15	45	5	0	0	3	0	32

	1	2	3	4	5	6	7	8	9	(i)	(ii)	(iii)	(iv)
1	5	3	0	0	11	15	2	0	0	36	14	31	4
2	0	851	14	0	0	0	0	15	1	881	97	30	76
3	0	38	555	12	0	0	1	1	12	619	90	64	131
4	0	3	39	378	6	0	18	0	2	446	85	68	70
5	1	0	0	3	153	36	11	0	0	204	75	51	93
6	2	2	0	8	34	117	17	2	0	182	64	65	85
7	1	7	22	41	42	25	155	0	1	294	53	139	53
8	0	5	0	0	0	9	0	135	0	149	91	14	18
9	0	18	56	6	0	0	4	0	40	124	32	84	16
										2935		546	546

MCA = 66.8%
OA = 81.4%
CL = 80.21%

Table 7.10(a and b) Confusion matrix produced using the same combination as in table (7.9) as an input for the watershed classifier.

meta-rhyolite class (2). Two of the nine classes were completely misclassified, and these were the carbonates (1) and meta-gabbro (9). The mean class accuracy for the nine classes was 55% with total error of omission or commission of 776 pixels.

When the watershed method was applied to the previous set (Table 7.12) the overall accuracy was, surprisingly, 70.1%, with 68.71% confidence limit. Five classes were recognised with mean class accuracy of 81.8%. Only one of the nine classes was completely misclassified (meta-gabbro, 9), which was confused with the meta-rhyolite (2), lithic greywacke (3) and andesite conglomerate (4) classes. The mean class accuracy for the nine classes was 54% with total error of commission and omission of 877 pixels.

By combining the hue images of the best three bands colour composite with the hue images of ratio and principal component (Table 7.13), the overall accuracy for the maximum likelihood was 73.4% with 72.06% confidence limit. Six classes were recognised, with mean class accuracy of 80.8% and accuracy ranging from 61% for the meta-andesite (6) to 93% for the meta-rhyolite (2). Two of the nine classes were completely misclassified: the carbonates (1) and meta-gabbro (9). The mean class accuracy for the nine classes was 55.6% with a total error of omission or commission of 781 pixels.

By applying the watershed method for the previous set the overall accuracy increased sharply to 87.3% with 86.29% confidence limit (Table 7.14). Seven classes were recognised with mean class accuracy of 86.6% and an accuracy ranging between 67% for quartz monzodionite (7) to 98% for meta-rhyolite (2). The mean class accuracy for the nine classes was 75.8% with total error of omission or commission of 373 pixels only. As in the previous area, this set produced the highest accuracy either as an overall or

Classifier Label

Reference Data Label	1	2	3	4	5	6	7	8	9
1	0	8	0	0	42	44	6	0	0
2	0	93	7	1	0	0	0	0	0
3	0	9	84	7	0	0	0	0	0
4	0	0	3	88	2	3	4	0	0
5	0	0	0	0	70	14	16	0	0
6	0	1	1	2	26	53	17	1	0
7	0	0	8	47	19	3	22	0	0
8	0	3	0	0	0	12	1	85	0
9	0	2	74	23	0	0	0	0	0

	1	2	3	4	5	6	7	8	9	(i)	(ii)	(iii)	(iv)
1	0	3	0	0	15	16	2	0	0	36	0	36	0
2	0	815	58	7	0	0	0	1	0	881	93	66	68
3	0	56	522	41	0	0	0	0	0	619	84	97	190
4	0	0	15	392	9	14	16	0	0	446	88	54	220
5	0	0	0	1	142	28	33	0	0	204	70	62	128
6	0	1	1	4	48	96	31	1	0	182	53	86	85
7	0	1	24	138	56	9	66	0	0	294	22	228	83
8	0	4	0	0	0	18	1	126	0	149	85	23	2
9	0	3	92	29	0	0	0	0	0	124	0	124	0
										2935		776	776

MCA = 66.8%
OA = 81.4%
CL = 80.21%

Table 7.11(a and b) Confusion matrix produced using combinations developed by this study of two hue images originated from the best three principal components (HP 3-2-1) and the best three bands (HB 7-4-1) as an input for the maximum likelihood classifier.

Classifier Label

Reference Data Label	1	2	3	4	5	6	7	8	9
1	8	0	0	0	42	50	0	0	0
2	3	81	7	0	0	0	0	9	0
3	2	7	90	1	0	0	0	0	0
4	0	0	11	79	1	0	7	1	0
5	0	0	0	0	65	18	14	3	0
6	1	0	1	2	26	46	10	14	0
7	0	1	15	38	12	9	25	1	0
8	0	1	0	0	1	4	0	94	0
9	0	2	96	2	0	0	0	0	0

	1	2	3	4	5	6	7	8	9	(i)	(ii)	(iii)	(iv)
1	3	0	0	0	15	18	0	0	0	36	8	33	38
2	26	711	62	3	0	0	0	79	0	881	81	170	51
3	11	45	559	4	0	0	0	0	0	619	90	60	273
4	0	0	48	354	6	1	33	4	0	446	79	92	124
5	0	0	0	0	133	37	28	6	0	204	65	71	107
6	1	0	1	4	48	84	18	26	0	182	46	98	87
7	0	2	43	111	36	25	74	3	0	294	25	220	79
8	0	1	0	0	2	6	0	140	0	149	94	9	118
9	0	3	119	2	0	0	0	0	0	124	0	124	0
										2935		877	877

MCA = 61%
OA = 70.1%
CL = 68.71%

Table 7.12(a and b) Confusion matrix produced from the same combination as in table (7.11) as an input for the watershed classifier.

Classifier Label

Reference Data Label	1	2	3	4	5	6	7	8	9
1	0	8	0	0	50	42	0	0	0
2	0	93	7	0	0	0	0	0	0
3	0	8	92	0	0	0	0	0	0
4	0	0	21	72	2	0	5	0	0
5	0	0	0	16	76	6	1	0	0
6	0	0	1	8	20	61	4	7	0
7	0	0	17	47	14	4	16	0	0
8	0	2	0	1	0	7	0	91	0
9	0	2	95	2	0	0	0	0	0

	1	2	3	4	5	6	7	8	9	(i)	(ii)	(iii)	(iv)
1	0	3	0	0	18	15	0	0	0	36	0	36	0
2	0	815	61	3	0	1	0	1	0	881	93	66	58
3	0	48	568	3	0	0	0	0	0	619	92	51	326
4	0	0	94	321	7	0	24	0	0	446	72	125	196
5	0	0	0	33	156	13	2	0	0	204	76	48	102
6	0	0	2	14	36	111	7	12	0	182	61	71	52
7	0	1	51	139	41	13	48	1	0	294	16	246	33
8	0	3	0	1	0	10	0	135	0	149	91	14	14
9	0	3	118	3	0	0	0	0	0	124	0	124	0
										2935		781	781

MCA = 55.66%
OA = 73.4%
CL = 72.06%

Table 7.13(a and b) Confusion matrix produced using combinations developed by this study of three hue images originated from the best three bands (HB 7-4-1), the best three principal components (HP 3-2-1) and the best three band ratios (HR 5/4-5/1-5/7) as an input for the maximum likelihood classifier.

Classifier Label

Reference Data Label	1	2	3	4	5	6	7	8	9
1	47	8	0	0	28	17	0	0	0
2	0	98	2	0	0	0	0	1	0
3	0	3	95	0	0	0	0	0	1
4	0	0	2	93	1	0	3	0	0
5	1	0	0	1	91	3	3	0	0
6	3	0	0	1	10	77	3	5	0
7	1	1	3	16	9	3	67	0	1
8	1	11	0	0	0	3	0	85	0
9	0	4	65	2	0	0	1	0	29

	1	2	3	4	5	6	7	8	9	(i)	(ii)	(iii)	(iv)
1	17	3	0	0	10	6	0	0	0	36	47	19	12
2	0	860	15	0	0	0	1	5	0	881	98	21	50
3	0	21	586	2	0	0	2	0	8	619	95	33	114
4	0	1	11	414	3	0	15	0	2	446	93	32	55
5	3	0	0	3	185	7	6	0	0	204	91	19	59
6	5	0	0	2	19	141	5	10	0	182	77	41	26
7	3	4	8	46	27	8	196	0	2	294	67	98	30
8	1	16	0	0	0	5	0	127	0	149	85	22	15
9	0	5	80	2	0	0	1	0	36	124	29	88	12
										2935		373	373

MCA = 75.8%
OA = 87.3%
CL = 86.29%

Table 7.14(a and b) Confusion matrix produced using the same combination as in table (7.13) as an input for the watershed classifier.

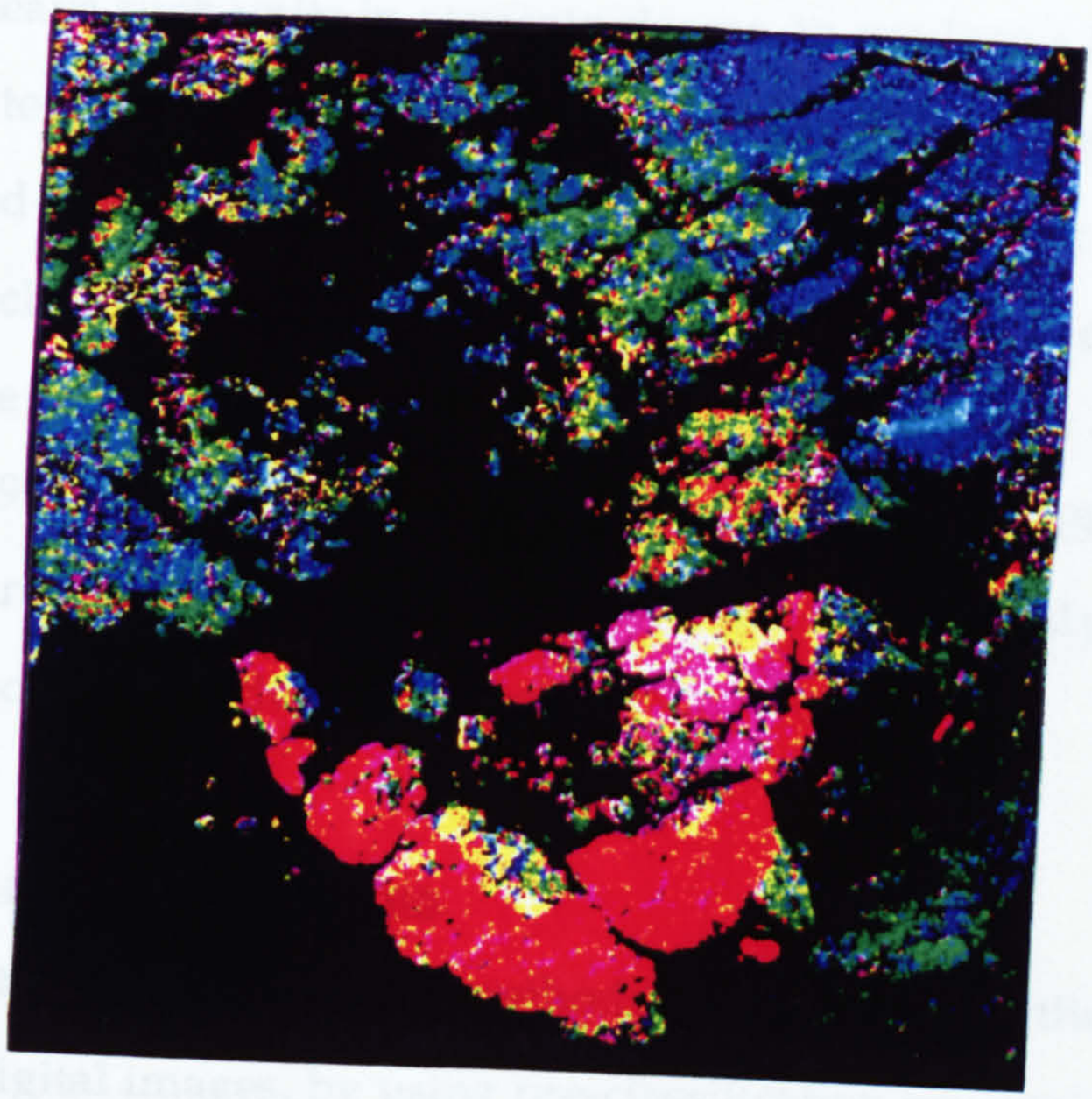

Figure 7.8. Density sliced, digital classified image (map), produced by the watershed algorithm for Jabal al Raha.

mean class accuracy with the least error of omission or commission. A density sliced image "map" for the classified image produced by this set is shown in Figure (7.8). Comparison of this figure, with the published geologic map (Chapter 2), indicates a very good agreement, for most of the units, except for the meta-gabbro unit, in which 65% of it was confused with the Qarnayn lithic greywacke, and also for the Shaila quartz monzodionite, where it was largely misclassified to meta-andesite and andesitic conglomerate units.

The low degree of accuracy associated with some rock units in both test areas is mainly due to their having very similar compositions. It was decided to leave such units in separate classes, to produce a more critical test for the strategies being evaluated in this chapter, but if such units were amalgamated with their spectrally and lithologically similar units, a greater degree of classification accuracy would have been achieved. It is unreasonable to expect objects too similar in the input data (such as classes (2), (4) and (9) in the Silsilah ring complex, and (1), (7) and (9) in the Jabal ar Raha test area) to be reasonably classified relying only on the pixel brightness recorded by the TM sensor.

7.8 Summary and conclusion

This study has explored methods of maximising the classification accuracy of digital images, by using pre-classification processing, and also by using a new method of classification.

This chapter demonstrates that a better degree of agreement, and hence a higher degree of accuracy, can be achieved by transforming the data from the RGB colour coordinate to the HSI coordinate. Applying such a transformation means the separation of the hue component (image) from

the saturation and intensity. The hue component is free from the shadow effect (which is the main cause of low classification accuracy for geological scenes) and represents only the spectral information of the different objects. Another important advantage of such a step is the dimensionality reduction of the data by two-thirds, which enables the use of information from other sources of data (e.g. band ratio, principal components).

This study has demonstrated that the combination of hue images of original bands with hue images of processed bands produced the most accurate classification. In addition, the watershed method gave the best accuracy of classification compared with the maximum likelihood method.

CHAPTER EIGHT

CONCLUSIONS AND SUGGESTIONS FOR FUTURE WORK

8.1 Conclusions

8.2 Suggestions for future work

8.1 Conclusions

Unlike the traditional photogeology techniques, which are well established in the geological community, digital image processing of satellite images is not as widespread as it should be. Haydn (1982) pointed out that the relatively limited use of the satellite images is mainly due to the badly processed images, that have been produced. Many of the hard copy products derived from satellite images can largely be regarded as the products of misunderstanding between the analysts on one hand, who rarely understand the geologists' needs (not application oriented), and the geologists (users) on the other hand, who are not experienced in remote sensing or digital image processing. The presentation of this satellite data in a highly enhanced product (hard copy) would give such a user the opportunity for efficiently directed field work.

Part of this thesis was particularly addressed to find the best way of presenting such enhanced product. Several 'traditional' methods (band ratio, principal component analysis) and more advanced techniques (decorrelation stretch and hue-saturation-intensity) were assessed. These techniques were compared for their ability to routinely produce a colour composite image with minimal information loss, and the optimal discrimination between different lithologies.

The results discussed in Chapter 6 showed that, although the results of both ratio and principal component techniques show some degree of discrimination between different lithologies, they have some disadvantages. For example, although ratio images do enhance the appearance of rocks containing the hydroxyls and iron bearing minerals (altered areas), they suffer from the suppression of albedo and topographic expression. The suppression of differences in albedo can cause lithologies

that have low albedo and those that have high albedo to be confused in the ratio images (e.g., the alkaline dacite and the alluvial deposits in Silsilah ring complex) (Figure 6.3). The suppression of topographic expressions makes it difficult to for example, transfer the information from the colour ratio composite (CRC) image to a topographic base map, or to locate the exact spatial distribution of the lithological units. In addition, the supposed elimination of shadow effects, by the ratio technique, is based on a theoretical assumption, that the earth's surface is Lambartian, which is not always true. The high amount of noise associated with ratio images is also a major disadvantage.

In the case of principal component technique, despite the colourful results in some of the test areas, these colours are difficult to interpret and are not dependent on the spectral variation. Furthermore, this technique uses the covariance matrix derived from the scene, and therefore the components, are scene dependent; thus the same rock type can (and usually does) appear with different colours in different images, making identification difficult. Textural information is also degraded with low signal to noise ratio, and this degrades to some extent the interpretability of the images.

A simpler and more understandable way of interpreting the TM data is to select three bands for display, as a colour composite. The use of statistical methods (e.g., OIF) to choose the best three band colour composite, frequently gave misleading results, since these methods do not take into account the difference between geologically significant variance and others. The analyst's judgment should remain a major factor in choosing between bands for colour composite images. It was found, using knowledge about reflection spectra, and visual examination of the different combinations,

that the display of TM band-7, TM band-4 and TM band-1 as red, green and blue respectively, gave the best image for lithological discrimination in the test areas.

The main criticism of the colour composite formed from these three bands (TM band-7, -4, -1 displayed as red, green and blue respectively), or in fact any three TM bands, was the restricted range of colours produced owing to the high degree of correlation between the bands. The decorrelation stretch technique was used to reduce this correlation. This technique did not produce any significantly better results. This may have been due to the fact that decorrelation stretch is based on a principal component transformation (which is dubious of itself) that selectively enhanced the noise.

In this study it was found that, by using a hue-saturation-intensity transformation the best results were obtained. This technique reduced the correlation between the bands, and gave a single colour composite image with both the spectral as well as spatial information enhanced. Further, the variation and purity of the colour was strongly enhanced without any distortion to the original.

This was made possible by transforming the RGB band colour composite, after equalising the means using BCET stretch, into HSI colour space. The saturation of the colours was increased by uniformly shifting the saturation to higher values. The intensity was controlled by an edge enhanced first principal component (Laplacian-addback) to provide a sharper image. This component was also shifted to a higher range, to enhance areas of low albedo. The transformation of these three components (HSI), after such manipulation, back to the RGB coordinate for display, produced an excellent output, which did not sacrifice any of the

information in the original data. Further, the colours can be related to the spectral reflectance curves, and remain stable from one image to another.

This technique with the methodology described here can be applied to enhance any other highly correlated data to produce an enhanced single colour product. An alternative, simpler way of using the first principal component, as a substitute for the intensity component, is to take the average of the six reflected bands (the first PC is a weighted sum of the reflecting bands).

This thesis also tested the canonical regression technique, with a new concept and strategy, that attempts to transform the imagery with respect to the major element chemical composition of the different lithologies. The method enables the construction of linear combinations of the bands, that are related to the chemical composition of the rocks. These canonical combinations can then be applied to unknown areas to predict their chemical composition. Results produced by this technique, although somewhat confusing, were regarded as encouraging. The application of such a technique using the methodology described here has some potential in combining Landsat TM-data with geochemical data.

Besides the image enhancement techniques that were designed to help the analyst in the visual interpretation of digital images. The last part of this thesis evaluated the accuracy of a new digital classification technique (The watershed), by comparing it to the maximum likelihood classification technique. In addition, this part also tested the effect of using pre-classification processing, in particular the 'hue' images. The 'hue' images were produced by transforming the original data from RGB to HSI coordinates and selecting the hue component. The main objective of such part was to improve classification accuracy.

The results in Chapter 7 of this thesis demonstrate, that the combination of hue images produced better results than using the original bands in the RGB coordinates. Furthermore, the combination of hue images of unprocessed bands (original) with the hue image of processed bands (hue image of principal component and band ratios) proved to be a better strategy that produced a more accurate classification than using the hue images of the original bands only. The watershed method gave the best accuracy compared with the maximum likelihood.

From the classification results, it was found that using original bands as an input for maximum likelihood classification produced an overall accuracy of 66.1% for the first test area, and 38.1% for the second test area. Using the same imagery as an input for the watershed, an overall accuracy of 74.7% for the first test area and 49.8% for the second test area was found. Using the hue images as an input for classification, an overall accuracy, for the maximum likelihood, of 86.1% in the first test area and 73.4% for the second area, was achieved. The watershed achieved an overall accuracy of 90.8% for the first test area and 87.3% for the second test area. Thus in both cases the watershed algorithm was clearly superior, and produced an acceptable degree of accuracy.

8.2 Suggestions for future work

In the case of canonical regression analysis, to fully justify its applicability, it is suggested that data with a higher spectral resolution should be used, e.g., Airborn Visible and Infrared Imaging Spectrometer (AVIRIS), or the High Resolution Imaging Spectrometer (HIRIS) records data in 224 spectral bands with spectral coverage between 0.4 μm to 2.5 μm. The HIRIS covers three times larger swathe width than AVIRIS and 2-5

times greater radiometric sensitivity but with 129 spectral bands covering the spectral range 0.4 μm to 2.5 μm.

It would also be useful if sample sets within the area under investigation could be extensively studied regarding the geochemical and mineral composition of the rocks. The higher spectral resolution will ensure more spectral sensitivity to the different lithologies and the higher number of bands will increase the number of canonical components produced. If the number of canonical components is equal to the number of chemical components, then it would be possible to find a more direct relation between both components. Furthermore, the higher spatial resolution will reduce the variation within the instantaneous field of view or the pixel area in the image.

In the field of visual enhancement or qualitative processing, high spatial resolution data, e.g. aerial photographs or SPOT panchromatic bands (10m), could be used to replace the intensity values in the hue-saturation-intensity colour space produced from a high spectral resolution, e.g TM data, provided careful registration between the images can be achieved. This step will (after transforming back to RGB coordinates) present an excellent product that shows the spectral advantages of the TM data with the textural advantages of the aerial photograph, or SPOT panchromatic.

In lithological classification, the use of higher spatial and spectral resolution imagery than the TM used here may increase accuracy, especially by using hue images in combination with the watershed algorithm.

The first Japanese Earth Resources Satellite (JERS-1), scheduled for launch in 1992, (Akiyama et al., 1989; Harding, 1989) carries an imaging sensor named Optical Sensor (OPS) that will collect information about the earth's surface in eight spectral bands (0.52-2.40μm) with 18 x 24 metre

ground resolution. From a geological point of view the availability of three bands in the range 2.0 to 2.4 μm, corresponding to the TM band-7, should improve the discrimination between differences associated with mineralization in alteration areas. Furthermore, this system also will have the advantage of simultaneous stereoscopic coverage (like SPOT stereoscopic coverage), provided by two bands located in the same spectral region (0.76-0.86 μm), one of which is nadir-viewing (band-3) and the other of which is forward-viewing. This system, therefore, will combine some of the advantages of both Landsat TM (spectral advantages) and SPOT (stereoscopic advantages). These advantages, and the uncertain future of the Landsat system, mean that the OPS could play an important role in the geological application of remote sensing.

In this thesis, two objectives were achieved: a) the quality of imagery, suitable for visual interpretation, has been improved, and b) the accuracy of automatic classification has been considerably improved. With the development of better imagery, the methods demonstrated in this thesis will be able to provide real solutions to the problems of geological remote sensing.

REFERENCES

Abrams, M.J. and Siegel, B.S. (1980), "Lithological Mapping," *Remote Sensing in Geology,* eds. B.S. Siegal and A.R. Gillespie (New York: Wiley), pp 381-418

Abrams, M.J. (1986), "Mapping of the Oman ophiolite using TM data," *Fifth Thematic Conference Remote Sensing for Exploration Geology* , Reno, Nevada, pp 85-91.

Abrams, M.J., Ashley, R.P., Rowan, L.C., Goetz, A.F.H. and Kahle, A.B. (1977), "Use of imaging in the 0.46-2.36 μm spectral region for alternation mapping in the cuprite mining district, Nevada," *U.S.G.S. Open File Report 77-585* .

Abrams, M.J., Brown, D., Lepley, L. and Sadowski, R. (1981), "Application of Remote Sensing to Porphyry Copper Exploration with Emphasis on the Proposed Landsat-D Thematic Mapper,"*1981 International Geoscience and Remote Sensing Symposium (IGARRS '81)* , IEEE Geoscience and Remote Sensing Society, June 8-10, 1941, Washington, D.C., pp 331-336.

Abrams, M.J., Brown, D., Lepley, L., and Sadowski, R. (1983), "Remote Sensing for Porphyry Copper Deposits in Southern Arizona," *Economic Geology* , Vol. 78, pp 591-604.

Abrams, M. and Kahle, A.B. (1984), "Recent Developments in Lithological Mapping Using Remote Sensing Data," *Remote Sensing for Geological Mapping* , eds. P. Teleki and C. Weber, Proceedings of the Seminar in Orleans, France pp 177-189.

Abrams, M.J., Rothery, D.A., and Pontual, A. (1988), "Mapping in the Oman ophiolite using enhanced Landsat Thematic Mapper images," *Tectonophysics* , Vol. 151, pp 387-401.

Adams, J.B., Evans, D.L., Farr, T.J, Smith, M., Staley, J.T., Palmer, F., Borns, F.J., Curtiss, B., Taylor-George, S., Roush, T. and Bjorkman, E. (1982), "Interpretation of weathered surfaces in arid regions using Landsat multispectral images," *The Thematic Conference on Remote Sensing of Arid and Semi-arid Lands,* Cairo, Egypt, pp 685-694.

Akiyama, Y., Komai, J., Yokoyama, T. and Okada, K. (1989), "Preliminary assessment of JERS-1 Optical Sensor based on the simulated Airborn data," *Proceedings of the Seventh Thematic Conference on Remote*

Sensing for Exploration Geology , Calgary, Alberta, Canada, pp 519-529.

Al-Dail, M., (1989) " The accuracy of Classification of Spot Imagery using the Watershed algorithm", *Msc. dessertation,* department of physics, electronics and manufacturing engineering, Dundee University, U.K.

Al-Sari, A.M., (1989). A Geological investigation of multispectral remote sensing data for the mahd Adh Dhahab and Jabal Said districts, western Saudi Arabia, *Ph.D thesis,* University of Durham, U.K.

Amos, B.J. and Greenbaum, D. (1989), "Alteration detection using TM imagery: the effect of supergene weathering in an arid climate," *International Journal of Remote Sensing* , Vol. 10, No. 3, pp 515-527.

Anderson, J.M. (1985), "The Physical Basis of Remote Sensing," *Proceedings of University of Dundee Summer School -- Remote Sensing Application in Civil Engineering* , U.K., pp 1-7.

Avery, T.E. and Berlin, G.L. (1985), *Interpretation of Aerial Photographs* , 4th ed. (Minneapolis: Burgess).

Barrett, E.C., and Curtis, L., (1982), *Introduction to Environmental Remote Sensing* , 2nd edition, Chapman and Hall, London.

Benie, G.B., and Thomson, K.P.B., (1992) "Hierachical image segmentation using local and adaptive similarity rules", *International Journal of Remote Sensing,* Vol. 13, No. 8, pp 1559-1570.

Berlin, G.L. and Chavez, P.S. (1986), "Quantitative procedure for producing colour-calibrated Thematic Mapper natural-colour images," *Fifth Thematic Conference on Remote Sensing for Exploration Geology* , Reno, Nevada, pp 639-648.

Bernstein, R. (1976), "Digital image processing of earth observation sensor data," *IBM Journal of Research and Development* , Vol. 20, pp 40-57.

Bernstein, R., Lotspiech, J.B., Myers, J., Kolsky, H.G. and Lees, R.D. (1984), "Analysis and processing of Landsat-4 sensor data using advanced image processing techniques and technologies," *IEEE Transactions on Geoscience and Remote Sensing* , Vol. GE-22, No. 3, pp 192-221.

Beucher, S. (1982), "Watersheds of function and picture segmentation," *Proceedings of IEEE International Conference on Acoustics, Speech and Signal Processing* , pp 1928-1931.

Blodget, H.W., Brown, G.F. and Moik, J.G. (1975), "Geological mapping in northwestern Saudi Arabia using Landsat multispectral techniques," *NASA Earth Resources Survey Symposium* , July 1975, Houston, Texas, NASA TM X-58168, pp 971-989.

Blom, R., Abrams, M. and Adams, M. (1980), "Spectral reflectance and discrimination of plutonic rocks in the 0.45 to 2.45 μm region," *Journal of Geophysical Research* , Vol. 85, No. B5, pp 2638-2648.

Bodechtel, J. and Frei, M. (1992), "Geoscientific achievements," *International Journal of Remote Sensing* ,Vol. 13, Nos. 6 and 7, pp 1305-1318.

Booth, D.J. and Oldfield, R.B. (1989), "A comparison of classification algorithms in terms of speed and accuracy after the application of a post-classification model filter," *International Journal of Remote Sensing* , Vol. 10, No. 7, pp 1271-1276.

Bramkamp, R.A., Ramirez, L.F., Brown, G.F., and Pocock, A.E., (1963), Geology map of the Wadi ar Rimah quadrangle, Kingdom of Saudi Arabia: U.S. Geological Survey Miscellaneous Geologic Investigations Map *I-206 A*, scale 1:500,000.

Brickey, D.W. (1986), "The use of Thematic Mapper imagery for mineral exploration in the sedimentary terrain of the Spring Mountains, Nevada," *Fifth Thematic Conference on Remote Sensing for Exploration Geology* , Reno, Nevada, pp 607-613.

Buchanan, M.D. and Pendegrass, R. (1980), "Digital image processing: can intensity, hue and saturation replace red, green and blue?" *Electro-optical Systems Design* , Vol. 12, No. 3, pp 29-36.

Buckingham, W.F., and Sommer, S.C. (1983), "Mineralogical Characterization of Rocks Surfaces formed by Hydrothermal Alteration and Weathering -- Application of Remote Sensing," *Economic Geology*, Vol. 78, pp 664-674.

Campbell, J.B. (1987), *Introduction to Remote Sensing* (New York and London: The Guilford Press).

Cañas, A.A.D. and Barnett, M.E. (1985), "The generation and interpretation of false colour principal component images," *International Journal of Remote Sensing* , Vol. 6, No. 61, pp 867-881.

Carper, W.J., Lillisand, T.M. and Kiefer, R.W. (1990), "The Use of Intensity-Hue-Saturation Transformation for Merging SPOT Panchromatic and

Multispectral Image Data," *Photogrammetric Engineering and Remote Sensing* , Vol. 56, No. 4, pp 459-467.

Carter, W.D. (1984), "Remote Sensing in Geology: A Decade of Progress," *Proceedings of IUGS and UNESCO Seminar on "Remote Sensing for Geological Mapping"* , BRGM, Orleans, France, pp 15-27.

Chavez, P.S. (1988), "An improved dark object subtraction technique for atmospheric scattering correction of mlutispectral data," *Remote Sensing of Environment* , Vol. 24, pp 459-479.

Chavez, P.S. Jr., Berlin, G.L. and Mitchell, W.B. (1977), "Computer enhancement techniques of Landsat MSS digital images for land use/cover assessment," *Proceedings of the Sixth Remote Sensing of Earth Resources Symposium* , Tullahoma, Tennesse., pp 259-275.

Chavez, P.S. Jr., Berlin, G.L. and Sowers, L.B. (1982), "Statistical Methods for Selecting Landsat MSS Ratios," *Journal of Applied Photographic Engineering* , Vol. 8, No. 1, pp 23-30.

Chavez, P.S. Jr., Everett, J., Kahle, A., Kieffer, H., Kitcho, C., Milton, N., Monat, D., (1983), "Thematic Mapper data analysis", *Frontiere for geological remote sensing from space,* eds. F.B. Henderson and Barrett, N. Rock (Falls Church, Va: American Society of Photgrammetry), pp 21-27.

Chavez, P.S. Jr., Guptill, S.C. and Bowell, J.A. (1984), "Image processing techniques for thematic mapper data," Technical Paper, *50th Annual Meeting of American Society of Photogrammetry* , Vol. 2, pp 728-742.

Chavez, P.S. Jr. and Kwarteng, A.Y. (1989), "Extracting spectral contrast in Landsat Thematic Mapper image data using selective principal component analysis," *Photogrammetric Engineering and Remote Sensing* , Vol. 55, No. 3, pp 339-348.

Cole, J.C., (1981), Reconnaissance geology of the Al Jurdhawiyah quadrangle, sheet 25/42 D, Kingdom of Saudi Arabia: U.S. Geological Survey Saudi Arabian Mission *Miscellaneous Map 44,* scale 1:100,000.

Cole, J.C., (1985), Reconnaissance geology of the Al Abanat quadrangle, sheet 25/42 D, Kingdom of Saudi Arabia: Saudi Arabian Deputy Ministry for Mineral Resources *Open-file Report USGS-OF-05-17,* scale 1:100,000.

Cole, J.C., (1988), Geology of the Aban al Ahmar quadrangle, sheet 25F, Kingdom of Saudi Arabia: Saudi Arabian Deputy Ministry for Mineral Resources *Open-file Report USGS-OF-04-9,* scale 1:250,000.

Cole, J.C., (1990) "Geological Setting", in Metallic- mineral assessment of the Aban al Ahmar quadrangle, sheet 25F, *USGS TR-07-4*, Directorate General of Mineral Resources Jeddah, Saudi Arabia, pp. 7-14.

Cole, J.C., and Bohannon, R.G., (1985), Reconnaissance geology of the An Nabhaniyah quadrangle, sheet 25/43 A, Kingdom of Saudi Arabia: Saudi Arabian Deputy Ministry for Mineral Resources *Open-file Report USGS-OF-05-19*.

Cole, J.C., and Hedge, C.E., (1986), Late Proterozoic geochronology in the northeastern shield of Saudi Arabia: Saudi Arabian Deputy Ministry for Mineral Resources *Technical Record USGS-TR-05-5*.

Colwell, R.N., ed. (1983), *Manual of Remote Sensing* , 2nd ed. (Falls Church, Va.: American Society of Photogrammetry).

Cracknell, A. and Hayes, L. (1991), *Introduction to Remote Sensing* (London: Taylor and Francis).

Crippen, R.E. (1986), "The regression intersection method of adjusting image data for band ratio," *Fifth Thematic Conference on Remote Sensing for Exploration Geology* , Reno, Nevada, pp 407-416.

Crippen, R.E. (1989), "Selection of Landsat TM band and band-ratio combinations to maximize lithologic information in color composite display," *The Seventh Thematic Conference on Remote Sensing for Exploration Geology* , Calgary, Alberta, Canada, pp 917-921.

Crosta, A.P. and Moore, J.M. (1989), "Geological mapping using Landsat Thematic Mapper imagery in Almeria Province, southeast Spain," *International Journal of Remote Sensing* , Vol. 10, No. 3, pp 505-514.

Curlis, D.J., Anderson, R.L. and Frazer, R.W. (1986), "Image creation and enhancement using the IHS color transform ," *Fifth Thematic Conference on Remote Sensing for Exploration Geology,* Reno, Nevada, pp 405-406.

Curran, P.J. (1985), *Principles of remote sensing* (New York: Longman Inc.).

Davis, L.S. (1975), "A survey of edge detection techniques," *Computer Graphics Image Processing* , Vol. 4, pp 248-270.

Davis, P.A. and Berlin, G.L. (1989), "Rock discrimination in the complex geologic environment of Jabal Salma, Saudi Arabia, using Landsat TM data," *Photogrammetric Engineering and Remote Sensing* , Vol. 55, No. 55, pp 1147-1160.

Drury, S.A. (1986), "Geological Applications of Airborne Thematic Mapper Data: Assynt: Sutherland," *NERC Special Topic: Remote Sensing Report* , 1986.

Drury, S.A. (1987), *Image Interpretation in Geology* (London: Allen and Unwin (Publishers) Ltd.).

Drury, S.A. (1990), *A guide to remote sensing interpreting images of the earth* (Oxford: Oxford University Press).

Drury, S.A. and Hunt, G.A. (1989), "Geological uses of remotely-sensed reflected and emitted data of lateritized Archaean terrain in Western Australia," *International Journal of Remote Sensing* , Vol. 10, No. 3, pp 475-497.

Drysdall, A.R., Ramsay, C.R. and Stoeser, D.B. (1986), "Introduction", Felsic Plotonic Rocks and Associated mineralization of the Kingdom of Saudi Arabia, Deputy Ministry for Mineral Resources, Jeddah, Saudi *Arabia Bulletin No. 29*, pp 1-9.

Du Bray, E.A., (1983), Reconnaissance geology of the Jabal as Silsilah quadrangle, sheet 26/42 D, Kingdom of Saudi Arabia: Saudi Arabian Deputy Ministry for Minerals Resources *Technical Record USGS-TR-03-4*, scale 1:100,000.

Du Bray, E.A., (1984), Geology of the Silsilah ring complex, Kingdom of Saudi Arabia: Saudi Arabian Deputy Ministry for Minerals Resources *Technical Record USGS-TR-04-19* .

Du Bray, E. (1986), "Jabal Silsilah tin prospect, Najd region, Kingdom of Saudi Arabia," *Journal of African Earth Sciences* , Vol. 4, pp 237-247.

Du Bray, E.A., (1988), Geology of the Silsilah ring complex and Associated Tin Mineralization, Kingdom of Saudi Arabia: *U.S. Geological Survey Professional paper; 1459*, USA Government Printing Office Washington.

Dymond, J.R. (1992), "How accurately do image classifiers estimate area?" *International Journal of Remote Sensing* , Vol. 13, No. 9, pp 1735-1742.

Ekstrom, M.P., ed. (1984), *Digital Image Processing* (Orlando: Academic Press).

Elachi, C. (1983), "Microwave and Infrared Satellite Remote Sensors," *Manual of Remote Sensing* , 2nd ed., ed. R.N. Colwell (Falls Church, Va.: American Society of Photogrammetry), Vol. 1, pp 571-650.

Elachi, C. (1987), *Introduction to the Physics and Techniques of Remote Sensing* (New York: John Wiley & Sons).

Elvidge, C. D. (1986), 'Use of calibration targets in the measurement of 2.22 mm mineral absorption features in Thematic Mapper data," *Fifth Thematic Conference on Remote Sensing for Exploration Geology* , Reno, Nevada , pp 427-438.

Estes, J.E. (1978), "The electromagnetic spectrum and its use in remote sensing," ed. B. Richeson, *Introduction to Remote Sensing of Environment* , (Dubuque, Iowa: Kendall/Hunt Publishing Co.), pp 15-43.

Estes, J.E., Hajic, E.J. and Tinney, L.R. (1983), "Fundamentals of Image Analysis: Analysis of Visible and Thermal Infra-red Data," *Manual of Remote Sensing* , 2nd edition, ed. R.N. Colwell, (Falls Church, Va: American Society of Photogrammetry), Vol. 1, pp 987-1124.

Feldman, S.C. and Taranik, J.V. (1986), "Correlation between high resolution remote sensing imagery and hydrothermal alteration, Tybo Mining District, Nevada," *Fifth Thematic Conference Remote Sensing for Exploration Geology* , Reno, Nevada, pp 279-297.

Ferrari, M.C. (1992), "Improved decorrelation stretching of TM data for geological applications: first results in northern Somalia," *International Journal of Remote Sensing* , Vol. 13, No. 5, pp 841-851.

Fielding, E.J. (1985), "Lithologic discrimination of volcanic and sedimentary rocks by spectral examination of Landsat TM data from the Puna, Central Andes Mountains," *Fourth Thematic Conference on Remote Sensing for Exploration Geology* , San Francisco, California, pp 619-630.

Fraser, S.J. (1990), "Discrimination and identification of ferric oxides using Thematic Mapper data: Newman case study," *International Journal of Remote Sensing* , Vol. 2, No. 3, pp 635-641.

Freden, S.C. and Gordon, F. Jr. (1983), "Landsat Satellites," *Manual of Remote Sensing* , 2nd ed., ed. R.N. Colwell (Falls Church, Va.: American Society of Photogrammetry), Vol.1, pp 517-570.

Gillespie, A.R. (1980), "Digital techniques of image enhancement," *Remote Sensing in Geology* , eds. B.S. Siegal and A.R. Gillespie (New York: John Wiley & Sons), pp 139-226.

Gillespie, A.R., Kahle, A.B., and Walker, R.E. (1986), "Color enhancement of highly correlated images, I: decorrelation and HSI contrast stretches," *Remote Sensing of Environment* , Vol. 20, pp 209-235.

Goetz, A.F.H. (1980), "Geological remote sensing in the 1980's," *Remote Sensing in Geology* , eds. B.S. Siegal and A.R. Gillespie (New York: John Wiley & Sons), pp 679-686.

Goetz, A.F.H. (1989a), "Spectral Remote Sensing in Geology," *Theory and Applications of Optical Remote Sensing* , ed. G. Asrar (New York: John Wiley & Sons), pp 491-526.

Goetz, A.F.H. (1989b), "Concepts and advancements in spectral remote sensing for geology," *Proceedings of the Seventh Thematic Conference on Remote Sensing for Exploration Geology* , Calgary, Alberta, Canada, p 13.

Goetz, A.F.H., Rock, B.N. and Rowan, L.C. (1983), "Remote sensing for exploration: an overview," *Economic Geology* , Vol. 78, No. 4, pp 573-590.

Goetz, A.F.H., and Rowan, L.C. (1981), "Geologic Remote Sensing," *Science* , Vol. 211, pp 781-791.

Goetz, A.F.H., Solomon, G.V.J.E. and Rock, B.N. (1985), "Imaging spectrometry for earth remote sensing," *Science* , Vol. 228, No. 4704, pp 1147-1153.

Gonzalez, R.C. and Wintz, P. (1987), *Digital Image Processing* , 2nd ed. (Wokingham, England: Addison-Wesley Publishing Company).

Greenbaum, D. (1987), "Lithological discrimination in central Snowdonia using airborne multispectral scanner imagery," *International Journal of Remote Sensing* , Vol. 8, pp 799-816.

Guha, P.K. and Mallick, S.B. (1985), "Digital MSS and spectral reflectance data in lithologic discrimination," *ITC Journal* , pp 42-46.

Guo, L.J. (1991), "Balance contrast enhancement technique and its application in image colour composition," *International Journal of Remote Sensing* , Vol. 12, No. 10, pp .

Guo, L.J. and Haigh, J.D. (1990), "A 3-dimensional feature space iterative clustering method for multispectral image classification," *Remote Sensing Science for the Nineties* , pp 2371-2375.

Guo, L.J., and Moore, J.McM., (1989), "Colour enhancement and shadowsuppression techniques for TM images," *Seventh Thematic Conference on Remote Sensing for Exploration Geology,* Calgary, Alberta, Canada, pp 901-915.

Gupta, R.P. (1991), *Remote Sensing Geology* (Berlin: Springer-Verlag).

Haack, B. and Jampolar, S. (1987), "Landsat TM and MSS digital data comparison: Imperial Valley," *The Twenty-First International Symposium on Remote Sensing of Environment,* Ann Arbor, Michigan, pp 853-861.

Harding, D.J. (1989), "Comparison of the capabilities of the Japanese Earth Resources Optical Sensor and the Landsat Thematic Mapper for lithologic mapping," *Proceedings of the Seventh Thematic Conference on Remote Sensing for Exploration Geology* , Calgary, Alberta, Canada, pp 484-486.

Hardy, J.R., (1983), "Data Collection by remote sensing for land resources survey", *Terrain Analysis and remote sensing,* ed. J.R.G. Townshend (London: George Allen & Unwin), pp 16-36.

Harris, R. (1987), *Satellite Remote Sensing: An Introduction* (London and New York: Routledge and Kegan Paul).

Haydn, R. (1982), "Some aspects of the presentation of remote sensing data," *Proceedings of an EARSel-ESA Symposium, Igls, Austria* , pp 77-80.

Haydn, R. (1983), "A Concept for the processing and display of Thematic Mapper data," *Proceedings of the Symposium on Landsat-4 Science Characterization Early Results* , NASA publication 2355 (Greenbelt, Md.), pp 217-237.

Haydn, R., Dalke, G.W., Henkel, J., Bare, J.E. (1982), "Application of the IHS colour transform to the processing of multisensor data and image enhancement," *Proceedings of the International Symposium on Remote Sensing of Arid and Semi-Arid Lands* , Cairo, Egypt, pp 599-616.

Henderson, F.B. and Rock, B.N., eds. (1983), *Frontiers for Geological Remote Sensing from Space* , American Society of Photogrammetry.

Holz, R.K., ed. (1985), *The Surveillant Science, Remote Sensing of the Environment* (New York: John Wiley & Sons).

Huckerby, J.A., Magee, R., Moore, J.McM. and Coates, D. (1986), "Thematic Mapper data applied to alteration zone mapping for gold exploration in southeast Spain," *Fifth Thematic Conference on Remote Sensing for Exploration Geology* , Reno, Nevada, pp 591-599.

Huggett, R., (1985), *Earth Surface Systems* (Berlin: Springer-Verlag).

Hunt, G.R. (1980), "Electromagnetic radiation: the communication link in remote sensing," *Remote Sensing in Geology* , ed. B.S. Siegal and A.R. Gillespie (New York: John Wiley & Sons), pp 5-45.

Hunt, G.R., Drury, S.A. and Rothery, D.A. (1986), "Techniques for choosing the optimum TM channel combinations for lithological mapping in semi-arid terrains," *Proceedings of the International Symposium, Mapping from Modern Imagery* , Edinburgh, Remote Sensing Society/ISPR Commission VII, pp 637-646.

Hunt, G.R. and Salisbury, J.W. (1970), "Visible and near-infrared spectra of minerals and rocks: I. Silicate minerals," *Modern Geology* , Vol. 1, pp 283-300.

Hunt, G.R. and Salisbury, J.W. (1971), "Visible and near-infrared spectra of minerals and rocks: II. Carbonates," *Modern Geology* , Vol. 2, pp 23-30.

Hunt, G.R. and Salisbury, J.W. (1976a), "Visible and near-infrared spectra of minerals and rocks: XI. Metamorphic rocks," *Modern Geology* , Vol. 5, pp 211-217.

Hunt, G.R. and Salisbury, J.W. (1976b), "Visible and near-infrared spectra of minerals and rocks: XII. Sedimentary rocks," *Modern Geology* , Vol. 5, pp 219-228.

Hunt, G.R., Salisbury, J.W. and Lenhoff, C.J. (1971), "Visible and near-infrared spectra of minerals and rocks: III. Oxides and hydroxides," *Modern Geology* , Vol. 2, pp 195-205.

Hunt, G.R., Salisbury, J.W., and Lenhoff, C.J. (1973a), "Visible and near-infrared spectra of minerals and rocks: VII. Acidic igneous rocks," *Modern Geology* , Vol. 4, pp 217-224.

Hunt, G.R., Salisbury, J.W., and Lenhoff, C.J. (1973b), "Visible and near-infrared spectra of minerals and rocks: VIII. Intermediate igneous rocks," *Modern Geology* , Vol. 4, 237-244.

Hunt, G.R., Salisbury, J.W. and Lenhoff, C.J. (1974), "Visible and near-infrared spectra of minerals and rocks: IX. Basic and ultrabasic igneous rocks," *Modern Geology* , Vol. 5, pp 15-22.

Hutchinson, C.F. (1982), "Techniques for combining Landsat and ancillary data for digital classification improvement," *Photogrammetric Engineering and Remote Sensing* , Vol. 48, No. 1, pp 123-130.

Hutsinpiller, A. and Taranik, J.V. (1986), "Detection of hydrothermal alteration at Virginia City, Nevada, using Airborne Imaging Spectrometer (AIS)," *Fifth Thematic Conference on Remote Sensing for Exploration Geology* , Reno, Nevada, pp 473-481.

IDRISI, A Grid-Based Geographic Analysis System , Graduate School of Geography, Clark University, Machassusts , U.S.A.

Jain, A.K. (1989), *Fundamentals of Image Processing* (Englewood Cliffs, N.J.: Prentice Hall).

Jaskolla, F. and Henkel, J. (1988), "Evaluation and digital processing of multispectral SPOT data,"*International Journal of Remote Sensing* , Vol. 9, Nos. 10 and 11, pp 1629-1637.

Jensen, J.R. (1986), *Introductory Digital Image Processing: A Remote Sensing Perspective* , (Englewood Cliffs, N.J.: Prentice-Hall).

Jenson, S.K. and Waltz, F.A. (1979), "Principal Component Analysis and Canonical Analysis in Remote Sensing," *Proceedings of the American Photogrammetric Society, 45th Annual Meeting* , Falls Church, Va., pp 337-348.

Kaufmann, H. (1984), "A Multiple Approach in Remote Sensing for Structural and Lithological Mapping by Use of MOMS/LANDSAT/ HCMM-Data," *Proceedings Integrated Approaches in Remote Sensing* , Guildford, U.K. , pp 337-347.

Kaufmann, H. (1988), "Mineral exploration along the Aqaba-Levant structure by use of TM data," *International Journal of Remote Sensing* , Vol. 9, Nos. 10 and 11, pp 1639-1658.

Kaufmann, H. and Pfeiffer, B. (1986), "Image optimization versus classification: an application oriented comparison of diffferent methods by use of Thematic Mapper data," *Proceedings of the Seventh International Symposium on Remote Sensing for Resources Development and Environmental Management* , Enschede, The Netherlands, pp 31-35.

Kepper, J., Logaski, T. and MacDonald, J. (1986), "Discrimination of lithologic units, alteration patterns, and major structural blocks in the Tonopah, Nevada area using Thematic Mapper data," *Fifth Thematic Conference on Remote Sensing for Exploration Geology* , Reno, Nevada, pp 97-115.

Kingston, M.J. and Crowley, J. (1989), "Lithologic mapping using AVIRIS data near Mountain Pass, California," *Proceedings of the Seventh Thematic Conference on Remote Sensing for Exploration Geology* , Calgary, Alberta, Canada, (Summary), p 15.

Krohn, D.M. (1986), "Spectral Properties (0.4-25 Microns) of Selected Rocks with Disseminated Gold and Silver Deposits in Nevada and Idaho, *Journal of Geophysical Research* , Vol. 91, No. 131, pp 767-783.

Kruse, F.A. (1986), "Use of Airborn Imaging Spectrometer data to map minerals associated with hydrothermally altered rocks in the northern Grapevine Mountains, Nevada and California," *Fifth Thematic Conference on Remote Sensing for Exploration Geology* , Reno, Nevada, pp 427-438.

Kruse, F.A. (1988), "Use of Airborn Imaging Spectrometer data to map minerals associated with hydrothermally altered rocks in the northern Grapevine Mountains, Nevada and California," *Remote Sensing of Environment* , Vol. 24, No. 1, pp 31-51.

Kruse, F.A. and Rains, G.L. (1984), "A technique for enhancing digital color images by contrast stretching in Munsell color space," International Symposium on Remote Sensing of Environment, *Third Thematic Conference on Remote Sensing for Exploration Geology* , Colorado Springs, Colorado, pp 755-760.

Lillisand, T.M. and Kiefer, R.W. (1987), *Remote Sensing and Image Interpretation* , 2nd edition (New York: John Wiley & Sons).

Liu, J.G. and Moore, J.McM. (1990), "Hue image RGB colour composition: a simple technique to suppress shadow and enhance spectral significance," *International Journal of Remote Sensing* , Vol. 11, No. 8, pp 1521-1530.

Lo, C.P. (1986), *Applied Remote Sensing* (London: Longman Scientific and Technical).

Loughlin, W.P., and Tawfiq, M.A., (1985), Discrimination of rock types and alteration zones from airborne MSS data: the Samran-Shayban and Mahd Adh Dhahab areas of Saudi Arabia, Proc. ERIM 4th Thematic

Conference: 'Remote Sensing for Exploration Geology', San Francisco, USA.

Lyon, R.J.P. (1975), "Mineral exploration applications of digitally processed Landsat imagery," *Proceedings of the First Annual William T. Pecora Memorial Symposium* , Sioux Falls, South Dakota, pp 271-292.

McBirde, J., Fielding, E. and Isacks, B. (1986), "Discrimination and supervised classification of volcanic flows of the Puna-Altipiano, Central Andes Mountains, using Landsat TM data," *Fifth Thematic Conference on Remote Sensing for Exploration Geology* , Reno, Nevada, pp 693-702.

McCabe, M.M. and Collins, P.V. (1985), "Image Processing Algorithms," *VLSI Image Processing* , ed. R.J. Offen (London: Collins), pp 52-98.

Magee, R.W., Moor, J.McM. and Coates, D. (1986), "Thematic Mapper data applied to mapping hydrothermal alteration in southwest New Mexico," *Fifth Thematic Conference on Remote Sensing for Exploration Geology* , Reno, Nevada, pp 373-382.

Mashhady, A.S., Hammad, M.A. and Reda, M. (1986), *Soil Resources and Land Potential for Al-Qasseem Region* (Riyadh, Saudi Arabia: King Saud University Press).

Mather, P.M. (1987), *Computer Processing of Remotely-Sensed Images: an Introduction* , (New York: John Wiley & Sons).

McCauley, J.F., Schaber, G.C., Breed, C.S., Grolier, M.J., Haynes, C.V., Issawi, B., Elachi, C., and Blom, R., (1982), " Subsurface Valleys and geoarcheology of the eastern Sahara revealed by shuttle radar" *Science* , Vol. 218, pp 1004-1019.

Meralli, L. (1992), "Acquisition, processing and distribution of experimental satellite data," *International Journal of Remote Sensing* , Vol. 13, Nos. 6 and 7, pp 1125-1136.

Morgan, J. and Szejwach, G. (1992), "Acquisition, processing and distribution of operational satellite data," *International Journal of Remote Sensing* , Vol. 13, Nos. 6 and 7, pp 1137-1152.

Mulder, N.J. (1980), "A view on digital image processing," XIVth ISP Congress, Hamburg, Commission III, *ITC Journal* , Vol. 3, pp 452-476.

Muller, J.P. (1988), *Digital image processing in remote sensing* (London and Philadelphia: Taylor and Francis).

Muller, Y. (1975), Geology and mineral exploration of the Al Jurdhawiyah area covering quadrangle 25/42 D: Bureau de recherches Geologiques et Minieres (Jeddah, Saudi Arabian Mission), *Report 75-JED-21* , scale 1:100,000.

Niblack, W. (1986), *An introduction to digital image processing* (London: Prentice-Hall International (UK) Ltd.).

Nicholas, D. (1983), "Digital hardware," *Manual of Remote Sensing* , 2nd ed., ed. R.N. Colwell (Falls Church, Va.: American Society of Photogrammetry), pp 841-871.

Oldfield,r.b. (1988), "Lithologic mapping of norheast Argentina with remote sensing data using Tonal, Textural and Contextual features," *Ph.D. thesis* , Aston University, U.K.

Podwysocki, M.H., Salisbury, J.W., Bender, L.V., Jones, O.D., and Mimms, D.L. (1983), "Analysis of Landsat-4 TM data for lithologic and image mapping purposes," *NASA Conference Publication 2326* , Vol. 2, pp 35-39.

Podwysocki, M.H., Brickey, D. and Salisbury, J. (1986), "Remote compositional mapping of rocks using reflected and emited radiance," *Fifth Thematic Conference on Remote Sensing for Exploration Geology* , Reno, Nevada, pp 713-714.

Pontual, A. (1987), "The effect of weathering minerals on the spectral response of rocks in Landsat TM imagery," *Advances in Digital Image Processing , Proceedings of the Remote Sensing Society Annual Conference* , Nottingham, pp 549-558.

Pontual, A., (1990), " Lithological Information in remotely sensed images and surface weathering in arid region", *Ph.D thesis,* Open University, U.K.

Power, R.W., Ramirez, L.F., Redmond, C.D., and Elberg, E.L., Jr., (1966), Geology of the Arabian Peninsula-Sedimentary geology of Saudi Arabia: *U.S. Geological Survey Professional paper 560-D* .

Qari, M.Y., (1990), geological Analysis of parts of the southern Arabian Shield based on Landsat TM imagery. *Ph.D. thesis,* Department of Geological Sciences, University College London, UK.

R-CHIPS Image Processing Software, User Guide , Version 3.0 , I.S. Limited, The Department of Geology, Reading University, Reading.

Rees, W.G. (1990), *Physical Principles of Remote Sensing* (Cambridge: Cambridge University Press).

Richards, J.A. (1986). *Remote Sensing Digital Image Analysis* (Berlin: Springer-Verlag).

Rosenfeld, A. and Kak, A.C. (1976), *Digital Picture Processing* (New York: Academic Press).

Rothery, D.A. (1985), "Interactive processing of satellite images for geological interpretation -- a case study," *Geological Magazine* , Vol. 122, No. 1, pp 57-63.

Rothery, D.A. (1987a), "Decorrelation stretching and related techniques as an aid to image interpretation in geology," *Advances in Digital Image Processing* , Proceedings of the Remote Sensing Society Annual Conference, Nottingham, pp 194-203.

Rothery, D.A. (1987b), "Improved discrimination of rock units using Landsat Thematic Mapper imagery of the Oman ophiolite," *Journal Geological Society London* , Vol. 144, pp 587-597.

Rothery, D.A. and Milton, E.J. (1981), "Lithological discrimination in an ophiolite terrain: Landsat MSS imagery and reflectance measurements in Oman," *Geological and Terrain Analysis Applications of Remote Sensing* , eds. J.A. Allen and M.J. Bradshaw (Remote Sensing Society), pp 3-23.

Rothery, D.A. and Francis, P.W. (1987), "Synergistic use of MOMS-01 and Landsat TM data," *International Journal of Remote Sensing* , Vol. 8, No. 3, pp 501-508.

Rothery, D.A. and Hunt, G.A. (1990), "Technical note: a simple way to perform decorrelation stretching and related techniques on menu-driven image processing systems," *International Journal of Remote Sensing* , Vol. 11, No. 1, pp 133-137.

Rowan, R.L. (1975), "Application of satellites to geological exploration, *American Scientist* , Vol. 63, pp 393-403.

Rowan, L.C., Wetlaufer, P.H., Goetz, A.F.H, Billingsley, F.C. and Stewart, J.H. (1974), "Discrimination of Rock Types and Detection of Hydrothermally Altered Areas in South-Central Nevada by the Use of Computer Enhanced ERTS Images," *U.S.G.S. Prof. Paper 883* .

Rowan, L.C., Goetz, A.F.H. and Ashley, R.P. (1977), "Discrimination of Hydrothermally Altered and Unaltered Rocks in Visible and Near Infrared Multispectral Images, *Geophysics* , Vol. 42, No. 3, pp 522-535.

Rowan, L.C. and Lathram, E.H. (1980), "Mineral exploration," *Remote Sensing in Geology* , eds. B.S. Siegal and A.R. Gillespie (New York: John Wiley & Sons), pp 553-605.

Rowan, L.C., Anton-Pacheco, C., Brickey, D.W., Kingston, M.J., Payas, A., Vergo, N. and Crowley, J.K. (1987), "Digital classification of contact metamorphic rocks in Extremadura, Spain using Landsat Thematic Mapper data," *Geophysics* , Vol. 52, No. 7, pp 885-897.

Sabins, F.F. Jr. (1987), *Remote Sensing: Principles and Interpretation* , 2nd edition (New York: W.H. Freeman and Company).

Schowengerdt, R.A. (1983), *Techniques for Image Processing and Classification in Remote Sensing* (New York: Academic Press).

Segal, D.B. (1982), "Theoretical basis for differentiation of ferric-iron bearing minerals, using Landsat MSS data," *Proceedings of the Symposium on Remote Sensing Environment* , 2nd Thematic Conference Remote Sensing Exploration Geology, Fort Worth, Texas, pp 949-951.

Segal, D.B., Merin, I.S. and Place, M.C. (1986), "Use of digitally processed laboratory reflectance spectra for the definition of probable microseepage-induced mineralogic variations, Lisbon Valley, Utah," *Fifth Thematic Conference Remote Sensing for Exploration Geology,* Reno, Nevada, pp 667-676.

Serra, J. (1982), *Image Analysis and Mathematical Morphology* (London and New York: Academic Press).

Settle, M. (1984), *The Joint NASA/Geosat test case project , Executive summary* , pt. 1, American Association Petroleum Geologist, AAPG Book Store, Tulsa, Oklahoma, U.S.A.

Sheffield, C. (1985), "Selecting band combinations from multispectral data," *Photogrammetric Engineering and Remote Sensing* , Vol. 51, No. 6, pp 681-687.

Short, N.M. (1982), *The Landsat Tutorial Workbook* , NASA Reference Publication 1078 (Washington: NASA Scientific and Technical Information Branch).

Short, N.M. (1984), "Accuracy of geologic maps produced from Landsat data," *International Symposium on Remote Sensing of*

Environment, Third Thematic Conference on Remote Sensing for Exploration Geology , Colorado Springs, Colorado, pp 711-721.

Siegal, B.S. and Abrams, M.J. (1976a), "Geologic mapping using Landsat data," *Photogrammetric Engineering and Remote Sensing* , Vol. 42, pp 325-337.

Siegal, B.S. and Abrams, M.J. (1976b), "Evaluation of classification techniques applied to geologic mapping using Landsat data," *Proceedings of the American Society of Photogrammetry* , 42nd Annual Meeting, Washington, D.C., pp 543-544.

Siegal, B.S. and Gillespie, A.R. (1980), *Remote Sensing in Geology* (New York: John Wiley & Sons, Inc.).

Singh, A. and Harrison, A. (1985), "Standardised principal components," *International Journal of Remote Sensing* , Vol. 6, No. 6, pp 883-893.

Smith, E.A., Barnes, D.P., Johnson, P.R., Bognar, B., Garfield, L. and Scheibner, E. (1984), A Review of the Geology, Mineralization, and Mineral Resource Potential of the Kingdom of Saudi Arabia , Saudi Arabian Directorate General of Mineral Resources, Jeddah, Saudi Arabia, *Open-File Report RF-OF-05-1*.

Soha, J.M. and Schwartz, A.A. (1978), "Multispectral histogram normalization contrast enhancement," *Fifth Canadian Symposium on Remote Sensing* , Victoria, pp 86-93.

Spatz, D., Taranik, J. and Hsu, L. (1987a), "Application of TM imagery to mapping volcanic rock assemblages at Tertiary Calderas of the basin and range province," *IGARSS Symposium Digest* , pp 1299-1308.

Spatz, D., Taranik, J. and Hsu, L. (1987b), "Desert varnish on volcanic rocks of the basin and range province: Composition, morphology, distribution, origin and influence on Landsat imagery," *The Twenty-First International Symposium on Remote Sensing of Environment, Ann Arbor, Michigan* , pp 843-852.

Spatz, D.M., Taranik, J.V. and Hsu, L.C. (1989), "Differentiating volcanic rock assemblages using Landsat Thematic Mapper data -- Influence of petrochemistry and desert varnish," *Advance Space Research* , Vol. 19, No. 1, pp (1)93-(1)98.

Stoeser, D.B. and Camp, V.E. (1985), "Pan-African microplate accretion of the Arabian Shield," *Geologic Society of America Bulletin* , Vol. 96, pp 817-826.

Suits, G.H. (1983), "The nature of electromagnetic radiation," *Manual of Remote Sensing* , ed. R.G. Reeve (Falls Church, Va.: American Society of Photogrammetry).

Sultan, M., Arvidson, R.E., Starchio, N.C. (1986), "Mapping of serpentinites in the eastern desert of Egypt by using Landsat Thematic Mapper data," *Geology* , Vol. 14, pp 995-999.

Swain, P.H. and Davis, S.M. (1978), *Remote Sensing: the Quantitative Approach* (New York: McGraw-Hill).

Townshend, J.R.G., ed. (1981), *Terrain Analysis and Remote Sensing* (London: George Allen and Unwin).

Townshend, J.R.G. (1992), "Land cover," *International Journal of Remote Sensing* , Vol. 13, Nos. 6 and 7, pp 1319-1328.

Townsend, T. (1986), "Detection of geologic features in Landsat TM imagery not revealed in Landsat MSS imagery," *Fifth Thematic Conference on Remote Sensing for Exploration Geology* , Reno, Nevada, pp 651-654.

Ulaby, F.T., Goetz, A.F.H. (1987), "Remote sensing techniques," *Encyclopedia of physical science and technology* (New York: Academic Press), Vol. 12, pp 164-196.

Volk, P., Haydn, R., Bodechtel, J. (1986), "Integration of remote sensing and other geodata for ore exploration -- a SW Iberian case study," *Proceedings of the International Symposium on Remote Sensing Environment , 5th Thematic Conference on Remote Sensing Exploration Geology* , Reno, Nevada, pp 733-744.

Watson, A.I. (1984), "The physical basis of remote sensing," *Proceedings Univ. Dundee Summer School "Remote Sensing Application in Civil Engineering* , Dundee U.K., pp 9-13.

Watson, A.I. (1987), "A new method of classification for Landsat data using the 'watershed' algorithm," *Pattern Recognition Letters* , Vol. 6, pp 15-19.

Watson, A.I., Vaughan, R.A., and Powell, M., (1992), "Classification using the watershed method," *International Journal of Remote Sensing,,* Vol. 13, No. 10, pp 1881- 1890.

Watson, R.D. (1972), "Spectral reflectance and photometric properties of selected rocks," *Remote Sensing of Environment* , Vol. 2, pp 95-100.

Whitney, G.G., Abrams, M.J., Goetz, A.F.H. (1983), "Mineral discrimination using a portable ratio-determining radiometer, *Economic Geology* , Vol. 78, pp 688-698.

Williams, D.L., Irons, J.R., Markham, B.L., Nelson, R.S., Toll, D.L., Latty, R.S. and Stauffer, M.L. (1983), "Impact of Thematic Mapper sensor characteristics on classification accuracy," *Proceedings of the IEEE International Geoscience and Remote Sensing Symposium* , pp 5.1-5.9.

Williams, R.S. Jr. (ed.) (1983), "Geological applications," *Manual of Remote Sensing* , 2nd ed., ed. R.N. Colwell (Falls Church, Va.: American Society of Photogrammetry), pp 1667-1951.

Williams, R.S. Jr. and Carter, W.D. (eds.) (1976), "ERTS-1: A new window on our planet," *U.S. Geological Survey Professional Paper 929* (Washington: U.S. Government Printing Office).

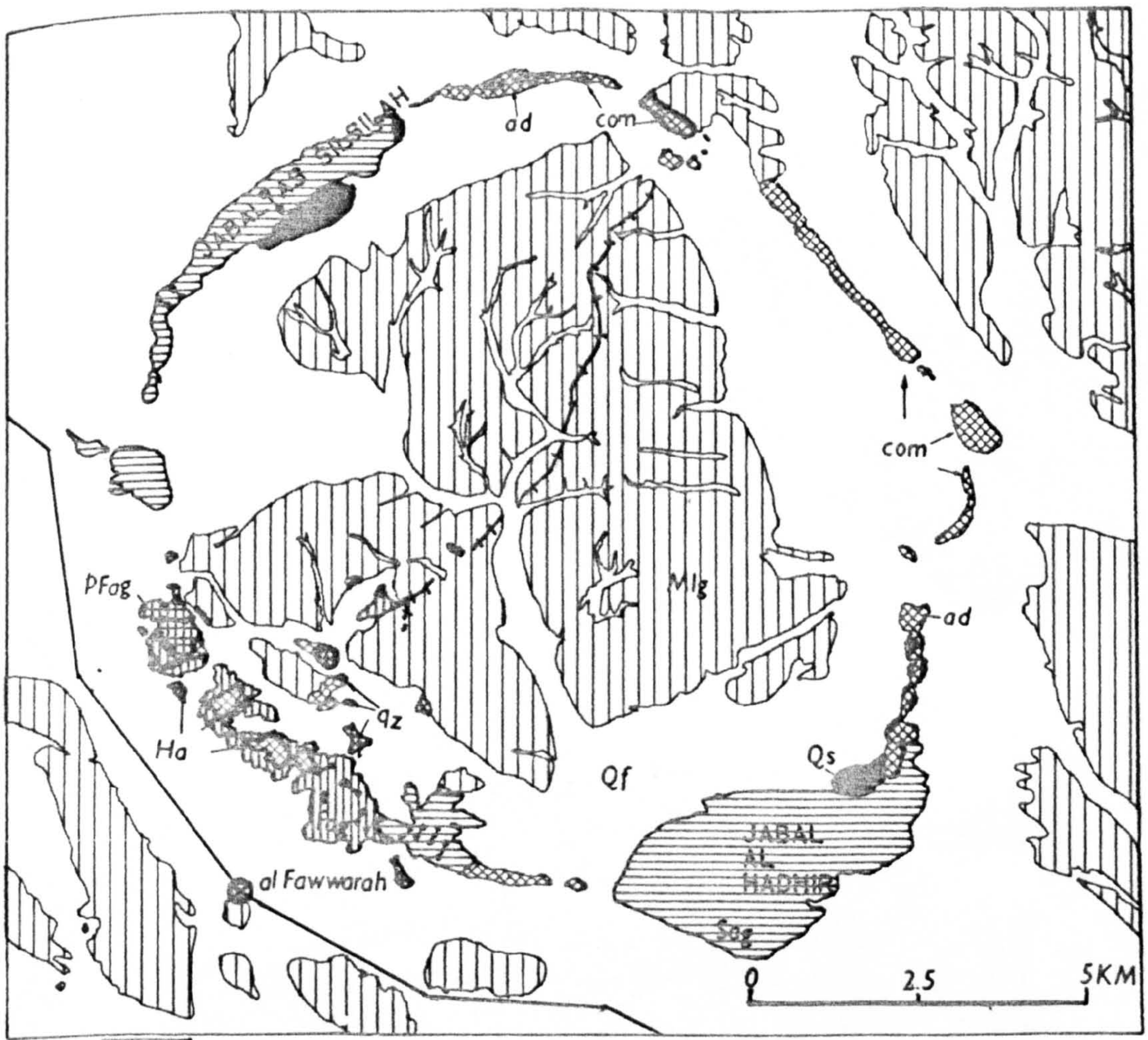

Eolin Sand

Qf Alluvial fan and Apron deposits

quartz vein

Fawwarah alkali-feldspar granite

quartz pegmatite

Ha Hadhir aplite

proto Fawwarah alkali-feldspar granite

Silsilah alkali granite

Commendite

alkaline dacite

Maraghan lithic graywacke

Figure 2.5. Geologic map of Silsilah ring complex, test area 1 (after Du Bray, 1988).

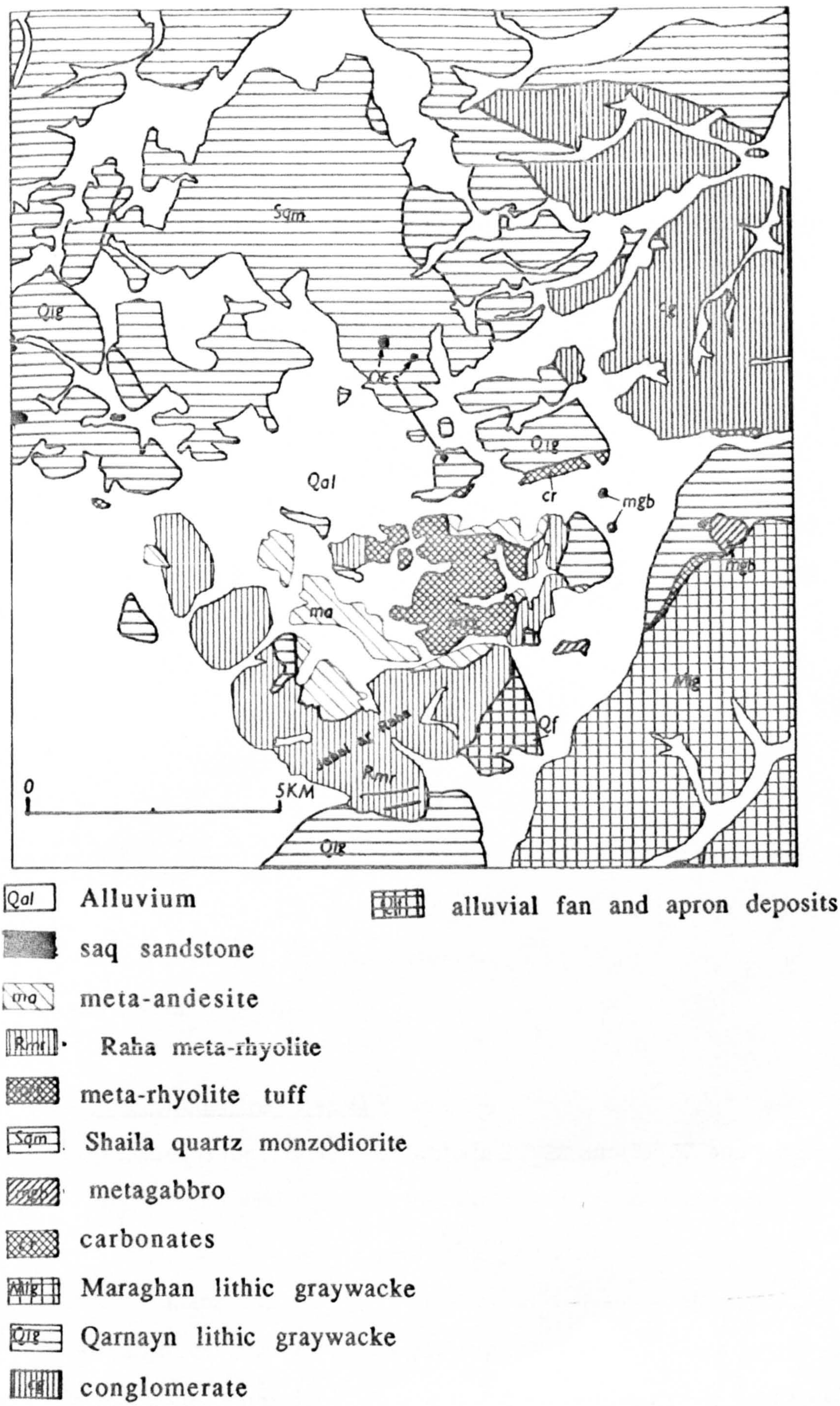

Figure 2.7. Geologic map of Jabal ar Raha, test area 2 (adapted from Du Bray, 1983).

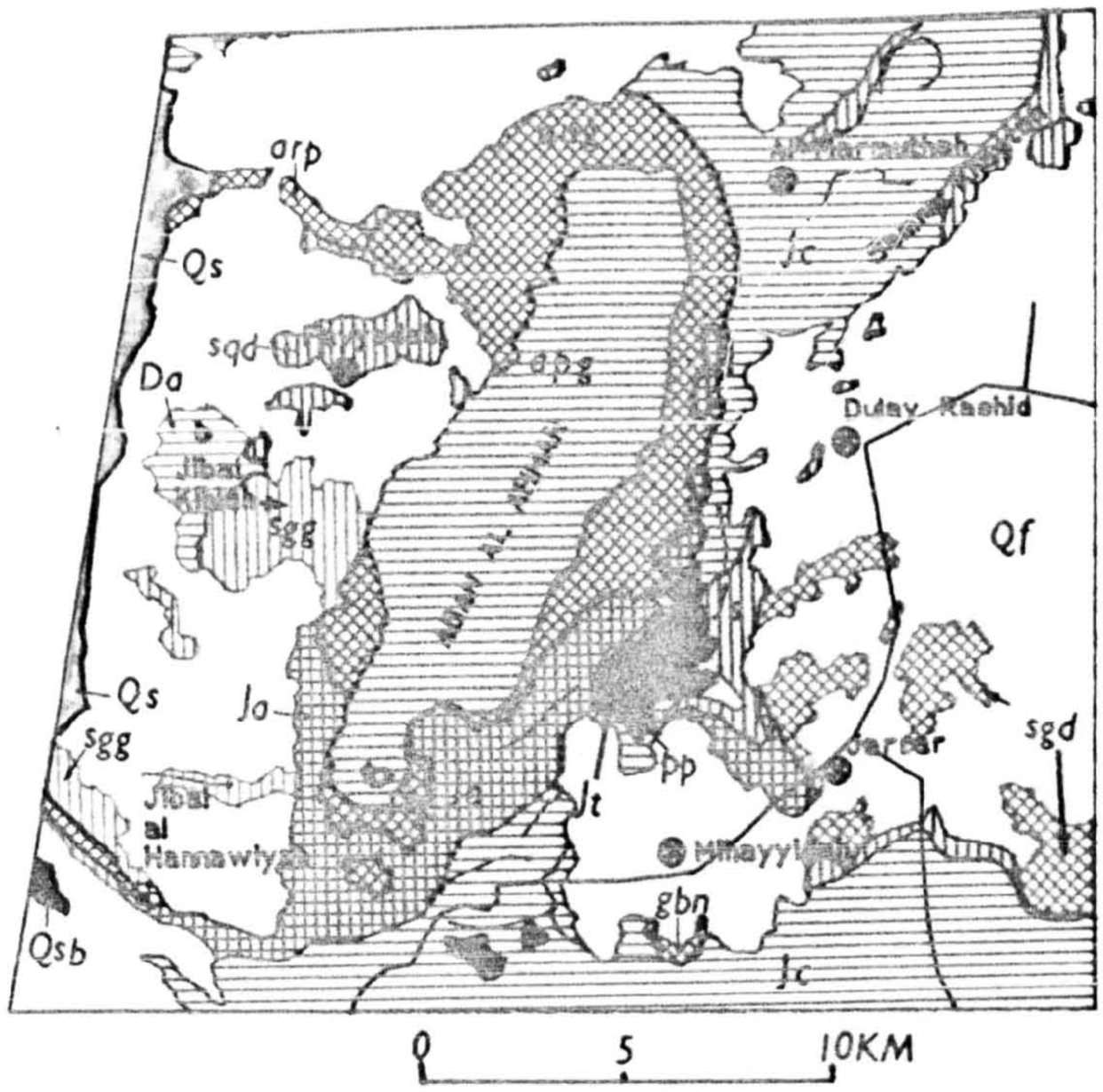

Qs eolian sand
sabkha deposits
Qf alluvial fan and apron deposits
rhyolite porphyry
arfvedsonite granite
perthite granite
gabbronorite
Isharat porphyry
sandstone
lapilli tuff
conglomerate
Muqawqi andesite
granodiorite
granophyre
Khaytan quartz diorite
Da Dhiran meta-andesite

Figure 2.8. Geologic map of Aban Ahmar, test area 3 (adapted from Cole, 1988).

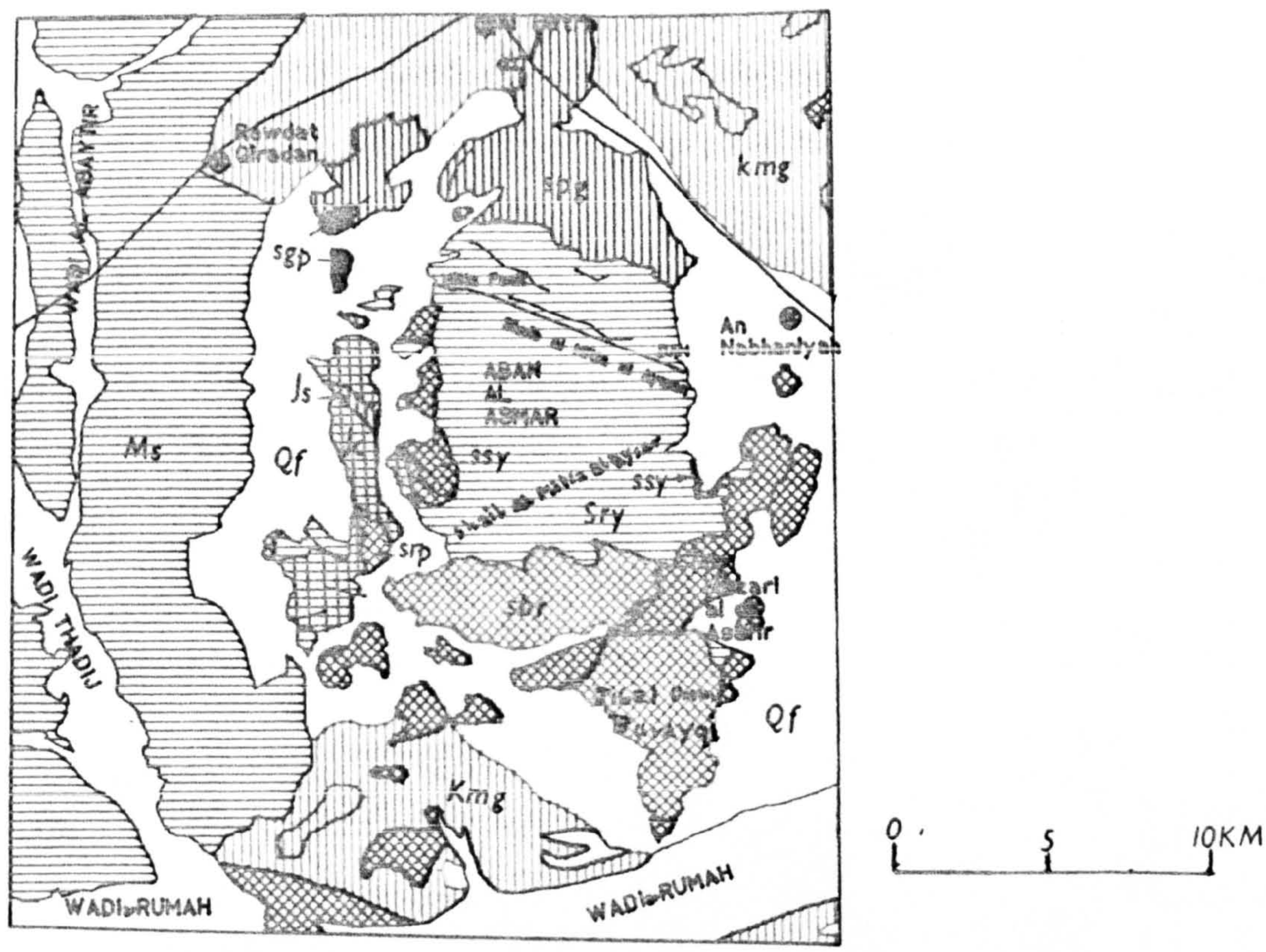

Qf alluvial fan and apron deposits

granite porphyry

quartz syenite

rhyolite porphyry

hornblend perthite granite

biotite perthite granite

sbr introsion breccia

Sry Samra rhyolite

Js sandstone member

conglomerate

Kmg monzogranit

Ms Maraghan sandstone

Figure 2.11. Geologic map of Aban Asmar, test area 4 (adapted from Cole, 1988).